



HAL
open science

Magnesium-based biodegradable materials: from surface functionalization to cellular evaluation

Laura Catalina Córdoba Román

► To cite this version:

Laura Catalina Córdoba Román. Magnesium-based biodegradable materials: from surface functionalization to cellular evaluation. Material chemistry. Université Pierre et Marie Curie - Paris VI; Instituto superior técnico (Lisbonne), 2016. English. NNT: 2016PA066237 . tel-01434181

HAL Id: tel-01434181

<https://theses.hal.science/tel-01434181>

Submitted on 13 Jan 2017

HAL is a multi-disciplinary open access archive for the deposit and dissemination of scientific research documents, whether they are published or not. The documents may come from teaching and research institutions in France or abroad, or from public or private research centers.

L'archive ouverte pluridisciplinaire **HAL**, est destinée au dépôt et à la diffusion de documents scientifiques de niveau recherche, publiés ou non, émanant des établissements d'enseignement et de recherche français ou étrangers, des laboratoires publics ou privés.

Université Pierre et Marie Curie
Instituto Superior Técnico

Ecole doctorale Physique et Chimie des Matériaux

Laboratoire Chimie de la Matière Condensée de Paris/Équipe Matériaux et Biologie

**Magnesium-based biodegradable materials: from surface
functionalization to cellular evaluation**

By Laura Catalina Córdoba Román

PhD thesis in Physics and Chemistry of Materials

Directed by Thibaud Coradin and Fátima Montemor

Defended and publicly presented on 4th of July 2016

Jury

Ludovic BELLOT-GURLET, *Professeur, Université Pierre et Marie Curie Paris 6, France – Reviewer*

Maria Teresa NOGUEIRA LEAL DA SILVA DUARTE, *Full Professor, Instituto Superior Técnico, Universidade de Lisboa, Portugal – Reviewer*

Emmanuel BELAMIE, *Directeur d'Études, École Pratique des Hautes Études, France – Reporter*

Thibaud CORADIN, *Directeur de Recherche CNRS-LCMC, Université Pierre et Marie Curie Paris 6, France – Director*

Johanes Matheus CORNELIS MOL, *Associate Professor, TU Delft /Delft University of Technology, Netherlands – Reporter*

Maria de Fátima GRILO DA COSTA MONTEMOR, *Associate Professor, Instituto Superior Técnico, Universidade de Lisboa, Portugal – Director*

João Carlos SALVADOR SANTOS FERNANDES, *Assistant Professor, Instituto Superior Técnico, Universidade de Lisboa, Portugal – Reviewer*

Titre de la thèse: Les alliages Magnésium biodégradables: fonctionnalisation de la surface et de l'évaluation cellulaire

Résumé

Les alliages de Magnésium (Mg) sont une nouvelle génération de matériaux biodégradables ayant une bonne ostéointégration et un module d'élasticité similaire à celle de l'os humain. Ces propriétés rendent ces matériaux attrayant pour produire des implants temporaires pour la réparation osseuse. Toutefois, les alliages Mg se dégradent rapidement *in vivo*, rendant nécessaire de contrôler leur vitesse de corrosion pour accompagner la régénération tissulaire. Parmi les approches proposées pour réduire la corrosion et la biocompatibilité des alliages Mg, les plus utilisées sont les couches de conversion et les revêtements de surface. Dans ce travail une approche synergique qui combine une réduction du taux de corrosion avec l'amélioration de la biocompatibilité des alliages Mg est proposée. De nouveaux revêtements bicouches ont été déposés sur la surface d'alliages AZ31 et ZE41 : (i) un revêtement de silane-TiO₂ déposé par dip-coating et (ii) des couches supérieures de collagène de type I et/ou de chitosane. Le revêtement inférieur a été efficace pour réduire la corrosion des alliages dans un fluide corporel simulé et en milieu de culture. La culture cellulaire *in vitro* de fibroblastes et ostéoblastes, a révélé que le dépôt additionnel de biopolymères a amélioré la réponse biologique du revêtement de silane-TiO₂. Ces résultats montrent qu'il existe un effet combiné des revêtements bicouches et de la composition des alliages sur la réponse à la corrosion et sur le comportement cellulaire. Ce travail apporte donc une nouvelle contribution à la compréhension de l'évolution de la corrosion des alliages Mg dans des environnements biologiques.

Mots-clés : alliages de magnésium, corrosion, implants biodégradables, revêtements, collagène, chitosane.

Título Ligas de Magnésio biodegradáveis: Funcionalização de superfícies e avaliação celular

Resumo

As ligas de magnésio (Mg) são consideradas como uma nova geração de materiais biodegradáveis, com boas propriedades de osteointegração e módulo de elasticidade semelhante ao do osso humano. Estas propriedades tornam as ligas de Mg materiais com elevado potencial para a fabricação de implantes metálicos biodegradáveis para aplicações em reparações ósseas que requerem suporte temporário. No entanto, as ligas de Mg são muito suscetíveis à corrosão e degradam-se rapidamente no ambiente *in vivo*, sendo o processo acompanhado de eventos indesejáveis como alcalinização e libertação de hidrogénio gasoso. Por estas razões é essencial controlar rigorosamente o processo de corrosão, de modo a que a velocidade de degradação do implante de Mg seja compatível com os processos de cicatrização dos tecidos e com as exigências mecânicas exigidas ao implante. As consequências da corrosão acelerada numa liga de Mg *in vivo* incluem a perda precoce das propriedades mecânicas do implante, assim como eventos nocivos associados à atividade de corrosão.

Com a finalidade de controlar a velocidade de corrosão das ligas de Mg, existem várias estratégias que têm vindo a ser propostas. As estratégias de proteção contra a corrosão mais utilizadas em ligas de Mg incluem os tratamentos de conversão e a aplicação de revestimentos de efeito barreira. Os revestimentos de superfície, de efeito barreira, podem ser orgânicos, híbridos ou inorgânicos e as suas propriedades físicas e químicas podem ser manipuladas consoante a resistência a corrosão pretendida. O método de deposição do revestimento geralmente influencia a espessura e a estrutura da matriz do revestimento, e consequentemente as suas propriedades barreira.

A principal função do revestimento é atuar como uma barreira física que visa controlar a velocidade de corrosão do metal após a sua exposição à solução corrosiva. Para aplicações biomédicas é exigido que este revestimento desenvolva interações favoráveis com as células ósseas e tecidos circundantes. De modo a maximizar a biocompatibilidade dos revestimentos têm sido desenvolvidas várias abordagens que incluem, por exemplo, a adição de partículas, de nanopartículas ou de fibras biocompatíveis, obtendo-se assim revestimentos compósitos. Os revestimentos modificados com partículas de hidroxiapatite são bastante comuns uma vez que a hidroxiapatite é um dos principais componentes do osso. De facto, o que se pretende é que a hidroxiapatite confira propriedades bioactivas ao revestimento.

Os materiais poliméricos naturais, encontrados na natureza, têm despertado muita atenção na comunidade científica nas últimas décadas. De entre estes materiais salientam-se, pelas suas propriedades biocompatíveis, vários bio polímeros como colagénio e quitosano. O colagénio é o principal componente estrutural dos tecidos conjuntivos, sendo a proteína mais abundante em mamíferos. O quitosano é o segundo polissacárido mais abundante depois da celulose e é derivado de fontes naturais como os fungos e alguns crustáceos. Estes biopolímeros possuem propriedades biológicas únicas, que a maioria dos materiais inorgânicos não conseguem oferecer, incluindo funcionalidades estruturais e multidimensionais. O colagénio e o quitosano têm sido produzidos para a preparação de *scaffolds*, para a produção de hidrogel e revestimentos. Tem-se verificado que é possível controlar a velocidade de corrosão de ligas de Mg em meio fisiológico utilizando revestimentos que combinam estes biopolímeros com outros compostos. Verifica-se também que esta combinação melhora substancialmente a biocompatibilidade de ligas de Mg e a atividade celular na superfície das mesmas.

Esta dissertação de doutoramento visa desenvolver novos revestimentos, combinando uma camada de efeito barreira obtida por sol-gel com uma camada polimérica biocompatível, para funcionalização da superfície de ligas de Mg AZ31 e ZE41 para aplicações em implantes ortopédicos.

A primeira fase visou o desenvolvimento e caracterização de um revestimento de silano-TiO₂ obtido por sol-gel para controlo da velocidade de corrosão. O revestimento foi aplicado por imersão (dip coating), obtendo-se uma espessura homogénea de 3 µm, e revelou-se eficaz na redução da atividade de corrosão das duas ligas em fluido corporal simulado (FCS) e em meio celular modificado Dulbeco (MCMD). Na segunda fase deste trabalho foi aplicada, sobre o revestimento de silano-TiO₂, uma segunda camada de colagénio tipo I ou quitosano de modo a melhorar o desempenho biológico das ligas de Mg. Em cada uma das ligas de Mg foram aplicados, em camadas consecutivas, os seguintes revestimentos: (i) silano-TiO₂/colagénio e (ii) silano-TiO₂/quitosano. A avaliação da resistência à corrosão foi efetuada por espectroscopia de impedância eletroquímica, tendo-se verificado que as camadas de bio polímero não afetavam as propriedades protetoras do revestimento à base de silano em cada um dos meios fisiológicos estudados, FCS e MCMD.

A presença do revestimento de silano-TiO₂ como camada barreira e a composição do meio corrosivo revelaram-se fatores muito importantes na velocidade de degradação das ligas e na composição dos produtos de corrosão. Os produtos de corrosão formados nas duas ligas

de Mg expostas a FCS consistiram essencialmente numa única camada de $Mg(OH)_2$ /hidroxiapatite de baixa cristalinidade. No entanto, em MCMD os produtos de corrosão apresentaram uma organização hierárquica de agregados esféricos de hidroxiapatite formados sobre uma camada de $Mg(OH)_2$. Durante a imersão, os produtos de corrosão transformaram-se em carbonatos de magnésio e carbonatos de cálcio.

Os ensaios *in vitro*, utilizando fibroblastos e osteoblastos, revelaram uma melhor resposta biológica na presença de colagénio e quitosano. Os vários ensaios efetuados permitiram determinar o desempenho biológico dos revestimentos de camada dupla em função do substrato. Verificou-se que os osteoblastos e os fibroblastos apresentavam maior viabilidade na liga ZE41 do que na liga AZ31. Verificou-se também que a viabilidade dos osteoblastos dependia fortemente da composição da superfície. Na presença de colagénio verificou-se que as células ficavam presas numa rede de fibras tridimensionais, como resultado das inúmeras fibras que se formaram a partir do colagénio tipo I.

A estratégia adotada neste trabalho mostrou ser um método viável para o controle da velocidade de corrosão e para a funcionalização da superfície de ligas de Mg para implantes ortopédicos biodegradáveis.

Palavras-chave: Ligas de magnésio, implantes biodegradáveis, revestimentos, colágeno, quitosano.

Title Mg-based biodegradable materials: from surface functionalization to cellular evaluation

Abstract

Magnesium (Mg) alloys are a new exciting generation of biodegradable materials with good osseointegration, and elastic modulus similar to that of human bone. These characteristics make Mg alloys very attractive materials to produce biodegradable metallic implants for bone repairing applications that require temporary support. However, Mg alloys degrade rapidly in the *in vivo* environment making necessary to control their corrosion rate to accompany the tissue healing processes. Discrepancies between the corrosion rate of the alloy and the healing rate of the surrounding tissue may result in adverse tissue reactions. The consequences of accelerated corrosion of Mg alloys implants *in vivo* may include early loss of mechanical properties of the implant and toxic events due to side-reactions and accumulation of corrosion products. To control the corrosion rate of Mg alloys several approaches have been proposed. The most used ones are conversion films and surface coatings. Coatings include inorganic, hybrid or organic layers whose physical and chemical characteristics can be tailored to control the corrosion rate of the underlying substrate. The coating deposition method generally influences the thickness and the matrix structure of the coating that also impact on its barrier properties.

The main role of the coating is to control the corrosion rate of the Mg alloy during early exposure to the corrosive environment; nevertheless, it must interact in a favorable manner with bone cells and the surrounding tissues. Several routes have been proposed to increase the biocompatibility of barrier coatings for corrosion protection. These include the incorporation of secondary components in the form of particles, nanoparticles or fibers into the coating to obtain hybrid/composite layers. Composite coatings containing hydroxyapatite particles are quite common since hydroxyapatite is one of the main components of the bone. Indeed, hydroxyapatite is expected to confer bioactive properties to the coating layer.

Natural polymer materials —those found in nature— have been drawing a lot of attention from researchers during the last decades. Among the various available biopolymers currently investigated, collagen and chitosan are remarkable. Collagen is the main structural component of connective tissues and the most abundant protein in mammals. Chitosan is the second most abundant polysaccharide after cellulose, derived from natural occurring sources such as fungi and some crustaceans. These biopolymers have unique biological properties that

most of inorganic materials do not offer, providing structural and multidimensional functionalities. Both collagen and chitosan have been produced into scaffolds, hydrogels and coatings. Collagen and chitosan coatings in combination with other components have shown to decrease the corrosion rate of Mg alloys in inorganic simulated body fluids. Additionally, these bio-coatings resulted on improved biocompatibility and cell delivery of Mg alloys.

In the present research work, we propose novel bi-layered coatings to functionalize the surface of AZ31 and ZE41 Mg alloys for bone repair applications. First, a bottom silane-TiO₂ coating to control the corrosion rate was formulated and deposited on both alloys by the dip-coating technique. The homogeneous 3 μm-thick silane-based coating was effective in slowing down the corrosion rate of substrates in simulated body fluid (SBF) and in Dulbecco's Modified Eagle's Medium (DMEM). Secondly, top layers of type I collagen and/or chitosan to enhance biological performances were developed. Two bi-layered coating architectures were implemented on each Mg alloy: (i) silane-TiO₂/collagen and (ii) silane-TiO₂/chitosan. Electrochemical impedance spectroscopy measurements evidenced that the outermost biopolymer layers did not have a detrimental effect on the barrier properties of the silane-based coating in both SBF and DMEM.

The composition of the corrosion products was defined by the presence of the silane-TiO₂ coating and the composition of the corrosive medium. In SBF the corrosion products of both AZ31 and ZE41 consisted mainly of a Mg(OH)₂/hydroxyapatite layer poorly crystalline. However, at early immersion in DMEM the corrosion products resulted in a hierarchical arrangement of hydroxyapatite sphero-aggregates that grew over a Mg(OH)₂ layer. As immersion time elapsed, the corrosion products transformed into magnesium carbonate and calcium carbonate compounds.

Cell *in vitro* tests, with fibroblasts and osteoblasts, revealed that the biopolymers enhanced the biological response of the silane-TiO₂ coating. Further characterization allowed us to determine the performance of the bi-layered coatings as a function of the substrate. The results showed that osteoblasts and fibroblasts have higher viability on ZE41 compared to AZ31 alloy. In general, osteoblasts exhibited high dependence on the surface composition. In the coating architecture containing collagen, the cells were trapped in a loose 3D mesh as result of a fibrillogenesis process underwent by the originally deposited type I collagen.

Our strategy showed to be a viable method to control the corrosion rate and to functionalize the surface of Mg alloys intended to fabricate biodegradable implants for bone repair applications.

Keywords: Magnesium alloys, biodegradable implants, coatings, collagen, chitosan.

Acknowledgements

Move to live in Europe aiming to get a Ph.D. degree has been a challenging-fruitful experience. I thought it was not going to be easy, and it resulted I was right. I am very grateful because of the difficulty level I had to face in everything, every day, in Portugal and in France from the first day I stepped on Europe. The most important thing I take from this journey: myself overcoming my own limitations.

I want to thank my supervisor in Portugal Fátima Montemor for selecting me and inviting me to be part of this project and for trusting my work. Thank you for supporting me whenever I needed it.

To my supervisor in France Thibaud Coradin, thank you for your always kind advice and support. Thank you for welcoming me in the laboratory in France and for all the paperwork you have had to deal with because of me at UPMC.

I want to thank Christophe Hélyary for guiding me and training me in working with cells. I enjoyed every sample. Thank you for your support and for the enriching discussions we had along with Thibaud.

Thank you to François Portier, Gervaise Mosser, Xiaoling Wang, Bernard Haye, Aurelien Tidu, Carole Aimé, Marine Blondeau and Nada Ben Ahmed for welcoming me in the laboratory in Paris. Thank you all for the nice lunches we shared together. Special thanks to Isabelle Génois for the many hours we spent together in the SEM analyzing my samples.

Thanks to my colleagues and friends Marta Alves, Maryna Taryba, Darya Snihirova, Catarina Santos, Natalia Flores, Mirela Lourenço, Yegor Morozov, Amir Zomorodian, Bruno Martins, Bruno Nunes, Pedro Nolasco, Joana Madeira and Tuyen Nguyen for being always willing to help and for the warm welcome in Lisbon since day one.

Very special thanks to Sofia Panão, Andreia Marques, Ana Lúcia Morais, Angélica Cáceres, Doris Colorado and Natalia Pereira for being my family in Lisbon and in Paris. Thank you all!!

Thanks my family and friends in Colombia for always keeping me in your hearts and supporting me through the distance.

Special thanks to the IDS-FunMat Consortium for giving me the opportunity to carry out my doctoral research within the framework of an European programme awarding me with a doctoral scholarship. Thanks for all the enriching meetings the Consortium promoted for we all the doctoral candidates. Thanks for the opportunities to learn from new cultures, taste new dishes and meet new people. I enjoyed every place and every moment!

I dedicate this book to the subtle Magic that is always here making possible the impossible.

It works!!

Here is the beginning of the journey...

LCCR

*“Nada impide Tomar la mente como un laboratorio y aplicar esa misma lógica —
redescubierta por la Física Cuántica— a lo que ocurre en y con la mente”*

El Efecto Observador indica que lo obtenido en lo real, depende directamente de lo que se espera obtener, es decir, de aquello que rige en lo Psíquico, y por tanto en lo Energético, y por tanto en el Físico...

*...todo Texto, toda Parábola, todo Relato De Enseñanza del Camino, tiene Cuatro niveles de lectura. El **Primer Nivel** consiste en la lectura habitual e ingenua que ubica al lector por fuera de lo que lee y como espectador pasivo de eso. Al **Segundo Nivel** se Accede Desocultando que todo Relato que provenga de La Religión Original, no está hablando sólo en general, sino que está íntimamente conectado con Quien lo lee...*

JL, El Otro Camino

This project was funded by



International Doctoral School
in Functional Materials
for Energy, Information technology and Health



TABLE OF CONTENTS

LIST OF FIGURES	xxi
LIST OF TABLES	xxv
LIST OF ACRONYMS AND ABBREVIATIONS	xxvii
1. INTRODUCTION.....	1
2. MAGNESIUM AS BIOMATERIAL.....	5
2.1. BRIEF HISTORY OF METALLIC MAGNESIUM AS BIOMATERIAL.....	5
2.2. THE CRUCIAL ROLE OF MAGNESIUM IN THE HUMAN BODY	6
2.3. DESIGNING CRITERIA OF BIODEGRADABLE Mg ALLOYS.....	7
2.3.1 Temporary support.....	7
2.3.2 Healing process support.....	9
2.3.2.1. Why Mg alloys minimize stress shielding effect?	10
2.3.3 Biodegradation.....	12
3. PROPERTIES AND SELECTION OF MAGNESIUM AND ITS ALLOYS	15
3.1. CORROSION MECHANISMS OF AZ31 & ZE41 ALLOYS	17
3.1.1. The role of microstructure on the corrosion behavior of AZ31 and ZE41 alloys...	18
3.2. HYDROGEN EVOLUTION OF Mg ALLOYS	19
3.3. INFLUENCE OF PHYSIOLOGICAL MEDIA ON CORROSION OF Mg ALLOYS	21
4. SURFACE PROTECTION AND FUNCTIONALIZATION STRATEGIES OF Mg ALLOYS	25
4.1. HOW SOL-GEL COATINGS IMPROVE THE CORROSION RESISTANCE OF Mg ALLOYS?.....	28
4.2. SURFACE FUNCTIONALIZATION OF Mg ALLOYS FOR BIOMEDICAL APPLICATIONS: A REVIEW	30
5. NATURALLY DERIVED BIOMATERIALS	37
5.1. COLLAGEN.....	37
5.1.1. Exploding collagen proficiency	39
5.2. CHITOSAN.....	42
5.2.1. Chitosan and its derivatives for bone applications	43
6. CELL/BIOMATERIAL INTERACTIONS.....	47
6.1. BONE STRUCTURE AND CELL MECHANICS.....	48
6.2. CELL BEHAVIOR ON BIOMATERIALS	50
6.2.1. In vivo vs. in vitro tests.....	52
7. THE RESEARCH AIM.....	53

7.1. THE APPROACH	53
8. THE METHODOLOGY	55
8.1. MATERIALS & SUBSTRATES PREPARATION.....	55
8.2. SYNTHESIS OF THE SOL-GEL COATING	55
8.3. SOL-GEL COATING DEPOSITION & THERMAL CONDITIONING	56
8.4. BUILD-UP OF BI-LAYERED COATINGS	56
8.5. <i>IN VITRO</i> CORROSION MEASUREMENTS BY ELECTROCHEMICAL TECHNIQUES	56
8.5.1. Electrochemical Impedance Spectroscopy	56
8.5.2. Localized SVET and SIET techniques	58
8.5.3. Localized electrochemical impedance spectroscopy	59
8.6. pH MEASUREMENTS.....	60
8.7. CONTACT ANGLE MEASUREMENTS	60
8.8. CELL BEHAVIOR CHARACTERIZATION	61
8.8.1. Samples setup for cell behavior experiments.....	61
8.8.2. Cell culture techniques and cell viability experiments	61
8.8.3. Cell distribution by fluorescence microscopy.....	62
8.8.4. Cell morphology characterization.....	63
8.9. MORPHOLOGY CHARACTERIZATION BY SEM & AFM.....	63
8.10. XRD & RAMAN CHARACTERIZATION	63
9. SILANE/TIO₂ COATING TO CONTROL THE CORROSION RATE OF MAGNESIUM ALLOYS IN SIMULATED BODY FLUID	65
9.1. MICROSTRUCTURE OF AS-RECEIVED AZ31 AND ZE41 ALLOYS.....	65
9.2. SURFACE MORPHOLOGY OF UNCOATED AND AS-PREPARED COATED ALLOYS	67
9.3. ELECTROCHEMICAL MONITORING OF THE CORROSION EVOLUTION	68
9.4. MORPHOLOGY AND COMPOSITION OF THE CORRODED SURFACES.....	70
9.5. CORROSION MECHANISMS AND MODELLING	75
9.6. LOCALIZED CORROSION BEHAVIOR OF COATED AZ31 AND ZE41 Mg ALLOYS	81
10. BI-LAYERED MULTIFUNCTIONAL SILANE-TiO₂/BIOPOLYMERS COATINGS TO CONTROL BIODEGRADATION OF Mg ALLOYS.....	87
10.1. MORPHOLOGY OF BI-LAYERED COATINGS.....	87
10.2. CORROSION BARRIER PROPERTIES OF THE BI-LAYERED SYSTEMS	89

10.2.1. Corrosion behavior in inorganic SBF solution	89
10.2.2. Localized impedance in SBF	98
10.2.3. Corrosion behavior in organic DMEM	101
10.2.3.1. Corrosion modelling of silane/TiO ₂ +collagen coated alloys	109
11. IN VITRO BIOLOGICAL PREFORMANCE OF BI-LAYERED AZ31 & ZE41 ALLOYS	115
11.1. CELL RESPONSE TO THE SURFACE CONDITION.....	115
11.1.1 Cell viability on uncoated alloys.....	115
11.1.2. Cell viability on silane-based coated and bi-layered alloys.....	117
11.1.3. Cell morphology on the different surfaces.....	118
12. INTEGRATED OVERVIEW AND CONCLUSIONS	127
13. OUTLOOK	131
ANNEX 1.....	133
14. BIBLIOGRAPHY	135

LIST OF FIGURES

Fig. 2.1. Considerations of element selection for developing biodegradable Mg-based alloys. source: [40]	8
Fig. 2.2. Fluoroscopic images of cross-section of (a) degradable polymer and (b) Mg rod implanted in a guinea pig femur harvested 18 weeks postoperatively. In vivo staining of newly formed bone by green fluorescent calcein. Bar = 1.5 mm; I = implant residual; P = periosteal bone formation; E = endosteal bone formation. source: [13].	10
Fig. 2.3. Phases of the bone remodelling process (left) source: [51] and determinants of human bone strength affected by bone remodelling (right). source: [52].	11
Fig. 2.4. Loads from the body weight on the lower limb skeleton (left) and stress shielding in hip prosthesis (middle). source: [54]. Stress shielding in locking compression plate fixing fractures in distal tibia (right). source: [21]. The blue lines indicate the transmission path of the loads.	12
Fig. 2.5. Ratio of residual cross-section/original cross-section area of Mg-1Zn-0.8Mn implant after different implantation durations. The vertical dashed line indicates the position of the cortical bone/bone medullary interface. Negative distance value indicates the distance to the interface in cortical bone. source: [56]	13
Fig. 3.1. Alloy development directions of magnesium depending on the main requirement. MMC's: metal matrix composites. source: [59]	15
Fig. 3.2. Optical micrographs of the microstructures of (a) as-extruded pure Mg of uniform grain size and mechanical twins (arrows) source : [71]; (b) as-extruded AZ31 showing equiaxed grains with some Mn-Al particles (dark) and mechanical twins (arrows) due to deformation induced during extrusion source: [72]; (c) as-cast ZE41 showing uniform grains surrounded by T-Mg ₇ Zn ₃ RE second phase, Zr ₄ Zn precipitates and some stained areas rich in Zn (circles). source: [70].	18
Fig. 3.3. Surface maps showing normal current density (j_z) distributions on Mg surface exposed to a 2 mol/dm ³ NaCl electrolyte, (a) 7, (b) 28, (c) 48 and (d) 68 min after commencing galvanostatic polarisation at 1 mA/cm ² . source: [75] adapted from [79].	20
Fig. 3.4. Electrochemical measurements of pure Mg in Hank's solution at 37 ± 0.5°C for 50h with different glucose contents. (a) Solution pH value, (b) open-circuit potential and (d) polarization curves. (d)-(f) SEM morphologies and EDX results expressed in wt.% for 3 g/L. source: [85].	23
Fig. 3.5. pH-potential diagram of Mg and its alloys in several simulated body solutions. BSA – bovine serum albumin. BSA 0.01 and BSA0.1 indicating SBF with 0.01 g/L and 0.1 BSA, respectively. MAO: micro-arc oxidation. source: [8]	24
Fig. 4.1. Bulk treatments and surface functionalization strategies to improve surface properties of Mg alloys... ..	25
Fig. 4.2. Applications of the sol-gel route. source: [94].	27
Fig. 4.4. Coating requirements and functions for stents and orthopaedic implants. source: [98].	31
Fig. 5.1. Representation of the triple helical structure of collagen. A single peptide chain (α -chain) is comprised of glycine (Gly), proline (X) and hydroxiprolin (Y) amino acids in a distinctive repeating pattern depending on the α -chain type. source: Modified from [135].	38
Fig. 5.2. (a) Representation of type I collagen synthesis. (a) Two α 1-chains and one α 2-chain form (b) procollagen; (c)–(d) removing loose termini of procollagen creates a type I tropocollagen molecule; (e) self-assembled tropocollagen form a fibril and (f) self-assembled collagen fibrils form a type I collagen fiber. source: [66].	39
Fig. 5.3. Scanning electron images of fibrillar gels of different concentrations: (a) 30 mg/ml, (b) 80 mg/ml source: [133].	39
Fig. 5.4. Scanning electron microscope images human bone marrow-derived stem cells on collagen fibers matrices derived from human skin (a) before cell seeding; (b) after 24h cell culture: ECM formation and cell ingrowth; (c) after 72h cell culture: cell-matrix-collagen integration. source:[140].	40
Fig. 5.5. SEM images of collagen coated AZ31 alloy by (a),(c) dip-coating and (b),(d) electrospinning technique. (c),(d) coating morphology after electrochemical impedance spectroscopy (EIS) experiments in Hank's solution. (e) Potentiodynamic polarization curves of uncoated (blank) and collagen coated AZ31 alloy with different methods. source: [144]	41

Fig. 5.6. (a) Chitin and chitosan structures and (b) scheme of 70% deacetylated chitosan after treating chitin in 40% NaOH at 120°C for 1–3 h. source: [146].	42
Fig. 5.7. Bode plots of (a) pure Mg and (b) AZ31 alloy in artificial sweat solution with time. The inset in (b) is the equivalent circuit for this condition. source: [151].	44
Fig. 5.8. SEM images of the calcium phosphate/chitosan coating morphologies immersed in m-SBF for different time intervals: (a) 3 days, (b) 30 days and (c) 90 days. source: [153].	45
Fig. 6.1. Scanning electron microscope images of (a) human fibroblast on a collagen matrix (cell extensions penetrate into the matrix and become entangled with collagen fibrils) source: [157] and (b) plump of human osteoblasts on bone surface (studded with many microvillus-like projections) source: [161]. (c) Hierarchical structure of bone ranging from the macroscale skeleton to nanoscale collagen and hydroxyapatite source: [162].	48
Fig. 6.2. Fluorescence images of cells cytoskeleton (human fibroblasts) showing the four quadrants of cell mechanics. On coverslips cells spread with lamellipodia and develop increase ruffles under pro-migratory conditions or stress fibers under pro-contractile conditions. In collagen matrices they spread with dendritic extensions under pro-migratory conditions or have retracted extensions under pro-contractile conditions source: [157].	50
Fig. 6.3. Morphology of (a) osteoblasts and (b) fibroblasts cultured for 7 days on sandblasted and acid etched (SLA) and commercially pure Ti and titanium-coated Thermanox discs with the according roughness value Ra (arithmetic average roughness). The nucleus was stained with DAPI (blue) and the cytoskeleton with Alexa Fluor 488 (green). Scale bar is 200 μm source: [165].	51
Fig. 7.1. Representation of the hybrid bi-layered multifunctional coatings produced on both AZ31 and ZE41 alloys: a bottom sol-gel of (3-glycidoxypropyl)-trimethoxysilane/titanium (IV) iso-propoxide and a top layer of collagen or chitosan.	53
Fig. 8.1. Sketch of samples preparation sequence and final setup of the bi-layered coatings.	56
Fig. 8.2. Photography of the equipment configuration for SVET/SIET experiments (left). Sketch depicting the sample setup with the artificial defect and the scanned area delimited with bee wax (right).	59
Fig. 8.3. Sketch depicting the sample setup and stepped trajectory of LEIS probe during experiments (left). Photography of the electrodes configuration used for LEIS experiments (right).	60
Fig. 8.4. Sample configuration and multi-well culture plates used for cell viability experiments.	61
Fig. 9.1. Optical and SEM micrographs showing the microstructure of the cross-plane alloys rods and EDX analysis. (a)–(b) α -Mg equiaxed grains with some Al-Mn precipitates (yellow arrows) and mechanical twins (black arrows). (c)–(d) α -Mg matrix with local Zn-rich areas (blue arrow), T-Mg ₇ Zn ₃ RE phase particles (yellow arrows) and Zr ₄ Zn precipitates (red arrows).	66
Fig. 9.2. Topographical AFM images of MgF ₂ layer on (a) AZ31 and (b) ZE41, (c) as-deposited coating. Secondary electron image of (d) as-deposited coating with EDX results and (e) backscattered electron image of coating cross section.	67
Fig. 9.3. OCP evolution of pre-treated and coated alloys in SBF (pH 7.4) at 37 \pm 1 °C.	68
Fig. 9.4. Bode plots of pre-treated (a) AZ31 and (b) ZE41 immersed in SBF (pH 7.4) at 37 \pm 1 °C. Symbols are impedance values Z and lines are phase angle values (ϕ).	69
Fig. 9.5. Bode plots of coated (a) AZ31_S and (b) ZE41_S immersed in SBF (pH 7.4) at 37 \pm 1 °C for 7 weeks.	70
Fig. 9.6. Morphology of uncoated and coated discs after EIS experiments in SBF at 37 \pm 1°C for 7 weeks: (a) AZ31, (b) ZE41, (c) AZ31_S and (d) ZE41_S.	71
Fig. 9.7. XRD patterns of the corrosion layers on coated (a) AZ31_S, (b) ZE41_S and pre-treated (c) AZ31, (d) ZE41. XRD patterns of pre-treated (e) AZ31 and (f) ZE41 before EIS.	72
Fig. 9.8. (a) XRD pattern of corrosion layer on AZ31 after 1 week and (b) Raman spectra of the corrosion layers on AZ31_S and ZE41_S after 7 weeks in SBF at 37°C.	73
Fig. 9.9. Raman spectra of the corrosion layer on (a) AZ31_S and (b) ZE41_S after 7 weeks compared to the characteristic Raman spectra of hydroxyapatite and chlorapatite [179].	74
Fig. 9.10. Cross-sectional secondary electron images of (a) AZ31_S and (b) ZE41_S after 7 weeks in SBF at 37°C. The inset in (a) depicts a plane-view of the AZ31_S corrosion layer after coating removal.	74

Fig. 9.11. (a) Equivalent circuit used to fit the EIS data. Evolution of the resistance for (a) AZ31_S and (b) ZE41_S. CPE parameter Q for (c) AZ31_S and (d) ZE41_S.....	78
Fig. 9.12. Current density (1b, 2b, 3b) and pH (3a, 3b, 3c) distribution at the surface of AZ31_S with the artificial defect upon exposure to the SBF solution at room temperature (~22°C) for 24h. The dashed line in 1a indicates the scanned area.....	81
Fig. 9.13. Current density (1b, 2b, 3b) and pH (3a, 3b, 3c) distribution at the surface of ZE41_S with the artificial defect upon exposure to the SBF solution at room temperature (~22°C) for 24h.....	82
Fig. 9.14. SEM images of the artificial defect of (1a) AZ31_S and (2a) ZE41_S after 24h of exposure to SBF at room temperature. Elemental distribution maps (1b-1d & 2b-2d) and EDX spectra (1e & 2e) of previously defined elements over the scanned area of AZ31_S and ZE41_S, respectively.	84
Fig. 10.1. SEM images of (a) AZ31_S, (b) ZE41_S, (c) ZE41_SC and (d) ZE41_SK. The insets in (a) and (b) show the topography of the alloys surface underneath the coating. Scale bar 10 μm.....	88
Further imaging of the samples cross-section showed that the thickness of the bi-layered systems was homogeneous and reproducible irrespectively of the alloy. The bottom sol-gel coating was 3.3 ± 0.2 μm-thick and the top biopolymer layers 1.3 ± 0.1 μm-thick (Fig. 10.3).	88
Fig. 10.2. Topographical AFM images of (a) AZ31_SK and (b) ZE41_SC and (e) phase contrast AFM image of an enlarged area in (b). R_q : surface roughness.....	88
Fig. 10.3. Cross-sectional backscattered electron image of the bi-layered systems deposited on the Mg alloys. .	89
Fig. 10.4. Contact angles of SBF and DMEM with the different surface conditions. The data were recorded within first 20 s of the droplet contact with the surface. The droplets profiles are with DMEM.....	89
Fig. 10.5. (a) OCP evolution and bode plots of (b) AZ31_SC, (c) ZE41_SC, (d) AZ31_SK and (e) ZE41_SK immersed in SBF at $37 \pm 1^\circ\text{C}$ for 7 weeks.....	90
Fig. 10.6. Morphology of the sol-gel+collagen coatings (a),(b) and the corroded surfaces of (c) AZ31_SC and (d) ZE41_SC, respectively, after EIS experiments in SBF at $37\pm 1^\circ\text{C}$ for 7 weeks and EDX results.....	92
Fig. 10.7. Morphology of corroded (a),(c) AZ31_SK and (b),(d) ZE41_SC after EIS experiments in SBF at $37\pm 1^\circ\text{C}$ for 7 weeks and EDX results.	96
Fig. 10.8. LEIS maps for (a) AZ31_S/SC and (b) ZE41_S/SC for different immersion times in 25% SBF. Maps recorded at different time points are shifted upwards with the time progress (S: sol-gel, SC: sol-gel+collagen).	98
Fig. 10.9. Pictures of samples used for LEIS experiments after 24h with formation of some blisters due to accumulation of H ₂ gas on the bi-layered side. (a) ZE41_S/SC and (b) AZ31_S/SK.....	99
Fig. 10.10. LEIS maps for (a) AZ31_S/SK and (b) ZE41_S/SK for different immersion times in 25% SBF. Maps recorded at different time points are shifted upwards with the time progress (S: sol-gel, SK: sol-gel+chitosan).	100
Fig. 10.11. Bode plots of the different surface conditions for both alloys immersed in DMEM at 37°C for 7 weeks. Left hand column corresponds to all surface conditions of AZ31 and right hand column to all surface conditions of ZE41. (a) AZ31, (b) AZ31_S, (c) AZ31_SC, (d) AZ31_SK, (e) ZE41, (f) ZE41_S, (g) ZE41_SC and (h) ZE41_SK.	102
Fig. 10.12. Morphology of corroded substrates after EIS experiments in DMEM for 7 weeks at $37 \pm 1^\circ\text{C}$. Left column shows all surface conditions for AZ31 (a,c,e,g) and right column all surface conditions for ZE41 (b,d,f,h). The inset in (d) shows the aggregates found on the corrosion layer of ZE41_S.	104
Fig. 10.13. SEM images of the corrosion products layer of (a) AZ31_SC, (b) ZE41_SC, (c) AZ31_SK and (d) ZE41_SK after 1 week of EIS experiments in DMEM at $31 \pm 1^\circ\text{C}$. The inset in (d) shows the cross-section of a sphero-aggregate and a primary seed (scale bar: 2.5 μm).	107
Fig. 10.14. Raman spectra of the corrosion layer of ZE41_SC after 1week of EIS experiments in DMEM compared to RUFF™ pattern [179] of hydroxyapatite (Ref. 060180).....	108
Fig. 10.15. (a) Equivalent circuits used to fit EIS data of AZ31_SC and ZE41_SC and values extracted from the fitting. (b),(d) show evolution of resistance and (c),(e) CPE parameter Q for AZ31_SC and ZE41_SC, respectively.	110
Fig. 10.16. SEM micrographs showing the surface morphology of the bi-layered coatings on (a) AZ31_SC and (b) ZE41_SC after EIS experiments in DMEM for 7 weeks at $31 \pm 1^\circ\text{C}$	112

Fig. 11.1. Cell viability of (a) fibroblasts and (b) osteoblasts seeded on the different surfaces, as obtained by the Alamarblue® test. pre-t: 12% HF pre-treated, sol-gel: silane-TiO ₂ , SC: sol-gel+collagen, SK: sol-gel+chitosan.	115
Fig. 11.2. Indirect contact assay results showing viability of both cell types for 7 days of culture in supernatants prepared by immersion of pre-treated alloys in cell culture medium at 37±1°C. Aliquots of supernatants were collected at day 1 (S1), day 3 (S3) and day 7 (S7). Fibroblasts and osteoblasts were seeded in multi-well plates and incubated for 24h to allow normal adhesion (gray bars); next, aliquots of supernatants (S1, S3, S7) were added to adhered cells and incubated for 7 days. Cell viability was measured at day 1, day 3 and day 7 for each set of cells in supernatants. Fibroblasts viability in supernatants with (a) AZ31 and (b) ZE41. Osteoblasts viability in supernatants with (c) AZ31 and (d) ZE41.	116
Fig. 11.3. Cell viability of (a) fibroblasts and (b) osteoblasts seeded on glass coated with the silane-TiO ₂ and the bi-layered coatings. S: silane-TiO ₂ , SC: sol-gel+collagen, SK: sol-gel+chitosan.	117
Fig. 11.4. SEM images of fibroblasts morphologies on AZ31 (left hand column) and ZE41 (right hand column) with the different surface conditions after 3 days of incubation (scale bar 10 μm, (f) 100 μm, (h) 5 μm). The insets are fluorescence microscopy images of the cells using live/dead staining after 1 day of incubation (scale bar 100 μm). (a) AZ31, (b) ZE41, (c) AZ31_S, (d) ZE41_S, (e) AZ31_SC, (f) ZE41_SC, (g) AZ31_SK and (h) ZE41_SK.	119
Fig. 11.5. Scanning electron micrograph of fibrillar collagen on ZE41_SC after immersion in DMEM for 7 days at 37°C (95% air with 5% CO ₂). Scale bar: 2.5 μm.	120
Fig. 11.6. SEM images of osteoblasts morphologies on AZ31 (left hand column) and ZE41 (right hand column) with the different surface conditions after 7 days of incubation (scale bar 10 μm, (d) 5 μm, (h) 20 μm). The insets are fluorescence microscopy images of the cells using live/dead staining after 1 day of incubation (scale bar 100 μm). (a) AZ31, (b) ZE41, (c) AZ31_S, (d) ZE41_S, (e) AZ31_SC, (f) ZE41_SC, (g) AZ31_SK and (h) ZE41_SK.	121
Fig. 11.7. HAP sphero-aggregates formed on AZ31_S under the sol-gel coating after 7 days in cell culture with osteoblasts. Cells are indicated by arrows. Scale bar: 25 μm.	123
Fig. 12.1. Schematic representation of the corrosion evolution of the Mg alloys over ~1 week of immersion in the presence of cells. (a) Blisters formation due to evolution of H ₂ gas along with the formation of a Mg(OH) ₂ corrosion layer at the substrate/coating interface; (b) precipitation of hydroxyapatite sphero-aggregates over the Mg(OH) ₂ layer and collagen fibrillogenesis; (c) as immersion time elapses the coating barrier properties deteriorates and the growing corrosion products induce cracking to the coating. Cells are able to reach the underlying substrate through the cracks and colonize some sphero-aggregates.	129

LIST OF TABLES

Table 1.1. Summary of properties of various metallic implants and natural bone. Source: [6,7].	2
Table 2.1. Distribution and concentrations of Mg in some organs and functions in a healthy adult. source: [37].	6
Table 2.2. General design constraints and criteria for a bioabsorbable metal stent. source: [42]	8
Table 2.3. Pathology and toxicology of Mg and some selected alloying elements. source: [7,40].	9
Table 3.2. Composition of blood plasma and most commonly employed solutions for corrosion testing of Mg alloys (concentrations in mM). source: [84].	22
Table 4.1. Some calcium phosphate coatings on Mg alloys for biomedical applications reported in literature between 2011 and 2013. source: modified from [98,112].	31
Table 4.2. Some studies on coatings for biodegradable Mg alloys published in 2015 and 2016.	32
Table 5.1. Relationship between structural parameters and properties of chitosans. source: [131]	43
Table 8.1. List of reagents to prepare 1000 ml of SBF (pH 7.4) and composition of the DMEM (pH 7) used in this work as detailed by the supplier Gibco® (Ref. 11880-028).	57
Table 9.1. Surface chemical composition of all tested conditions before and after EIS measured by EDX.	71
Table 10.1. Surface chemical composition of all condition after EIS experiments in DMEM at $37 \pm 1^\circ\text{C}$ measured by EDX. The points measured are indicated in Fig. 10.12.	105

LIST OF ACRONYMS AND ABBREVIATIONS

2D	Two Dimensional
3D	Three Dimensional
β -TCP	β -Tricalcium Phosphate
ACL	Anterior Cruciate Ligament
AFM	Atomic Force Microscope
AMS INSIGHT	Bioabsorbable Metal Stent Investigation in Chronic Limb Ischemia Treatment
ASTM	American Society for Testing Materials
ATR-FTIR	Attenuated Total Reflectance Fourier Infrared
AZ31	Magnesium alloy 3 wt. % Al, 1 wt. % Zn
AZ31_S	Sol-gel coated AZ31 alloy
AZ31_SC	Sol-gel and Collagen coated AZ31 alloy
AZ31_SK	Sol-gel and Chitosan coated AZ31 alloy
AZ51	Magnesium alloy 5 wt. % Al, 1 wt. % Zn
AZ91	Magnesium alloy 9 wt. % Al, 1 wt. % Zn
BSA	Bovine Serum Albumin
CP	Chitosan-Calcium Phosphate
CaP	Calcium Phosphate
CP-Mg	Commercially Pure Magnesium
CP-Ti	Commercially Pure Titanium
CPE	Constant Phase Element
c-SBF	Conventional Simulated Body Fluid
DAPI	Diamidino-2-phenylindole
DCPD	Dicalcium Phosphate Dehydrate
DD	Deacetylation Degree
DMEM	Dulbecco's Modified Eagle's Medium

EBSD	Electron Backscattered Diffraction
EBSS	Earle's Balance Salt Solution
ECM	Extracellular Matrix
EDP	Electrophoresis Deposition
EDS	Energy Dispersive Spectroscopy
EDX	Energy Dispersive X-ray Diffraction
EIS	Electrochemical Impedance Spectroscopy
EW10X04	Magnesium alloy 1 wt. % Nd, 0.48 wt. % Y, 0.43 wt. % Ca
EW62	Magnesium alloy 6 wt. % Nd, 2 wt. % Y
FBS	Fetal Bovine Serum
FEG-SEM	Field Emission Gun Scanning Electron Microscope
FGMgCO ₃ Ap	Functionally Graded Carbonate Apatite containing Magnesium
FTIR	Fourier Transformed Infrared Spectroscopy
GO/HapNP	Graphene oxide/hydroxyapatite Nanoparticles
GPTMS	3-Glycidoxypropyltrimethoxysilane
HAP	Hydroxyapatite
H _{evo}	Hydrogen Evolution
HGF	Human Gingival Fibroblasts
HOB	Primary Human Osteoblasts
HUVEC	Human Umbilical Vein Endothelial Cells
IL	Interfacial Layer
IR	Infrared
LEIS	Localized Electrochemical Impedance Spectroscopy
MAO	Micro-arc Oxidation
MEM	Minimum Essential Medium
m-SBF	Modified Simulated Body Fluid
NDE	Negative Difference Effect

NHDF	Normal Human Dermal Fibroblasts
OCP	Open Circuit Potential
PBS	Phosphate buffered Saline
PCL	Polycaprolactone
PFA	Paraformaldehyde
PI	Propidium Iodide
PLA	Poly(lactic Acid)
PROGRESS-AMS	Clinical <u>P</u> erformance and Angiographic <u>R</u> esults of the Coronary <u>S</u> tenting with <u>A</u> bsorbable <u>M</u> etal <u>S</u> tents
R	Resistance
RCO	Rat Calvarial Osteoblasts
S1	Supernatant day 1
S3	Supernatant day 3
S7	Supernatant day 7
SBF	Simulated Body Fluid
SC	Sol-gel Collagen
SCE	Saturated Calomel Electrode
SEM	Scanning Electron Microscope
SIET	Scanning Ion-selective Electrode Technique
SK	Sol-gel Chitosan
SVET	Scanning Vibrating Electrode Technique
TEOS	Tetraethyl Orthosilicate
VSMC	Vascular Smooth Muscle Cells
WE43	Magnesium alloy 4 wt. % Y, 3 wt. % RE
XHP-Mg	Ultra-high purity Magnesium
XRD	X-ray Diffraction
YSZ/PCL	Yttria Stabilized Zirconia/Polycaprolactone

ZE41	Magnesium alloy 4 wt. % Zn, 1 wt. % RE
ZE41_S	Sol-gel coated ZE41 alloy
ZE41_SC	Sol-gel and Collagen coated ZE41 alloy
ZE41_SK	Sol-gel and Chitosan coated ZE41 alloy
ZK30	Magnesium alloy 3 wt. % Zn, 0.5 wt. % Zr
ZM21	Magnesium alloy 2 wt. % Zn, 0.8 wt. % Mn

1. INTRODUCTION

In an industrialized context the term “corrosion degradation” is commonly considered as a drawback. This sounds comprehensible since corrosion affects the useful service of our possessions and makes suppliers of goods and services to incur into costs that are then passed on to the consumers. Consequences of corrosion include economic ones due to damage of equipment and/or loss of product efficiency, and social ones related to suppliers/consumers’ health and safety. For instance, a sudden failure of a facility or structure due to corrosion may cause explosions and/or pollution events, while materials degradation because of corrosion may cause depletion of natural resources. As a result, several billions of dollars are invested annually to reduce corrosion costs and to gain scientific knowledge since product design is an important step to control corrosion.

In the biomaterials context, corrosion is a major issue. Prior to the current definition of a biomaterial, the prevailing view was that successful biomaterials should play an inert role in the body [1]. Under this perspective, biomaterials were initially thought and selected from those that were considered highly corrosion resistant. Metals have been used as implants since the British physician and surgeon William Lane introduced stainless steel as metal plate for bone fracture fixation in 1895 [2]. Since the beginning, metallic implants faced corrosion and strength-related problems [2]. The consequences of their corrosion *in vivo* included weakening of the implant because of disintegration and toxic events due to accumulation of corrosion products on the surrounding tissues and organs. Up to now the metals successfully used as orthopaedic implants have been 316L stainless steel medical grades, Ti6Al4V alloy and CoCrMo alloy. They have been exploited due to their structural function and inertness, with an excellent combination of strength and ductility and safely bearing either under static or dynamic loads. The latter, is the superior characteristic of metals over polymers and ceramics [2]. On the other hand, these materials do not possess relevant biofunctionalities like bone conductivity, blood compatibility and bioactivity [2] and the stress shielding effect, which will be discussed hereinafter, became an issue affecting the long term implantation of these metals.

Since the beginning of the year 2000, novel classes of degradable metallic biomaterials have been drawing researchers and clinicians attention. Biodegradable metallic implants were thought to provide a temporary support on healing processes or diseased tissues and progressively degrade thereafter [3]. In a study published in 2005 [4], 91% of the patients who participated in a survey agreed that the removal surgery is the most negative aspect of a metallic implant. Increased treatment and hence increased rehabilitation time have relevant impact in patients’ lives and expenditures. In the same study [4], 95% of the patients declared that they would prefer their fracture to be treated with a biodegradable implant. With researchers and clinicians in agreement with patients’ preferences, the former definition of a

biomaterial had to be upgraded. The paradigm of the inert biomaterial was shifted and a new concept of biofunctional/bioactive biomaterials was introduced. Under this concept, the material elicits a response from the body and the body elicits a response from the material [1]. This makes biodegradation phenomena more interesting, but also much more challenging.

Magnesium, zinc and iron-based alloys have been proposed as biodegradable metallic implants up to now. Magnesium (Mg) and its alloys present a considerable number of advantages compared to iron and zinc alloys. Among the most relevant are: (i) Mg elastic modulus is close to that of bone (Table 1.1) minimizing stress shielding effects and (ii) Mg is a necessary co-factor used by 700-800 enzyme systems that participate in vital metabolic processes in the human body [5].

Table 1.1. Summary of properties of various metallic implants and natural bone. *Source:* [6,7].

Materials	Young's Modulus (GPa)	Ultimate tensile strength (MPa)
Natural cortical bone ¹	3–30	130–180
Mg alloys	41–45	65–258
Pure iron	205	245
Stainless steels*	189–205	620–695
Ti-based alloys*	105–125	758–1200
Co-Cr alloys*	240	900–1540

*Non-biodegradable metallic implants, taken for comparison purpose.

Despite the evident benefits of using Mg alloys, their particular corrosion behavior has hampered their successful application as biodegradable implants in clinical therapy. So far, the largest progress has been achieved for bioabsorbable Mg stents [8]. Mg alloys are highly reactive and their corrosion response depends upon several factors such as the composition of the exposure environment [9,10], the presence of impurity elements [11,12] and the alloy composition [13,14]. Several Mg alloys series have been investigated. The most popular are Mg-aluminium (Al) alloys [15–17], Mg-rare-earths (RE) alloys [18–20] and recently, Mg-calcium (Ca) alloys [21–23]. The role of the alloying is crucial for improving the corrosion resistance and the strength, for example, aluminium improves both the strength and the corrosion resistance of the metal [24] and rare earths elements —generally lanthanum (La), cerium (Ce), scandium (Sc) and yttrium (Y)— increase strength, ductility and corrosion resistance in high chloride environments [24]. Calcium does not have the strengthening effect of Al or RE, but improves corrosion resistance when included in low quantities as well as being an essential element in the human body, playing an important role in cell signalling [24].

Conversion films and surface coating are considered effective routes to improve corrosion resistance and biocompatibility of Mg alloys. Wang et al. [25] classified these

¹ The compact bone of the shaft of a bone that surrounds the marrow cavity [224].

methods as chemical, physical and physico-chemical when combining both. Commonly, physico-chemical methods are the most investigated. Generally, the initial chemical pre-treatment is used to improve the adhesion of a secondary physical coating [25]. Nevertheless, a single surface treatment might not meet the requirements of Mg alloys in some working conditions [26]. Therefore, surface modifications combining two or more kinds of surface treatments to form multi-layered coatings have been developed rapidly during last few years [26]. The aim of this approach is not a simple addition of the properties of the multiple layers but the synergistic effects, allowing to further modulate biodegradation of Mg alloys [25,26]. Literature unveils various kinds of materials that can be successfully deposited onto the substrates by combining inorganic and organic substances. Furthermore, it is widely accepted that natural biomaterials —those found in nature— may be either incorporated into the coatings formulation or deposited as complementary layers to provide further functionalities such as enhanced biocompatibility and cell delivery. The coating may go from being a physical barrier to be an active component that mimics the characteristic profile of the surrounding native tissue. Collagen and chitosan are examples of natural biomaterials originated from tissue-based and plant-based sources. These materials do not release cytotoxic products and their degradation process may be modulated by modifying the starting processing conditions [27].

This thesis offers a review of the present knowledge in the field of biodegradable Mg-based metal implants. We encompass a wide chronological period starting from the first clinical application of Mg as biomaterial until the current advances and approaches to functionalize Mg-based materials as a new generation of biodegradable metallic implants. Based on the current literature, we also discussed the criteria for the design of orthopaedic biodegradable implants made of Mg alloys. From there, we propose novel bi-layered coatings to control the biodegradation of Mg alloys for bone repair applications. First, we formulated a hybrid silane/TiO₂ coating to slowdown the corrosion rate of AZ31 and ZE41 alloys. Next, the incorporation of collagen and chitosan biopolymers as top-most layers to enhance biological performances was achieved. *In vitro* corrosion tests allowed to determine the barrier properties of the sol-gel coating in simulated body fluid and in Dulbecco's modified Eagle's medium. The influence of the biopolymers as top-most layers on the sol-gel coating barrier properties was elucidated. Additionally, cell *in vitro* test with osteoblast and fibroblast cells allowed us to determine the biological performances of the bi-layered systems in terms of cell activity as a function of: (i) the substrate or alloy, (ii) the sol-gel coating, (iii) the sol-gel/biopolymer combination —with collagen or chitosan— and, (iv) the bi-layered systems without the influence of the alloys. The results showed that our approach is viable to be implemented as method to functionalize the surface of biodegradable Mg alloys. Particularly, the bi-layered ZE41 alloy with collagen showed the best results of adhesion/proliferation of fibroblast and osteoblast cells.

2. MAGNESIUM AS BIOMATERIAL

2.1. BRIEF HISTORY OF METALLIC MAGNESIUM AS BIOMATERIAL

The history of magnesium (Mg) started when it was first recognized as an element in 1755 by the Scottish physician and chemist Joseph Black. In 1808, the British chemist Sir Humphrey Davy isolated Mg from a mixture of magnesia (MgO) and mercuric oxide (HgO). The first metallic samples of magnesium produced at an industrial scale were commercialized for use in pyrotechnical and photographic applications around the year 1862 [28]. In 1878, the physician Edward C. Huse successfully used Mg wires as ligatures to stop bleeding vessels in a radial artery and in the operation for varicocele [28]. After the treatment of few patients, Huse observed the wires degraded slowly and the period of time to complete degradation was dependent on the size of the Mg wire used [28]. In 1892, the also physician Erwin Payr from Austria implemented versatile clinical applications and reported advances in the field of biodegradable Mg implants [28]. Two of his publications around the year 1900 proposed that tissue water content, dissolved salts in blood and cells chemical processes were responsible for the corrosion of Mg *in vivo* [28]. Few years after, Belgium orthopaedist Albin Lambotte extended *in vivo* experiments in rabbits and dogs to clinical studies in humans [29,30]. The supplier for Payr's experiments was the Austrian company I. Rohrbeck which produced pure Mg sheets, plates and wires among other shapes. However, this company was not the pioneer commercializing Mg. In 1886, the Aluminium and Magnesium Fabric in Germany built a plant for Mg production by electrolysis of molten carnallite (KMgCl₃·6H₂O). Ten years after, the company Griesheim-Elektron further developed the process and became the main producer worldwide until 1916 [28]. In 1937, the currently in force British company Magnesium Elektron Ltd. started large scale Mg production.

During first half of 20th century, Mg alloys were introduced into orthopaedic and trauma surgery [28] and good biocompatibility was observed in clinical studies [31,32]; however, the fast degradation resulted in a large amount of hydrogen accumulated as subcutaneous gas bubbles. This issue discontinued Mg investigation and its application as biomaterial [13,28]. Soon after, a new kind of stainless steel introduced in 1920s displaced Mg alloys as the preferable orthopaedic implant materials. Simultaneously, Mg and its alloys continued being used in a wide variety of structural and non-structural applications including automotive, materials-handling and aerospace equipment [33]. Presently, Mg alloys are considered valuable for structural applications because of their light-weight and good strength and stiffness at both room and elevated temperatures.

A standard system of alloy and temper designations was adopted in 1948 [33]. In general terms, the system works indicating the two principal alloying elements, the amount of the two principal alloying elements and the temper condition, e.g. either as-fabricated or heat

treated. With the advanced capabilities in alloy systems available at that time, Mg regained interests as metallic implant. Researchers as F. Witte [10,13], L. Xu [34,35] and M.P. Staiger [14,36] retook the study of Mg alloys as biodegradable implants materials. Since then, aluminium-zinc magnesium series (AZ) have been one of the most highly studied due to their commercial availability. One important outcome was that Mg alloys degrade *in vivo* depending on the composition of the alloying elements [13]. Consequently, Mg alloys of decreased corrosion rate due to the addition of rare earth elements were produced [13].

Yet, efforts are being made to elucidate how local environment and surface modification influence the corrosion mechanisms of Mg alloys both *in vitro* and *in vivo*. Within this context, not only researchers but clinicians should work collectively and make awareness that to be successfully applied as biomaterials, Mg alloys need specific knowledge and meticulous approaches.

2.2. THE CRUCIAL ROLE OF MAGNESIUM IN THE HUMAN BODY

Magnesium (Mg) is an element widely distributed throughout our natural world. In the nature, it is found in salt or in mineral form due to the high level of reactivity of the free element [24]. Magnesium has a key role in important biological functions in both plants and animals. It is the fourth most abundant element within the human body and the most abundant intracellular divalent cation (Mg^{2+}) [24]. In the extracellular fluids Mg levels range from 0.7 to 1.05 mmol/L where homeostasis² is maintained by the kidneys and the intestine [36]. Due to the efficient excretion of this element in the urine, incidents of hyper-magnesium are scarce [37]. A healthy-human adult contains 20–28 g of Mg distributed to various organs. Some of the most important are listed in Table 2.1. Approximately half of the total physiological Mg is stored in bone tissue [36]. Several studies have shown that Mg have a stimulatory effect on the growth of new bone tissue [38,39]. Therefore, bone represents a Mg reservoir that buffers extracellular Mg concentration [37].

Table 2.1. Distribution and concentrations of Mg in some organs and functions in a healthy adult. *source:* [37].

Percent distribution	Concentration
Bone (60–65%)	0.5% of bone ash
Muscle (27%)	6-10 mmol/kg wet weight
Other cells (6–7%)	6–10 mmol/kg wet weight
Extracellular (<1%)	
Sweat	0.3 mmol/l (in hot environment)
Secretions	0.3–0.7 mmol/l

Despite the several benefits of Mg^{2+} in the human environment, the use of Mg alloys as biodegradable implants may result in an excess of stored and circulating Mg which could

² The state of equilibrium in the body with respect to various functions and to the chemical compositions of the fluids and tissues [225].

potentially manifests in hypermagnesemia³ [24]. Some effects of hypermagnesemia may be acute breakdown of muscle tissue and subsequent renal malfunction [24]. Cardiovascular function may be also impaired with high serum Mg concentrations resulting in hypotension with increased risk of cardiac arrest [24]. The primary clinical treatment for hypermagnesemia involves a controlled diet reducing the intake of Mg [24]. In the case of a Mg-based implant degrading within the human body, certainly, a different approach must be adopted. Hence, controlling corrosion rate of Mg alloys is an important aspect of assessing Mg-based biodegradable implants for orthopaedic applications.

2.3. DESIGNING CRITERIA OF BIODEGRADABLE Mg ALLOYS

Up to date, there have been three generations of biomaterials in terms of clinical requirements. First, a biomaterial was expected to be inert and to not harm the host tissue in any way [7]. Then, clinicians searched for more complex surfaces that could bond to the host tissue [7]. Magnesium alloys are part of a third generation of biomaterials that aim to a new strategy of tissue engineering and regeneration. These materials are expected to degrade and allow native tissue to integrate with the implant and gradually replace it [7]. According to these new functionalities, designing criteria of a biodegradable implant must be consequently different from the designing criteria of an inert permanent implant.

The concept of degradable biomaterials derives from three main features: (i) temporary support; (ii) healing process support and (iii) degradation [3].

2.3.1 Temporary support

The question/doubt that arises in respect to the mechanical support provided by a biodegradable implant is: will the degradable implant maintain its mechanical integrity during the required period? [3]. By meticulous selection and design of the material based on the specific function of the implant and the physiological conditions of the implantation site [3] it is possible to address the answer to this question. Clearly, selection criteria and specific design of a biodegradable implant depend on the intended application [40]. For example, Staiger et al. [36] projected that Mg and its alloys for load bearing orthopaedic implants—screw, pins, needles and others— should maintain mechanical integrity over a time scale of 12–18 weeks while bone tissue heals. McBride [41] reported that a typical Mg-Al-Mn 1g screw to treat traumatized bone would completely degrade in 120 days. Similarly, Bowen et al. [42] summarized the criteria design proposed by different researches for bioabsorbable metallic stents made of Mg alloys, as listed in [Table 2.2](#).

³ An abnormally large concentration of magnesium in the blood serum [226].

Table 2.2. General design constraints and criteria for a bioabsorbable metal stent. *source:* [42]

Criterion	Constraints	Source
Bioabsorption	Mechanical integrity for 3–6 months	[43]
	Mechanical integrity for 6–12 months	[44]
	Full absorption in 12–24 months	[43,45]
Biocompatibility	Nontoxic, non-inflammatory, hypoallergenic	[43]
	No harmful release or retention of particles	
Mechanical properties	Yield strength > 200 MPa	[43]
	Tensile strength > 300 MPa	
	Elongation to failure > 15–18%	
Microstructure	Maximum grain size of ~30 μm	[43]
	Maximum grain size of 10–12.5 μm	[44]
Hydrogen evolution	< 10 $\mu\text{l H}^2 \text{ cm}^{-2} \text{ day}^{-1}$	[46]
Corrosion rate	Penetration rate < 20 $\mu\text{m year}^{-1}$	[47]

It is currently known that physical and mechanical properties of Mg alloys may be improved by e.g. thermo-mechanical treatment and suitable alloying [3]. For instance, hot rolling⁴ and hot extruding⁵ can improve strength of Mg alloys while alloying with Al, Zn and Zr can improved both strength and elastic modulus [7]. However, there are several considerations for element selection for developing biodegradable Mg-based alloys, as described by Chen et al. [40] in Fig. 2.1. The localized corrosion of Mg alloys is an important factor to examine since an extensive local corroded area (cavity) may result in early mechanical failure of the implant [24], considering that these cavities act as stress raisers⁶.

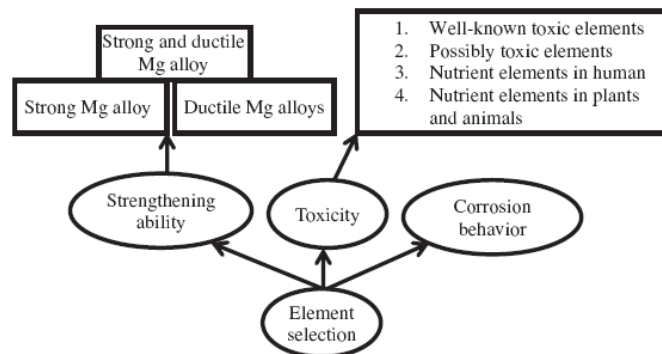


Fig. 2.1. Considerations of element selection for developing biodegradable Mg-based alloys. *source:* [40]

Besides the importance of mechanical properties and corrosion performances, which are generally the main interest of researchers, clinicians stress the relevance of toxicity assessment that must be considered during material design [3]. Hence, to design

⁴ The reduction of the cross-sectional area of metal stock or the general shaping of metal products through the use of rotating rolls [227].

⁵ Extrusion is the conversion of an ingot or billet into lengths of uniform cross section by forcing metal to flow plastically through a die orifice [227].

⁶ Structural discontinuities such as notches or holes that cause local increase in stress [228].

biodegradable implants it is important to consider elements selection and amounts based on the biological safe limit and release kinetic of the elements used in the material [7]. The pathology and toxicology of selected elements of relevant importance for the present work are listed in Table 2.3.

Table 2.3. Pathology and toxicology of Mg and some selected alloying elements. *source:* [7,40].

Element	Blood serum level	Biological role	Toxicology	Daily allowance
Mg	0.9 mmol/L	Activator of several enzymes; coregulator of protein synthesis and muscle contraction; stabilizer of DNA and RNA	Almost no evidence of toxicity of Mg	400 mg
Al	2.1–4.8 µg		Neurotoxicity and accumulation in bone	< 300 mg
Rare earths ^a	< 47 µg	Compound of drugs for cancer treatment	Accumulation in bone and liver	4.2 mg
Zn	46 µmol/L	Essential trace element; appears in all enzyme classes	Neurotoxic and hinder bone development at higher concentration	15 mg
Zr	< 250 mg		High concentration in liver and gall bladder	3.5 mg
Mn	1 µmol/L	Activator enzyme; essential trace element; Mn deficiency is related to osteoporosis, diabetes mellitus, atherosclerosis	Excessive amount results in neurotoxicity	4 mg

^aThe total amount of RE (Ce, La, Nd, Pr, Y) should not exceed 4.2 mg day⁻¹

In conclusion, the design criteria for the next generation of biodegradable Mg alloys should aim good combination of appropriate mechanical properties, suitable corrosion behavior and excellent bioactivity [40]. Mechanical properties and corrosion performance directly depend on bulk microstructure, which results from alloying composition, processing history, heat treatment and impurity control [40].

2.3.2 Healing process support

Healing process support refers to the ability of either do not interfere negatively with the tissue healing process or to stimulate i.e. bone formation. It is then important to determine how the degradable biomaterials and their biocorrosion products are going to interact with the surrounding healing tissues. Several *in vitro* studies have been carried out in order to assess Mg-based implants performances. These *in vitro* tests have been also used for screening purposes to help material selection and alloy design process [3].

By using various cells types focused on the bone and blood vessel related applications Gu et al. [48] performed cytotoxicity and hemocompatibility experiments. The results showed that Mg-1Al, Mg-1Sn and Mg-1Zn alloys indicated no negative effect on viabilities of blood vessel related cells (ECV304 and VSMC) [48]. On the other hand, Mg-1Al and Mg-1Zn alloys showed no significant reduced viability of fibroblasts (L-929 and NIH3T3) and

osteoblasts (MC3T3-E1) cells [48]. These tests concluded that Mg-1Al and Mg-1Zn binary alloys might be appropriate for stent materials as well as for orthopaedic implants.

Witte et al. [13] compared the *in vivo* degradation (small rod implanted in guinea pig femur) of four Mg alloys with additions of Al and RE elements (Nd, Ce and La) against the performance of a degradable polymer (poly-96L/4D-lactice). After 18 weeks of implantation, the surface of the four Mg implants was coated with a newly formed mineral phase rich in calcium which was in direct contact with the surrounding bone (Fig. 2.2). A thick layer composed mainly of calcium ions replaced the corroded mass of the Mg alloys [13]. The results showed that the Mg implants enhanced the mineral apposition⁷ rate compared to the degradable polymer [13].

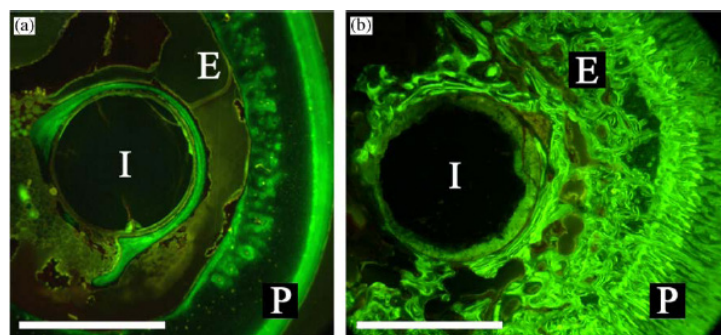


Fig. 2.2. Fluoroscopic images of cross-section of (a) degradable polymer and (b) Mg rod implanted in a guinea pig femur harvested 18 weeks postoperatively. *In vivo* staining of newly formed bone by green fluorescent calcein. Bar = 1.5 mm; I = implant residual; P = periosteal bone formation; E = endosteal bone formation. *source:* [13].

Considering the reported results by Gu et al. [48] and Witte et al. [13], there is a strong rationale for Mg alloys to support bone repairing process. Furthermore, during healing process the bone needs to be assisted by mechanical stimulation to form new bone. Next, we briefly discuss the mechanisms for new bone formation and how Mg alloys can minimize the stress shielding effect which might hinders bone remodelling process.

2.3.2.1. Why Mg alloys minimize stress shielding effect?

When the bone fractures, the separated fragments may displace or lose their alignment in the form of an angulation [21]. Orthopaedic surgeons attempt to restore the normal anatomy of the fractured bone to the correct alignment by performing a surgical procedure called *reduction* [21]. After the *reduction*, the fractured bone is able to heal without any deformity. Implants may be defined as devices that are placed over or within bones to hold a *fracture reduction* [21].

⁷ The placement or position of adjacent structures or parts so that they can come into contact [229].

Bone remodelling is a continuous process of synthesis and destruction that gives bones its mature structure and maintains normal calcium levels in the body [49]. Fig. 2.3 (left) illustrates the five distinct phases of the bone remodelling process chronologically from left to right (see [50] for detailed review). Bone fracture healing is similar to embryonic bone formation in many ways and involves three stages: inflammation, repair and remodelling [50].

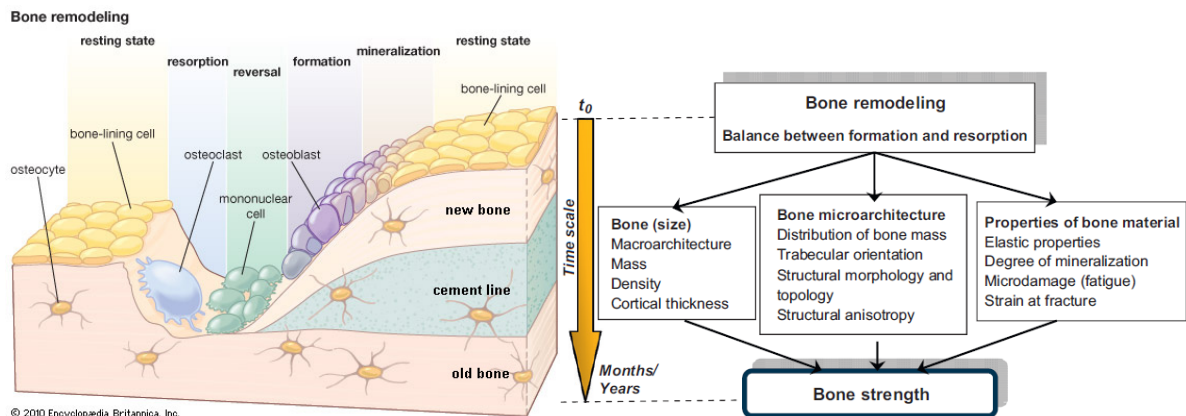


Fig. 2.3. Phases of the bone remodelling process (left) source: [51] and determinants of human bone strength affected by bone remodelling (right). source: [52].

Bone remodelling is controlled by metabolic as well as mechanical factors [53]. Bone contains sensor cells that monitor mechanical strains, compare it to a physiologically desirable range of values (see Fig. 2.3, right), and activate corrective biological processes when the sensed variable falls outside this range [53]. This process of transmuting mechanical signals into biochemical signals is called *mechanotransduction*. When the mechanical stimulus is too low, remodelling removes bone and, when it is too high, remodelling adds bone [53].

When a *fracture reduction* is treated with an implant made of a material that is too stiff compared to bone, the implant shields the healing bone from being exposed to mechanical loads [21] hindering repairing and remodelling. This *stress shielding* effect (see Fig. 2.4) may then result in clinical issues such as damage healing process, early implant loosening and even damage of adjacent anatomical structures [21].

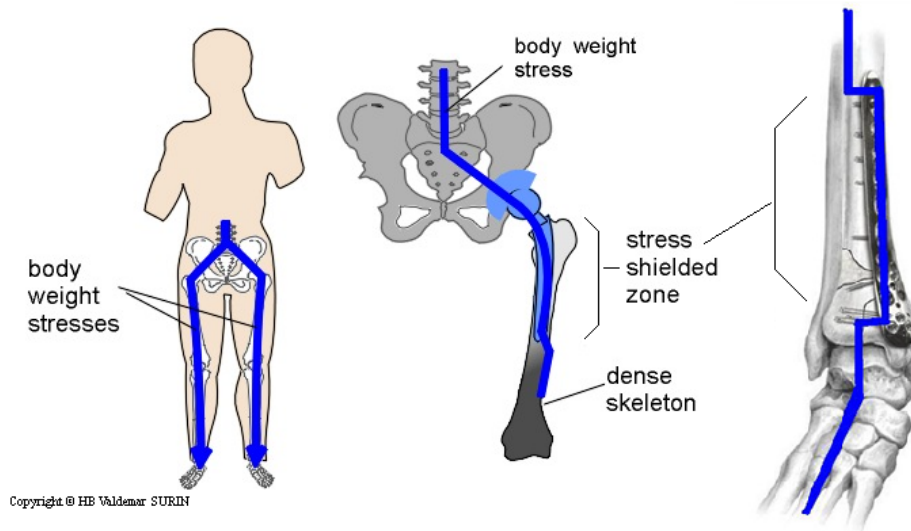


Fig. 2.4. Loads from the body weight on the lower limb skeleton (left) and stress shielding in hip prosthesis (middle). *source:* [54]. Stress shielding in locking compression plate fixing fractures in distal tibia (right). *source:* [21]. The blue lines indicate the transmission path of the loads.

Current implant materials mismatch bone elastic properties (see [Table 1.1](#), pg. 2). Commercially available screws and plates for bone fixation are made of Ti6Al4V, stainless steels and cobalt-chromium alloys. These materials conventionally used as permanent metallic implants, have continuously met any of the above-mentioned problems resulting in social and economic additional costs. Only in patients older than 60 years it is acceptable to leave the metal *in situ* [21]. From this perspective, Mg-based alloys have a high potential as temporary metallic implants. Their close elastic modulus —Young’s modulus— to cortical bone (see [Table 1.1](#), pg. 2) is expected to minimize the *stress shielding* effect.

2.3.3 Biodegradation

At this point, it is convenient to take into consideration one of the prevalent definitions of biodegradable materials. Recently, Boutrand [55] introduced as definition of biodegradable: *capable of being broken down (or decomposed) into smaller fragments or molecules through the action of cells, enzymes, dissolution of mechanical processes. Biodegradation is typically the first phase in the process of bioabsorption; however, some materials are biodegradable but not bioabsorbable⁸, resulting in storage within tissues or organs.*

The question concerning biodegradation process would be: will the degradation kinetics match the healing period and will the degradation products be transported and eliminated from the body without causing local or systemic accumulations? [3]. Several researchers have aimed to answer this question. Various animal models implantation trials have shown that proposed biodegradable Mg alloys degrade in the *in vivo* environment. In the

⁸ Capable of being absorbed, whether metabolized or not, and eliminated by tissues and organs [55].

same study aforementioned (section 2.3.2) performed by Witte et al. [13] the results showed that Mg-Al-Zn and Mg-RE alloys degraded *in vivo* during the implantation period (up to 18 weeks). Additionally, the investigated alloys exhibited different degradation rates attributed to the differences in the alloys composition. Those containing RE elements seemed to be more suitable for the use as implants materials in bone surgery [13].

Zhang et al. [56] implanted high-purity Mg-1Zn-0.8Mn rod samples into rats femora and monitored degradation over 6 months. By measuring the residual implant cross-section area (residual area/original area) the authors determined the *in vivo* degradation rate of the Mg alloy. The lower the ratio, the faster the degradation rate [56]. The Mg alloy rods were implanted perpendicularly into the rat femur to evaluate the degradation in cortical bone and in bone marrow (trabecular bone⁹). Fig. 2.5 summarizes the results of degradation after different postimplantation durations where it is possible to see that more degradation occurred in the marrow channel [56]. Therefore, implantation site is an important factor determining degradation rate of Mg alloys.

Additional blood biochemical examinations postimplantation revealed that the values of the items measured —i.e. Mg²⁺, Ca²⁺, P, Cl⁻, alkaline phosphatase, uric acid, among others— were still between the recommended level range indicating that the degradation of the Mg-Zn-Mn alloy did not cause disorder to the liver or kidneys [56].

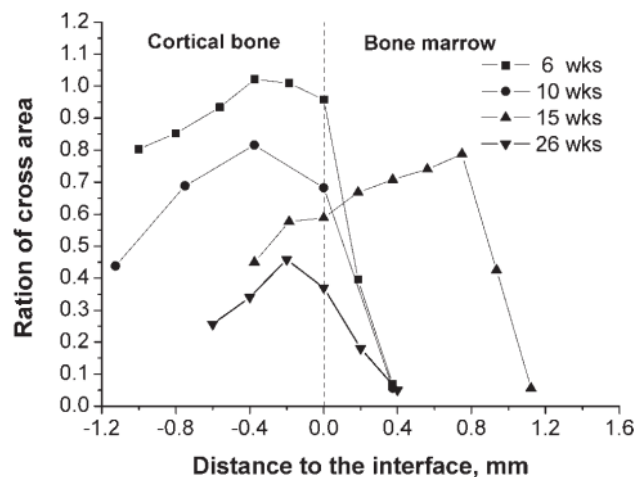


Fig. 2.5. Ratio of residual cross-section/original cross-section area of Mg-1Zn-0.8Mn implant after different implantation durations. The vertical dashed line indicates the position of the cortical bone/bone medullary interface. Negative distance value indicates the distance to the interface in cortical bone. *source:* [56]

Recent implantation trials in humans showed positive results. The PROGRESS-AMS (absorbable metal stent) Mg alloy stent successfully implanted in 63 patients for stenosis treatment degraded completely within four months [57]. No myocardial infarction, late

⁹ Also called cancellous bone, is porous bone enclosing numerous large spaces that give a honeycombed or spongy appearance. The spaces between are often filled with marrow and blood vessels [230].

thrombosis or death occurred. Some further modifications were recommended to prolong degradation time [57]. Additionally, the AMS INSIGHT showed to be safe for treating peripheral arterial disease, but did not show yet efficacy in long-term patency [58].

Indeed, the here discussed findings indicate that degradable Mg alloys are a new exciting class of materials for tissue engineering applications. However, the science behind the technology to design these materials is still immature [3]. Hermawan et al. [3] pointed out the importance of carefully examine design criteria along with a conscious selection of the available technologies. The authors suggest some fundamental approaches in order to gain more understanding in regard to *in vivo* degradation and cell-material interactions in their review [3].

3. PROPERTIES AND SELECTION OF MAGNESIUM AND ITS ALLOYS

In its metallic form, Mg is a light-weight material with a density (1.74 g/cm^3) 2.5 times and 4.5 times lower than titanium and steel, respectively [36]. Magnesium high strength-to-weight ratio makes it suitable for load bearing applications. Historically, Mg has been extensively used in automotive and aircraft industries. Being the lightest of all metals, manufacturers opted for replace denser materials by Mg-based alloys [59]. The improvement in properties demanded by large-scale potential users of Mg alloys, rose the need for alloying development [59]. Different approaches were taken depending on the required properties, as specified in Fig. 3.1.

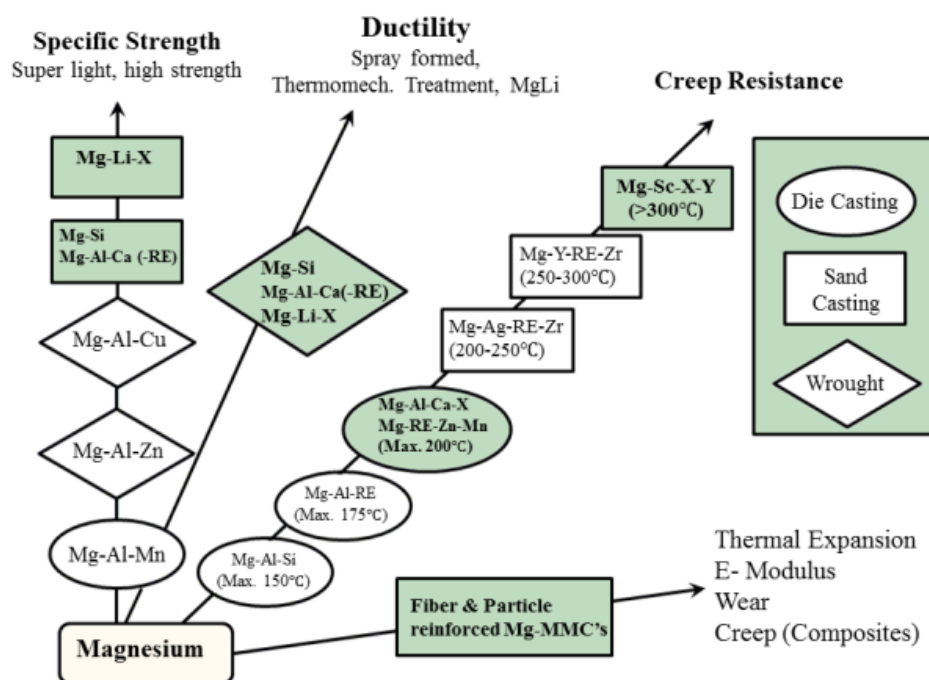


Fig. 3.1. Alloy development directions of magnesium depending on the main requirement. MMC's: metal matrix composites. *source:* [59]

There are two primary groups of Mg-based alloys. The first group contains aluminium (Al) as main alloying element with trace additions of zinc and manganese. The aluminium-zinc series (AZ) cover the majority of the Mg applications. The AZ series have moderated corrosion resistance and improved mechanical strength [36]. Improvements in these features are mainly due to changes in microstructural characteristics. Enhanced mechanical strength is associated to both solid solution¹⁰ and precipitation strengthening¹¹ [24]. One of the proposed mechanisms for the enhanced corrosion resistance of Al-containing series is the formation of

¹⁰A solid crystalline phase containing two or more chemical species in concentrations that may vary between limits imposed by the phase equilibrium [231].

¹¹Hardening caused by precipitation of a constituent from a supersaturated solid solution [231].

an Al₂O₃ layer on the surface which is insoluble in chloride containing solutions [60]. However, too high concentration of Al (8–9 wt.%) reduces corrosion resistance due to the increased content of Mg₁₇Al₁₂ intermetallic compound¹², promoting galvanic corrosion¹³ [61].

Despite the improvement in mechanical properties and corrosion resistance of AZ series, some doubts have arisen concerning the pathological effects of Al in the human body. An *in vivo* study made by Witte et al. [13] of two Al-containing Mg alloys showed that AZ91 (9 wt.% Al, 1 wt.% Zn) and AZ31 (3 wt.% Al, 1 wt.% Zn) alloys degraded at similar rates. Additionally, enhanced bone formation was observed around the AZ91 and AZ31 implants after 6 and 18 weeks [13]. Witte et al. argued that even though the biocompatibility of Al is limited, it seems to be a valid alloying element for Mg alloys in body contact [13]. Since AZ91 and AZ31 alloys exhibited similar biodegradation rates, researchers focused more on the AZ31 alloy due to its reduced Al content.

The second main group of Mg alloys contains a mixture of rare earths (RE) elements in combination with another metal, generally zinc or yttrium, and small additions of zirconium to promote a fine grain structure and enhance mechanical properties [36]. Cerium (Ce), lanthanum (La), scandium (Sc) and yttrium (Y) are the RE generally added to Mg alloys. Like Al, these elements increase the strength by both solid solution and precipitation hardening [24]. The corrosion resistance in high chloride environments is also improved due to the formation and stabilization of an oxide-rich layer [62]. In this case, the concern that arises with the presence of RE elements in the human body is their relatively unknown effects. However, some studies have revealed that positive or negative effects may result depending on the considered RE elements. Within a historical context, some RE are known for have both anti-carcinogenic and anticoagulant properties [63] and may have positive effects in cell viability, as demonstrated by Feyerabend et al. [64]. However, the consensus is still divergent and the recommendations point to use RE elements cautiously since information for several RE remains scarce [65].

In the same study aforementioned conducted by Witte et al. [13] the results showed that a degraded implant of the WE43 alloy (4 wt% Y, 3 wt% RE) was gradually replaced by a conversion layer coating of calcium and phosphorous. The RE elements were found homogeneously distributed in the corrosion layer of the implant surface and in the remaining implant material, but not in the surrounding bone [13].

Zinc-rare earth series (ZE) Mg alloys were developed to meet the need for alloys with medium strength and improved castability in comparison to AZ series [33]. Being the two primary groups of Mg alloys commercially available, the Al-containing and the RE-

¹²An intermediate phase in an alloy system having narrow range of homogeneity and relatively simple stoichiometric proportions. Nearly all are brittle and of stoichiometric composition [231].

¹³Occurs when a metal or alloy is electrically coupled to another metal or conducting non-metal in the same electrolyte. Their dissimilar potentials cause electron flow between them [232].

containing series have been the most investigated as potential biodegradable implants. The mechanical properties of the two Mg alloys studied in the present work in comparison to pure Mg are summarized in Table 3.1.

Table 3.1. Mechanical properties and composition limits of AZ31 and ZE41 magnesium alloys in comparison to pure Mg. *source:* [33].

Material	Density (g/cm ³)	Young's Modulus (GPa)	Yield strength (MPa)	Ultimate tensile strength (MPa)	Elongation (%)
Mg 99.8%	1.74	40	21	90	6
AZ31	1.77	45	200	255	12
ZE41	1.82	45	140	205	3.5

Elem. Wt.%	Al	Zn	RE	Mn	Zr	Ni	Cu
AZ31 ^a	2.4–3.6	0.5–1.5	–	0.15 min	–	0.03 max	0.1 max
ZE41 ^b	–	3.5–5	0.75–1.75	0.15 max	0.4–1	0.01 max	0.1 max

^a 0.1 Si max

^b Rare earths as mischmetal (La, Nd, Ce and others). Other impurities 0.3 max (total).

3.1. CORROSION MECHANISMS OF AZ31 & ZE41 ALLOYS

The rapid corrosion of Mg and its alloys in the physiological media is the main limitation in the use of these materials for orthopaedic applications. The corrosion rate of the implanted metal not only influences the healing period of the adjacent tissue but also influences the loss of mechanical properties of the implant during degradation [66]. The corrosion mechanisms of Mg in aqueous environments are represented by the following reactions [8]:



As identified in the Eq. 3, the overall reaction consists of the production of magnesium hydroxide and hydrogen gas. The Mg(OH)₂ layer formed is partially protective since it is slightly soluble in water [67]. However, in electrolytes containing chloride (Cl⁻) ions, such as the *in vivo* environment, Mg(OH)₂ reacts with chloride ions to produce highly soluble MgCl₂ [24,36]. Chloride ions are also responsible for localized corrosion or pitting of Mg alloys. Pitting is observed for Cl⁻ concentrations exceeding 30 mmol/L, it is the case of the physiological environment where Cl⁻ ions are present at levels on the order of 150 mmol/L [36]. The occurrence of pitting and the formation of the soluble MgCl₂, promotes a rapid dissolution of Mg substrate with the subsequent production of hydrogen gas and hydroxide ions [24].

In physiological environments, there are two main types of corrosion that affect Mg and its alloys. For materials with dual-phase microstructures the corrosion is typically localized, resulting in the formation of pits on the surface [24]. Secondary phases are promoted by precipitation of impurities or alloying elements. These second phases also act as a local cathode resulting in micro-galvanic corrosion [24]. The microstructures of AZ31 and ZE41 alloys have already been investigated and different second-phases have been identified.

3.1.1. The role of microstructure on the corrosion behavior of AZ31 and ZE41 alloys

Fig. 3.2 depicts the microstructure of as-extruded AZ31 and as-cast ZE41 in comparison to commercially pure Mg (CP-Mg). CP-Mg microstructure is composed by a matrix of α -phase grains. The resulted morphology and grain size of α -Mg are dependent on the thermo-mechanical history of the material.

AZ31 alloy microstructure is composed of an α -Mg matrix with some Al-Mn precipitates (black dots in Fig. 3.2b). The presence of small amounts of manganese in commercial Mg-Al alloys (see Table 3.1, pg. 17) may cause formation of Al_8Mn_5 or $Al_{11}Mn_4$ intermetallic compounds [68]. The β - $Mg_{17}Al_{12}$ phase, present in AZ91 alloy, is not prone to precipitate in AZ alloys with low Al content, such as AZ31 alloy. Generally, Zn is added to increase solubility of Al into the α -Mg matrix [69].

Fig. 3.2c shows the microstructure of as-cast ZE41 alloy with uniform α -Mg grains surrounded by the T- Mg_7Zn_3RE second phase and some Zr_4Zn precipitates. The stained areas within the α -Mg grains (circles) correspond to areas with high concentration in Zn [70].

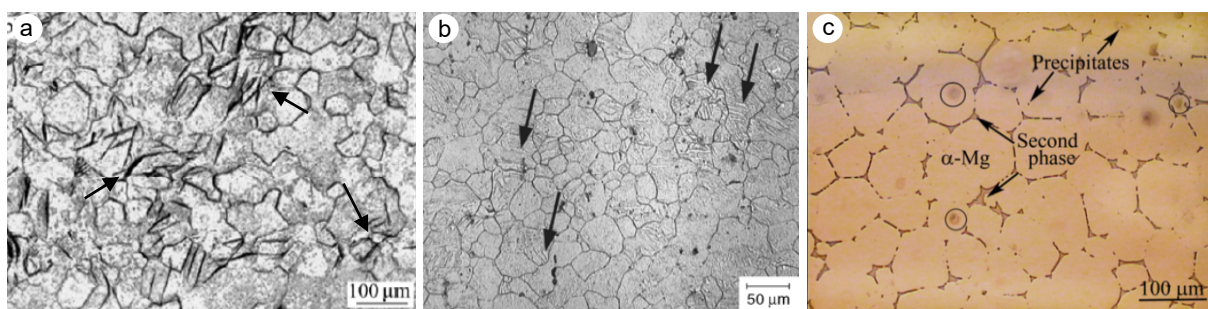


Fig. 3.2. Optical micrographs of the microstructures of (a) as-extruded pure Mg of uniform grain size and mechanical twins¹⁴ (arrows) *source* : [71]; (b) as-extruded AZ31 showing equiaxed grains with some Mn-Al particles (dark) and mechanical twins (arrows) due to deformation induced during extrusion *source*: [72]; (c) as-cast ZE41 showing uniform grains surrounded by T- Mg_7Zn_3RE second phase, Zr_4Zn precipitates and some stained areas rich in Zn (circles). *source*: [70].

Lopez et al. [73] investigated the corrosion behavior of AZ31 alloy with different grain sizes in NaCl solution and in phosphate-buffer solution (PBS). The best corrosion

¹⁴ Two portions of a crystal with a definitive orientation relationship formed in a metal during plastic deformation by simple shear of the structure [72].

behavior was obtained for the AZ31 alloy with finest grain size ($\sim 4 \mu\text{m}$) with respect to the alloy with larger grain size ($\sim 25 \mu\text{m}$) in PBS. Furthermore, at initial stages of immersion pitting¹⁵ corrosion was associated with the presence of Al-Mn precipitates [73]. Localized corrosion occurred earlier in PBS than in NaCl solution. However, after long immersion periods (4–6 days) in PBS a layer of corrosion products of $\text{Mg}(\text{OH})_2$ rich in phosphorous promoted protection against further action of chloride ions [73]. Pardo et al. [61] confirmed that corrosion attack of AZ31 alloy in 3.5 wt.% NaCl occurs at α -Mg/Al-Mn precipitates interfaces by means of the formation of galvanic couples.

Neil et al. [74] characterized the corrosion morphology of ZE41 alloy immersed in 0.001 M NaCl for 18 hours. They determined the sequence of corrosion initiation and propagation over immersion. First, pitting corrosion on the α -Mg matrix around the T- $\text{Mg}_7\text{Zn}_3\text{RE}$ phase occurred followed by deep corrosion attack at the Zr-rich regions. Then, corrosion continued by pitting within the α -Mg grains. The attack in the centre of the grains was attributed to the presence of Zr-Zn particles [74]. Control size of these particles is thought to be an important microstructural feature influencing corrosion of ZE41 alloy [74].

3.2. HYDROGEN EVOLUTION OF Mg ALLOYS

Dissolution of Mg in aqueous solutions is different from other metals since Mg can support cathodic hydrogen evolution (H_{evo}) on its surface during anodic polarisation [75]. H_{evo} is characterized by the rate of the reaction increasing with anodic polarisation. This phenomenon is called the negative difference effect (NDE) [75]. Different theories to explain NDE have arisen during the last century; however, by using advanced characterization techniques the understanding of Mg dissolution in aqueous solutions have been clarified [75]. Some of the main outcomes are: (i) the corrosion film formed on the Mg surface sustains and enhances H_{evo} , (ii) cathodic activation may also be catalysed by an enrichment of noble elements or impurities on the Mg surface which influences H_{evo} [75].

Various authors [76–78] proposed corrosion film-based explanations for NDE. These models attribute NDE to the Mg oxide/hydroxide corrosion film breakdown during anodic polarisation, while film coverage was assumed to decrease during anodic polarisation [75].

William et al. [79] performed *in situ* scanning vibrating electrode technique (SVET) on pure Mg and visualized cathodic and anodic areas distribution on the surface during anodic polarization in NaCl solution. They demonstrated that localized cathodic areas propagate and growth on anodically polarized Mg surfaces more rapidly with increasing applied anodic current density (Fig. 3.3). This followed the trend in H_{evo} rates which the authors verified by volumetric measurements separately from SVET measurements.

¹⁵ Localized corrosion of a metal surface, confined to a point or small area that takes the form of cavities [233].

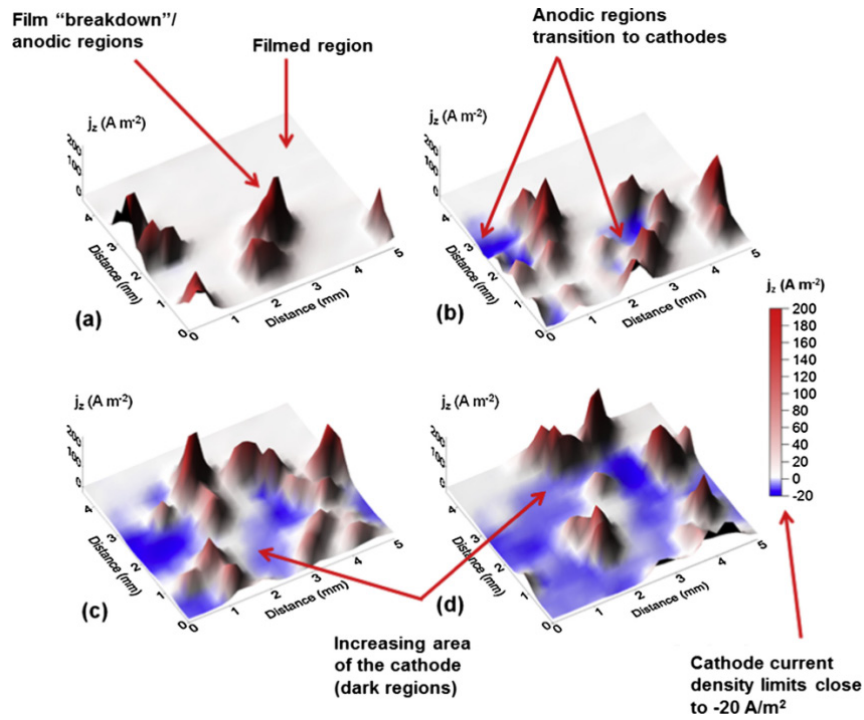
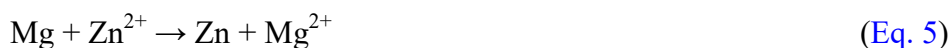


Fig. 3.3. Surface maps showing normal current density (j_z) distributions on Mg surface exposed to a 2 mol/dm³ NaCl electrolyte, (a) 7, (b) 28, (c) 48 and (d) 68 min after commencing galvanostatic polarisation at 1 mA/cm². *source:* [75] adapted from [79].

Several studies have validated that the formed Mg oxide/hydroxide film on Mg alloys can accumulate alloying elements or impurities in high concentrations [75]. The alloying elements may be also observed at the metal/corrosion film interface. As the oxide film grows inwards into the alloy, the alloying elements may be entrapped within the corrosion film [80]. As represented in Eq. 3, H_{ev0} can take place as an electrochemical reaction and during film formation. The presence of alloying elements nobler than Mg in the corrosion film may act as preferred sites for high rates of H_{ev0} increasing the overall rate of the reaction forming Mg(OH)₂ [75]. However, the nature of the alloying elements determines the corrosion performance of the metal/film system. For example, some studies suggest that the presence of Al in the corrosion film, and Zn at the metal/film interface slowdown the dissolution rate of Mg alloys and consequently the film growth rate [80,81]. An additional benefit of alloying with Zn is that Zn-rich Mg alloys exhibit reduced H_{ev0} [7]. Cheng et al. [7] proposed two mechanism of this effect:



The Zn²⁺ ions in solution in the vicinity of the bulk material tend to be consumed by the reaction in Eq.5. Additionally, Zn²⁺ and Mg²⁺ ions in solution compete for binding with

the free OH^- ions (Eq. 2, pg. 17), if $\text{Zn}(\text{OH})_2$ forms (Eq. 4) this ultimately would decrease the amount of H_2 [7]. Whether for a targeted application the goal is to reduce H_{evo} , the amount of Zn added must be cautiously selected since solubility of alloying elements in Mg is limited. Adding Zn in amounts close to that of solubility limits may result in the formation of second phases (see Fig. 3.2, pg. 18) that act as local cathodes modifying corrosion rate.

Since H_{evo} is an intrinsic phenomenon of Mg and its alloys exposed to aqueous solutions, it must be taken into consideration in the investigation of Mg alloys for surgical applications. Implants made of Mg alloys may result in the production of hydrogen gas within the *in vivo* environment and to have important effects on the adjacent tissues. Nevertheless, some authors have reported the occurrence of hydrogen gas pockets in the tissues next to the implant surface as harmless. Witte et al. [13] reported that four different Mg alloys implanted in the guinea pig femora exhibited clinically and radiographically visible subcutaneous gas bubbles. The gas pockets appeared within one week after surgery; however, disappeared after 2–3 weeks with no adverse effects observed in the guinea pigs [13]. Furthermore, fibrous tissue formation in resorbed areas of a Mg implant impregnated with bubbles of hydrogen gas have shown to stop local bleeding by a tamponade effect [28].

H_{evo} measurement on corrosion of Mg alloys is a test widely performed by researches. Measuring the volume of H_2 gas produced is equivalent to measuring mass loss of Mg since 1mol of hydrogen gas directly corresponds to the dissolution of 1mol of Mg [82]. The setup of a typical H_{evo} experiment is simple and it makes possible to trace H_2 gradual change in solution throughout the test at several time points. However, H_{evo} does not provide any information regarding the corrosion mechanisms of Mg [82]. There are some experimental limitations too: (i) differences in atmospheric pressure and temperature can affect the H_2 volume measured, (ii) part of the hydrogen evolved will dissolve into the solution and cannot be measured, (iii) the electrochemical cell must be completely sealed in order to avoid the gas to escape from the apparatus [24,82]. In addition, the majority of the studies that have reported H_{evo} of Mg alloys and compared with mass loss measurements did not find the idealized 1:1 ratio [82]. Kirkland et al. [82] reported this disparity between theoretical and experimental results within the range of 0.6 ± 0.08 . The authors argued that the reason for this variation remains unclear; however, it is an indication that the experimental setup used for H_2 collection is not highly efficient. This confirms the importance of performing H_{evo} experiments in combination with other techniques to confirm the obtained results [82].

3.3. INFLUENCE OF PHYSIOLOGICAL MEDIA ON CORROSION OF Mg ALLOYS

The major approach to assess corrosion rate of Mg alloys is to measure their *in vitro* electrochemical activity in simulated body solutions. However, commonly used solutions contain inorganic components similar to those of human body plasma (Na^+ , K^+ , Mg^{2+} , Ca^{2+} ,

Cl⁻, HCO₃⁻, HPO₄²⁻, SO₄²⁻) while human body physiological media is much more complex containing amino acids, proteins, lipids and cells [83]. Table 3.2 lists the composition of the most commonly used solutions for testing corrosion of Mg alloys in comparison to blood plasma and Minimum Essential Medium (MEM) used for cell culture. Differences between *in vitro* and *in vivo* corrosion rates of Mg alloys have been found and a main reason is the differences in the medium composition. Recently, Martinez et al. [84] made an exhaustive review of the existing results for corrosion rates of Mg alloys to elucidate the lack of correlation between *in vitro* and *in vivo* corrosion behavior. The authors observed that for 19 different Mg alloys selected —with exception of the Mg6Zn alloy— the *in vivo* corrosion rates were lower than the *in vitro* ones [84]. The values indicated that the obtained corrosion rate *in vivo* is on average 1–4 times lower than the corrosion rate obtained *in vitro*. However, when corrosion rates were grouped according to the corrosion media, *in vitro* and *in vivo* values were similar. Corrosion media that better mimic the physiological conditions can make possible to achieve corrosion rate values that reliably predict Mg alloys behavior *in vivo* [84]. *In vitro* corrosion tests have been performed using several methods and experimental conditions —usually at temperatures not in the physiological range— and the results are not necessarily comparable [84].

Table 3.2. Composition of blood plasma and most commonly employed solutions for corrosion testing of Mg alloys (concentrations in mM). *source:* [84].

	Component	Blood plasma	Hank's solution	SBF	MEM
Inorganic	Na	142	142	142	143
	K	5.0	5.8	5.8	5.4
	Mg	1.5	0.8	1.5	0.4
	Cl	103	145	147.8	125
	Ca	2.5	2.5	2.5	1.8
	HPO ₄	1.0	0.4	1.0	0.9
	SO ₄	0.5	0.8	0.5	0.4
	HCO ₃	27	4.2	27	26
Organic	Glucose	3.6–5.2	–	–	5.6
	Albumin (g l ⁻¹)	35–50	–	–	–
	Amino acids (g l ⁻¹)	Variable	–	–	0.95
	Vitamins (g l ⁻¹)	Variable	–	–	8.10

A very recent study made by Zeng et al. [85] evaluated the *in vitro* degradation of pure Mg in Hank's solution with different additions of glucose. Fig. 3.4 summarizes some relevant electrochemical results and scanning electron microscope images of the tested conditions. A more positive potential was observed for the sample immersed in the solution with the largest glucose content. The higher OCP —for 3 g/L of glucose— suggested a more protective corrosion products layer formed on the sample. The corrosion potential results depicted in Fig. 3.4c showed that increasing glucose content in Hank's solution decreased the corrosion

rate of pure Mg [85]. The authors ascribed the rapid pH decrease after 5 hours of immersion (Fig. 3.4a) to the transformation of glucose into gluconic acid ($C_6H_{12}O_7$). Additionally, glucose promoted the formation of calcium phosphate (CaP) compounds (Fig. 3.4d–f) which can be accounted for the decreased corrosion rate with increasing glucose content [85]. Zeng et al. [85] deeply discussed the associated corrosion mechanisms and concluded that the adsorption of glucose on the Mg surface is helpful for the aggregation of Ca^{2+} ions into the corrosion products due to the chelation¹⁶ of glucose with these ions.

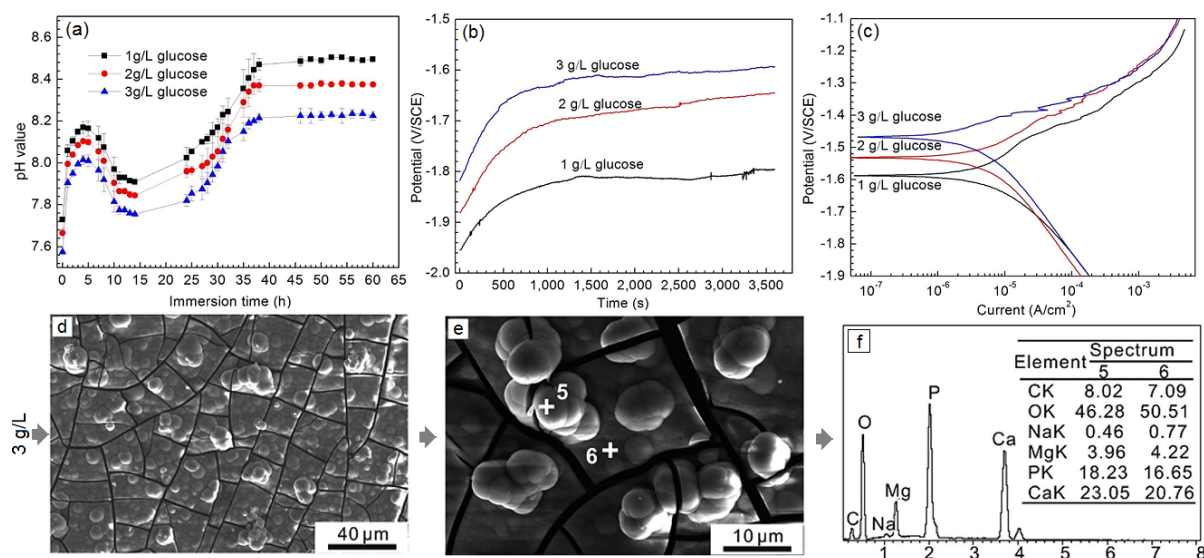


Fig. 3.4. Electrochemical measurements of pure Mg in Hank's solution at $37 \pm 0.5^\circ C$ for 50h with different glucose contents. (a) Solution pH value, (b) open-circuit potential and (d) polarization curves. (d)–(f) SEM morphologies and EDX results expressed in wt.% for 3 g/L. source: [85].

Similarly, Zhang et al. [83] reported that proteins supplemented in cell culture medium slowed down the *in vitro* corrosion rate of Mg-Nd-Zn-Zr alloy due to protein integration into the corrosion products layer. Additionally, coculture experiments with primary human umbilical vein endothelial cells (HUVEC, $37^\circ C$, 5% CO_2 , humid, sterile) accelerated the corrosion rate of the alloy. The authors suggest two possible reasons of this fact: (i) the promotion of proteins desorption due to the presence of cells and (ii) storage of Mg ions in medium during metabolism and proliferation which might accelerate the oxidation reaction of the Mg alloy [83]. This result should not be extrapolated to other situations since different cell types may respond differently to the same alloy under the same experimental conditions.

To complete, Zeng et al. [8] reported a modified pH-potential diagram of Mg and its alloys in various simulated body solutions containing proteins such as albumin¹⁷. Fig. 3.5

¹⁶ Chelate is a chemical compound in the form of a heterocyclic ring, containing a metal ion attached by coordinate bonds to at least two nonmetal ions [234].

¹⁷ Any of a class of water-soluble proteins that are found in egg white, blood serum, milk, and many other animal and plant tissues [235].

depicts the diagram where it is possible to see that the presence of bovine serum albumin (BSA) shifts the open-circuit-potential toward nobler values when compared with inorganic SBF. In fact, the BSA shifts the potential over the hydrogen line and below the oxygen line in the diagram which is the hydrogen ions stable region, suggesting that the formation of hydrogen gas is suppressed [8]. Liu et al. [86] explained this by the fact that albumin is adsorbed on the surface of the Mg substrate, the corrosion layer mainly composed by $Mg(OH)_2$ grows rapidly and the divalent Mg^{2+} interacts with BSA easily. The formed corrosion layer containing albumin constitutes a layer of high corrosion resistance [86].

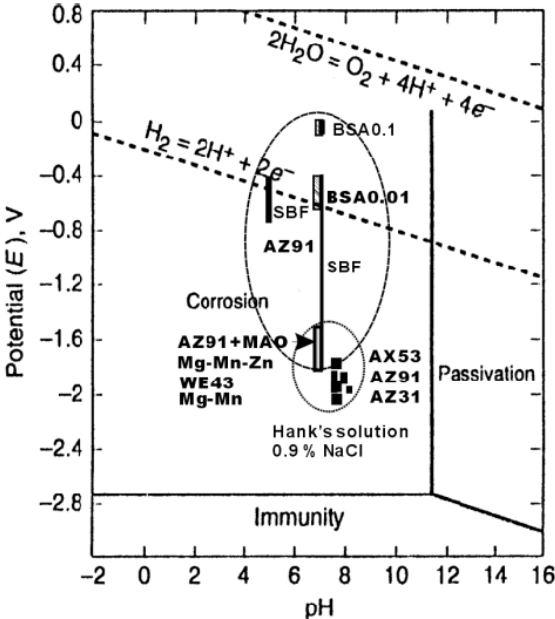


Fig. 3.5. pH-potential diagram of Mg and its alloys in several simulated body solutions. BSA – bovine serum albumin. BSA 0.01 and BSA0.1 indicating SBF with 0.01 g/L and 0.1 BSA, respectively. MAO: micro-arc oxidation. *source:* [8]

4. SURFACE PROTECTION AND FUNCTIONALIZATION STRATEGIES OF Mg ALLOYS

It is clear why the development of biodegradable implants has been growing during last decades in medical science. Despite the high potential of Mg-based materials, still there are some issues —as already discussed in the previous chapters— that need to be properly addressed in order to introduce implants made of Mg alloys as end-products in the market. Although purifying and alloying are effective to improve corrosion resistance of Mg alloys, further surface modification is required to delay the physical contact of the corrosive environment with the material surface delaying the initiation of corrosion processes and to create more biocompatible interfaces. Fig. 4.1 summarizes the surface treatment methods currently implemented to modify the surface properties of Mg alloys.

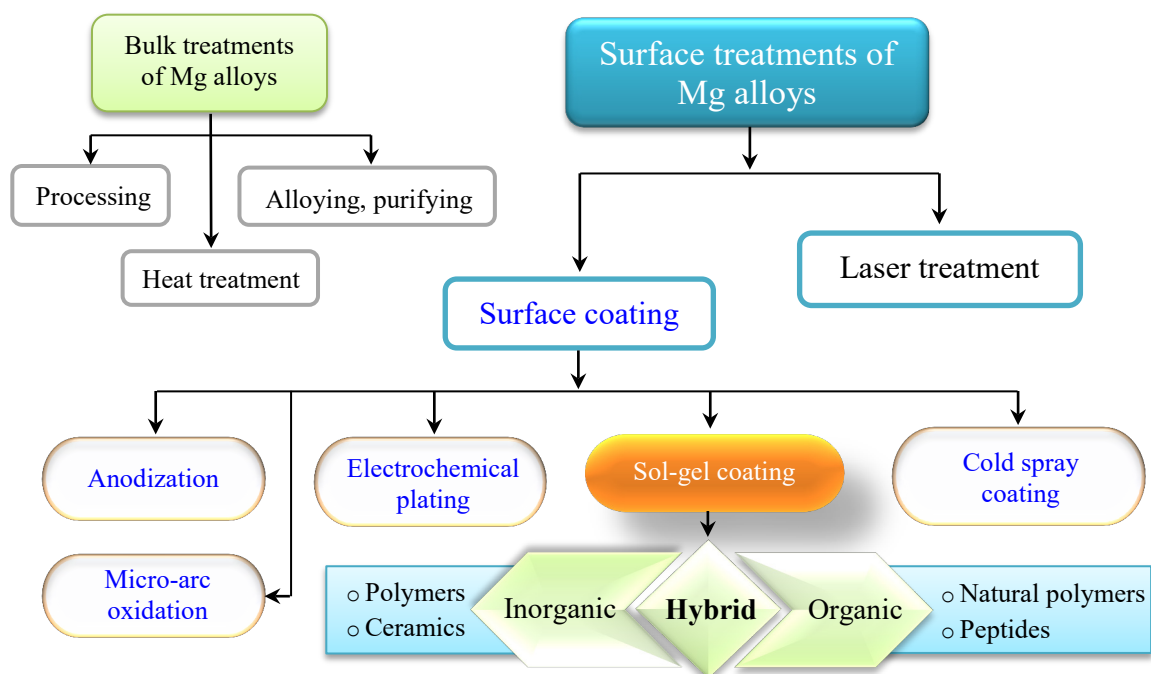


Fig. 4.1. Bulk treatments and surface functionalization strategies to improve surface properties of Mg alloys.

Up to now, many surface treatments have been developed for corrosion protection of Mg alloys. Among surface coating methods, various wet and dry techniques can be employed to improve corrosion resistance, hardness, wear resistance and appearance of the surface. Dry methods are commonly eco-friendly, however, they are high cost and unsuitable to coat parts with complex shape and large sizes [87]. On the other hand, most wet methods are more economical, easy to use, offer various possibilities in terms of surface functionalities [87] and effectively coat complex shape pieces.

Anodizing is a wet method widely used for Mg and its alloys. In this process the surface of the metal —which serves as an anode of an electrical circuit— is converted to an

oxide/hydroxide film through an electrolytic oxidation process. The anodizing process parameters —time, temperature, applied current density, etc.— greatly influence the final properties of the anodic film formed [87].

Electrochemical plating can be divided into electroplating and electroless plating. Electroplating —commonly known as electrodeposition— employs an external power source to provide an electrical signal that reduces cations of a particular metal in solution and produce a metallic coating [88]. Electroless plating relies upon the auto-catalytic reduction process of metal ions in an aqueous solution containing a chemical reducing agent, no external power source is required [88]. Coatings produced by electroplating are well adhered and provide good corrosion protection. However, plating is a complex process needing multi-step pre-treatment procedures essential for successful plating upon Mg alloys [88]. Multi-step pre-treatment is critical when considered in the context of the Mg alloy microstructure effects making also necessary considering the metal side of the interface as a decisive parameter of the plating process [88]. Still, there is a notable lack of systematic investigation of electrochemical plating coatings for Mg alloys [88].

Micro-arc oxidation (MAO) is a novel anodizing engineering process that uses an electrolytic bath. By applying high potentials the metal surface is converted into a dense-hard ceramic oxide coating [89]. Compared with conventional anodizing, MAO produces thicker coatings of high hardness and excellent bonding strength with the substrate [89]. MAO coatings can prevent galvanic corrosion and stress corrosion cracking of Mg alloys [89]. Furthermore, coatings produced in silicate electrolytes showed higher corrosion resistance compared to those produced from phosphate electrolytes on AZ91 and AZ31 alloys [89,90]. Since MAO coatings have shown to significantly improve the corrosion resistance of Mg alloys, it is then important to tailor the features of the deposited coating to the required properties of the final application, as already discussed in chapter 2. The purpose of surface treating implants made of Mg-based materials is to control their corrosion response to the desired levels and not to completely avoid it.

Cold spray coating technologies have been mainly used for repairing and restoring large damaged areas on components where deep corrosion occurred. Particularly, they can be used to repair Mg alloys used in aircraft and automotive components [91]. Cold spray is a solid-state coating process that uses a supersonic gas jet to accelerate solid powder particles —velocities ranging from 300 to 1200 m.s⁻¹— against the substrate to produce metal bonding by rapid plastic deformation of the impacting particles [91,92]. Compared to thermal spray, cold spray coatings do not develop intrinsic defects due to liquefaction and solidification of the impacted particles [92]. This route produces dense coatings with low porosity which is a desired feature for corrosion protection [92].

To the best of our knowledge, there are a scarce number of investigations on cold spray coatings to control degradation rate of Mg alloys for biomedical applications. In 2013,

Noorakma et al. [93] successfully deposited a cold spray hydroxyapatite coating on the AZ51 Mg alloy. The coating thickness ranged from 20 to 30 μm and showed signs of dissolution after 1 day in SBF solution, with signs of regeneration after 10 days of immersion [93]. Still, there are several parameters to be controlled during cold spray coating such as temperature, pressure, particle size, carrier gas and post-treatment. Here, coating complex geometries is a limitation of this technology too.

Sol-gel coating is a widely used technique to improve corrosion resistance of Mg alloys. It is a low temperature alternative to the preparation of glasses and ceramics [94]. Li [94] schematically summarized sol-gel applications developed since this route was first reported by the French chemist J. Ebelman in 1845.

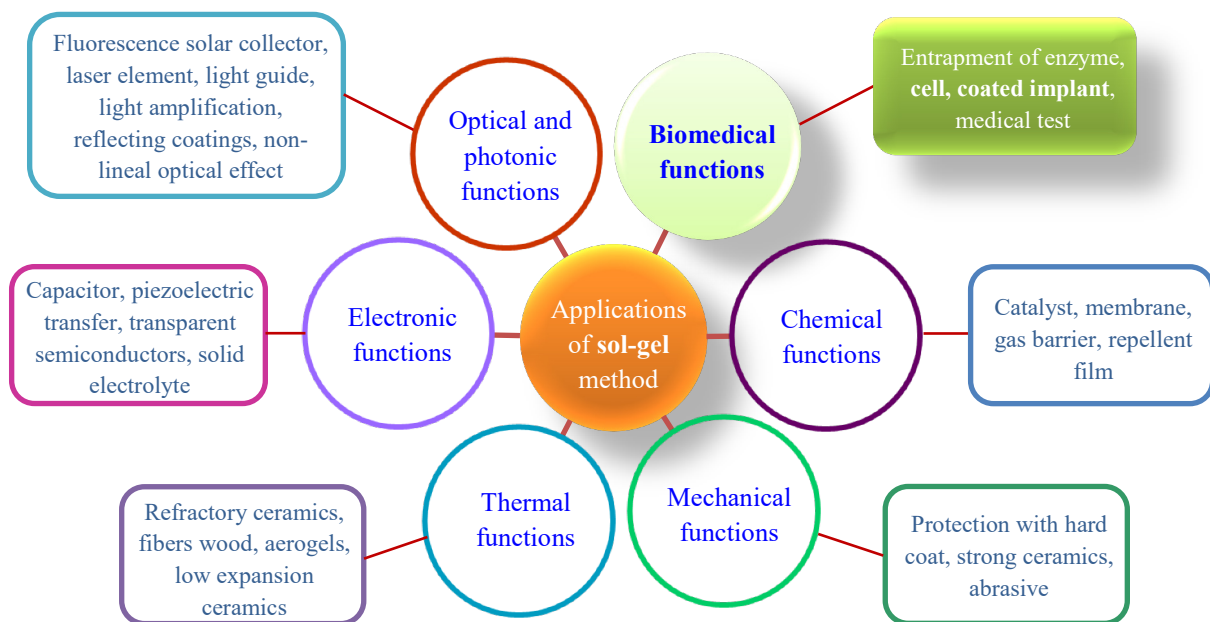


Fig. 4.2. Applications of the sol-gel route. *source:* [94]

The development of science and technology of sol-gel has been growing exponentially since the end of the 20th century, particularly the organic-inorganic hybrids [94]. As a possible substitute for environmentally unfriendly surface treatments, sol-gel coating systems offer corrosion protection, good adhesion to metallic surfaces and good physical bonding to organic top coats applied over the cured sol-gel [94]. Furthermore, sol-gel technology is cost-effective and requires simple application procedures that can be easily adapted by industry [94].

4.1. HOW SOL-GEL COATINGS IMPROVE THE CORROSION RESISTANCE OF Mg ALLOYS?

In the sol-gel process an oxide network is generated by progressive condensation reactions of molecular precursors —the starting compounds— in a liquid medium [94]. Depending on the type of precursors the synthesis is divided into: (i) aqueous solutions of metal salts; (ii) metal alkoxide¹⁸ precursors; and (iii) mixed organic/inorganic precursors [94]. Currently, the non-aqueous approach is the most used instead of the aqueous method. The non-aqueous approach is initiated with a metalloid alkoxide precursor (M(OR)_x) in solution or with organic precursors in an alcohol a low-molecular mass organic solvent [94]. Typically, R is an alkyl¹⁹ group and M a networking forming element (e.g. Si, Ti, Zr, etc.). Alkoxysilanes are commonly used to prepare corrosion protective coatings; one of the most thoroughly used is tetraethyl orthosilicate (TEOS). Metal alkoxides are popular because they react easily with water [95].

There are three stages involved in the sol-gel process: (i) hydrolysis; (ii) condensation and polymerization to form chains and particles; and (iii) drying and aging [94]. In the hydrolysis reaction the hydroxyl ions attach to the metal atom [95]. For example, for the case of TEOS the reactions are [95]:

Hydrolysis



Condensation



or



Hydrolysis may be partial or total depending on the amount of water and catalyst present. Two molecules partially hydrolyzed can link together, in the condensation reaction as described in Eq. 7 and Eq. 8 [95]. By definition both hydrolysis and condensation could liberate low-molecular mass by-products, such as water and alcohol that are removed during drying step. When further condensation occurs, large silicon containing molecules can form during the polymerization leading to shrinkage of the network [94,95]. After the sol-to-gel

¹⁸ Metal alkoxides are members of the family of metalorganic compounds which have an organic ligand attached to a metal or metalloid atom [95].

¹⁹ Ligand formed by removing one hydrogen (proton) from an alkane molecule [95].

transition —gelation²⁰— the processes of change during aging are polymerization, coarsening, and phase transformation [95].

Various sol-gel coatings for corrosion protection of Mg alloys have been reported in literature. Particularly, organic functional silanes present good adhesion to the metallic substrate through chemical bonding providing good corrosion protection [94]. Moreover, chemical bonding is also possible between a deposited sol-gel and top coat organic paint systems, due to the presence of functional groups in the hybrid sol-gel film [96]. Fig. 4.3 shows a schematic representation of two possible ways for enhancing chemical compatibility of an epoxy-based and an amino-containing paint system to a sol-gel film by functionalizing the organic component of the hybrid sol-gel. Incorporating organic components into the inorganic ones opens up a wide range of possibilities for functionalization and tailoring the final application [96].

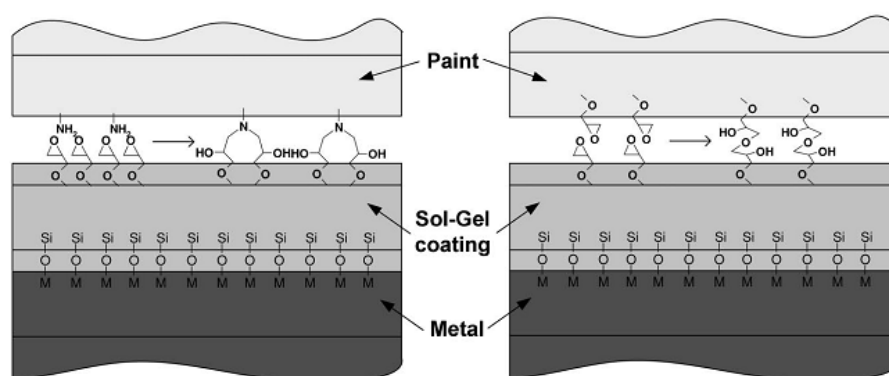


Fig. 4.3. Representation of enhanced compatibility of different paint systems with an epoxy-functional hybrid sol-gel coating. *source:* [96].

Hybrid sol-gel coatings have high potential for several applications since they combine the properties of organic polymers and the properties of ceramics. Besides of increasing functional compatibility with organic or hybrid paint systems, the organic component increases density and flexibility while the inorganic component increases scratch resistance, durability and adhesion to the metallic substrate [96]. Moreover, some studies suggest that hybrid sol-gel coatings possess good biocompatibility [97].

Due to the high susceptibility of Mg alloys to corrosion, various pre-coatings such as anodized and fluoride conversion coatings are used when depositing low pH processing sols [94]. Furthermore, sols may contain aggressive corrosive ions such as Cl^- and consequently cannot be directly applied on the Mg alloy since they will react with the substrate leading to insufficient coating adhesion [94].

²⁰ The gel point represents the moment when the last link is formed in the chain of bonds that constitutes the spanning cluster and the solution loses fluidity [95].

Sol-gel films including titanium dioxide (TiO_2) and 3-glycidoxypropyltrimethoxysilane (GPTMS) have been coated on Mg alloys showing good corrosion protection [98]. TiO_2 coatings applied by the sol-gel method have been investigated on 316L stainless steel [99] and commercially pure titanium (CP-Ti) [100] in order to enhance the biological properties of these materials. Hu et al. [101] investigated the in vitro degradation of nano- TiO_2 coated AZ31 Mg alloy in Hank's solution. They performed various annealing treatments of sol-gel deposited nano- TiO_2 films at different temperatures and holding times. The results showed that the longer the annealing time the lesser the number of defects in the film, contributing to an enhanced corrosion resistance [101].

GPTMS is one of the most important precursors and it is commonly used for the preparation of organic-inorganic hybrids sol-gel coatings [102]. This is a combination of glycidoxy (organic) and silicon alkoxy (inorganic) groups having the ability to simultaneously form an organic network of polymerized glycidoxy groups and an inorganic SiO_2 network through hydrolysis and condensation reactions of alkoxy groups [102]. Silane coatings have shown to be effective in decreasing the corrosion rate of Mg alloys in SBF solution [103,104]. Alternatively, sol-gel coatings offer the possibility of incorporating fibers, nanoparticles and nanocontainers providing additional functionalities to the coating, such as improved mechanical properties, self-healing functions and enhanced bioactivity [105]. This approach allows creating various functionalities demanded by real applications. Thus, by combining different materials/components makes possible to optimize the coating performances according to the end-product requirements. An advantage of organically modified sol-gel systems is the improvement of mechanical properties preventing crack formation of the sol-gel film during the drying/curing process [96]. Finally, biocompatible coatings prepared by the sol-gel method have shown to be more bioactive than those of the same composition applied using other methods. Particularly, improved calcium and phosphate precipitation onto implant surfaces have been evidenced [100].

4.2. SURFACE FUNCTIONALIZATION OF Mg ALLOYS FOR BIOMEDICAL APPLICATIONS: A REVIEW

Various surface coatings have been introduced for Mg-based orthopaedic implants, e.g., plates and pins and interference screws to improve biocompatibility and corrosion resistance. This is also the case of Mg-based stents for cardiovascular applications. Nevertheless, there are similarities and differences of coatings used in stents and in orthopaedic implants [98]. For example, for stents biodegradable polymers with suitable mechanical properties, good biocompatibility and controlled drug release are of high interest. Drug-eluting is a property that has been mainly explored in coatings for coronary stents and scarcely in coatings for implants [98]. Ma et al. [98] summarized and classified similarities and differences in coatings for vascular stents and orthopaedic implants (Fig. 4.4).

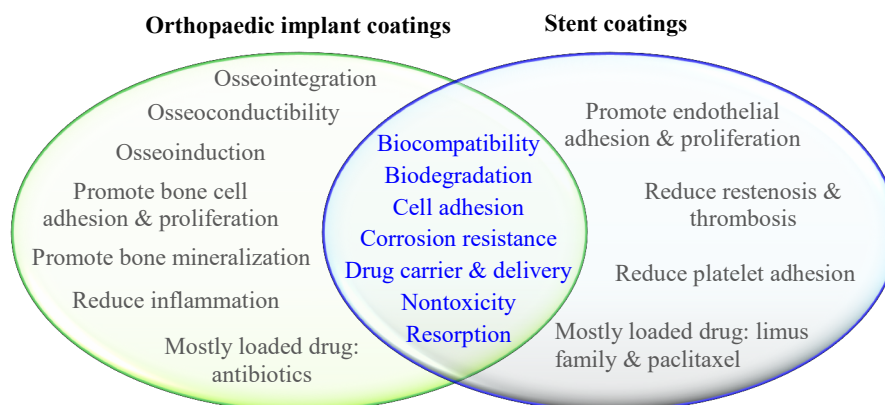


Fig. 4.4. Coating requirements and functions for stents and orthopaedic implants. *source:* [98].

Metal coatings [106], metallic oxide/hydroxide coatings [107], chemical conversion coatings [108], inorganic coatings [109] and polymer coatings [110] have been so far developed for Mg alloys [98]. For orthopaedic implants, the most widely investigated coatings are calcium phosphate and hydroxyapatite (HAP) due to their structural similarities to human bone [98]. They provide biological properties for adsorption of proteins and adhesion of cells to the implant surface [111].

Several authors such as Ma et al. [98], Hornberger et al. [112] among others have reviewed the research carried out in the field of coatings on Mg alloys for biomedical applications. In these reviews the authors concluded that calcium phosphate coatings produced by conversion or deposition methods are the ones most frequently studied. Table 4.1 list some representative studies on calcium phosphate (CaP) coatings as sorted by Ma et al. [98] and Hornberger et al. [112]. The listed coatings were reported in literature between 2011 and 2013.

Table 4.1. Some calcium phosphate coatings on Mg alloys for biomedical applications reported in literature between 2011 and 2013. *source:* modified from [98,112]

Authors	Substrate	Coating	Method	Corr. solution/ °T	Results
Yang et al. [113]	AZ31	Amorphous Ca/Mg-phosphate	Chemical conversion	In vivo implantation in rabbit's thighbone	No inflammation observed after 8 weeks post-operation. New bone tissue formed around the implant.
Roy et al. [114]	Mg-4Y	β -TCP and HAP	Sol-gel + heat treatment	DMEM without Fetal Bovine Serum (room temperature)	The coating did not slowdown degradation kinetic of the substrate but increased bioactivity
Jo et al. [115]	Mg	MgO, Ca and P	Anodization or MAO + chemical conversion in cell-culture medium	SBF (37°C)	MgO coating improved corrosion resistance. Improved biocompatibility after post-treatment of MgO with cell-culture medium

Table 4.1. (continued)

Abdal-hay et al. [116]	AZ31	HAP-doped PLA	Cold spray	Hank's solution (37°C)	Improved corrosion resistance and improved MC3T3 cell response
Bakhsheshi-Rad et al. [117]	Mg-Ca-Zn	Nano-HAP/MgF ₂ ; DCPD/MgF ₂	Chemical conversion + electrodeposition	SBF (room temperature)	Reduced Hevo and improved nucleation site of apatite
Niu et al. [118]	Mg-Nd-Zn-Zr	CaHPO ₄ ·2H ₂ O (Brushite)	Chemical conversion	Hank's solution (37°C) + in vivo implantation in rabbit's tibia	Improved corrosion resistance in Hank's solution and in vivo; uncoated and coated Mg alloy induced bone growth in vivo

DMEM: Dulbecco's Modified Eagle's Medium; β-TCP: beta tricalcium phosphate; PLA: polylactic acid, DCPD: dicalcium phosphate dehydrate

As observed in Table 4.1 several methods are used to deposit CaP coatings on Mg alloys. Depending on the experimental conditions, spontaneous precipitation can be divided into biomimetic deposition and wet-chemical precipitation [111]. Biomimetic deposition is performed from artificially prepared simulating solutions —e.g. Hank's balanced salt solution, SBF—, while solutions for wet-chemical deposition are simpler in composition and contain non-biomimetic ions [111]. The final composition of CaP layers obtained by wet-chemical methods depends on the bath solution and on the substrate bulk composition. The resulting coatings can include besides CaP, amorphous carbonated calcium/magnesium phosphate, Mg phases and are mostly amorphous containing small amounts of crystallized HAP [112]. In general, the results show that controlled degradation and improved bioactivity can be achieved by adjusting the CaP phases along with using alloys instead of pure Mg as the substrate [112].

We made a brief examination of the most recent research work on coatings for biodegradable Mg alloys published during 2015 and 2016. Still, CaP coatings lead as the preferred choice of researchers. Some of the reviewed studies are summarized in Table 4.2. Moreover, it was found that newly developed biodegradable Mg alloys are being explored, such as EW62 (6 wt.% Nd, 2 wt.% Y) and EW10X04 (1 wt.% Nd, 0.48 wt.% Y, 0.43 wt.% Ca) [119].

Table 4.2. Some studies on coatings for biodegradable Mg alloys published in 2015 and 2016.

Authors	Substrate	Coating	Method	Corrosive solution/°T	Results
Singh et al. [120]	Mg-3Zn	HAP	Sol-gel/dip coating	SBF (37°C)	Enhanced corrosion resistance and osteogenic cell adhesion and viability
Yao et al. [121]	AZ31B	MgO/brushite/HAP	MAO + hydrothermal treatment	SBF (room temperature)	The hydrothermal layer had a sealing effect for MAO coating improving corrosion resistance.

Table 4.2. (continued)

Santos et al. [122]	XHP-Mg	GO/HapNP/phosphate coating	Electrophoretic deposition	SBF (37°C)	The coating exhibited lower current density compared to the single phosphate coating and uncoated XHP-Mg.
Zeng et al. [123]	AZ31	Crystalline $Zn_3(PO_4)_2 \cdot 4H_2O$ / $Mg_3(PO_4)_2/Ca_3(PO_4)_2$ with traces of non-crystalline MgF_2/CaF_2	Chemical conversion	3.5% NaCl (room temperature)	Better barrier properties of Zn-Ca-Ce-P coating than Zn-Ca-P coating. The coatings led to an increase in H_{evo} rate.
Bakhsheshi-Rad et al. [124]	Mg-Ca	MgO/MgAl ₂ O ₄ -PLA	MAO + dip coating	SBF (room temperature)	Hydrophobic PLA sealed porous of MAO coating improving corrosion resistance.
Bakhsheshi-Rad et al. [125]	Mg-Ca	NiCrAlY/nano-YSZ/PCL	Atmospheric plasma spraying + dip coating	3.5% NaCl (room temperature)	PCL provided protection to the substrate by sealing the porous nano-YSZ coating.
Dunne et al. [119]	WE43; EW62; EW10X04	HAP	Blast coating	PBS (37°C)	The process produces discontinuous coating. Decreased corrosion rate and H_{evo} .
Zomorodian et al. [126]	AZ31	PCL/nano-HAP/cephalexin	Sol-gel/dip coating	Hank's solution (room temperature)	HAP and cephalexin induce defects in the PCL coating and reduce the barrier properties compared to unmodified PCL.
Shen et al. [127]	AZ31	$Na_2CaSi_3O_8/Ca_5(PO_4)_2(SiO_4)_6$	Sol-gel/dip coating	SBF (37°C)	Improved corrosion resistance with high adhesion strength of coating/substrate.

XHP-Mg: ultra-high purity Mg; GO/HapNP: graphene oxide /hydroxyapatite nanoparticles; PBS: phosphate buffered saline; c-SBF: conventional Simulated Body Fluid; EBSS: Earle's Balance Salt Solution; PLA: polylactic acid; YSZ/PCL: yttria stabilized zirconia/polycaprolactone

It appears that MAO technique to produce protective coatings for Mg alloys is gaining popularity amongst researchers. One advantage of this technique is that it produces coatings of good abrasion resistance and high bonding strength to the substrate. However, due to the porous structure MAO coatings are not able to provide long term corrosion protection [124]. Therefore, additional layers have been employed to seal the pores of MAO coatings. Yao et al. [121] developed two kinds of hydrothermal layers deposited onto a porous MgO coating on AZ31B Mg alloy. Both flake-like HAP/dicalcium phosphate dehydrate (DCPD) and rod-like HAP layers increased thickness and decreases roughness of the MAO coating. Furthermore, the layers presented an excellent sealing effect of the porous improving the corrosion resistance of the AZ31B alloy [121]. Bakhsheshi-Rad et al [124] produced a duplex coating of MgO-MgAl₂O₄/PLA on a Mg-Ca alloy. The results showed that sealing the porous of MAO layer by PLA polymer coating considerably enhanced the corrosion resistance of the

alloy in SBF solution [124]. In general, barrier properties of MAO coatings on Mg alloys have shown dependence on process parameters such as pulse frequency, oxidation time, electrolyte concentration and voltage [128].

Coating Mg alloys by the sol-gel route has shown good results providing effective corrosion protection and good properties of the as-deposited coating. Shen et al. [127] prepared a bioglass-ceramic coating (see Table 4.2) on AZ31 substrates through the sol-gel route followed by heat treatment. The higher the sintering temperature (350–500°C) the more compact the coating structure; however, increasing the temperature also deteriorated the adhesion strength of coating/substrate. The authors were able to tailor the sintering temperature to the best corrosion resistance of the coated system determined by electrochemical tests in SBF solution. Similarly, Singh et al. [120] successfully coated a Mg-3Zn Mg alloy with HAP by the sol-gel method. The mechanical integrity of the coating was established as a function of the substrate surface roughness and the sintering temperature of the coating [120]. The corrosion resistance of the coated system increased with the sintering temperature. Bone cells were found to be viable and proliferate on the HAP-coated Mg-3Zn alloy. Then, heat treatment of sol-gel coatings must be controlled and optimized too in order to achieve the desired structural and adhesive properties as well as the required corrosion barrier properties of the sol-gel derived coating on Mg alloy implants.

It is important to remark that heat treatments modify the bulk properties of the Mg alloy via the microstructure. Modifications in the substrate bulk microstructure directly impact on the mechanical and the corrosion properties of the material. Hence, characterization of the bulk properties after performing heat treatments as final step of the coating process should be as important as the characterization of the as-deposited surface layer.

In addition, from the studies listed in Table 4.2 it is evidenced that still the research tendency is to test *in vitro* corrosion performances by using inorganic aqueous solutions — e.g. Hank's solution and SBF— as well as at temperatures not in the physiological range. The relevance of considering these parameters to evaluate biodegradation of Mg alloys implants was already discussed in chapter 3.

It is clear that surface coating of Mg alloys improves the corrosion resistance and the biocompatibility of these materials. However, considering the complexity of the biological environment in the human body some work still needs to be done to achieve the optimum surface for biodegradable Mg implants. The proper surface should be multifunctional to reach the requirements for the biomedical application [129]. Composite coatings that combine properties of different coatings/layers including biofunctional organic molecules may be a promising strategy. In 2014, Tian and Liu [129] made a critical review on surface modifications of Mg alloys. The authors discussed the advantages and disadvantages of the current used methods and gave suggestions for their utilization considering that surface design of Mg-based materials should be based on the application situation. As main conclusions,

Tian and Liu [129] suggested that the proper surface of a Mg implant could be designed as follows:

- An inner-most layer highly adhered to the substrate to control the corrosion rate.
- An intermediary layer for further enhanced corrosion resistance and biocompatibility, such as degradable polymers or CaP-based coatings.
- An outer-most layer grafting different organic molecules to control cells behavior and to obtain specific biofunctions.

Compared with biodegradable synthetic polymers, natural occurring polymers have shown to have much higher biocompatibility as well as improved bioactivity [98]. Wound healing and tissue engineering are some research areas where natural polymers have been successfully applied [98]. In the next chapter, we introduce a general overview of natural polymers collagen and chitosan and discuss their potential use as surface coatings to enhance biological response of Mg alloys.

5. NATURALLY DERIVED BIOMATERIALS

Naturally derived materials are an important sub-group of biomaterials for use as tissue engineering templates due to their biocompatibility, bioactivity and their intrinsic morphological resemblance of the natural extracellular matrix [130]. The extracellular matrix or ECM is a multi-component structural 3D network synthesized and assembled by the resident cells [130]. It includes an array of multidomain biomacromolecules such as collagens, glycoproteins, proteoglycans and elastic fibres [130].

The advantage of using natural biomaterials is their inherent ability to promote biological recognition by assisting cell functions [130]. In addition to the helical macromolecules present in the ECM such as collagen, other naturally occurring biomaterials are essential for the functionality of a wide variety of structured materials [130]. Naturally derived biomaterials may be divided into two groups: (i) protein-based biomaterials and (ii) polysaccharide-based biomaterials. Among protein-based biomaterials, collagen is remarkable. It is the most dominant protein in several types of human soft and hard connective tissues [130]. Due to its multifunctional properties, collagen has high potential for the design of new resourceful ECM-like biomaterials. On the other hand, among polysaccharides-based biomaterials, chitosan is a promising material with high potential for bioapplications due to its unique structure and multidimensional properties [131]. The source material for chitosan (chitin), is the second most abundant organic material —after cellulose— in the amount produced annually by biosynthesis [132].

Herein, we will introduce important basic concepts of collagen and chitosan properties as biomaterials and will provide a brief state of the art of relevant investigations exploring their convenient use for bioapplications.

5.1. COLLAGEN

Collagen is a collective noun referring to a specific family of proteins all built up in the same way: three polypeptide chains (α -chains) folded into a triple helical structure [133] as represented in [Fig. 5.1](#). It is the most abundant protein in the ECM of human soft and hard connective tissues [134]. Collagen not only plays a key role in fibrous structural components but also helps in manufacturing the structural architecture of the skin, skeletal systems and various internal organs [130]. It is a natural-versatile biomaterial that can be formed into highly organized 3D matrices, intrinsically biocompatible and biodegradable [130]. At the cellular level, intracellular bonds formed by the collagen fibers provides an architectural function and even supply cells of oxygen and nutrients [130].

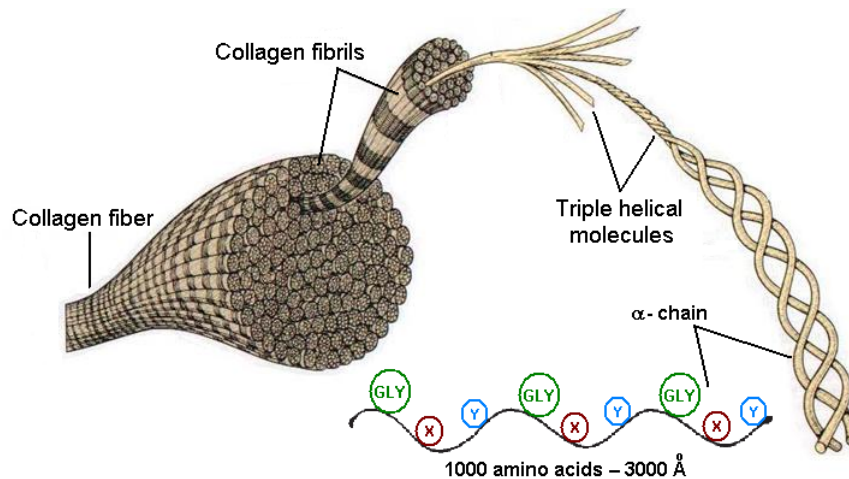


Fig. 5.1. Representation of the triple helical structure of collagen. A single peptide chain (α -chain) is comprised of glycine (Gly), proline (X) and hydroxyproline (Y) amino acids in a distinctive repeating pattern depending on the α -chain type. *source:* Modified from [135].

A single polypeptide α -chain contains about 1.000 amino acids of 3.000 Å in length [136]. There are genetically distinct chains with the same configuration but different composition and sequence of their amino acids, leading to different types of α -chains [136]. The combination of the three α -chains determines the type of the resulting collagen molecule among all 28 types identified in mammals [133,136]. Type I collagen (2 α_1 -chain and 1 α_2 -chain) accounts for more than 90% of the total collagen found in nature [133], other types are present in relatively minor amount. One major feature of collagen I is its ability to self-assemble into highly organized supramolecular structures, namely fibrils [133,137,138]. The fibrils dimensions and their polydispersity are responsible for the living tissue mechanical properties [133]. Larger entities formed by fibrils —collagen molecules aggregated side by side— are typically called fibers —collagen fibrils associated into bundles— (Fig. 5.2). The self-assembly process of chemical binding between α -chains to form a fibril and/or between fibrils to form a fiber, is called fibrillogenesis (see [133,137] for further review).

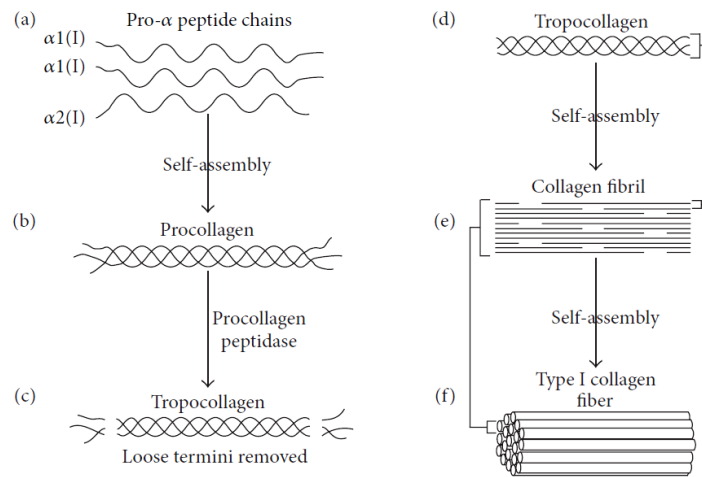


Fig. 5.2. (a) Representation of type I collagen synthesis. (a) Two $\alpha 1$ -chains and one $\alpha 2$ -chain form (b) procollagen; (c)–(d) removing loose termini of procollagen creates a type I tropocollagen molecule; (e) self-assembled tropocollagen form a fibril and (f) self-assembled collagen fibrils form a type I collagen fiber. *source:* [66].

5.1.1. Exploding collagen proficiency

It has been observed that under *in vitro* conditions collagen from diluted acid solutions resembles the microstructure of those collagens observed *in vivo* [133]. *In vitro* fibrillogenesis is triggered by neutralization and/or warming the solutions [139].

Gobeaux et al. [133] demonstrated that simple physico-chemical parameters determine the molecular organization of type I collagen in solution: i.e. (i) concentration, (ii) pH and (iii) ionic strength. They demonstrated that collagen concentration had a definitive impact on the fibrils size. Increased concentration led to larger fibrils and to a less open porosity of collagen gels (Fig. 5.3). Furthermore, fibril orientation reflected the molecular order in the initial acidic solutions: isotropic at 30 mg/ml and oriented at 80 mg/ml [133]. With respect to pH, Gobeaux et al. [133] reported that fibrils assembled spontaneously and were stable over the wide pH 6.2-12 range.

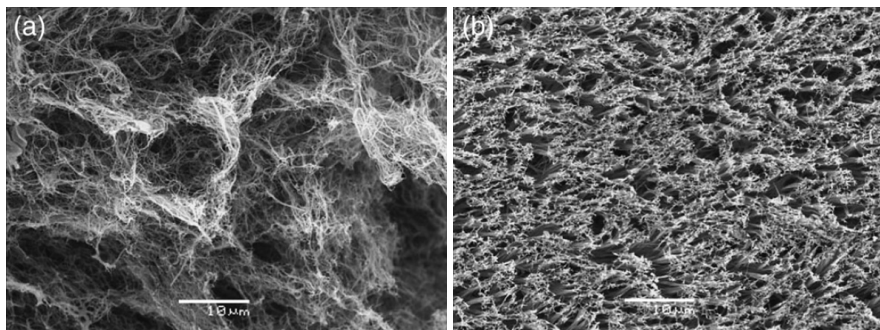


Fig. 5.3. Scanning electron images of fibrillar gels of different concentrations: (a) 30 mg/ml, (b) 80 mg/ml *source:* [133].

Chen and Liu [130] discussed the potential of collagen I to create desirable biomimetic environments for osteoblastic cells offering the possibility of exploring ECM cues for bone repair and regeneration. In this sense, collagen I matrices may be used as cell vehicle for bone tissue engineering applications. It has been recognized that collagen I —besides many other ECM components— is able to modulate cell adhesion, migration and proliferation (Fig. 5.4) [130]. Therefore, it is extensively used as scaffold for cell transplantation for regulate cellular functions via cell-matrix interactions [140].

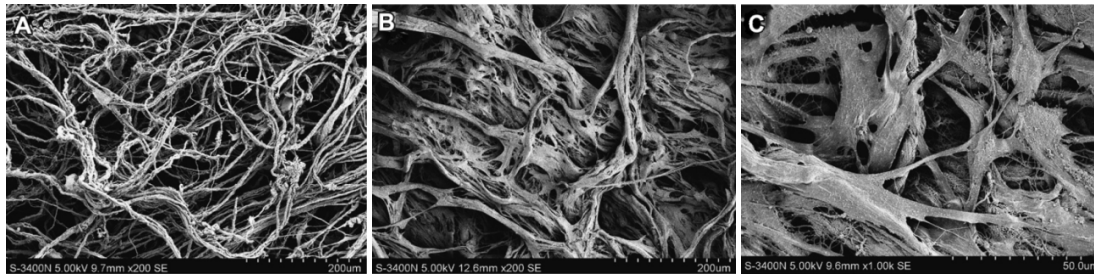


Fig. 5.4. Scanning electron microscope images human bone marrow-derived stem cells on collagen fibers matrices derived from human skin (a) before cell seeding; (b) after 24h cell culture: ECM formation and cell ingrowth; (c) after 72h cell culture: cell-matrix-collagen integration. *source*: [140].

The synthesis of collagen *in vivo* comprises intracellular and extracellular phases [136]. Collagen is mainly synthesized by fibroblasts with the intracellular processes starting at the nucleus (see [136] for detailed explanation). However, dense collagen matrices are acellular, different from collagen hydrogels that initially entrap cells [141]. Giraud-Guille et al. [141] studied the interaction of fibroblastic and osteoblastic cells with collagen matrices. They demonstrated that concentrated collagen hydrogels (3 mg/ml) had enhanced cell behavior and mechanical properties than normal collagen hydrogels (1 mg/ml). On the other hand, dense collagen matrices prepared at 40 and 300 mg/ml offered promising materials for denser connective tissues, such as bone [141].

A recent study made in 2014 by Mushahary et al. [142] showed that collagen I coatings deposited on Mg-5Zr and Mg-5Zr-Ca magnesium alloys enhanced the surface energy and the hydrophobicity of these materials. Furthermore, the presence of collagen I strongly influenced the protein binding capacity onto the alloys surfaces leading to better osteoblasts activity [142]. *In vivo* experiments in rabbits suggested that collagen I enhanced bone formation after 1 month of implantation.

A composite hydroxyapatite/collagen coating on AZ31 alloy achieved chemical bonding between hydroxyapatite and collagen similar to natural bone [143]. In this study, Wang et al. [143] observed that the composite coating improved the corrosion resistance of the Mg alloy in 1.5-fold Hank's solution as well as suppressed the sharp pH rising and the released Mg^{2+} from the substrate to extensive degree.

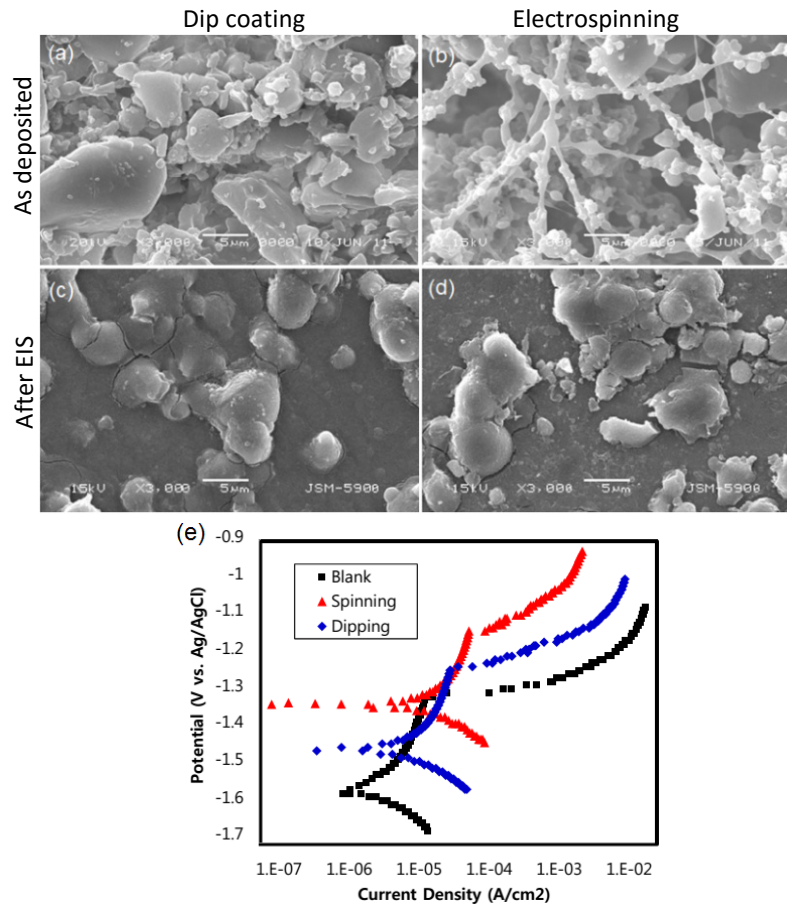


Fig. 5.5. SEM images of collagen coated AZ31 alloy by (a),(c) dip-coating and (b),(d) electrospinning technique. (c),(d) coating morphology after electrochemical impedance spectroscopy (EIS) experiments in Hank's solution. (e) Potentiodynamic polarization curves of uncoated (blank) and collagen coated AZ31 alloy with different methods. *source:* [144]

Park et al. [144] coated the AZ31 alloy with collagen by using two different techniques: (i) dip coating and (ii) electrospinning and investigated the *in vitro* corrosion behavior. The results showed that the coating morphology and barrier properties varied depending upon the deposition method. The electrospin coating consisted of beaded collagen fibres of diameter ranging from 90 to 700 nm (Fig. 5.5b) while dip-coating produced an agglomeration of irregular collagen particles of heterogeneous size (Fig. 5.5a). Potentiodynamic polarization curves of uncoated and coated AZ31 alloy in Hank's solution showed that the collagen coating deposited by electrospinning presented the best corrosion resistance among the tested conditions [144]. In general, collagen coating deposited by both electrospinning and dip-coating techniques improved the corrosion resistance of AZ31 alloy in Hank's solution. Finally, precipitation of calcium phosphate onto the collagen coating resulted in the change of morphology, as observed in Fig. 5.5c–d, after electrochemical impedance spectroscopy (EIS) measurements. Unfortunately, the authors were not clear enough in specifying the immersion period of the EIS experiments.

Summarizing, the findings discussed above evidence the multiple relevant roles of collagen-based materials making possible to produce scaffolds, porous matrices, hydrogels and coatings. To date, collagen-based materials have been used for wound dressing, sutures and drug delivery systems. Particularly, collagen morphogenesis makes it suitable for both soft and hard tissues regeneration applications. It seems that researches are joining effort to find collagen new sources as well as exploring new processing conditions and potential novel or improved applications [145].

5.2. CHITOSAN

Chitosan is another natural polymer with high potential for bioapplications that during the past 20 years, has gained popularity in biomedical and other industrial areas due to its unique structure and multidimensional properties [131]. Chitosan is derived from natural occurring sources such as fungi and the exoskeletons of some crustaceans and insects [131] with novel properties such as biocompatibility, biodegradability and wound-healing activity [132]. It is a polyelectrolyte²¹ with reactive functional groups and the N-deacetylated²² derivative of chitin (Fig. 5.6a), the second most abundant natural amino polysaccharide after cellulose [146]. Chitin in aqueous 40-50% (w/v) NaOH solution at 90–120°C for 4 to 5 hours results in its N-deacetylation. The degree of deacetylation (DD) —or the content of glucosamine (C₆H₁₃NO₅)— and the polymer molecular weight depend upon the treating conditions [131]. Fig. 5.6b represents the deacetylation process of chitin to obtain 70% deacetylated chitosan.

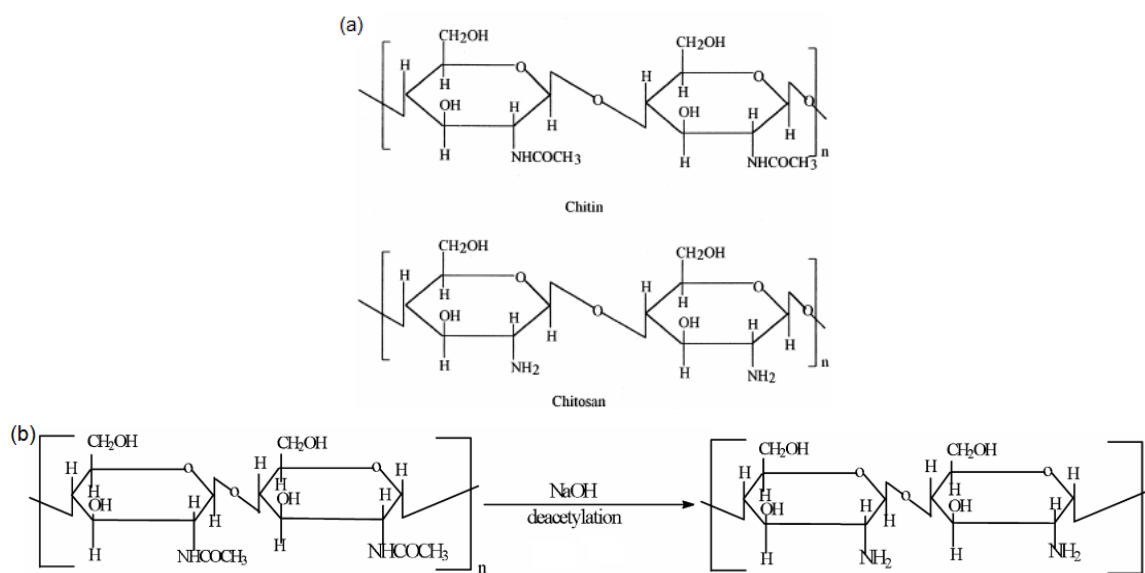


Fig. 5.6. (a) Chitin and chitosan structures and (b) scheme of 70% deacetylated chitosan after treating chitin in 40% NaOH at 120°C for 1–3 h. *source:* [146]

²¹ A polymer, such as protein or some polysaccharides, having ionic or ionizable constituents [236].

²² Deacetylation is the removal of an acetyl group (–COCH₃) from a molecule [237].

Chitin is readily obtained from crab or shrimp shells. The processing involves proteins removal and dissolution of calcium carbonate which is present in crab shells in high concentrations [146]. Chitosans with main structural differences —DD and molecular weight— result in specific chemical and biological properties variations (see Table 5.1) [131]. Low molecular weight chitosan is generally comprised within the 20–190 kDa range with DD < 75% and high molecular weight is generally comprised within the 190–375 kDa with DD > 75% [131]. Crystallinity is also affected by DD, it is maximum for 0% deacetylated chitin and for 100% deacetylated chitosan [131]. A high molecular chitosan enhances viscosity of acidic solutions with increasing chitosan concentration and DD which affect biological performances such as wound-healing and biodegradation [131]. Chitosan has been shown to degrade *in vivo* mainly by enzymatic hydrolysis which appears to target acetylated residues resulting in biocompatible degradation products of chitosan oligosaccharides²³ of variable length [132]. The degradation rate is inversely proportional to the degree of crystallinity which in turn depends on the DD as observed in Table 5.1. High DD (>75%) results in chitosans with low degradation rate that may last several months *in vivo* minimizing local inflammation [131,132]. Very fast degradation of chitosan may cause amino saccharide accumulation and produce inflammatory responses [131].

Table 5.1. Relationship between structural parameters and properties of chitosans. *source:* [131]

	Property	Structural characteristics
Chitosans	Solubility	↑DD
	Crystallinity	↓DD
	Biodegradability	↓DD, ↓Molecular weight
	Viscosity	↑DD
	Biocompatibility	↑DD

↑ Directly proportional, ↓ inversely proportional

5.2.1. Chitosan and its derivatives for bone applications

Chitosans are being widely studied for bone tissue engineering due to they are biocompatible, biodegradable and can be formed into porous structures which improves osteoconduction²⁴. Several studies have focused on chitosan-calcium phosphates (CP) combinations, chitosan would improve mechanical properties of the CP ceramic phase via matrix reinforcement [132]. Furthermore, it has shown to promote cell growth and mineral rich matrix deposition by osteoblasts cells in culture [131].

Kawakami et al. [147] developed a hydroxyapatite/chitosan composite paste to be implemented as bone filler material and evaluated its osteoconductive properties. They observed new bone formation into the matrix of the self-hardened paste after 1 week post-

²³ A carbohydrate that consists of a relatively small number of monosaccharides [238].

²⁴ Provision of a scaffold for the growth of new bone [239].

implantation on the surface of the tibia. Bone formation continued through week 20 demonstrating suitability of this material as bone graft [147]. Zhao et al. [148] fabricated 3D-porous scaffolds of hydroxyapatite/chitosan-gelatin composites that showed enhanced adhesion and proliferation of rat calvaria osteoblasts. Chitosan-hydroxyapatite multilayer nanocomposites exhibited high strength and bending modulus making the material suitable for applications such as internal fixation of long bone fractures, as demonstrated by Hu et al. [149]. Compressive modulus of β -tricalcium phosphate (β -TCP) macroporous scaffolds was improved from 4 MPa to 11 MPa by the addition of chitosan. The biocompatibility of the scaffolds was evaluated on rabbits suggesting that these chitosan/ β -TCP composites can be used in non-loading bone regeneration [150].

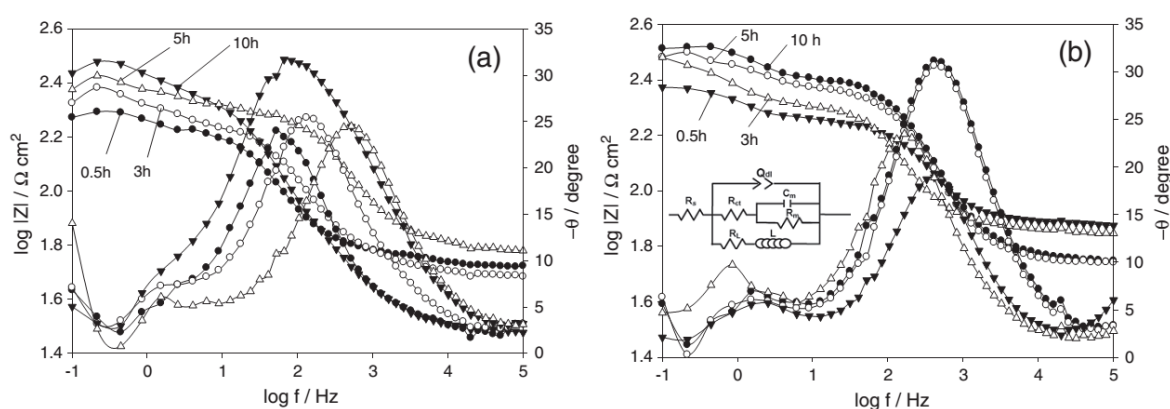


Fig. 5.7. Bode plots of (a) pure Mg and (b) AZ31 alloy in artificial sweat solution with time. The inset in (b) is the equivalent circuit for this condition. *source:* [151].

The combination of chitosan with other materials seems to be the main approach in several studies. Chitosan has been used in combination to other materials as coating on metals to improve surface biocompatibility/bioactivity. Bumgardner et al. [152] found that coating titanium with chitosan via silane-glutaraldehyde chemistry increased osteoblasts attachment and proliferation. On the other hand, chitosan has also shown to improve corrosion resistance of Mg and its alloys. Fekry et al. [151] coated CP-Mg, AZ91 and AZ31 alloys with different chitosan concentrations (5, 10 and/or 15% chitosan in 1% acetic acid solution). *In vitro* corrosion test in artificial sweat solution (0.1% urea, 0.5% NaCl and 0.5% lactic acid) showed that corrosion resistance increased with the immersion time in the testing solution (Fig. 5.7).

Chitosan coatings showed good adherence to the substrates and provided a protective-interfacial corrosion film. The authors attributed the increase in corrosion resistance to the change in chemical composition of the corrosion film due to adsorption of urea, decrease in alkalinity and incorporation of Cl^- into the film [151]. Additionally, decreased corrosion rate was observed with increasing chitosan concentration.

Zhang et al. [153] investigated the degradation of a micro-arc oxidized (MAO) AZ91 alloy with a calcium phosphate/chitosan composite coating in modified simulated body fluid

(m-SBF). The coating was effective to slow down the corrosion rate of the AZ91 alloy in m-SBF. The coating morphology changed from a flake-like one with fine needles to a spherical-shaped one with a honeycombed-like structure with increasing immersion time [153], as depicted in Fig. 5.8. This demonstrated good bioactivity of the calcium/phosphate coating which is estimated by the capability of inducing precipitation and mineralization of calcium phosphate on the implant surface [35,153]. Furthermore, the authors verified that the degradable rate of the AZ91 alloy in m-SBF may be controlled by varying the composite coating thickness [153].

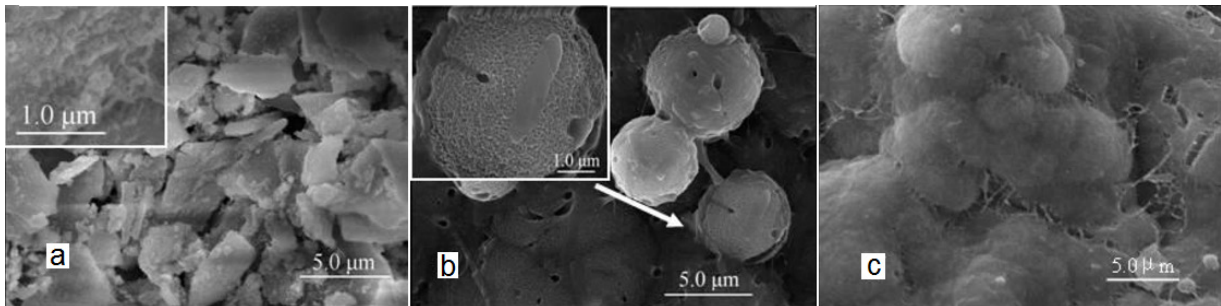


Fig. 5.8. SEM images of the calcium phosphate/chitosan coating morphologies immersed in m-SBF for different time intervals: (a) 3 days, (b) 30 days and (c) 90 days. *source:* [153]

There is no doubt that chitosans are versatile-natural polymers that can be formed into scaffolds, hydrogels, fibers and coating layers for a wide variety of tissue engineering applications. Their versatility relies on their distinct set of physico-chemical combinations resulting from the deacetylation degree and the fabrication process. However, there is still need of improving chitosans mechanical properties for bone regeneration applications [131,132] as well as elucidating how properties of chitosan materials may be affected by sterilization procedures that must be addressed in various implant applications [132].

6. CELL/BIOMATERIAL INTERACTIONS

Tissue engineering applications are now booming along with the development of the third generation of biomaterials. In orthopaedic applications, the understanding of the interaction between cells and the material is of crucial importance. For an implant to be successful, bone apposition—or osseointegration—to the surface is essential as well as the material must have no deleterious effects on cells [154]. The deposition of bone onto an implant requires a non-toxic surface but also that it favour cell adhesion, spreading and proliferation [154]. It has been shown that cell motility and proliferation rate can be influenced by the degree of cell attachment to the surface [154]. Hence, designing the surface of an implant to match the required bioactivity is as crucial as selecting the bulk composition, optimizing the mechanical properties and modulating the corrosion behavior. For example, the formation of a fibrocartilagenous²⁵ interface is essential for load transfer between soft and hard tissues [155], namely muscle and bone, respectively. A practical example would be the reconstruction of a torn anterior cruciate ligament (ACL) in the knee; it is made by inserting a graft into the bone to replace the damaged ligament. If there is no formation of a fibrocartilagenous interface between the graft and the bone, it eventually may lead to the graft failure [155]. Wang et al. [155] demonstrated that fibroblasts-osteoblasts interactions at the graft/bone junction play an important role in fibrocartilage formation. In the same way, a well-designed implant surface should support and encourage cell function or, at least, do not have a detrimental effect on its behavior.

Several implantable products are still developed and used clinically over long periods of time—in some cases years—until it is established that their performance is satisfactory or not [55]. This approach have proven to be challenging and unsuitable because of the clinical issues with patients and the inaccurate selection of pre-clinical performance models [55]. The biocompatibility of biomaterials is closely related to cell behavior on contact with them and particularly to cell adhesion to their surface [156]. The latter made that *in vitro* tests using different cell types became a widely used technique to evaluate biocompatibility and bioactivity of biomaterials. These tests provide safety information on cytotoxicity, cell proliferation and cell differentiation²⁶ [55]. Nevertheless, the criteria for the selection of an appropriate *in vitro* model may not be arbitrary since there are several factors from the *in vivo* environment that are not considered for the *in vitro* tests. Factors affecting cellular function include cell/biomaterial interactions as well as the biochemical and the mechanical environment [50]. Therefore, the nature of tissues surrounding the bone in the implantation

²⁵ Variety of cartilage that contains visible type I collagen fibers; appears as a transition between tendons or ligaments or bones [240].

²⁶ The process by which a cell becomes specialized in order to perform a specific function, as in the case of a liver cell, a blood cell or a neuron [241].

site should define the cell type used in the *in vitro* experiments. According to this reasoning, we will consider fibroblast and osteoblast cells as the relevant ones for the present work.

6.1. BONE STRUCTURE AND CELL MECHANICS

Connective tissues in the body of an adult are present as a variety of tissues ranging from blood to bone [157]. Most connective tissues provide mechanical support and the framework for other tissues of the body [157]. The major component of ordinary connective tissue is type I collagen and fibroblasts are the cell type primarily responsible for its biosynthesis and remodelling [157]. Fibroblasts are the principal active cells of connective tissue (Fig. 6.1a), are large (10–50 μm), flat and spindle-shaped performing processes that extend out from the ends of the cell body [158]. Fibroblasts play an important role in wound healing; following the injury, fibroblasts migrate to the damaged site where they deposit new collagen and facilitate the healing process [158]. Promoting fibroblasts attachment to the implant surface would aid in the integration of soft connective tissue, improving vascularity²⁷ at the biomaterial surface and decreasing the chance of fibrous encapsulation [159]. Broadly, repair and healing can be described in four well-defined but overlapping stages: (i) haemostasis²⁸, (ii) inflammation, (iii) proliferation and (iv) remodeling [160].

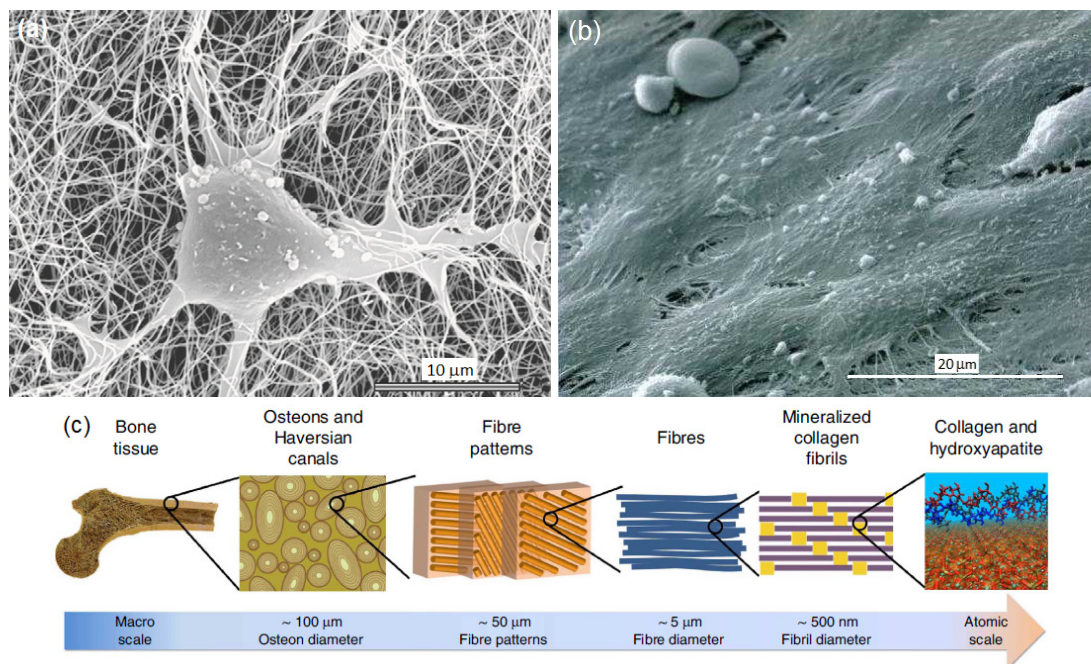


Fig. 6.1. Scanning electron microscope images of (a) human fibroblast on a collagen matrix (cell extensions penetrate into the matrix and become entangled with collagen fibrils) *source*: [157] and (b) plump of human osteoblasts on bone surface (studded with many microvillus-like projections) *source*: [161]. (c) Hierarchical structure of bone ranging from the macroscale skeleton to nanoscale collagen and hydroxyapatite *source*: [162].

²⁷ Of a tissue, characterized by, or containing cells or vessels that carry or circulate fluids, such as blood or lymph through the body of an animal or plant: *vascular tissue*, *vascular disease* [242].

²⁸ Stopping of bleeding or arrest of blood circulation in an organ or part [243].

Bone tissue consist of an inorganic mineral phase —calcium and phosphates— and an organic phase where collagen is the major protein (Fig. 6.1c) [163]. Type I collagen comprises about 95% of the entire collagen content of bone and about 80% of the total proteins present in bone [163]. Osteoblast produce several cell products, including enzymes, growth factors²⁹, hormones and collagen, part of the unmineralized component of the bone is called osteoid³⁰ [164]. Osteoblasts (Fig. 6.1b) are the cells responsible for the synthesis and mineralization³¹ of bone during both initial bone formation and later bone remodelling [164].

Cell adhesion to biomaterials covers different stages: (i) attachment in the short-term which involves events like physico-chemical interactions between the cell and the material by ionic forces, van der Waals forces, etc.; and (ii) adhesion in the longer term involving various biological molecules such as extracellular proteins, cell membrane proteins and cytoskeleton³² proteins which interact together to regulate gene expression [156]. On planar surfaces cells can modulate their cytoskeletal function depending on the surface mechanics [157]. When interacting with soft matrices such as collagen, cells exhibit different patterns of signaling and migration and are able to remodel matrices both locally and globally [157]. Fig. 6.2 illustrates the four quadrants of cell mechanics on planar surfaces compared to collagen matrices as described by Rhee et al. [157]. In the horizontal axis cell mechanics is expressed as function of growth factors, blood type (left) and serum type (right). The vertical axis depends on the tension state of cell/matrix interactions. High tension accounts for a rigid surface such as glass or plastic coverslips (Fig. 6.2 top) and low tension for relaxed collagen matrices (Fig. 6.2 bottom) [157]. The cytoskeleton architecture is essential to the maintenance of cell shape and cell adhesion [156]. When cells assemble in long bundles, cell membrane protrudes with finger-like shape known as filopodia; when assembled in the mesh form the membrane supports sheet-like protrusions known as lamellipodia [156].

²⁹ A substance that induce growth of a cell or an organism [244].

³⁰ Organic matrix of bone that has not undergone calcification (young bone) [245].

³¹ Deposition of calcium hydroxyl apatite salts converting osteoid to rigid bone. Dependent on mineral availability, enzyme action, osteoblasts and osteoclasts activity, hormones and vitamin D [246]. Osteoclast is a large multinuclear cell found in growing bone that resorbs bony tissue [247].

³² The internal framework of a cell composed largely of actin filaments and microtubules [248]. Actin is a protein responsible for the contraction and relaxation of muscle [249].

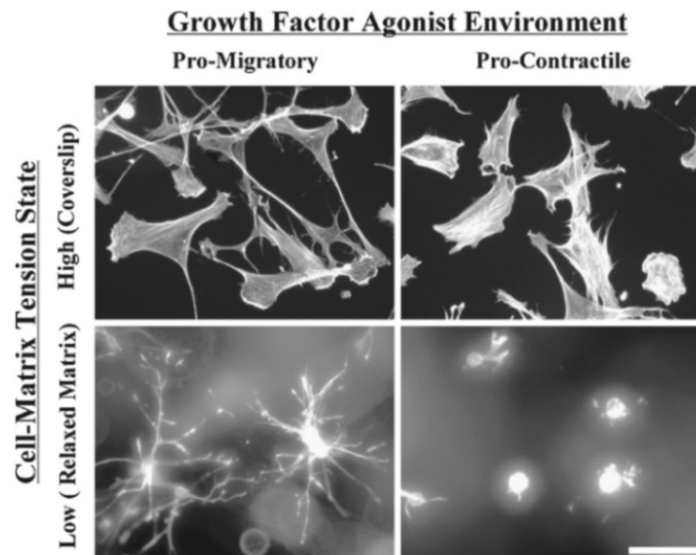


Fig. 6.2. Fluorescence images of cells cytoskeleton (human fibroblasts) showing the four quadrants of cell mechanics. On coverslips cells spread with lamellipodia and develop increase ruffles under pro-migratory conditions or stress fibers under pro-contractile conditions. In collagen matrices they spread with dendritic extensions under pro-migratory conditions or have retracted extensions under pro-contractile conditions *source*: [157].

Minor differences in cell morphology are observed in the high-tension quadrants between pro-migratory and pro-contractile states. On coverslips cells spread with filopodia and develop increased ruffles under pro-migratory while under pro-contractile develop stress fibers [157]. Cells with prominent stress fibers and focal adhesions are not typically observed in tissues except under activated conditions such as wound repair [157]. Focal adhesions are discrete regions in the cell membrane approximately 0.1–2 μm wide and 2–10 μm in length closely associated with the substrate [159]. Cells in a pro-migratory low tension state protrude dendritic extensions whereas under pro-contractile state these extensions undergo transient retraction. Eventually, cells under pro-contractile low tension state may re-protrude but with a more bipolar morphology resembling tissue fibroblast under resting conditions [157].

6.2. CELL BEHAVIOR ON BIOMATERIALS

Cell/material interactions are affected by several aspects of the material according to its topography, chemistry and surface energy [156]. These parameters determine the cell mechanics on the contact and therefore its adhesion. The quality of this adhesion will influence cell morphology and their posterior proliferation and differentiation [156]. Several *in vitro* studies available in literature have proven the capacity of cell to discriminate between different surface chemistries [156]. All surfaces are different from the corresponding bulk of the material, they contain unsaturated bonds which lead to the adsorption of layers of contaminants and reactive layers [156]. Consequently, surface treatment or modification must be considered when preparing the surface of a biomaterial.

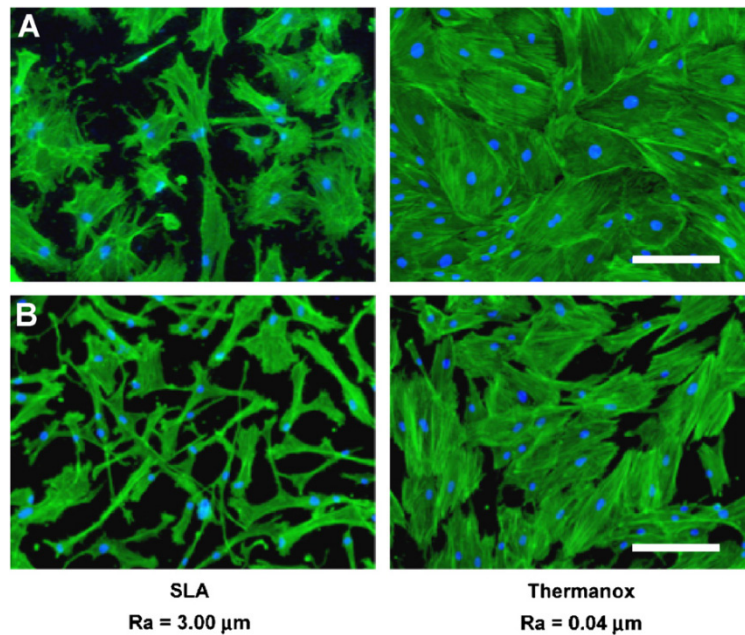


Fig. 6.3. Morphology of (a) osteoblasts and (b) fibroblasts cultured for 7 days on sandblasted and acid etched (SLA) and commercially pure Ti and titanium-coated Thermanox discs with the according roughness value Ra (arithmetic average roughness). The nucleus was stained with DAPI (blue) and the cytoskeleton with Alexa Fluor 488 (green). Scale bar is 200 μm source: [165].

Morphological parameters such as surface roughness have shown to influence cell behavior. Kunzler et al. [165] demonstrated that response of cells to roughness is different depending on the cell type. In this study the authors prepared a surface to produce roughness gradients that covered a wide range of roughness values on one substratum. The foot print of rat calvarial osteoblasts (RCO) showed a variation in size at different positions on the roughness gradient, they remained small on the roughest end and increased considerably as the roughness decreased [165]. Additionally, RCOs proliferation rate increased with increasing surface roughness. On the other hand, human gingival fibroblasts (HGF) showed decreased proliferation with increasing roughness. In terms of morphology, both RCOs and HGF showed the same trend [165]. Chesmel et al. [166] reported that on smooth surfaces bone cells were randomly oriented while they aligned parallel in an end-to-end fashion on a surface with 5 μm -deep grooves [156]. Surface energy —hydrophilicity, hydrophobicity, surface charge— is also of great importance for cell behavior. Generally, cell adhesion is better on hydrophilic surfaces [156]. Cell spreading has shown to be significantly improved on positively charged surfaces. Shelton et al. [167] characterized spreading of rat calvarial osteoblast cultured on positively or negatively charged polymeric substrates. On positively charged surfaces osteoblasts flattened out so closely that the cell membrane was not distinguishable when observed by transmission electron microscope [167]. When plated on a surface with patterned surface chemistry, osteoblasts rapidly started to organize on the positive charged regions [167].

The surface energy of the material is also conditioned by the composition of the fluid in which it is immersed [168]. Proteins may be adsorbed on the surface and potentially undergo structural rearrangements. Therefore, the behavior of the adsorbed protein may not only be related to its interaction with the charge of the surface but also to the protein's potential for change [168], as already discussed in section 3.3. Correspondingly, cell adhesion, morphology and proliferation may be altered as well.

Cell adhesion is also affected by mechanical stimulation. Since mechanical aspects of cell/materials interactions are out of the scope of this work it will not be herein discussed. However, because of its relevance in the field of biomaterials for bone repair applications, we recommend to further review references [50] and [156] where the authors widely covered important aspects of mechanical loads effects on bone cells and bone mechanotransduction. To a proper selection of cell *in vitro* tests conditions good understanding of the above-mentioned features is necessary.

6.2.1. In vivo vs. in vitro tests

Generally researchers target ethical approval before performing *in vivo* studies but should primarily focus on replacing *in vivo* by *in vitro* studies whenever it is possible [55]. If *in vivo* assessments are needed, then researches should fine-tune the adopted protocol to profit the maximum from the data collected reducing the number of animals to a minimum [55].

Certainly *in vitro* vs. *in vivo* considerations must be carefully addressed. *In vitro* models are generally static and are not sufficient to demonstrate performances of bone implants during advanced stages of product development [55]. On the other hand, *in vivo* tests allow identifying implant problems that are not possible to determine *in vitro*. However, still there are technological limitations for evaluating the implant performance during the implantation period. Measuring mass loss, hydrogen evolution and corrosion products composition is not as accessible as it is using *in vitro* tests. For this reason, some researchers using animal models have chosen to sacrifice the animals and extract the bone fraction harboring the implant part to characterize it *in situ*. Several technical and ethical aspects must be then recognized when selecting between *in vitro* and *in vivo* experiments. *In vivo* animal models not always consider anatomical position factors, e.g. bone vs. cartilage. In human models the age of the patient is also important since juniors undergo faster bone resorption than seniors. *In vitro* experiments do not consider changes in the material in response to the biological fluids and tissues. Further, cell culture models tend to examine the response of single cell types [168].

Despite of the shortcomings, cell culture models still provide very useful information on cytotoxicity, cell adhesion/proliferation and cell differentiation. Methods are easily standardized, quantifiable and reproducible [55]. Furthermore, *in vitro* tests allow elucidating cells mechanics which in turn provide pathways to formulate functional biomaterials.

7. THE RESEARCH AIM

7.1. THE APPROACH

The main goal of the present project is the development of a novel strategy to functionalize the surface of Mg-based materials in order to use them as biodegradable implants for orthopaedic applications.

Currently, the approaches for mitigate corrosion activity of Mg alloys in inorganic physiological solutions have shown to be effective, being surface coating the main approach adopted by researchers. For a particular coating composition, the final properties will strongly depend on the coating deposition method as well as on the processing parameters, as already discussed in chapter 4. Nevertheless, synergistic approaches that combine tailored corrosion resistance and improved biological performances of Mg alloys along with cost-effectiveness stand-alone technologies are still needed.

Our approach is the development of hybrid bi-layered multifunctional coatings of easy implementation from the scientific, technological and application point of view. We aimed that the proposed coatings can be applied onto different Mg-based substrates or even further onto other types of metallic biomaterials. Therefore, to achieve the aforementioned objective the adopted strategy was (Fig. 7.1):

- Coat the surface of the AZ31 and ZE41 Mg alloys with a hybrid silane-TiO₂ sol-gel coating by the dip-coating technique. This sol-gel layer would improve the corrosion resistance of the Mg-based substrates.
- Functionalization of the outer sol-gel coating surface by applying a top-most layer of collagen and/or chitosan biopolymers to enhance cell adhesion/proliferation and facilitate tissue regeneration. The outermost biopolymer layers were applied by the dip-coating technique too.

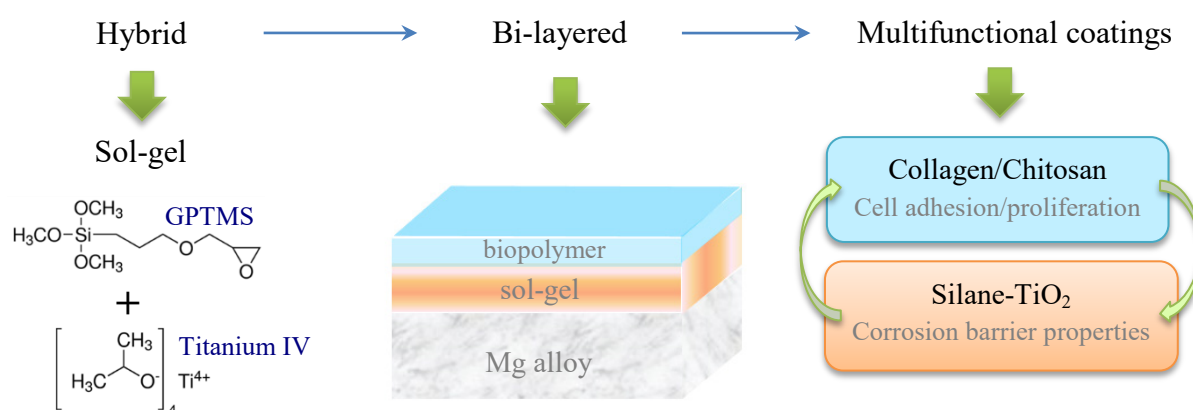


Fig. 7.1. Representation of the hybrid bi-layered multifunctional coatings produced on both AZ31 and ZE41 alloys: a bottom sol-gel of (3-glycidoxypropyl)-trimethoxysilane/titanium (IV) iso-propoxide and a top layer of collagen or chitosan.

Our methodology intends to be highly flexible in terms of procedures being suitable to coat metallic pieces with complex shape. After application of the bi-layered systems the testing hypothesis was then:

- The hybrid sol-gel coating increases the corrosion resistance of the Mg alloys while the biopolymer layers enhance cell response and viability.

To that end we aimed to answer the next questions:

- Do the biopolymer top layers modify the barrier properties of the sol-gel coating?
- Does the nature of the substrate influence the bi-layered coatings performance?
- Does the *in vitro* testing electrolyte affect the corrosion response and the bioactivity of the Mg alloys?

8. THE METHODOLOGY

8.1. MATERIALS & SUBSTRATES PREPARATION

The materials used in this study were supplied by Magnesium Elektron Company and by Goodfellow Company. Extruded rods of AZ31 and ZE41 Mg alloys (ASTM designation) of 25 mm in diameter were cut into discs 3 mm-thick with a Struers Minitom precision cutter implemented with a Buehler wafering blade (series 15HC diamond). All samples were cut at low rotation speed lubricating with IsoCut® fluid Buehler. The nominal composition of the Mg alloys was already specified in [Table 3.1](#).

The discs were grinded sequentially with 180, 400, 800 and 1000 SiC grit papers while lubricated with ethanol ($\geq 96\%$, Sigma-Aldrich). After grinding the discs were rinsed with ethanol and dried with air stream. For surface chemical treatment the grinded discs were immersed in 12% hydrofluoric acid (puriss p.a., Sigma-Aldrich) solution for 15 minutes to promote the formation of a MgF_2 layer. Some studies [169–171] have shown that corrosion resistance of Mg alloys in SBF solution is improved by fluoride surface treatment. Furthermore, fluoride layer may act as a coupling between the substrate and a secondary physical coating or layer improving adhesion [170]. The 12% HF pre-treated samples are referred as AZ31 and ZE41 henceforth.

For microstructural characterization grinded discs were mechanically polished with 6 μm diamond compound Metadi® II (Buehler) followed by a final polishing with 0.05 μm Alpha Micropolish® Al_2O_3 (Buehler). The polished discs were chemically micro-etched with acetic-picral (5 ml acetic acid + 6 g picric acid + 10 ml H_2O + 100 ml ethanol 95%) [72].

8.2. SYNTHESIS OF THE SOL-GEL COATING

Based on previous investigations [172], the coating composition was formulated and optimized for the purpose of this work. A hybrid sol-gel was prepared by mixing two different alkolsols: (i) (3-glycidoxypropyl)-trimethoxysilane ($\geq 98\%$ GPTMS, Aldrich) and (ii) titanium (IV) iso-propoxide ($\geq 97\%$ $\text{Ti}(\text{OiPr})_4$, Aldrich). The first silane-based alkolsol was prepared by acidic hydrolysis (diluted aqueous HNO_3 pH 0.5) of GPTMS in iso-propanol in a volume ratio GPTMS:2-propanol: H_2O of 8:8:1. The solution was stirred for 1 hour at room temperature. The second alkolsol was prepared by the hydrolysis of 70% iso-propanol of $\text{Ti}(\text{OiPr})_4$ in iso-propanol in the presence of acetylacetonate (Acac, analytical standard). Diluted HNO_3 aqueous solution (pH 0.5) was added for the final volume ratio TIP:Acac: H_2O of 5:3:1 of 5:3:1. The solution was stirred for 25 minutes at room temperature. Finally, the silane-based and the Ti-based solutions were mixed in a volume ration of 1.5:1. The final hybrid solution was ultrasonically agitated for 1 hour and aged for an additional hour at room temperature.

8.3. SOL-GEL COATING DEPOSITION & THERMAL CONDITIONING

The sol-gel was deposited on the 12% HF pre-treated discs by the dip coating technique: three immersion times of 10 seconds of duration each with a withdrawal speed of 17 cm/min. As a final step in the deposition procedure the coated discs were thermally treated at 120°C for 90 minutes in non-controlled atmosphere. The curing process was intended to remove solvent excess and consequently increase rigidity of the deposited layer. The coated AZ31 and ZE41 are denoted as AZ31_S and ZE41_S (S: sol-gel), respectively.

8.4. BUILD-UP OF BI-LAYERED COATINGS

Collagen and chitosan from diluted acid solutions were deposited onto AZ31_S and ZE41_S discs as uppermost layers. Two bi-layered systems were produced for each Mg alloy: (i) sol-gel + collagen and (ii) sol-gel + chitosan. Prior to the deposition of the top-biopolymer layers, the sol-gel coated discs were sterilized by soaking in ethanol ($\geq 96\%$, Sigma-Aldrich) for 30 minutes. Diluted 0.005 M acetic acid solutions at a concentration of 3 mg/ml in collagen (extracted and purified from rat tail tendon) or chitosan (from shrimp shells $\geq 75\%$ deacetylated, Sigma) were prepared under sterile conditions. The sterilized AZ31_S and ZE41_S discs were manually dipped into the collagen and chitosan solutions two times for 10 seconds each allowing drying for 15 minutes between dips at room temperature. The sol-gel/biopolymer coated discs were denoted as AZ31_SC, ZE41_SC (SC: sol-gel + collagen), AZ31_SK and ZE41_SK (SK: sol-gel + chitosan). Fig. 8.1 shows a schematic representation of the steps followed for the samples preparation. The bi-layered coatings were also performed on glass slides substrates following the same procedures used for the Mg alloys substrates.

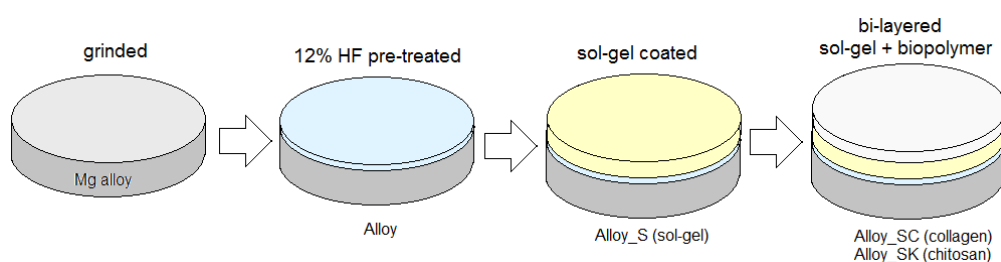


Fig. 8.1. Sketch of samples preparation sequence and final setup of the bi-layered coatings.

8.5. *IN VITRO* CORROSION MEASUREMENTS BY ELECTROCHEMICAL TECHNIQUES

8.5.1. Electrochemical Impedance Spectroscopy

Electrochemical impedance spectroscopy (EIS) technique was used to characterize the corrosion performance of uncoated (12% HF pre-treated), sol-gel coated, and bi-layered

samples with collagen or chitosan. The study was performed in two different solutions: (i) simulated body fluid (SBF) and (ii) Dulbecco's modified Eagle's medium (DMEM). The composition of both solutions is specified in [Table 8.1](#).

Table 8.1. List of reagents to prepare 1000 ml of SBF (pH 7.4) and composition of the DMEM (pH 7) used in this work as detailed by the supplier Gibco® (Ref. 11880-028).

Reagent	SBF	
	g/L	
NaCl		8.035
NaHCO ₃		0.355
KCl		0.255
K ₂ HPO ₄ ·3H ₂ O		0.231
MgCl ₂ ·6H ₂ O		0.311
1M-HCl		40 (ml)
CaCl ₂		0.292
Na ₂ SO ₄		0.072
TRIS (CH ₂ OH) ₃ CNH ₂		6.118
1M-HCl		0-5 (ml)
DMEM		
Amino Acids	Molecular Weight	mg/L
Glycine	75	30
L-Arginine hydrochloride	211	84
L-Cystine 2HCl	313	63
L-Histidine hydrochloride-H ₂ O	210	42
L-Isoleucine	131	105
L-Leucine	131	105
L-Lysine hydrochloride	183	146
L-Methionine	149	30
L-Phenylalanine	165	66
L-Serine	105	42
L-Threonine	119	95
L-Tryptophan	204	16
L-Tyrosine	181	72
L-Valine	117	94
Vitamins		
Choline chloride	140	4.0
D-Calcium pantothenate	477	4.0
Folic Acid	441	4.0
Niacinamide	122	4.0
Pyridoxine hydrochloride	204	4.0
Riboflavin	376	0.4
Thiamine hydrochloride	337	4.0
i-Inositol	180	7.2
Inorganic Salts		
CaCl ₂ ·2H ₂ O	147	264
Fe(NO ₃) ₃ ·9H ₂ O	404	0.1
MgSO ₄ ·7H ₂ O	246	200
KCl	75	400
NaHCO ₃	84	3700
NaCl	58	6400
NaH ₂ PO ₄ ·2H ₂ O	154	141
Other components		
D-Glucose (Dextrose)	180	1000
Sodium Pyruvate	110	110

The EIS experiments were carried out in natural aerated conditions at 37°C for a maximum period of 7 weeks. The measurements were recorded at open circuit potential using a Gamry Ref.600 potentiostat applying an AC voltage of 10 mV in the 10⁵ Hz down to 10⁻² Hz frequency range. During measurements 9 points per frequency decade were collected. The conventional three-electrode electrochemical cell consisted of the Mg alloy disc as working electrode with an exposed area of 3.1 cm², saturated calomel electrode (SCE) as reference and as counter electrode a platinum coil. A Faraday cage was used in all experiments to avoid electromagnetic interferences. To fit the impedance plots and extract numerical data the results were analysed with ZView3® software.

8.5.2. Localized SVET and SIET techniques

To evaluate localized corrosion phenomena and localized pH evolution, scanning vibrating electrode (SVET) and scanning ion-selective technique (SIET) were used, respectively. The first technique detects local current density changes originated by potential differences in the surface as consequence of ionic fluxes generated between anodic and cathodic sites [173]. The latter provides information about local concentration of specific ions in solution —H⁺ in the present case— tracing changes in the pH associated with electrochemical processes [173]. In coated metallic substrates, the corrosion processes can be localized in small areas where the coating delaminates leading to changes in the electrochemical potential, current density and acid-base equilibrium reactions [173]. Then, the above mentioned techniques were used to obtain spatially resolved electrochemical and pH potentiometric measurements with microprobes and microelectrodes, respectively.

The commercial equipment used in this study was manufactured by Applicable Electronics™ and controlled using ASET software (Science Wares™). The equipment contains the following parts: a main amplifier-potentiostat and a preamplifier with a 10¹⁵ Ω input impedance. To position the microprobe/microelectrode the preamplifier is mounted on a 3D computerized stepper-motor system. This system allows micrometer precision when positioning the microprobe/microelectrode over the sample. A digital video camera with zoom lens located above the microelectrode and the sample provides magnification up to 400 times.

For SVET measurements, an insulated Pt-Ir probe (Microprobe Inc.) with a spherical layer ($d = 12 \pm 2 \mu\text{m}$) of platinum black deposited on the tip probe was used as vibrating electrode. The probe was positioned $100 \pm 3 \mu\text{m}$ above the sample. The vibration amplitude in vertical (Z) and horizontal (X) planes was $32 \mu\text{m}$ peak to peak. The probe diameter was $18 \mu\text{m}$ and the vibration frequencies in Z and X planes were 124 Hz and 325 Hz, respectively. Only the data from the vertical plane vibration (Z) were taken into consideration.

For SIET measurements, an Ag/AgCl/SBF pH-selective glass-capillary microelectrode was used as the external reference electrode. Micropipettes of silanized glass were backfilled

with the inner filling solution and tip-filled with an H⁺-selective ionophore-based membrane. The glass-capillary tip diameter was $2 \pm 0.3 \mu\text{m}$. Calibration of the H⁺-selective microelectrode using commercially available pH buffers (Fluka) within the pH 2–10 range was made before and after measurements to correlate the recorded data with the Nernst equation [174] and consider possible potential drifts. The H⁺ local activity was detected $30 \pm 3 \mu\text{m}$ above the sample surface.

To evaluate the localized corrosion and pH evolution artificial defects 500 μm -length (Fig. 8.2) were created on coated AZ31_S and ZE41_S samples using a microindenter Ernst Leitz Wetzlar with a load of 500 gr. The artificial defect aims to mimic a local delaminated area that emerges in the coated samples at advanced stages of immersion (> 1 week). By creating the defect prior to immersion in solution, it is possible to trace the corrosion products formation/growth in both buried and non-buried areas around the defect and the phenomena influenced by their formation, e.g. pH variations. The artificial defect was in the centre of the scanned area of $0.9 \text{ mm} \times 0.6 \text{ mm}$ approximately. The rest of the surface's sample was isolated by covering with bee wax. The local current density and pH were mapped at 31×31 grid generating 961 data points. Periodical measurements were taken during exposure to SBF (Table 8.1) at room temperature for 24 hours. SVET and SIET techniques were performed separately on different samples with identical preparation. All measurements were performed using a Faraday cage to avoid electromagnetic interferences. Coated AZ31_S and ZE41_S samples were tested only.

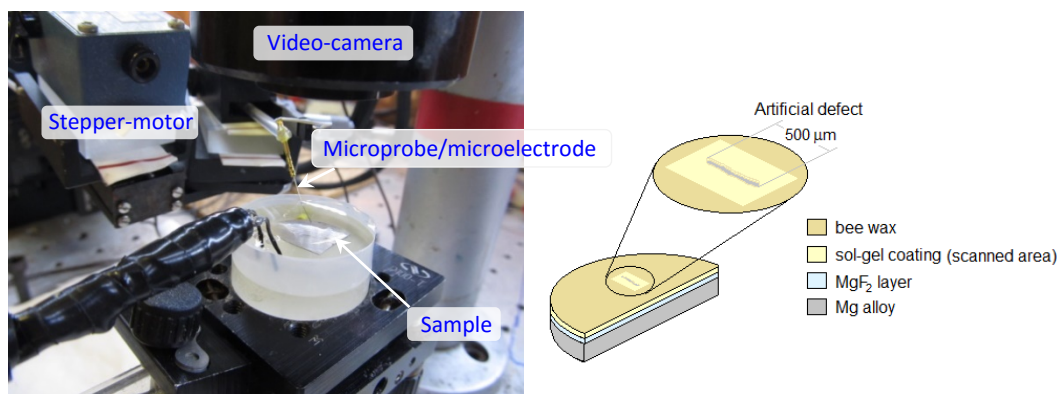


Fig. 8.2. Photography of the equipment configuration for SVET/SIET experiments (left). Sketch depicting the sample setup with the artificial defect and the scanned area delimited with bee wax (right).

8.5.3. Localized electrochemical impedance spectroscopy

Localized electrochemical impedance spectroscopy (LEIS) measurements were carried out using a Solartron 1286 electrochemical interface and a Solartron 1250 frequency response analyser coupled with a Uniscan electrochemical station. LEIS equipment uses a five-electrode configuration consisting of a conventional three-electrode cell: (i) saturated calomel

electrode (SCE) as reference, (ii) platinum coil as counter electrode and (iii) sample as working electrode; and the LEIS probe (Pt bi-electrode) to measure the local potential gradient in solution above the sample surface. For LEIS measurements a special sample setup was made. The samples had two different regions with different surface preparation: (i) sol-gel coated and (ii) bi-layered with either collagen or chitosan. The preparation procedures were the same described in sections 8.2–8.4. The final sample setup is represented in Fig. 8.3. For LEIS mapping the probe was stepped across a defined area centred at the boundary of the two different surface conditions as represented in Fig. 8.3. The dimension of the scanned area was 14 mm². All the recorded maps were taken with an excitation frequency of 10 Hz in order to follow the slowest corrosion processes occurring at the metal surface. All the LEIS experiments were performed in 25% SBF solution at room temperature. Diluted solutions aid to maximize the lateral resolution.

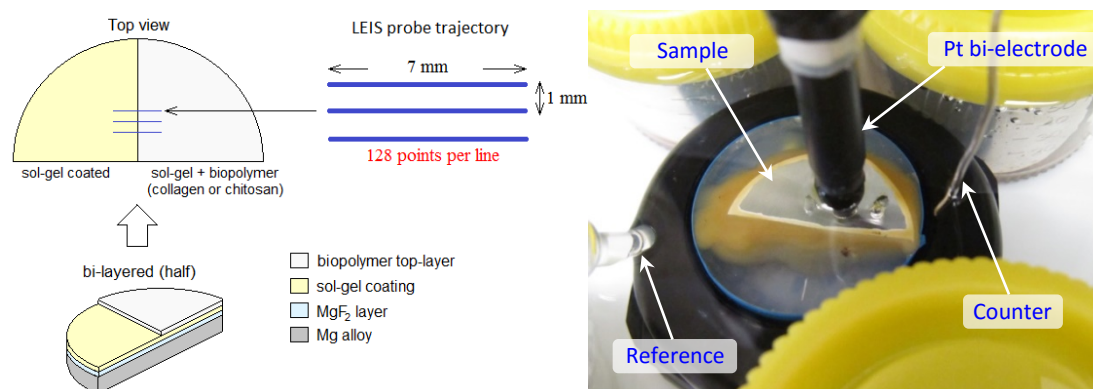


Fig. 8.3. Sketch depicting the sample setup and stepped trajectory of LEIS probe during experiments (left). Photography of the electrodes configuration used for LEIS experiments (right).

8.6. pH MEASUREMENTS

The pH evolution of SBF solution at 37°C with immersed uncoated AZ31 and ZE41 discs was made at discrete time-points over 7 weeks. Two different surface conditions of each alloy were immersed in solution: (i) as-grinded and (ii) 12% HF pre-treated. Both conditions were prepared following the same procedures described in section 7.1. The measurements were made with an Eutech Instruments PC700 pH-meter.

8.7. CONTACT ANGLE MEASUREMENTS

The free energy of all surface preparations of AZ31 and ZE41 alloys was assessed by measuring static contact angle (θ) of SBF and DMEM with sessile drop method at room temperature. 2 μ l drops generated with a micrometric syringe were deposited onto the surface and recorded within first 20 seconds of contact with a video-camera JAI CV-A50 attached to a microscope Wild M3Z which was connected to a frame grabber Data Translation DT3155.

The microscope was operated by the ADSA-P software (Axisymmetric Drop Shape Analysis-Profile). Three different spots over a single surface were measured and results were expressed as the arithmetic mean \pm standard deviation.

8.8. CELL BEHAVIOR CHARACTERIZATION

8.8.1. Samples setup for cell behavior experiments

For this study a homemade sample configuration was designed to perform cell viability experiments. To confine the cell suspension onto the surface of interests (see Fig. 8.1) a polyethylene cylinder (inner \varnothing 20 mm \times height 10 mm \times wall thickness 1 mm) was glued on top of the discs by using a medium-viscosity silicone of fast curing at room temperature (Kwik-Sil®, World Precision Instruments). The polyethylene cylinders were previously sterilized following the same procedure described in section 7.1. The sets were then placed into 6-well flat-bottomed cell culture plates. The tissue culture plate (polystyrene) was used as control sample (Fig. 8.4).



Fig. 8.4. Sample configuration and multi-well culture plates used for cell viability experiments.

8.8.2. Cell culture techniques and cell viability experiments

Normal human dermal fibroblasts (NHDF) and primary human osteoblasts (HOB) were cultured under standard conditions (95% air humidified atmosphere with 5% CO₂ at 37°C) in Dulbecco's modified Eagle's medium (DMEM), 10% fetal calf serum, 100 units ml⁻¹ penicillin, 100 µg ml⁻¹ streptomycin and 0.25 µg ml⁻¹ fungizone. All components were Gibco® BRL. Cells were cultured in tissue culture flasks and passaged at subconfluency of 70–80%. To isolate cells from culture flasks a treatment with 0.1% trypsin and 0.02% EDTA was made. The cells were rinsed and re-suspended in the above-mentioned culture medium. For cell culture experiments, cells were seeded in a density of 4×10^4 cells cm⁻². Fibroblasts and osteoblasts cells were seeded on both AZ31 and ZE41 alloys with all surface preparations: (i) 12% HF pre-treated, (ii) sol-gel coated (S), (iii) sol-gel/collagen (SC) and (iv) sol-gel/chitosan (SK).

Alamarblue® reagent was used to assess cellular health. Healthy cells reduce a non-fluorescence blue component (resazurin) to a bright pink fluorescent molecule (resorufin) generating a quantitative measure of viability. Cell viability was measured at 1 and 3 days for fibroblasts and at 1 day, 3 days and 7 days for osteoblasts to characterize cell attachment/proliferation. To performed alamarblue® test at each time-point the culture medium was removed from the samples and replaced by 300 µl of fresh DMEM (for cell culture) with 10% (v/v) resazurin. The samples were kept under culture standard conditions for 4 hours. After this period, the solutions were transferred into semi-micro cuvettes (Ratiolab® USA) and 700 µl of negative control (DMEM in Table 8.1) were added. The absorbance of these solutions was measured with a spectrophotometer UVIKONXL (USA) at 570 nm with a reference wavelength of 600 nm. For each surface preparation viability experiments were performed in triplicate and results were expressed as the arithmetic mean ± standard deviation.

Alamarblue® test was also performed on AZ31_S and ZE41_S samples without the presence of cells in order to determine any possible interference from either the Mg alloys or the coating. After 4 hours of incubation the reagent on AZ31_S and ZE41_S was still non-fluorescent blue.

The sol-gel coating and the bi-layered systems with the biopolymers were reproduced on glass slides and tested with both fibroblasts and osteoblasts in order to characterize cell behavior as a function of the surface composition, namely the by-layered coatings. The same characterization was made on 12% HF pre-treated commercially pure Mg (CP-Mg, Magnesium Elektron Company) to determine the influence of alloying elements on cell behavior.

8.8.3. Cell distribution by fluorescence microscopy

For cell distribution characterization by fluorescence microscopy the cultured cells were fixed with 4% paraformaldehyde (PFA) for at least 1 hour. For simultaneous fluorescence staining of viable and dead cells a double staining Kit (Sigma-Aldrich) containing Calcein-AM and Propidium Iodide (PI) solutions was used. 10 µl of Calcein-AM and 5 µl of PI were added into 5 ml of PBS to prepare assay solution. Prior to stain step cells were washed three times with PBS to remove residual PFA. 100 µl of assay solution were added to cells and the mixture incubated at 37°C for 15 minutes. AXIO D1 Imager fluorescence microscope with 490 nm excitation signal was used to simultaneous monitor viable and dead cells.

In some particular cases, the sol-gel coating fixed the labelling dye Calcein-AM hindering the visualization of cells due to high fluorescence from the coating. As alternative route, diamidino-2-phenylindole (DAPI, 1:5000 dilutions in phosphate-buffered saline, PBS)

was used for nuclei labelling of viable cells. After 10 minutes in contact with DAPI the cells were rinsed three times (5 min each) with PBS to remove the dye excess.

8.8.4. Cell morphology characterization

For morphological characterization cells were fixed in 1.5% glutaraldehyde in 0.1 M sodium cacodylate buffer (pH 7.3) for 1 hour, dehydrated through an ascending alcohol series of 50%, 70% and 95% for 5 minutes in each concentration followed by two 10 minutes changes of 100% alcohol. The dehydrated samples were kept overnight inside a desiccator. The samples were sputtered with gold and examined to determine cell morphology and distribution in a scanning electron microscope (SEM) Hitachi S-3400N.

8.9. MORPHOLOGY CHARACTERIZATION BY SEM & AFM

Morphology characterization of as-prepared samples was made by Nanosurf Easyscan 2 and Bruker® atomic force microscopes (AFM). Images of topography, vibration amplitude and phase contrast were obtained in non-contact (tapping) mode at different positions and magnifications. The scans were made in air at room temperature by using silicon probes Point Probe® Plus (NanoAndMore GMBH).

For morphological and chemical characterization of all prepared conditions before and after *in vitro* experiments a field emission gun scanning electron microscope (FEG-SEM) JEOL-JSM7001F equipped with an energy dispersive spectroscopy (EDS) microanalysis was used. The samples were coated with carbon using a sputter coated system. Additionally, a diffracted backscattered electron detector (EBSD) appended to the SEM was used to assess crystallinity of the sol-gel coating.

To characterize cross-sections of the different prepared conditions the samples were embedded into an epoxy resin (Buehler) mould at room temperature and grinded up to 2500 SiC grit paper in ethanol.

The microstructure of the AZ31 and ZE41 discs was assessed with FEG-SEM and with Olympus PMG-3 optical microscope.

8.10. XRD & RAMAN CHARACTERIZATION

X-ray diffraction (XRD) analyses were performed to determine the phase constituent of as-received Mg alloys matrix and of the corrosion products of immersed samples using Cu K_α radiation in a Bruker D8 ADVANCE diffractometer operating at 40kV and 30mA.

Raman spectra were acquired in a LabRAM HR800 Evolution Horiba, with a solid-state laser source operating at 532 nm with a 180° backscattered geometry, 600 lines/mm grating spectrograph and laser beam power of 20 mW.

9. SILANE/TiO₂ COATING TO CONTROL THE CORROSION RATE OF MAGNESIUM ALLOYS IN SIMULATED BODY FLUID

This chapter discusses the characterization of the barrier properties of the silane/TiO₂ coating deposited on both AZ31 and ZE41 alloys. Lamaka et al. [175] proposed a protective silane/TiO₂ coating to seal the pores of an anodic oxide layer loaded with corrosion inhibitors deposited onto ZK30 Mg alloy. The anticorrosion behavior of their system resulted to be highly protective for the ZK30 alloy in aggressive NaCl solution. Based on the hybrid polymeric coating proposed by Lamaka et al. [175] we reformulated the coating composition and adjusted the deposition parameters to tailor the desired corrosion rate of AZ31 and ZE41 alloys in SBF. Prior to the coating deposition the grinded substrates were chemically treated with 12% HF solution to promote the formation of a MgF₂ layer to improve the corrosion resistance of the alloys. The 12% HF pre-treated alloys will be referred as AZ31 and ZE41 henceforth, while the sol-gel coated alloys will be referred as AZ31_S and ZE41_S.

The majority of the results reported in this chapter constitute a paper recently published in *Corrosion Science* 104 (2016) 152–161 with the same title. We employed electrochemical impedance spectroscopy (EIS) to monitor the corrosion evolution of the alloys in SBF at $37 \pm 1^\circ\text{C}$ for 7 weeks. The corrosion mechanisms and the nature of the corrosion products of the coated systems are deeply discussed and correlated to the coating morphology before and after of the immersion tests.

9.1. MICROSTRUCTURE OF AS-RECEIVED AZ31 AND ZE41 ALLOYS

[Fig. 9.1a–b](#) show the microstructure of the AZ31 rod (cross-plane). It consists of a structure of α -Mg equiaxed grains of heterogeneous size ranging from 13–50 μm and some Al-Mn particles (yellow arrows). In [Fig. 9.1b](#) the inset indicates the composition of the Al-Mn particles measured by EDX. Considerable mechanical twins (black arrows) are visible due to the deformation induced during extrusion fabrication process. The β -Mg₁₇Al₁₂ phase was not detected neither by SEM nor optical microscope observations. As discussed by Ding et al. [176] β -Mg₁₇Al₁₂ phase is not prone to precipitate in AZ31 alloy due its lower aluminium content in comparison to AZ91 alloy.

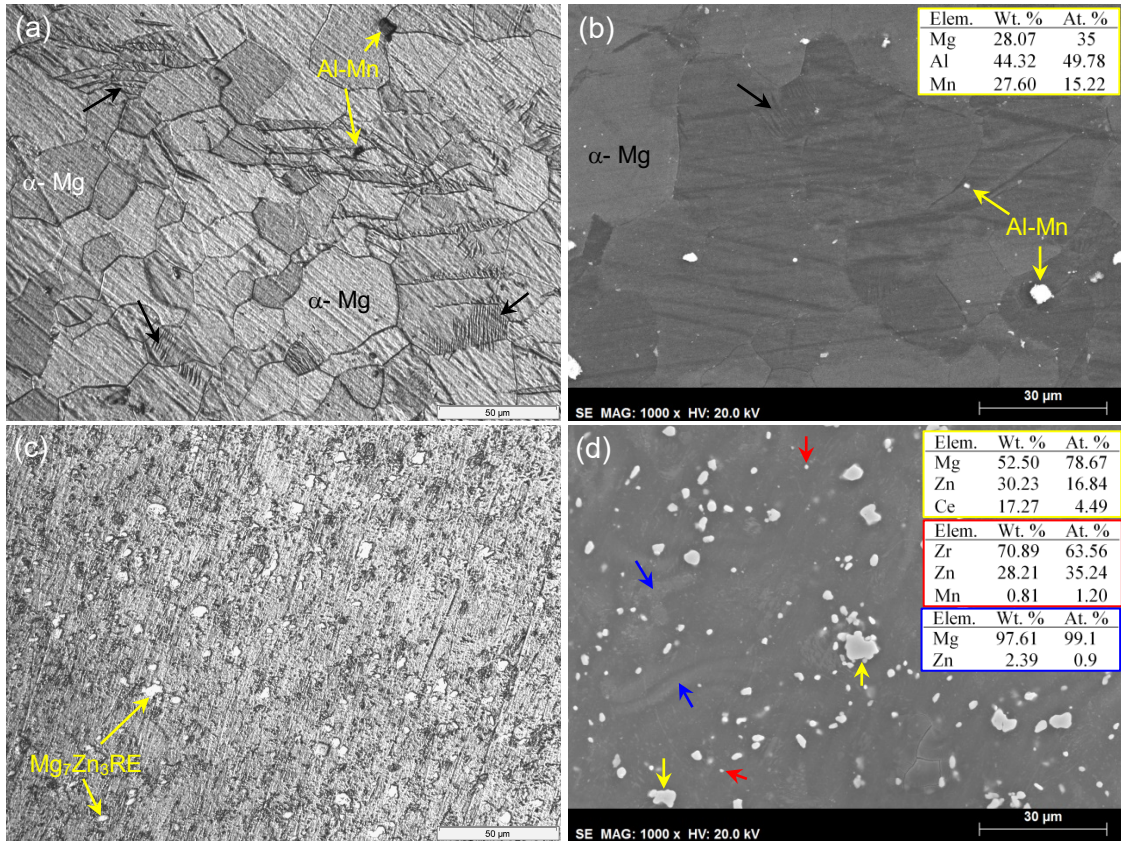


Fig. 9.1. Optical and SEM micrographs showing the microstructure of the cross-plane alloys rods and EDX analysis. (a)–(b) α -Mg equiaxed grains with some Al-Mn precipitates (yellow arrows) and mechanical twins (black arrows). (c)–(d) α -Mg matrix with local Zn-rich areas (blue arrow), T-Mg₇Zn₃RE phase particles (yellow arrows) and Zr₄Zn precipitates (red arrows).

Fig. 9.1c–d show the microstructure of the ZE41 rod (cross-plane) which is composed of various constituents: (i) a matrix of small α -Mg grains of $4.5 \pm 1 \mu\text{m}$ only observable at high magnifications (not shown); (ii) local stained Zn-rich areas in the α -Mg matrix (blue arrows, light grey areas in Fig. 9.1d); (iii) irregular-shaped particles of T-Mg₇Zn₃RE phase ranging from 4 to 7 μm in size; (iv) and small Zr₄Zn precipitates with small quantities of Mn (red arrows). Zirconium is added to Mg alloys as grain refiner and exhibits a decrease in solubility in solid Mg with decreasing temperature [74], which may explain the occurrence of the Zr₄Zn precipitates at room temperature. Both T-Mg₇Zn₃RE phase and Zr₄Zn precipitates are randomly distributed in the α -Mg matrix. The insets in Fig. 9.1d show the EDX results for the different constituents. The observed morphology of the T-Mg₇Zn₃RE phase may be related to the breakdown of the T-phase during extrusion process. When the as-cast ingot is forced to plastically flow in the extruded direction the T-Mg₇Zn₃RE phase breaks down into smaller particles with the distribution observed in the Fig. 9.1c–d in the rod’s cross-plane.

9.2. SURFACE MORPHOLOGY OF UNCOATED AND AS-PREPARED COATED ALLOYS

Fig. 9.2a–b depict the topographic AFM images of the MgF₂ layer formed on the AZ31 and ZE41 discs. Previous studies [169,177] reported that acid treatment with hydrofluoric acid provides a MgF₂ layer on Mg alloys, decreasing their corrosion rate in SBF solution [169]. The surfaces of the pre-treated alloys reveal MgF₂ crystal strings following the surface roughness (Fig. 9.2a–b). The morphology of the layer formed on AZ31 showed more compact structure when compared to the layer on ZE41, filling the cleavages between grinded scratches.

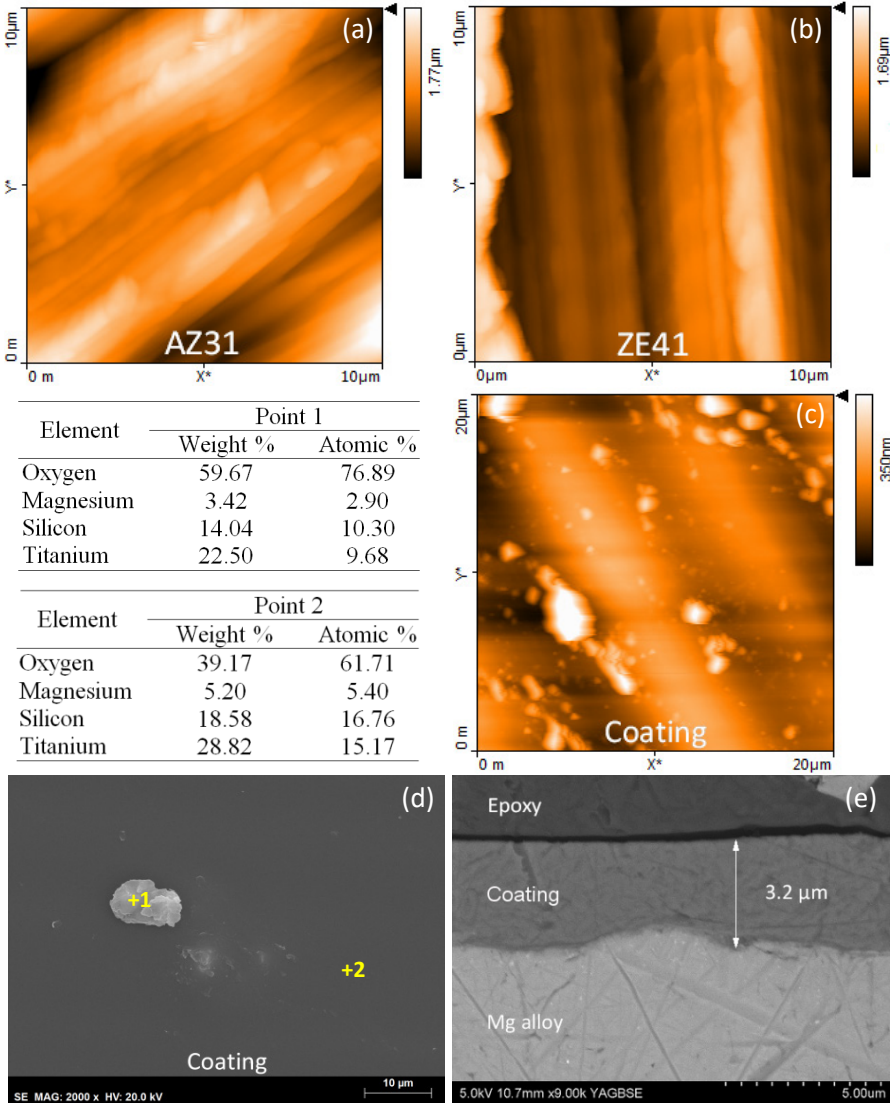


Fig. 9.2. Topographical AFM images of MgF₂ layer on (a) AZ31 and (b) ZE41, (c) as-deposited coating. Secondary electron image of (d) as-deposited coating with EDX results and (e) backscattered electron image of coating cross section.

Fig. 9.2c–d depict AFM and SEM images of the coating, respectively. Irregular-shaped aggregates ranging from 1–10 μm in diameter were found on the as-deposited coating. Their distribution over the surface was random with some crowded areas (Fig. 9.2c). EDX analysis of the aggregates (Fig. 9.2d) revealed that they consisted of Si and Ti oxides, most likely undissolved particles during the sol-gel preparation step. Topographical AFM images confirmed a smooth and rather homogeneous coating surface of small roughness R_q 21.9 ± 2.1 nm apart from the agglomerates. SEM images showed that the coating did not present relevant defects, such as micro-cracks or micro-pores. Additional analysis by electron backscattered diffraction (EBSD) did not reveal the Kikuchi patterns, suggesting that the coating and the aggregates had predominantly an amorphous structure. This is in accordance to the irregular shape of the agglomerates. The coating showed a homogeneous thickness of $\sim 3.2 \pm 0.4$ μm irrespectively of the alloy (Fig. 9.2e).

9.3. ELECTROCHEMICAL MONITORING OF THE CORROSION EVOLUTION

Following the characterization of the uncoated and coated alloys, the corrosion behavior was studied by EIS at open circuit potential. The measurements were performed by immersing the samples in SBF (7.4 pH) solution at $37 \pm 1^\circ\text{C}$. Fig. 9.3 shows the open circuit potential (OCP) evolution of pre-treated (AZ31 and ZE41) and coated (AZ31_S and ZE41_S) alloys. The OCPs of the pre-treated discs increased to more positive values during first 3 days and remained constant about -1.52 V until 2 weeks. Then, the OCPs showed minor fluctuations around this value remaining nearly constant until week 7th. The initial rise in OCP can be related to the formation of a layer of corrosion products with protective barrier properties.

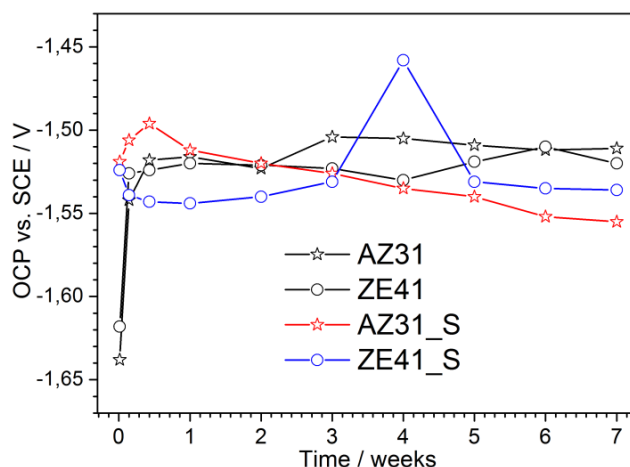


Fig. 9.3. OCP evolution of pre-treated and coated alloys in SBF (pH 7.4) at $37 \pm 1^\circ\text{C}$.

The presence of the coating shifts the initial OCPs toward more positive values compared to the uncoated alloys. The OCP of AZ31_S increased slowly during first 3 days

whereas that OCP of ZE41_S decreased. After 3 days, OCP of AZ31_S slowly decreased due to degradation of the coating barrier properties. On the other hand, the OCP of ZE41_S stabilized after 3 days followed by a small increase until week 3rd. Then, the OCP showed a temporary increase to -1.46 V around 4 weeks. This feature was also reflected on the EIS results and will be discussed below along with characterization of the corrosion products.

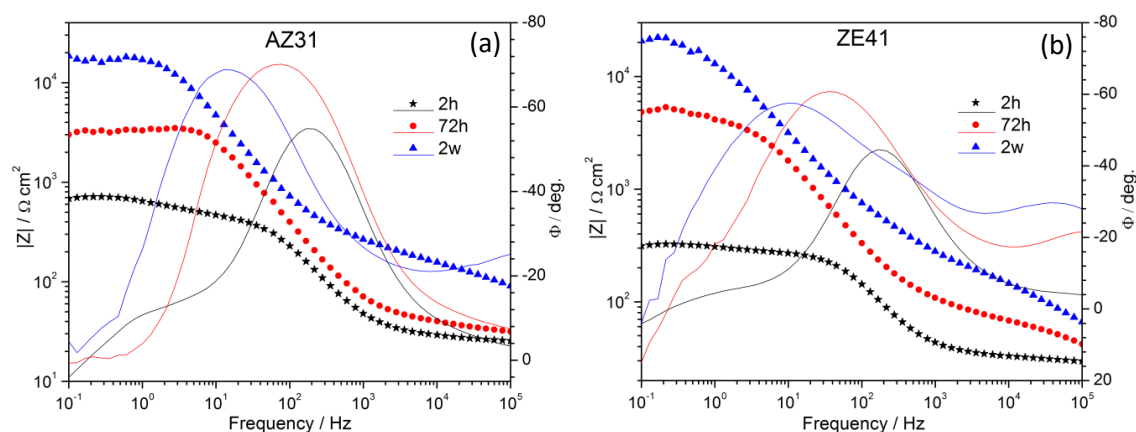


Fig. 9.4. Bode plots of pre-treated (a) AZ31 and (b) ZE41 immersed in SBF (pH 7.4) at 37 ± 1 °C. Symbols are impedance values $|Z|$ and lines are phase angle values (ϕ).

Representative Bode plots obtained for the HF pre-treated alloys and the coated alloys are depicted in Fig. 9.4 and Fig. 9.5, respectively. The low frequency impedance values of the coated alloys at early immersion were two orders of magnitude higher compared to the pre-treated samples, evidencing that the coating provides an effective barrier effect.

The initial low frequency impedance values of the coated alloys were similar, around $6 \times 10^4 \Omega \cdot \text{cm}^2$ (see Fig. 9.5). However, with time relevant changes were observed. First, low frequency (10^{-1} Hz) impedance of AZ31_S showed minor fluctuations during first 72 hours. Next, impedance decreased being one order of magnitude lower around week 4th. At the same time, the high frequency time constant (10^3 – 10^5 Hz) gradually vanished due to deterioration of the coating barrier properties.

In the case of ZE41_S, impedance dropped during first 72 hours to a value almost one order of magnitude lower compared to AZ31_S at the same immersion time. However, impedance of ZE41_S revealed a significant increase at later stages. From 2nd to 4th week of immersion the low frequency impedance reached values of $\sim 2 \times 10^5 \Omega \cdot \text{cm}^2$. After this period, the impedance decreased once again to values of $\sim 9 \times 10^3 \Omega \cdot \text{cm}^2$ after week 7th. Unlike AZ31_S, the high frequency time constant of ZE41_S was always detected in the spectra during the immersion period. In both coated alloys there were evident signs of corrosion activity. To further detail the nature and morphology of the corrosion products a detailed characterization was carried out.

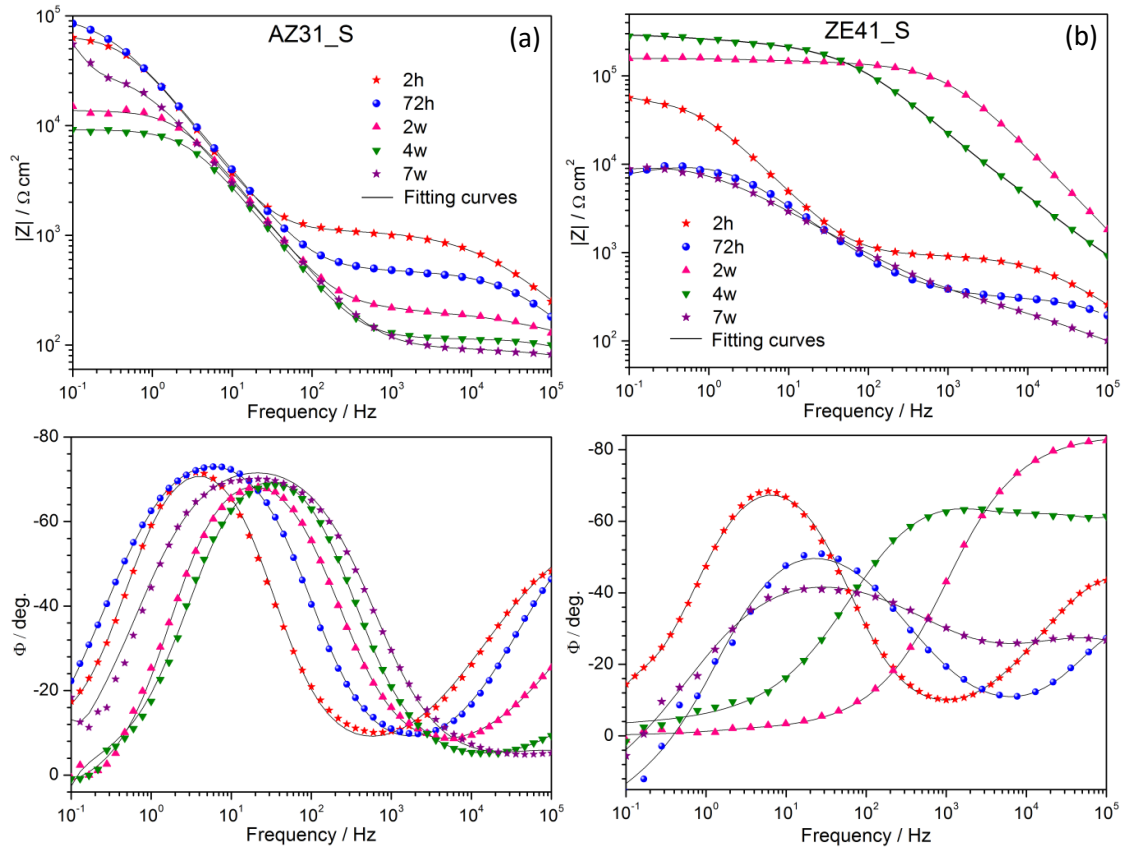


Fig. 9.5. Bode plots of coated (a) AZ31_S and (b) ZE41_S immersed in SBF (pH 7.4) at 37 ± 1 °C for 7 weeks.

9.4. MORPHOLOGY AND COMPOSITION OF THE CORRODED SURFACES

Fig. 9.6 depicts the surface morphology of uncoated and coated discs after EIS experiments for 7 weeks. The cracks formed on the corrosion products layers, as observed in Fig. 9.6a–b, may be due to volumetric contraction during dehydration process after electrolyte removal and the vacuum atmosphere during SEM analysis. Defects as cracks and local delamination evolved in the coating for both AZ31_S and ZE41_S (see Fig. 9.6c–d). The arrow in Fig. 9.6d indicates a delaminated area with flake-like shape. These defects, as well as cracks, were randomly scattered over the entire surfaces. The morphology of the delaminated areas is likely due to local accumulation and growth of corrosion products at the substrate/coating interface as well as to hydrogen evolution (H_{evo}). Visual inspection of the coated samples during immersion revealed the progressive formation of pits. In the ZE41_S discs the first pits appeared after week 1st. In the case of AZ31_S, identical pits appeared during week 3rd.

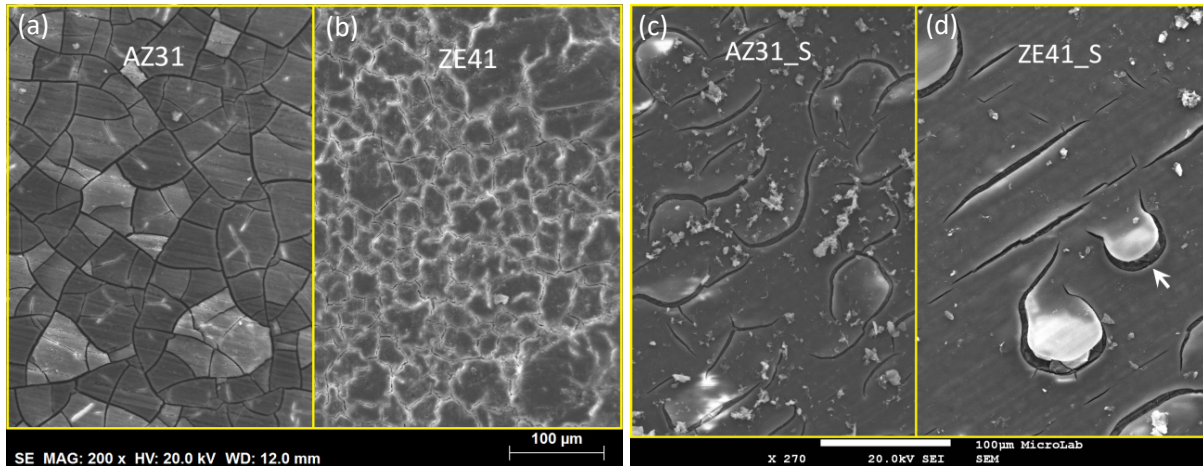


Fig. 9.6. Morphology of uncoated and coated discs after EIS experiments in SBF at 37±1°C for 7 weeks: (a) AZ31, (b) ZE41, (c) AZ31_S and (d) ZE41_S.

EDX analysis of the pre-treated samples revealed the elemental composition of the corrosion products layers. The presence of Mg, O, Ca, P and C was detected (Table 9.1). The results evidenced the incorporation of Ca, P and C into the corrosion products. Nevertheless, part of the carbon content may come from atmosphere impurities and part from surface deposits too. Calcium and phosphorus come from SBF solution.

Table 9.1. Surface chemical composition of all tested conditions before and after EIS measured by EDX.

Before EIS	Elemental composition, atomic %								
	O	Mg	Al	Before EIS	O	Mg	Zn		
pre-treated AZ31	19.09	77.09	2.61	pre-treated ZE41	15.23	80.62	2.71		
Corrosion layer*	O	Mg	Ca	P	C	Cl	Si	Ti	Ca/P
AZ31	38.47	11.49	1.71	2.03	40.95	0.32	–	–	0.84
ZE41	45.08	16.22	1.74	2.26	33.58	0.73	–	–	0.77
AZ31_S	76.00	15.82	2.82	1.18	–	2.08	2.09	0.59	2.39
ZE41_S	71.99	17.08	3.01	1.47	–	2.21	2.56	1.89	2.04

*After 7 weeks in SBF at 37±1°C

To perform EDX analysis on the corrosion products of the coated discs the coating was manually removed. The corrosion layers of AZ31_S and ZE41_S contained higher amount Mg, O, Ca and Cl elements compared to the pre-treated discs. These results suggest that the local environment created by the presence of the coating along with the corrosion processes may promote the formation of P and Ca-enriched corrosion products. Additional XRD measurements confirmed that the corrosion layers consisted of Mg(OH)₂. Broad diffraction peaks, as observed in Fig. 9.7a–b, may suggest poor crystallinity of these layers. In the case of AZ31 the peaks of Mg(OH)₂ were not detected by XRD. There may be two possible explanations of this fact: (i) either the corrosion layer on AZ31 at 7 weeks is amorphous, (ii) or the layer is not thick enough to be detected by XRD. Fig. 9.8a shows a XRD pattern of AZ31 after 1 week of immersion where the peaks corresponding to Mg(OH)₂

are clearly observable. This result suggests that crystallinity of the corrosion layers, particularly on AZ31, decreased with the immersion time. In aqueous solutions with high chloride concentrations $\text{Mg}(\text{OH})_2$ reacts with Cl^- to produce highly soluble MgCl_2 [67,178]. According to this, one hypothesis may be that the former $\text{Mg}(\text{OH})_2$ layer might become MgCl_2 and dissolve gradually into the solution. In Fig. 9.4a–b (pg. 69) it is possible to see that setting-up of the corrosion layers on uncoated discs took place during first 3 days. This is in close agreement with the steep OCP rise for the same period of time as observed in Fig. 9.3.

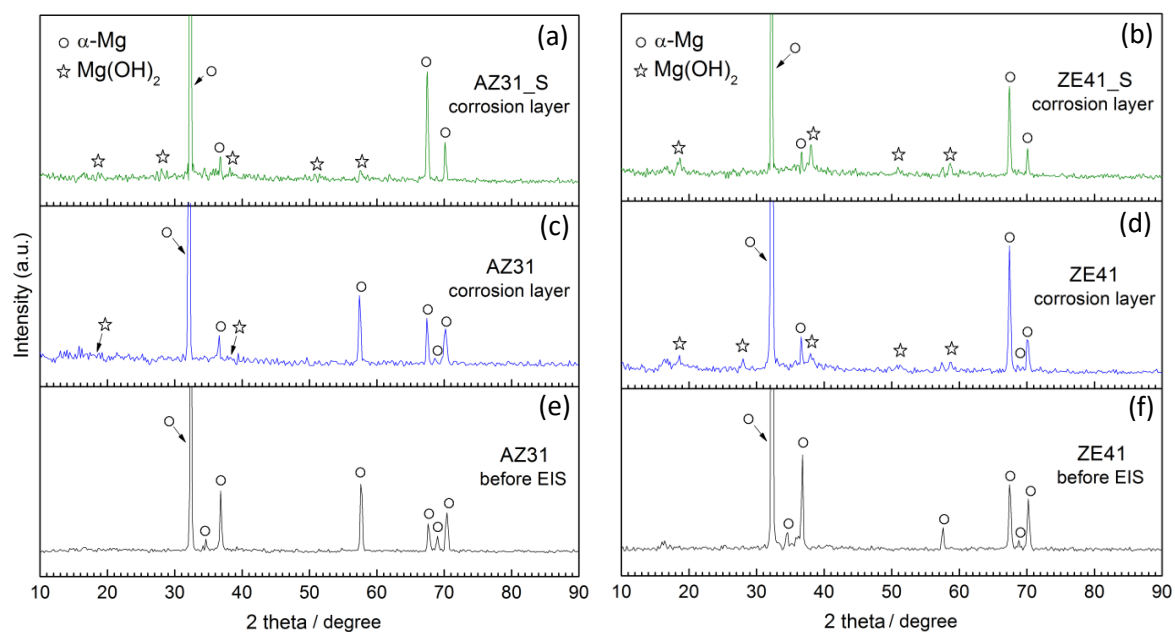


Fig. 9.7. XRD patterns of the corrosion layers on coated (a) AZ31_S, (b) ZE41_S and pre-treated (c) AZ31, (d) ZE41. XRD patterns of pre-treated (e) AZ31 and (f) ZE41 before EIS.

Further Raman characterization supported the aforementioned hypothesis. Fig. 9.8b displays the Raman spectrum of the corrosion layer on AZ31_S and ZE41_S at week 7th. The peak at 3648 cm^{-1} corresponding to the O-H fundamental of $\text{Mg}(\text{OH})_2$ on the high frequency side was detected on both samples. Since Raman scattering is sensitive to the degree of crystallinity, broader peak and decreased intensity of AZ31_S corrosion layer may indicate lower crystallinity when compared to the corrosion layer of ZE41_S.

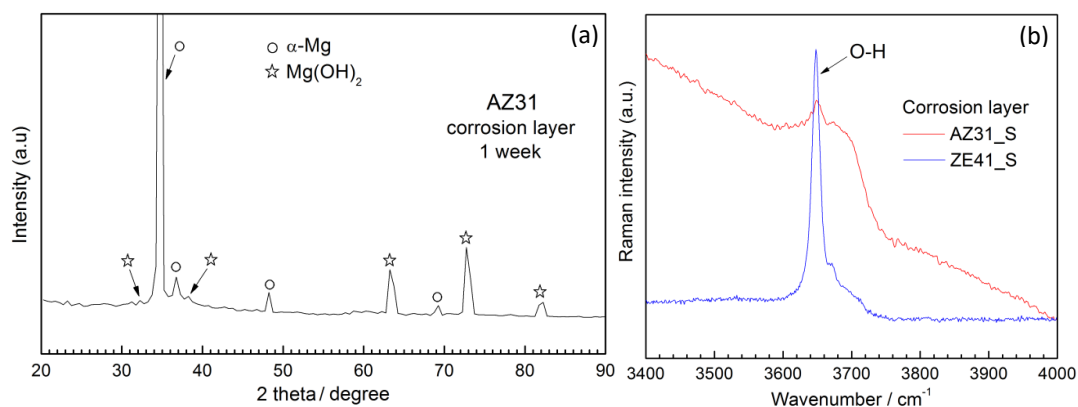


Fig. 9.8. (a) XRD pattern of corrosion layer on AZ31 after 1 week and (b) Raman spectra of the corrosion layers on AZ31_S and ZE41_S after 7 weeks in SBF at 37°C.

Further Raman results confirmed the presence of Ca and P in the corrosion layer of both coated discs, as reported in EDX results in [Table 9.1](#). The corrosion layers consisted then in a mixture of $\text{Mg}(\text{OH})_2$ and hydroxyapatite (HAP) for both AZ31_S and ZE41_S. The [Fig. 9.9](#) depicts Raman spectra of coated discs in comparison to RRUFFTM patterns [179] of hydroxyapatite (Ref. 060180) and clorapatite (Ref. 060192). It has been reported in previous studies [180] that precipitation kinetics is critical for the purity of HAP and its crystallographic characteristics. Most of the synthetic methods to produce HAP crystals from supersaturated aqueous solutions led to the formation of non-stoichiometric products. This is due to the presence of vacancies and ion substitutes in the crystal lattice such as hydrogen phosphates, carbonates, potassium and chlorides, among others [180]. Usually, these species are introduced into the precipitating system with the reactants. Hence, synthesized HAPs incorporating any of the above-mentioned ions undergo significant changes and have different crystal morphology compared to the stoichiometric one [180]. This may explain the differences observed in the Raman spectra of AZ31_S and ZE41_S. Correspondingly, the Ca/P molar ratios listed in [Table 9.1](#) suggest that in the present case the HAPs precipitated from SBF differ from stoichiometric HAP whose Ca/P molar ratio is 1.67. Other authors [181] have also reported that during immersion in SBF, the corrosion of Mg alloys is accompanied by the formation of corrosion products such as magnesium hydroxide, carbonates and phosphates.

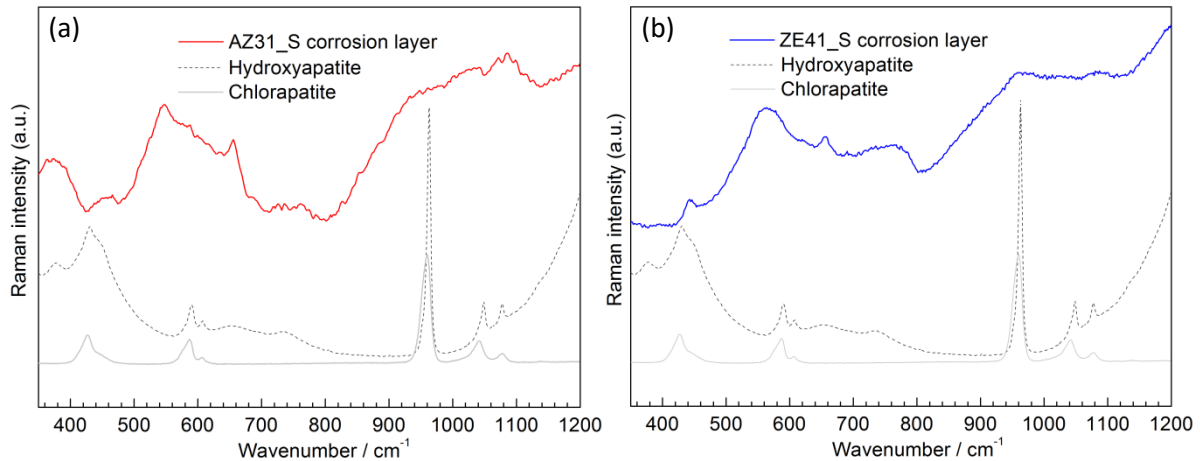


Fig. 9.9. Raman spectra of the corrosion layer on (a) AZ31_S and (b) ZE41_S after 7 weeks compared to the characteristic Raman spectra of hydroxyapatite and chlorapatite [179].

Cross-sectioning of coated samples revealed additional features of the corrosion layers. **Fig. 9.10a** shows the cross-section of AZ31_S where a rather thin corrosion layer with a thickness in the range of 4–5 μm is observed. Nevertheless, the layer seems to have a dense structure. The local delamination of the coating due to accumulation of corrosion products is also seen in **Fig. 9.10a**. This corresponds to the flake-like shaped delaminated areas aforementioned and depicted in **Fig. 9.6c–d**. The occurrence of localized corrosion (pits) was also observed on both AZ31_S and ZE41_S corrosion layers (not shown). The local environment created by the pit formation may promote the pile-up and growth of corrosion products around the pit. Apart from these areas, the thickness of the AZ31_S corrosion layer seemed quite homogeneous.

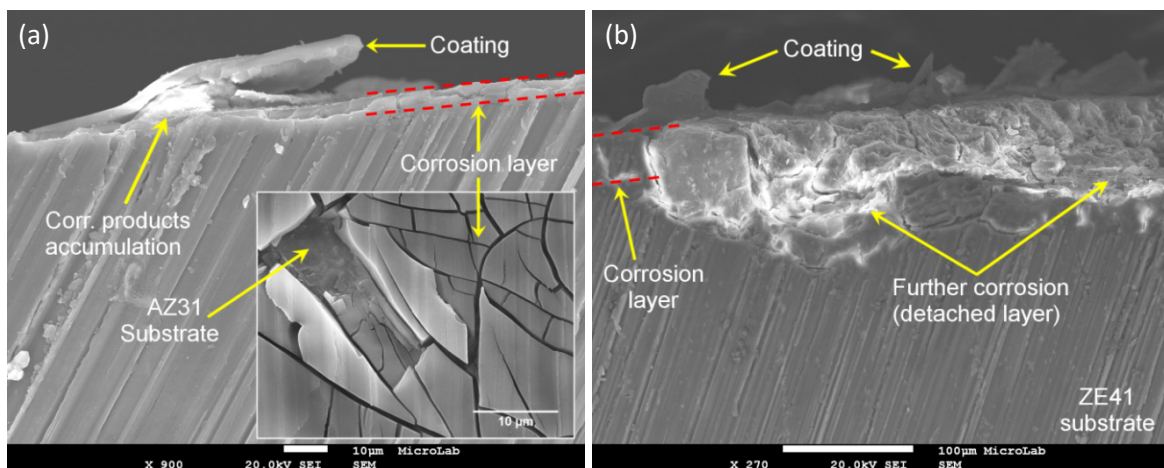


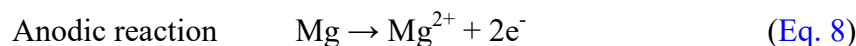
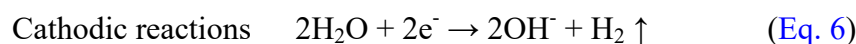
Fig. 9.10. Cross-sectional secondary electron images of (a) AZ31_S and (b) ZE41_S after 7 weeks in SBF at 37°C. The inset in (a) depicts a plane-view of the AZ31_S corrosion layer after coating removal.

In the case of ZE41_S, a non-uniform corrosion layer of thickness ranging from 20 to 40 μm was observed (**Fig. 9.10**). Large areas where the layer was detached possibly due to further corrosion were also found. Some of these areas reached about 90 μm in depth. This

may explain the wide OCP variations of ZE41_S as observed in Fig. 9.3. During first 3 days of immersion the OCP of ZE41_S slightly dropped probably due to deterioration of the coating barrier properties. Next, the OCP stabilized and started rising slowly until week 3rd. It appeared that the corrosion layer formation took place during this period of time. Then, thickening and densification of the layer could happen from week 3rd to week 4th. However, the occurrence of pits in the corrosion layer enables the electrolyte to reach the metal surface and further corrosion causes selective detachment of the layer. The proposed corrosion mechanism would explain the OCP drop after 4 weeks of ZE41_S and will be further discussed together with the parameters extracted from the EIS fitting.

9.5. CORROSION MECHANISMS AND MODELLING

The most representative redox reactions responsible for the overall corrosion process of Mg alloys are listed below [172]:



As indicated by Eq. 9, the main products of the corrosion reaction are hydrogen gas and insoluble magnesium hydroxide. The local conditions may also promote the formation of hydroxides of the alloying elements and hydrated oxides [182].

The main role of the coating is to hinder water and oxygen access to the Mg substrate and especially to slow down the corrosion rate at early stages of immersion. This is possible due to the formation of stable Si-O-metal bonds which provide good adhesion to the substrate delaying corrosion onset [172]. The coating matrix is composed of a TiO₂- and SiO₂-containing network with good barrier properties that hinders electrolyte uptake and protects the underlying metal from accelerated corrosion [183]. However, in the present case the main objective of coating is to control the corrosion process and not to prevent it completely. Consequently, a thin coating was prepared allowing the electrolyte to gradually reach the metal substrate and the corrosion processes start. The corrosion activity leads to chemical and physical degradation of the coating due to initial swelling and subsequent setting-up of corrosion products. The local alkaline environment at the metal/coating interface promotes corrosion products growth inducing mechanical stresses to the coating which results in delamination and cracking. These defects further facilitate the electrolyte access to the alloy surface and the evolution of the corrosion processes.

Taking into account that the coating thickness and morphology was reproducible for both alloys, it can be suggested that the response of the coated discs over immersion reflects the respective corrosion susceptibility of the alloy. The impedance modulus of AZ31_S showed a more stable behavior when compared to that of ZE41_S, as observed in Fig. 9.5. The low frequency impedance of ZE41_S revealed a significant increase after 2 weeks suggesting the formation of a protective layer of corrosion products (see Fig. 9.5b). However, this protective effect was temporary and the impedance modulus decreased at a later stage. The ZE41 magnesium alloy contains rare-earth (RE) elements that may form protective RE oxides and hydroxides, decreasing the corrosion rate [184,185]. Then, it is reasonable to assume that the formation of the corrosion layer on ZE41_S took place during first 2 weeks of immersion followed by densification from 2 to 4 weeks. Once the electrolyte reached the underlying substrate, hydrogen gas was produced through water reduction reaction represented in Eq. 6 and by the reaction of adsorbed Mg^+ intermediates and water [186]. Simultaneously, second phase precipitates present in the microstructure, such as T-Mg₇Zn₃RE phase and Zr₄Zn particles in ZE41 (see Fig. 9.1), act as cathodes that dissolve the adjacent α -Mg matrix resulting in a fast production of OH⁻ ions (Eq. 7) that in turn lead to a fast local rise in pH. The local pH increase induced the local deposition of large amounts of corrosion products. Variations in the composition of the MgF₂ layer of each alloy were also expected due to the differences in the alloys bulk composition modifying the barrier properties of this layer. After 4 weeks, nucleation and growth of defects in the ZE41 corrosion layer due to the presence of aggressive Cl⁻ ions allowed further corrosion and consequently a decrease of the impedance values (Fig. 9.5).

In contrast, the initial corrosion rate of AZ31_S was slower compared to ZE41_S. There may be two complementary reasons of this fact: (i) at early immersion the corrosion resistance of AZ31 alloy in SBF is higher than that of ZE41 alloy and, (ii) the coating barrier properties degrade slower on AZ31 alloy. The first rationale may be supported by the impedance values of the uncoated samples plotted in Fig. 9.4. The matrix of ZE41 contains high number of second-phase precipitates (Fig. 9.1c–d) which means high number of micro-galvanic couples. The large area fraction of finely divided T-Mg₇Zn₃RE and Zr₄Zn particles may lead to accelerated dissolution of the α -Mg phase. On the contrary, AZ31 has considerably smaller Al-Mn particles/ α -Mg phase area fraction (Fig. 9.1a–b) and hence lesser number of micro-galvanic couples. The second rationale may be explained by the middle-high frequency time constant that gradually vanished over immersion (Fig. 9.5a). Additionally, the corrosion layer formed on AZ31_S seemed to have a quite dense and homogeneous structure (Fig. 9.10a). All the above mentioned, may be responsible for the rather stable behavior of AZ31_S during immersion [187].

To detail the EIS results numerical fitting of the experimental data was carried out using the equivalent circuit depicted in Fig. 9.11. In this model, constant phase elements (CPE) representing non-ideal capacitors were considered instead of pure capacitors. Non-ideal capacitor behavior may be due to factors such as electrode porosity, non-uniform current distribution and variations of the coating composition [188]. The physical interpretation of the equivalent circuit is also depicted in Fig. 9.11 and accounts for the presence of three time constants: (i) one at high frequencies describing the barrier properties of the coating; (ii) a second one in the medium frequency range assigned to interfacial corrosion layer and, (iii) a third one at low frequencies assigned to localized corrosion activity. The χ^2 of the regression was around 10^{-3} .

In Fig. 9.11a CPE_{coat} accounts for the capacitive response of the coating and CPE_{IL} for the capacitive response of the interfacial layer (IL). It is important to note that at the beginning of the experiments the interfacial layer corresponds to the MgF_2 layer. However, with time this layer transforms into the corrosion products that build up underneath the coating. Likewise, R_{coat} and R_{IL} account for the resistance of the solution inside the narrow coating pores and the resistance of the pores in the IL, respectively.

Fig. 9.11b–e depict the evolution of the different parameters extracted from the numerical fitting. The initial values of the pore resistance (R_{coat}) for both coated alloys were similar. This is reasonable since at the beginning of the immersion the coating governs the corrosion response. In this case the as-deposited coatings had similar thickness and morphology on both alloys. The barrier properties of the coating can, thus, be characterized by R_{coat} and CPE_{coat} . When R_{coat} decreases and CPE_{coat} increases the coating barrier properties deteriorate and its protective ability decreases. In Fig. 9.11d the initial increase in Q for CPE_{coat} ($0.66 < n < 0.89$) of AZ31_S may be attributed to electrolyte uptake, hereinafter the coating barrier properties started to degenerate. From the behavior of the Q parameter for CPE_{coat} of ZE41_S it may be considered that the coating barrier properties deteriorate faster on ZE41 alloy. This is probably due to the increased corrosion activity of this alloy at early stages of immersion. Consequently, deposition and growth of the corrosion layer may occur at a faster rate inducing mechanical stresses to the coating matrix that result in structural defects, compromising the physical integrity of the coating at an earlier stage.

At the beginning of immersion R_{IL} of AZ31_S was higher compared to R_{IL} of ZE41_S. As depicted in Fig. 9.11a–b, the MgF_2 layer on AZ31 alloy had a more compact structure when compared to the same layer on ZE41 alloy. As immersion elapses, the MgF_2 layer gradually dissolves and is replaced by the layer of corrosion products. Therefore, a more permeable MgF_2 layer along with higher corrosion susceptibility can lead to the fast drop in R_{IL} of ZE41_S during first 24 hours.

The impedance of a CPE is given by the following equation [188]:

$$Z_{CPE}(\omega) = Q^{-1}(j \cdot \omega)^{-n} \quad \text{with } -1 < n < 1 \quad (\text{Eq. 10})$$

where j is the imaginary number and ω is the angular frequency ($\omega = 2\pi f$, with f as the frequency). The Q parameter of CPE becomes equal to capacitance when $n = 1$ and equal to resistance when $n = 0$. An inductor corresponds to $n = -1$. The n values corresponding to CPE_{IL} of AZ31_S, indicated that the interfacial layer behavior is closer to an ideal capacitor ($0.88 < n < 0.95$). This confirms that the $Mg(OH)_2/HAP$ layer formed on AZ31_S (see Fig. 9.10a) was quite stable over immersion being responsible for the passive corrosion behavior [187].

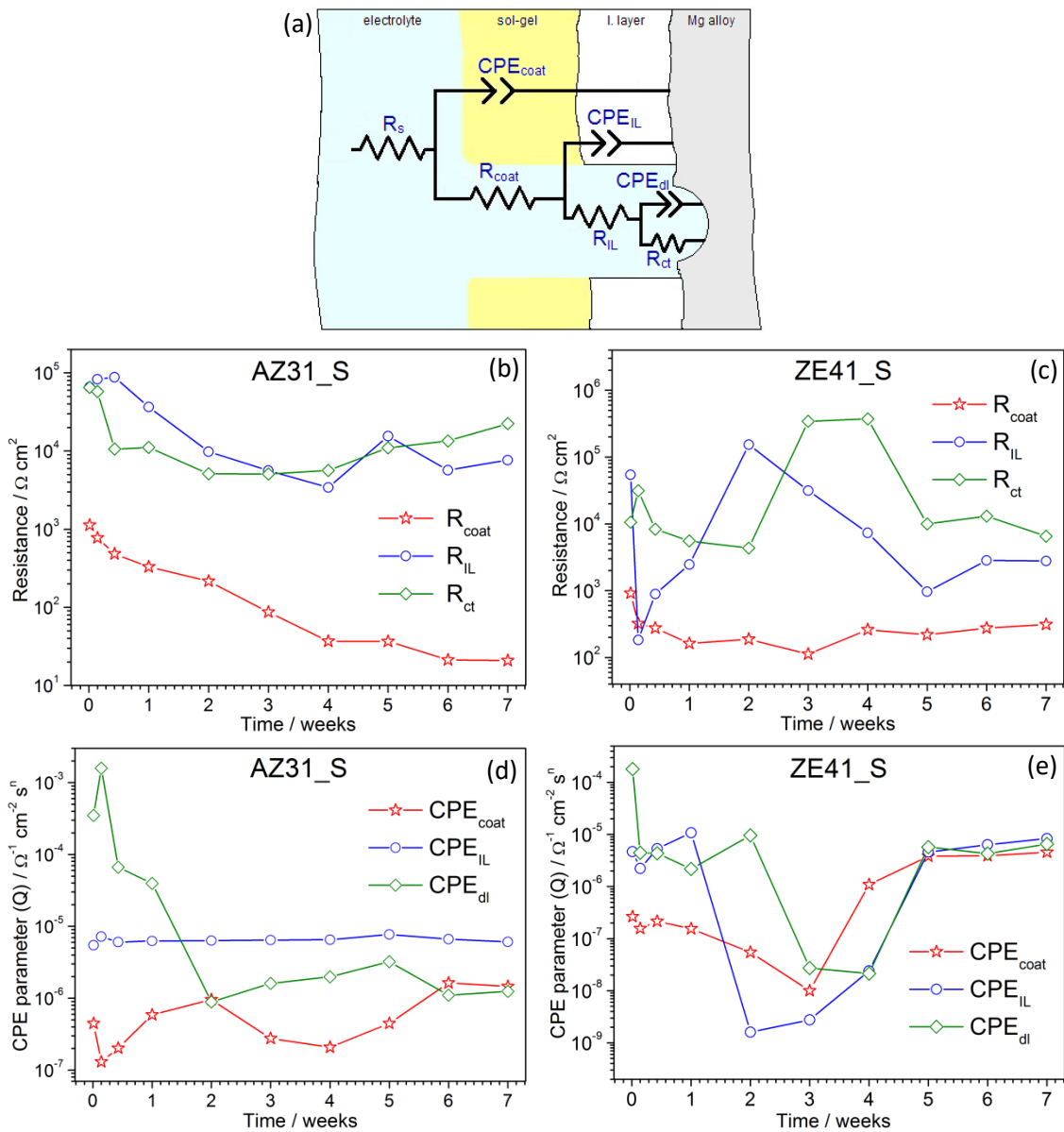


Fig. 9.11. (a) Equivalent circuit used to fit the EIS data. Evolution of the resistance for (a) AZ31_S and (b) ZE41_S. CPE parameter Q for (c) AZ31_S and (d) ZE41_S.

The charge transfer resistance (R_{ct}) closely followed the R_{IL} variations. The Q values of the double layer capacitance of AZ31_S (CPE_{dl} , $0.90 < n < 0.98$) decreased from 24 hours to week 1st probably due to coating swelling. At this point the corrosion processes had already started. The precipitation/accumulation of corrosion products blocked the pores and defects in the coating through which the ions from the electrolyte are transported. The ions cannot reach the substrate and consequently the CPE_{dl} decreased. The subsequent decline of the coating barrier properties reactivates these pathways and corrosion processes can proceed.

The wide fluctuations in R_{IL} and CPE_{IL} ($0.62 < n < 0.95$) of ZE41_S indicated that its corrosion layer structure varied over immersion (Fig. 9.11c–e). An increase in the R_{IL} means that the IL structure becomes more compact [181]. In the same way, a decrease in the Q parameter for CPE_{IL} may be attributed to thickening of the layer [189]. The capacitance of parallel plates is expressed by the following expression [181]:

$$C = \epsilon A/d \quad (\text{Eq. 11})$$

where ϵ is permittivity of the dielectric material between plates and A and d the area and separation of the parallel plates of the capacitor, respectively. Analogically, Q is equivalent to capacitive response (C) and d to the corrosion layer thickness. As observed in Fig. 9.11c–e, the initial increase in both R_{IL} and Q for CPE_{IL} of ZE41_S suggest that the corrosion layer forms from 24 hours to week 1st. After 1 week, the continuous rise in R_{IL} and the corresponding decrease in Q for CPE_{IL} may indicate densification and thickening of the IL, respectively. As depicted in Fig. 9.10b, large areas of the $Mg(OH)_2/HAP$ layer on ZE41_S were detached. These areas may expose either a new-fresh-metallic surface that reacts with the electrolyte to initiate the formation of a new fraction of the corrosion layer, or a cavitated zone in the corrosion layer that may become thicker afterwards. If this process is cyclic, it can be reflected in wide variations of the resistance and the capacitive response with the overall impedance response being governed by the process with the highest Q value [62].

Lamaka et al. [172] studied the corrosion performance of ZK30 (3.0 wt% Zn, 0.3 wt% Zr) Mg alloy coated with a hybrid GPTMS:Ti coating doped with Ce^{3+} ions. The study demonstrated that precipitation of $Ce(OH)_3$ and $Ce(OH)_4$ contributed to seal the corrosion layer structure, leading to a temporary increase of its resistance. Alkalinization at the substrate/coating interface is likely to promote the formation of rare-earth hydroxides that may contribute to the initial stability of the ZE41_S corrosion layer. The fact that these hydroxides were not detected by EDX analysis may be due to their lower content in comparison to other elements. In respect to x-ray diffraction results, the equipment used in this study may have low analytical limit and therefore patterns from precipitates in low quantity and crystal phases traces are difficult to detect. Moreover, Raman results suggested that the ILs of both AZ31_S and ZE41_S were poorly crystalline. Ascencio et al. [188]

studied the influence of immersion time on the corrosion mechanisms of WE43 (4.0 wt% Y, 3.0 wt% RE) Mg alloy in modified SBF. They found that changes in the impedance response at advanced stages of immersion (120 hours) were due to rupture of the corrosion layer and lateral growth of stable pits [188]. Furthermore, from combined ATR-FTIR and XRD results they demonstrated that the top-most corrosion layer was composed of an amorphous $\text{Mg}(\text{OH})_2$ and carbonated apatite mixture [188].

The response of R_{ct} and Q for CPE_{dl} ($0.76 < n < 0.98$) of ZE41_S showed that these parameters were governed initially by the coating properties, and thereafter by the formation and breakdown of the protective corrosion layer. After week 5th, the resistance and the capacitive response of ZE41_S stabilized. This may be due to enlarged coating delaminated areas. When delaminated areas extent and reach a large fraction of the total coated surface, the corrosion becomes almost uniform and the electrochemical response is close to that expected for the uncoated metal.

The presence of Ca and P in the corrosion products layer revealed that the SBF influences the nature of the corrosion products, as reported by Ascencio et al. [188]. Li et al. [190] suggested that a $\text{Mg}(\text{OH})_2$ layer provides favourable sites for hydroxyapatite nucleation via calcium immobilization on its surface. These nuclei grow spontaneously, consuming the calcium and phosphate ions from the surrounding fluid [191,192]. As pH rises, the ion strength of the electrolyte increases and hence the ionic activity inducing formation of Ca-P nuclei and their posterior growth. The formation of the nuclei induces changes in the barrier properties of the formed interfacial $\text{Mg}(\text{OH})_2$ layer and can contribute for the observed impedance fluctuations too. Worth of notice is the fact that Ca and P were detected in higher quantities in the coated discs. This might be related to more concentrated local alkalization in the buried areas where the coating delaminates.

Thin TiO_2 -modified silane coatings can be used to slowly control the corrosion rate of AZ31 and ZE41 Mg alloys. The coating barrier properties degrade faster on the rare-earth containing ZE41 alloy, due to its decreased corrosion resistance at early stages of immersion. However, the build-up of a thick $\text{Mg}(\text{OH})_2$ /hydroxyapatite layer, as observed in the SEM analysis, induces wide variations on the corrosion activity as confirmed by electrochemical impedance results. Contrarily, the $\text{Mg}(\text{OH})_2$ /hydroxyapatite layer formed on the coated AZ31 alloy is thinner and shows a more stable behavior, degrading slowly over time. In all the tested materials the results reveal the formation of calcium- and phosphate-enriched corrosion products. However, the presence of the coating determines the composition of the calcium and phosphate compounds formed. The increase of the calcium to phosphate molar ratio in the coated discs can be assigned to a non-stoichiometric hydroxyapatite, as demonstrated by the Raman analysis. The presence of these compounds is an essential feature for the increased biocompatibility of these materials in bone repair applications.

9.6. LOCALIZED CORROSION BEHAVIOR OF COATED AZ31 AND ZE41 Mg ALLOYS

Scanning ion-selective electrode technique (SIET) and scanning vibrating electrode technique (SVET) were applied to characterize the localized corrosion behavior of the silane-TiO₂ coated Mg alloys. An artificial defect of 500 μm in length was made in order to expose a small area of the substrate to the electrolyte solution (Fig. 9.12-1a). The artificial defect aims to mimic a localized corroding area where the coating was delaminated (see Fig. 9.6c-d and Fig. 9.10a). Both SIET and SVET measurements were carried out separately on different samples in SBF solution at room temperature.

Fig. 9.12 and Fig. 9.13 show the SIET and SVET maps of AZ31_S and ZE41_S, respectively, obtained at different delayed time scans. Both pH and current density showed important variations over immersion.

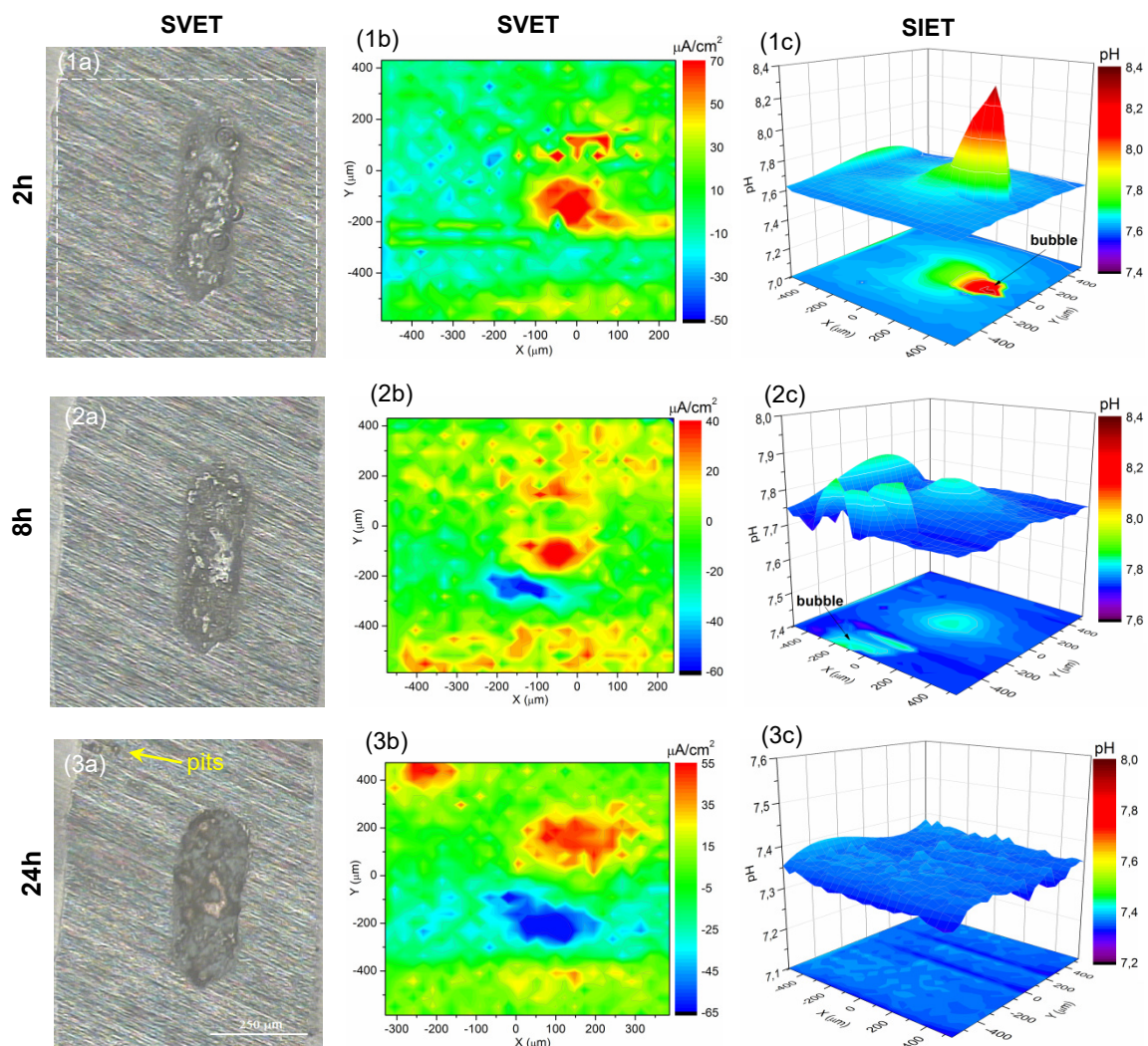


Fig. 9.12. Current density (1b, 2b, 3b) and pH (3a, 3b, 3c) distribution at the surface of AZ31_S with the artificial defect upon exposure to the SBF solution at room temperature ($\sim 22^\circ\text{C}$) for 24h. The dashed line in 1a indicates the scanned area.

At the beginning of the immersion, formation of H_2 gas bubbles was observed on both AZ31_S and ZE41_S samples. After 2h, the pH measured around the defect of AZ31_S was ~ 7.8 and the pH measured around a formed gas bubble was ~ 8.2 (Fig. 9.12-1c). The corresponding SVET scan in Fig. 9.12-1b showed high corrosion activity after 2h of immersion reaching current density values of about $70 \mu A \cdot cm^{-2}$ in the anodic zone (red-orange area in colour). After 8h the pH did not show considerable variations compared to the pH after 2h of immersion (Fig. 9.12-2c). On the other hand, the anodic current density decreased to values of $\sim 40 \mu A \cdot cm^{-2}$ along with the formation of a cathodic zone (blue area in colour) at the defect (Fig. 9.12-2b). Both cathodic and anodic zones at the defect increased after 24h with a slight increase of the anodic current density to $\sim 55 \mu A \cdot cm^{-2}$ (Fig. 9.12-3b). New anodic areas appeared due to the formation of pits on the substrate (see arrow in Fig. 9.12-3a). After 24h there were no relevant pH gradients over the scanned area of AZ31_S with a steady pH value of ~ 7.4 .

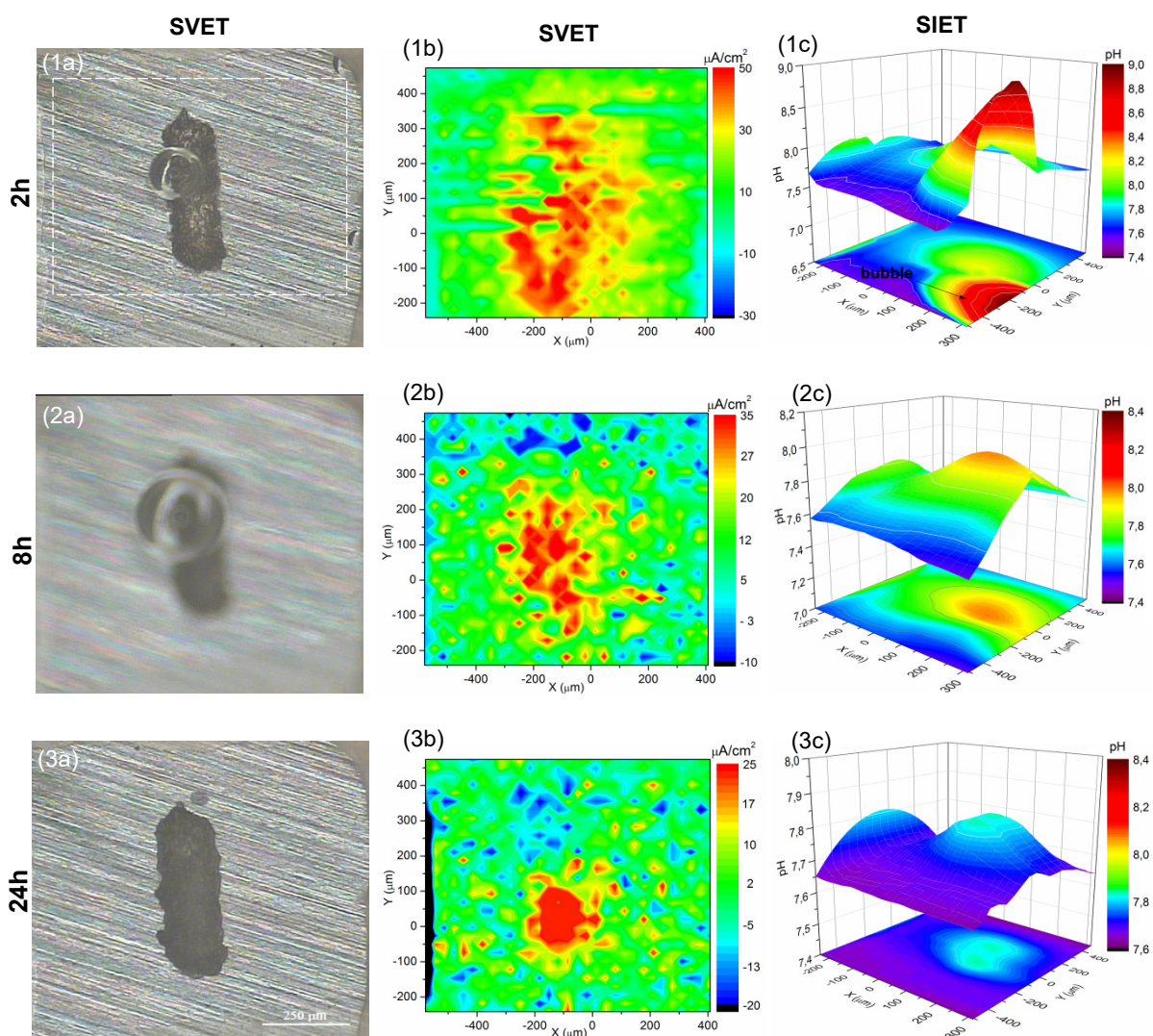


Fig. 9.13. Current density (1b, 2b, 3b) and pH (3a, 3b, 3c) distribution at the surface of ZE41_S with the artificial defect upon exposure to the SBF solution at room temperature ($\sim 22^\circ C$) for 24h.

In the case of ZE41_S the pH variations showed a similar trend when compared to AZ31_S; however, there was still a pH gradient evidenced after 24h (Fig. 9.13-3c). Initially, alkalinisation towards the defect along with formation of H₂ bubbles was observed. Next, as immersion elapsed the pH values around the artificial defect gradually decreased from ~8.1 at 2h to ~7.8 at 24h. At the beginning of the immersion increased H_{ev0} was observed on ZE41_S comparatively to AZ31_S. Chen and Thouas [7] suggested that Zn-rich Mg alloys exhibit reduced H_{ev0} and proposed a mechanism for this behavior. First, Zn²⁺ and Mg²⁺ ions in solution compete for binding the free OH⁻ ions. Then, if Zn(OH)₂ forms this ultimately would decrease the amount of H₂ reducing H_{ev0} [7]. Whether OH⁻ ions are consumed in the formation of both Zn(OH)₂ and Mg(OH)₂ this would decrease the pH solution too, which may explain the pH values of AZ31_S after 24h (Fig. 9.12-3c). On the other hand, the presence of elements nobler than Mg in the corrosion film —e.g. RE elements— may act as preferred spots for high H_{ev0} rates which would increase the rate formation of Mg(OH)₂ [75]. The aforementioned may explain the increased H_{ev0} rate of ZE41_S.

SVET maps showed that the difference between the highest anodic current density values (red-orange) and the lowest cathodic current density values (blue) of ZE41_S was 80 μA·cm⁻² after 2h. Concomitantly, the difference between anodic and cathodic current densities of AZ31_S was 120 μA·cm⁻² for the same immersion time. The larger difference between anodic and cathodic current density values for AZ31_S suggests that this sample had higher corrosion activity than ZE41_S. However, SVET mapping after 2h did also show that on AZ31_S there was a small-localized-anodic area inside the defect (Fig. 9.12-1b) while on ZE41_S the anodic zone appeared to be all the exposed area of the defect (Fig. 9.13-1b). Therefore, the results indicate that at the beginning of the immersion the anodic reaction of AZ31_S was more localized and more active than that of ZE41_S. Similarly to AZ31_S, a cathodic zone appeared next to the anodic zone at the defect.

Other authors have studied the current density distribution of pure Mg in electrolytes containing Cl⁻ ions. In 2013, Williams et al. [79] determined the current density distribution of pure Mg in NaCl containing electrolyte using in-situ SVET. Their results showed that anodic dissolution of pure Mg is highly localized and accompanied by significantly cathodic activity [79]. The original local anodes rapidly propagate away from their initiation sites and leave behind areas strongly activated which rapidly develop into strong local cathodes. The authors also demonstrated that H_{ev0} on Mg remains a cathodic process and that the surface area occupied by cathodes progressively increased with time [79]. This effect was observed in SVET maps of both AZ31_S and ZE41_S in Fig. 9.12 and Fig. 9.13, respectively. The cathodic reaction of Mg gives place to H_{ev0} which is followed by local alkalinization of the solution [193]. Then, increased cathodic surface area would lead to increased H_{ev0} in the case of pure Mg. SIET results showed that local alkalinization of the solution on AZ31_S is suppressed after 24h while on ZE41_S it still remains. These results are in accordance with

the reduced H_{evo} of Zn-rich Mg alloys suggested by Chen and Thouas [7] and with the hypothesis of increased H_{evo} due to the presence of elements nobler than Mg in the corrosion products layer postulated by Thomas et al. [75].

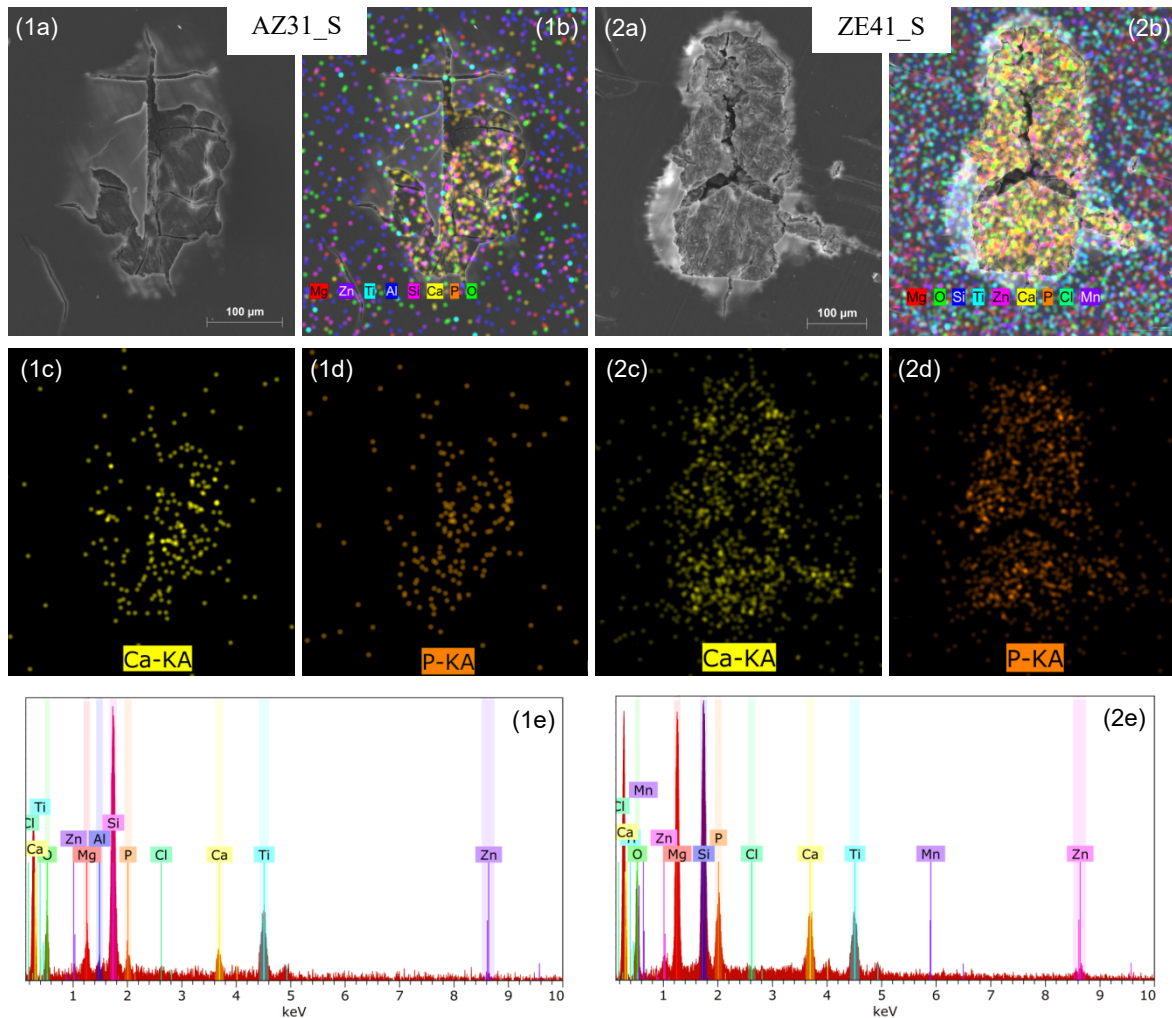


Fig. 9.14. SEM images of the artificial defect of (1a) AZ31_S and (2a) ZE41_S after 24h of exposure to SBF at room temperature. Elemental distribution maps (1b-1d & 2b-2d) and EDX spectra (1e & 2e) of previously defined elements over the scanned area of AZ31_S and ZE41_S, respectively.

After SVET and SIET experiments the samples were analyzed by SEM. The images in Fig. 9.14-1a and 2a show that the artificial scratch was completely covered by corrosion products after 24h of exposure to the corrosive medium. EDX mapping indicated that the corrosion products are rich in Ca and P (Fig. 9.14-1c,1d and Fig. 9.14-2c,2d). As already discussed in chapter 9.4, the corrosion products layer of both coated alloys after 7 weeks of immersion is composed by a mixture of $\text{Mg}(\text{OH})_2/\text{HAP}$. SVET and SIET results showed that formation of this layer already takes place at early stages of immersion. On both AZ31_S and ZE41_S anodic and cathodic activity were detected before 2h of immersion (not shown) along with local alkalization of the solution.

This study helps to elucidate the corrosion processes occurring at small areas where the coating locally delaminates. Considering all the above mentioned the progression of the corrosion processes may be described as follows:

- 1) The coating gradually swells due to electrolyte uptake leading to chemical and physical degradation of the coating.
- 2) Aggressive ions, such as Cl^- , are transported through the growing coating micro-defects reaching the underlying substrate and the corrosion processes start.
- 3) Local dissolution of the Mg matrix at anode sites (Eq. 8, pg. 75), water-induced decomposition by electron capture and H_{evo} at cathode sites (Eq. 6, pg. 75) create a local micro-environment that promotes the buildup of corrosion products.
- 4) $\text{Mg}(\text{OH})_2$ forms (Eq. 9, pg. 75) providing favorable sites for HAP nucleation via Ca immobilization on its surface. HAP nuclei spontaneously grow and consume Ca and P ions of the surrounding fluid [190]. Ions substitutes present in solution incorporate into the corrosion products crystal lattice resulting in a poor-crystalline non-stoichiometric $\text{Mg}(\text{OH})_2/\text{HAP}$ layer.
- 5) Local alkalization at the metal/coating interface promotes growing of corrosion products which induce mechanical stresses to the coating, leading to its delamination and cracking.
- 6) The coating failures further facilitate the electrolyte access to the substrate promoting the progression of the corrosion processes.

SVET results showed that the nature of the alloying elements influences the current density values and the size and distribution of anodic and cathodic regions. More localized anodic activity was found on AZ31_S comparatively to ZE41_S. Together with the results reported in chapter 9, these findings confirm the complexity and variability of the corrosion response of Mg systems whose performances are highly dependent not only on the original bulk composition, but on the surface treatment too.

10. BI-LAYERED MULTIFUNCTIONAL SILANE-TiO₂/BIOPOLYMERS COATINGS TO CONTROL BIODEGRADATION OF Mg ALLOYS

This chapter presents the corrosion behavior of the bi-layered coatings applied on both AZ31 and ZE41 alloys. An outer-most layer of collagen or chitosan was deposited onto the sol-gel coated AZ31_S and ZE41_S conditions by the dip-coating technique. The bi-layered samples with collagen are denoted as AZ31_SC and ZE41_SC (SC: sol-gel + collagen) and with chitosan as AZ31_SK and ZE41_SK (SK: sol-gel + chitosan). The corrosion behavior of all surface conditions was characterized by EIS in both SBF and DMEM with 10% fetal calf serum, 100 units ml⁻¹ penicillin, 100 µg ml⁻¹ streptomycin and 0.25 µg ml⁻¹ fungizone, however, it will be referred only as DMEM henceforth. The experiments were performed at 37 ± 1°C for 7 weeks. The influence of the electrolyte composition on the corrosion response of bi-layered and uncoated samples is discussed and correlated with the nature of the corrosion products and the corrosion mechanisms. Additional characterization of bi-layered alloys by localized electrochemical impedance spectroscopy (LEIS) in 0.25×SBF was performed in order to determine the role of the biopolymers on the dual-layer coatings barrier properties.

This chapter and the next chapters 11 and 12 contain unpublished work and the presented results will be submitted to a scientific journal soon.

10.1. MORPHOLOGY OF BI-LAYERED COATINGS

SEM and AFM images of the as-deposited biopolymer layers are depicted in [Fig. 10.1](#). For convenience of the reader SEM images of the as-deposited silane-TiO₂ coating are here again displayed (R_q 21.9 ± 2.1 nm). The insets in [Fig. 10.1a–b](#) show the morphology of the 12% HF pre-treated alloys surface underneath the coating with surface roughness R_q 406 ± 99 nm and 356 ± 31 nm of AZ31 and ZE41, respectively.

After deposition of collagen and chitosan layers, SEM imaging indicated that the obtained surfaces were smooth and homogeneous ([Fig. 10.1c–d](#)). The cracks in the collagen layer in [Fig. 10.1c](#) probably were formed during the vacuum conditions inherent to SEM. Topographical AFM images of chitosan and collagen layers are shown on [Fig. 10.2](#). The chitosan layer consisted of a rather smooth-homogeneous aggregation of nanoparticles with a R_q value of 1.6 ± 0.4 nm ([Fig. 10.2a](#)). Likewise, collagen layer consisted of nanomolecules agglomerations of average roughness $R_q = 6.6 ± 0.8$ nm ([Fig. 10.2b](#)). [Fig. 10.2c](#) is a phase contrast AFM image of an enlarged area in ZE41_SC that details the morphology of the nanomolecules with average size 90 nm.

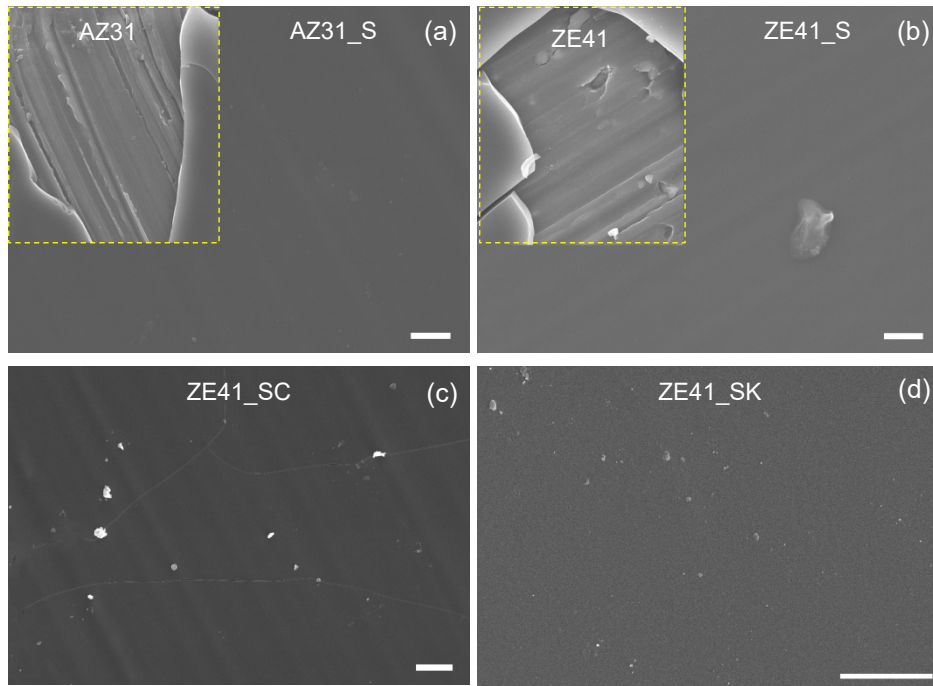


Fig. 10.1. SEM images of (a) AZ31_S, (b) ZE41_S, (c) ZE41_SC and (d) ZE41_SK. The insets in (a) and (b) show the topography of the alloys surface underneath the coating. Scale bar 10 μm .

Further imaging of the samples cross-section showed that the thickness of the bi-layered systems was homogeneous and reproducible irrespectively of the alloy. The bottom sol-gel coating was $3.3 \pm 0.2 \mu\text{m}$ -thick and the top biopolymer layers $1.3 \pm 0.1 \mu\text{m}$ -thick (Fig. 10.3).

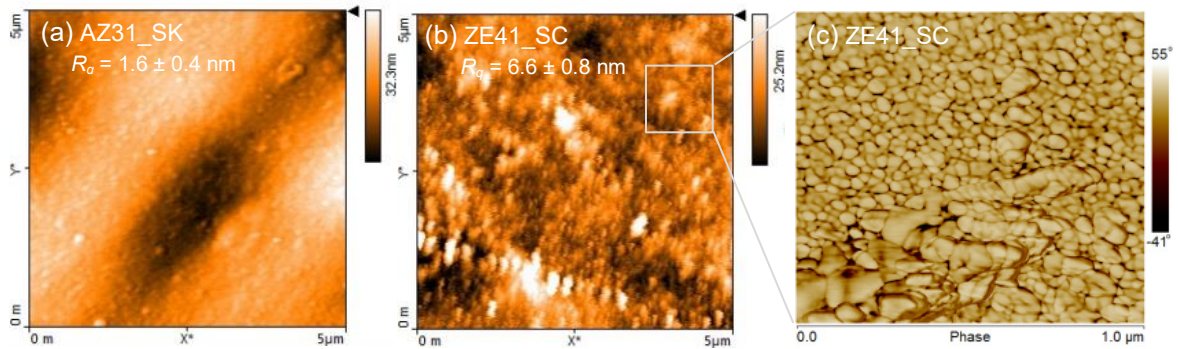


Fig. 10.2. Topographical AFM images of (a) AZ31_SK and (b) ZE41_SC and (c) phase contrast AFM image of an enlarged area in (b). R_q : surface roughness.

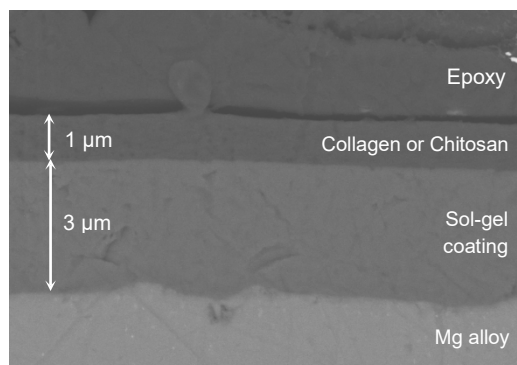


Fig. 10.3. Cross-sectional backscattered electron image of the bi-layered systems deposited on the Mg alloys.

The drop-shape analysis method was used to determine the contact angle of SBF and DMEM with different surface conditions (Fig. 10.4). Only the type I collagen layer did significantly modify the wetting behavior of the sol-gel coated alloys, leading to a sharp increase in contact angle. Other authors have already reported that type I collagen enhances surface energy and hydrophobicity of Mg alloys [142].

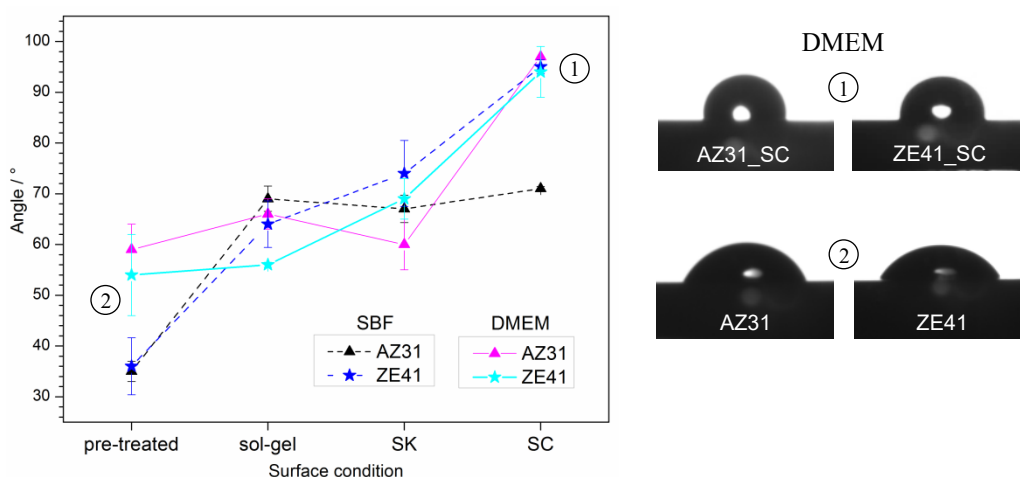


Fig. 10.4. Contact angles of SBF and DMEM with the different surface conditions. The data were recorded within first 20 s of the droplet contact with the surface. The droplets profiles are with DMEM.

10.2. CORROSION BARRIER PROPERTIES OF THE BI-LAYERED SYSTEMS

10.2.1. Corrosion behavior in inorganic SBF solution

The corrosion behavior of the bi-layered systems was characterized by EIS experiments at open circuit potential (OCP) in SBF at $37 \pm 1^\circ\text{C}$. Fig. 10.5 shows the OCP evolution of the bi-layered alloys along with representative Bode plots obtained for each condition over 7 weeks. The initial OCP of ZE41_SC is close to that of ZE41_S in Fig. 9.3 (pg. 68) remaining near constant over immersion with minor fluctuations around -1.52 V vs. SCE. On the other hand, the OCP of AZ31_SC showed a sharp increase during first 3 days and dropped again to values around -1.52 V vs. SCE after 1 week. The bi-layered conditions with chitosan AZ31_SK and

ZE41_SK exhibited a similar OCP response. The values of AZ31_SK first increased to more positive values during first 24h and next remained near stable around -1.52 V. Among all bi-layered conditions, the ZE41_SK showed the most stable response with a gradual increase from -1.56 V vs. SCE around 2h to -1.52 V vs. SCE after 1 week remaining nearly constant from there on.

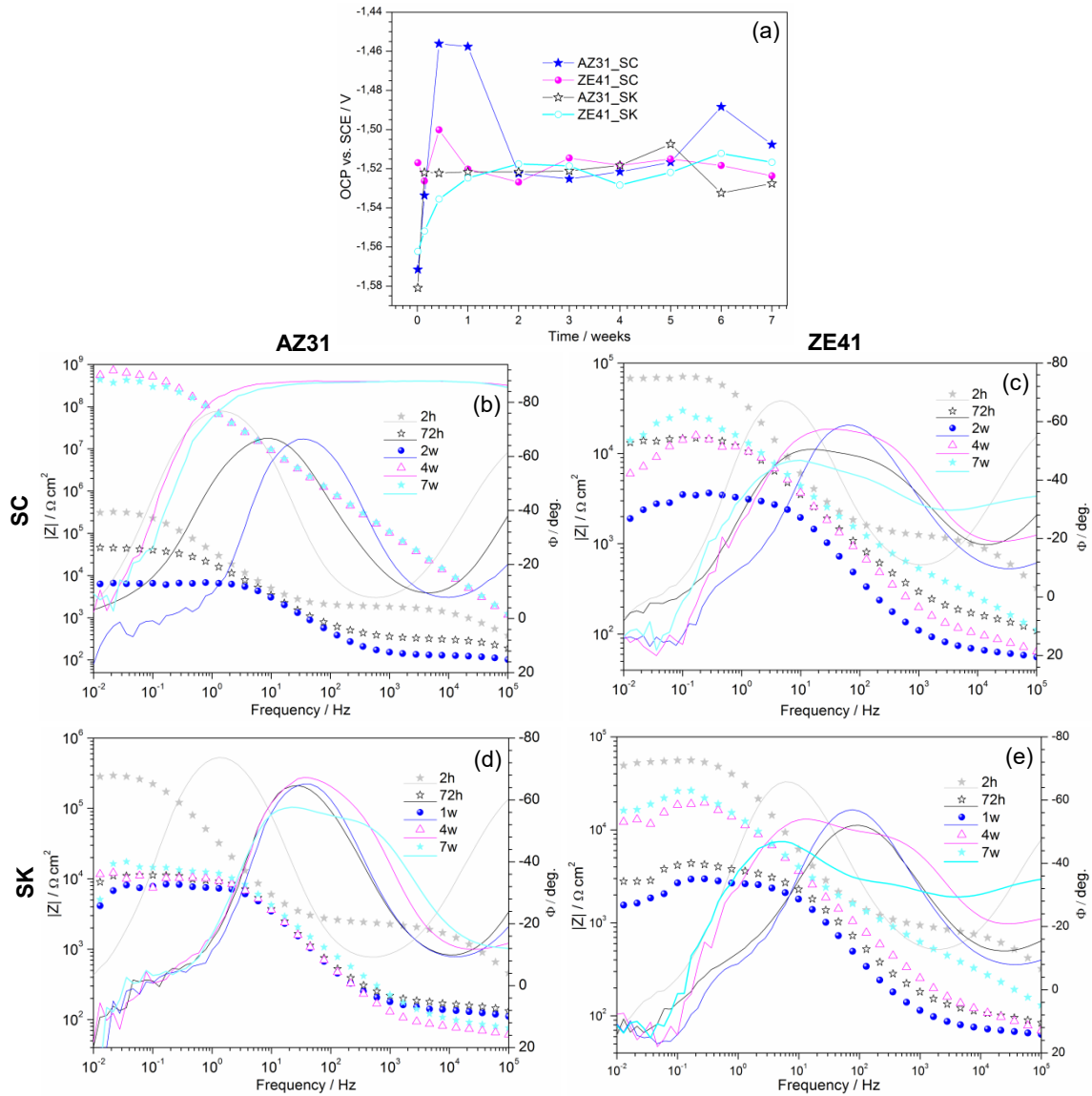


Fig. 10.5. (a) OCP evolution and bode plots of (b) AZ31_SC, (c) ZE41_SC, (d) AZ31_SK and (e) ZE41_SK immersed in SBF at $37 \pm 1^\circ\text{C}$ for 7 weeks.

At the beginning of the immersion the low frequency (10^{-2} –1 Hz) impedance values of AZ31_SC and ZE41_SC increased compared to AZ31_S and ZE41_S (Fig. 9.5, pg. 70), correspondingly. Particularly on ZE41_SC the low frequency impedance increased in about one order of magnitude ($\sim 7 \times 10^5 \Omega \text{ cm}^2$), suggesting that the collagen layer provide additional protection to the ZE41 alloy. This is in agreement with the results in Fig. 10.4 were a high SBF contact angle with ZE41_SC ($95 \pm 1.4^\circ$) was observed.

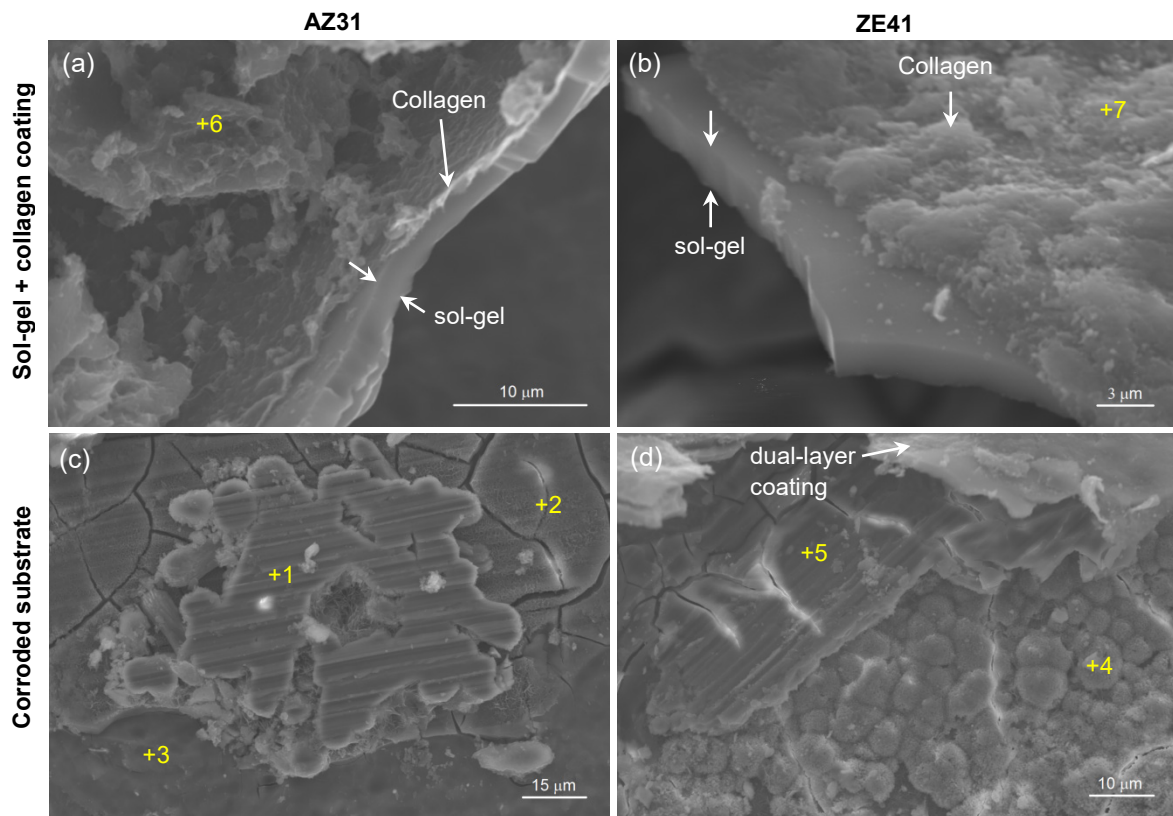
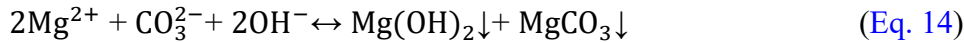
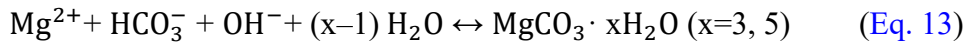
As immersion elapsed some differences on the corrosion response of AZ31_SC and ZE41_SC at advanced immersion times were observed. First, low impedance values gradually decreased between 2h and 2 weeks. The sol-gel/collagen (SC) coating response was similar on both alloys (Fig. 10.5b–c). However, after 4 weeks impedance of AZ31_SC sharply increased in about four orders of magnitude to values $\sim 5 \times 10^8 \Omega \text{ cm}^2$. This effect is attributed to the formation of the layer of corrosion products. The shape of the impedance plot and the high frequency (10^3 – 10^5 Hz) phase angle value close to -90° of AZ31_SC (Fig. 10.5b), indicate that the corrosion layer behaves closer to an ideal capacitor. In the case of the corrosion layer of ZE41_SC, the impedance modulus measured after 4 weeks ($\sim 6 \times 10^4 \Omega \text{ cm}^2$) suggests that it is much less protective than the corrosion layer of AZ31_SC.

Fig. 10.6 shows some SEM micrographs and EDX analysis of selected regions of AZ31_SC and ZE41_SC samples after 7 weeks in SBF. Deep corrosion attack is observed on both AZ31_SC and ZE41_SC. The cracks observed in Fig. 10.6b-c resulted from the shrinkage of the corrosion layers during dehydration as well as the vacuum atmosphere inside the SEM chamber. The EDX results suggest that the corrosion products of AZ31_SC are composed by: (i) an inner-most layer probably of magnesium hydroxide and magnesium carbonate ($\text{Mg}(\text{OH})_2/\text{MgCO}_3$) with some Al and Zn content (Fig. 10.6c, point 3); (ii) an intermediate layer with the same components above-mentioned; however, reduced Mg content and increased C and O content (Fig. 10.6c, point 2). Low quantities of Ca, P and Cl were detected in this layer too; (iii) on top of the intermediate layer islets of Ca-O-C aggregates probably CaCO_3 randomly distributed over the surface (Fig. 10.6c, point 1). The gradient of composition of the corrosion products inwards into the substrate may be the reason for the differences in morphology observed. The inner-most layer seems to be quite dense with little number of cracks (Fig. 10.6c, point 3) while the intermediate layer seems to be brittle (Fig. 10.6d, point 2). This outcome will not be here discussed since it is out of the scope of this work; however, it is recommended to consider characterizing the corrosion layer in terms of mechanical properties since in the real situation the Mg implant will be under load-bearing conditions while corrosion degradation occurs. The gradient of composition will then result in a gradient of properties in the corrosion layer.

It has been already discussed by other authors [60] that Al-containing Mg alloys when corroding can form Al_2O_3 into the corrosion products layer. Despite some Al was detected on the corrosion layer of AZ31_S, the O/Al ratio is too high for considering that Al_2O_3 was formed. As the corrosion products film can growth inwards into the substrate, the alloying elements can be entrapped within the corrosion products [80]. Other authors have reported formation of $\text{Al}(\text{OH})_3$ together with Al_2O_3 into the corrosion products of Al-rich Mg alloys [194].

Zeng et al. [178] investigated the corrosion evolution of the AZ31 alloy in saline solutions with additions of Cl^- , HCO_3^- , HPO_4^{2-} and SO_4^{2-} ions. They proposed a six steps

model involving $Mg(OH)_2$ and $MgCO_3$ formation mechanisms into the corrosion film of the alloy: (i) first, the electrochemical dissolution of Mg and donation of electrons (Eq. 8, pg. 75) and (ii) the water-induced decomposition by electron capture and H_{evo} (Eq. 6, pg. 75) take place; (iii) next, the hydrolysis of HCO_3^- followed by (iv) the formation of $MgCO_3$ as follows [178]:



Elemental composition, atomic %

EDX	Mg	C	O	Ca	P	Cl	Al	Zn
Point 1	11.53	37.46	58.61	29.45	–	0.42	–	–
Point 2	15.27	37.12	43.41	0.12	0.56	1.61	1.68	–
Point 3	45.27	33.01	20.28	–	–	–	1.12	0.33
Point 4	7.68	29.34	52.75	10.12	–	–	–	0.11
Point 5	16.66	21.30	42.52	16.64	0.49	0.35	–	0.53
Point 6 ^a	14.52	32.71	50.81	–	0.17	1.02	0.65	0.12
Point 7 ^b	9.27	42.83	41.18	1.36	1.12	0.14	–	0.24

^aSi 0.42, Ti 2.24; ^bSi 2.21, Ti 1.57

Fig. 10.6. Morphology of the sol-gel+collagen coatings (a),(b) and the corroded surfaces of (c) AZ31_SC and (d) ZE41_SC, respectively, after EIS experiments in SBF at $37 \pm 1^\circ C$ for 7 weeks and EDX results.

(v) during this period $[Mg^{2+}]$ and $[OH^-]$ continuously increase while $[HCO_3^-]$ decreases and, consequently, only $Mg(OH)_2$ forms (Eq. 9, pg. 75) [178]; (vi) finally, the dissolution of $Mg(OH)_2$ through the reaction with chloride according to the next reaction [178]:



At the beginning of the immersion the coating hinders the electrolyte to reach the underlying substrate with a low electrolyte uptake rate. At this point, the amount of Mg^{2+} and OH^- is relatively low. As immersion elapses the quantity of Mg^{2+} increases until the saturation point, which indicates the precipitation of Mg(OH)_2 [178]. In solutions containing HCO_3^- ions, magnesium carbonate species are more stable than Mg(OH)_2 which preferentially leads to the precipitation of magnesium carbonate hydrates [178]. However, Mg(OH)_2 and MgCO_3 have similar solubilities, which means that they can be formed simultaneously through the reactions described in Eq. 14 [178].

Since the presence of C was not detected on the corrosion layer of neither AZ31_S nor ZE41_S as evidenced from the EDX results in Table 9.1 (pg. 71), it may be presumed that collagen layer change the amount of HCO_3^- ions present in solution probably due to collagen hydrolyzation. Xin et al. [195] investigated the influence of aggressive ions on the corrosion behavior of biodegradable Mg alloys in physiological environment. They stated that HCO_3^- ions can stimulate corrosion of Mg alloys during early immersion but also induce rapid surface passivation due to the precipitation of MgCO_3 in the corrosion products that can subsequently inhibit pitting corrosion [195]. The latter may explain the high impedance value of AZ31_SC after 4 weeks of immersion (Fig. 10.5b). SBF solution has a HCO_3^- ion concentration of 4.1 mmol/L [196]; for $[\text{HCO}_3^-] > 12$ mmol/L a precipitated film of MgCO_3 can inhibit pitting corrosion of Mg [178]. Whether collagen hydrolyzation potentially increases the HCO_3^- ions concentration in solution, it may promote the formation of a compact layer of MgCO_3 . This layer would efficiently isolate the Mg alloy surface from the electrolyte resulting in the high impedance modulus of AZ31_SC from 4 to 7 weeks. SEM observations confirmed that the morphology of this inner-most layer of $\text{Mg(OH)}_2/\text{MgCO}_3$ was quite homogeneous with no signs of pitting.

The corrosion products of ZE41_S consisted of (i) an inner-most layer of probably calcium carbonate (CaCO_3) sphero-aggregates with some Mg content (Fig. 10.6d, point 4) and (ii) a rather smooth outer-most layer of probably $\text{Mg(OH)}_2/\text{MgCO}_3$ with some traces of P, Cl and Zn (Fig. 10.6d, point 5). As in the case of AZ31_SC, the high C content detected in the ZE41_SC corrosion products is expected to come from the collagen layer. Retting et al. [197] demonstrated that during corrosion degradation of a Mg-RE alloy in modified SBF (m-SBF) a considerable fraction of Ca was replaced by Mg in the corrosion layer. This may explain the Mg content in the CaCO_3 spheroaggregates of ZE41_SC. Jamesh et al. [177] investigated the corrosion behavior of CP-Mg and a ZM21 (2 wt.% Zn, 0.81 wt.% Mn) Mg alloy in Ringer's solution for 92h. They found the aragonite form of CaCO_3 in the corrosion products of both CP-Mg and ZM21. Other authors have discussed that CaCO_3 is the predominant product under stable temperature conditions and around pH values of 11 [198].

The pH evolution determined by SIET reported in chapter 9.6, showed that the pH around the artificial defect of ZE41_S reached maximum values of ~ 8.0 (Fig. 9.13, pg. 82). However, in the buried areas where the substrate is not in direct contact with the electrolyte the pH is expected to reach much higher values. By performing additional pH monitoring of uncoated pre-treated disc of both AZ31 and ZE41 alloys over 7 weeks in SBF at $37\pm 1^\circ\text{C}$ we corroborated that both conditions reached pH values higher than 10 after 1 week of immersion (not shown).

Uan et al. [199] suggested that the growth of CaCO_3 on the surface of Mg alloys occurs in two-stages: (i) lateral growth of the CaCO_3 layer to form a thin continuous film and (ii) thickening of the CaCO_3 layer. By performing a detailed characterization of the corrosion product layer formed on CP-Mg and ZM21 Jamesh et al. [177] demonstrated that the first and the second stage of CaCO_3 growth occurred on the ZM21 alloy whereas thickening is delayed for CP-Mg. This may be an indication that Zn influences precipitation and growth of CaCO_3 during the first stages of immersion. The lower Zn content of AZ31 in comparison to ZE41 along with the presence of Al in larger amount than Zn can promote formation of different constituents into the corrosion product layer, as discussed above. It is worthy of notice that the two Mg alloys here studied have different microstructures (see Fig. 9.1, pg. 66), particularly the ZE41 alloy has a complex one. The intermetallic phases have different corrosion potentials in respect to the matrix resulting in different dissolution rates on different spots of the surface and thus can form different oxide/hydroxide layers. It is known that corrosion layers formed on the surface of different phases of Mg alloys by standard electrolytes—such as NaCl—have different compositions [197]. In our study, besides using an electrolyte with complex composition the corrosion tests duration was considerably much longer than the ones found in literature which are commonly less than a week. Williams et al. [79] demonstrated that local current density distributions of anodic and cathodic reactions on pure Mg are time-dependent which is in agreement with our results (chapter 9.6). Furthermore, Jamesh et al. [177] stated that the corrosion layer composition of a rare-earth containing Mg alloy change over time. They performed corrosion test for no longer than 120h.

SEM micrographs in Fig. 10.6a-b show the surface morphology of the coatings with collagen after EIS experiments in SBF for 7 weeks. Mg, C and O were detected on the coating surface of both conditions (Fig. 10.6, point 6 & 7). In the case of ZE41_S some Ca and P were detected too. EDX results suggest that the deposits are probably MgCO_3 -collagen composites. Yamasaki et al. [38] synthesized functionally graded carbonate apatite containing Mg (FGMgCO_3Ap) mixed with collagen in order to investigate its biological properties for bone substitutes applications. Their results demonstrated that the synthesized FGMgCO_3Ap had similar crystallographic properties to that of bone, i.e. poorly crystallized. Mg is found to retard the crystallinity and increases the solubility of hydroxyapatites [38]. It may be

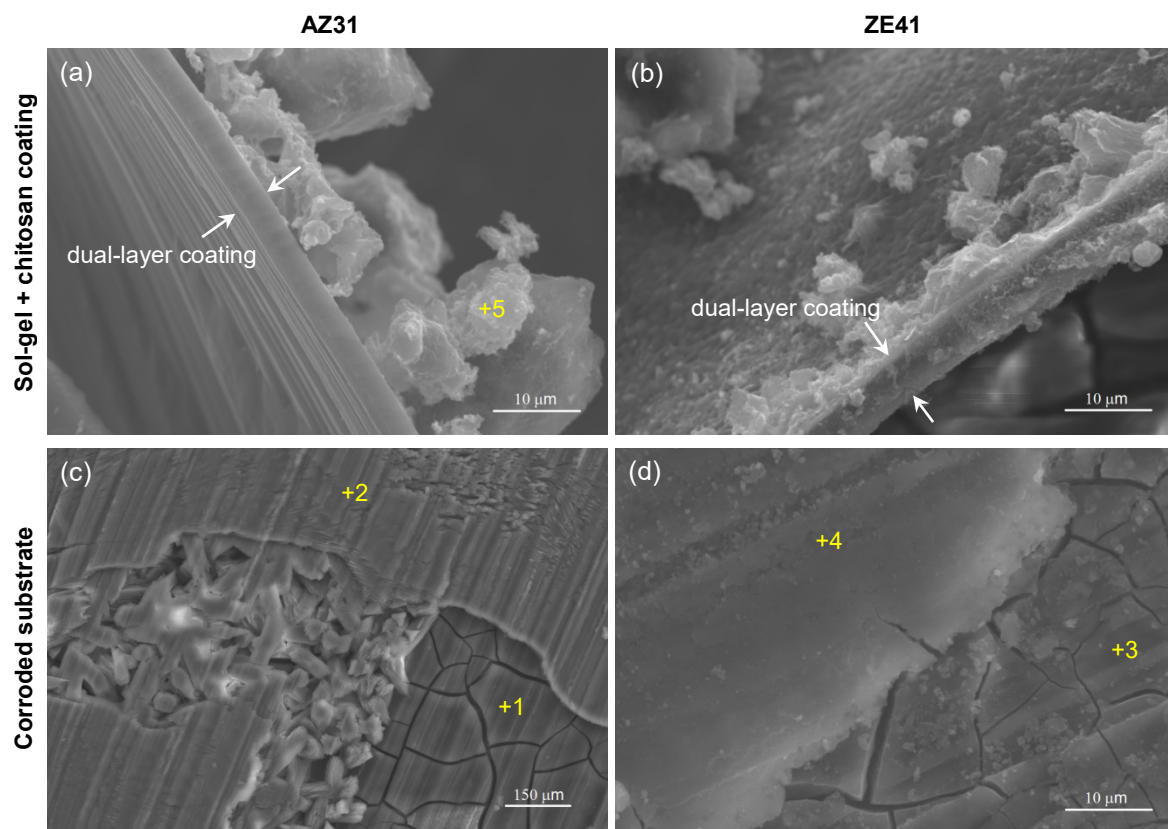
presumed that the Mg^{2+} ions in solution that come from the substrate dissolution are adsorbed onto the surface of the coating to form $MgCO_3$. Yamasaki et al. [38] also demonstrated that modified gradational Mg^{2+} ions on the apatite crystals mixed with collagen ($MgCO_3$ Ap-collagen) improved osteoblast adhesion in respect to the same composite without Mg (CO_3 Ap-collagen). Thus, precipitation of $MgCO_3$ on the coating surface of AZ31_SC and ZE41_SC may signify good adhesion of osteoblasts onto these layers.

The Bode plots of AZ31_SK and ZE41_SK in Fig. 10.5d–e show that the chitosan layer does not have a detrimental effect on the barrier properties of the silane/ TiO_2 coating on both alloys. Indeed, chitosan increased low frequency impedance of AZ31_SK after 2h compared to AZ31_S for the same immersion time (Fig. 9.5a, pg. 70). Afterwards, impedance of AZ31_SK decreased to $\sim 10^4 \Omega \text{ cm}^2$ and remained almost constant until week 7th. In the case of ZE41_SK, it showed similar behavior than ZE41_SC as observed in Fig. 10.5e.

The Bode plot in Fig. 10.5d showed different corrosion response of AZ31_SK as compared to AZ31_SC. Similar to the collagen layer, the chitosan provided additional corrosion protection to the AZ31 alloy increasing the low frequency impedance modulus in almost one order of magnitude ($\sim 3 \times 10^5 \Omega \text{ cm}^2$) around 2h. However, there are some differences in the corrosion evolution of both AZ31_SK and AZ31_SC. After 2h of immersion, the low frequency impedance modulus of AZ31_SK dropped to $\sim 10^4 \Omega \text{ cm}^2$ remaining stable around this value for the rest of the experiment. This is in close agreement with the OCP evolution for the referred condition, as depicted in Fig. 10.5a.

In the case of ZE41_SK there were not significant differences in the corrosion evolution compared to its analogous condition with collagen. The ZE41_SK impedance modulus at low frequency decreased from $5 \times 10^4 \Omega \text{ cm}^2$ to $3 \times 10^3 \Omega \text{ cm}^2$ during first 3 days and then increased to $\sim 10^4 \Omega \text{ cm}^2$ after 4 weeks, remaining stable until the end of the immersion.

EDX analyses of the SK conditions revealed the nature of the corrosion products. Fig. 10.7c-d depict the morphology of the corroded substrates after 7 weeks in SBF. The chemical analyses suggested that corrosion products of AZ31_SK are formed by: (i) a bottom layer of $Mg(OH)_2/MgCO_3$ and (ii) a top layer of $CaCO_3$. This top layer was not continuous and covered a very small fraction of the overall surface (Fig. 10.7c, point 2). On the other hand, EDX results suggested that the corrosion products of ZE41_SK consisted of a layer of combined $Mg(OH)_2/MgCO_3$ with decreasing Ca and P content and increasing Cl content outwards the surface. The latter may indicates that the corrosion layer of ZE41_SK gradually dissolves through the reaction in Eq. 15 to transform into $MgCl_2$. The high C content is presumed to come from the chitosan layer in the same way than the samples with collagen.



Elemental composition, atomic %								
EDX	Mg	C	O	Ca	P	Cl	Al	Zn
Point 1	22.10	32.06	43.00	–	0.12	0.98	1.61	–
Point 2	0.46	31.95	49.32	18.27	–	–	–	–
Point 3	14.06	42.18	40.17	1.09	1.76	0.23	–	0.40
Point 4	18.49	38.29	42.59	0.10	0.16	0.38	–	–
Point 5	11.35	33.99	50.05	0.82	1.04	0.94	0.96	–

Fig. 10.7. Morphology of corroded (a),(c) AZ31_SK and (b),(d) ZE41_SC after EIS experiments in SBF at $37\pm 1^\circ\text{C}$ for 7 weeks and EDX results.

SEM observations revealed precipitation of probably MgCO_3 onto the dual-layer coatings with chitosan for both tested conditions (Fig. 10.7a-b). Formation of MgCO_3 may be explained by the same mechanisms already described in the cases with collagen.

XRD and Raman measurements were performed in order to detail the composition of the corrosion products. With XRD technique only peaks from the Mg substrate were detected for all tested conditions. With Raman technique no evident peaks were detected. The above mentioned suggest that the corrosion layers formed on the alloys are predominantly amorphous. Another method is needed to verify the composition of the deposits in the corrosion layers. Fourier transformed infrared spectroscopy (FTIR) could be used, however, it should be considered that diatomic ions such as Mg^{2+} and Ca^{2+} are not detectable with IR-techniques as they are not excited by IR light [197]. Retting et al. [197] systematically explored the nature of the corrosion layers on a Mg-RE alloy formed in different electrolytes. Their results showed that the most realistic simulated body fluids lead to formation of amorphous corrosion product layers. Moreover, by using less complex solutions to identify

the ions participating in the corrosion processes Retting et al. [197] demonstrated that Mg is built into all corrosion layers regardless the composition of the solution. Mg is found to retard crystallinity and enhances solubility of hydroxyapatites [38]. All the previous mentioned is in close agreement with our findings for both uncoated and coated alloys.

There are two relevant statements declared by Retting et al. [197] in their paper: (i) *Ca ions are only precipitated together with phosphates on the surface, forming calcium phosphates*; and (ii) *of course it is not possible to interpret this thickness quantitatively in these in vitro experiments, but it clearly shows that the corrosion layers formed are not protective*. The first statement is in close agreement with our findings considering that the authors studied the corrosion behavior of a bare Mg-RE alloy. In chapter 9.4, we demonstrated that CaP composites are deposited onto the corrosion products of both uncoated and coated AZ31 and ZE41 alloys and that the presence of the silane-based coating determines the Ca-to-P ratio of these composites (Table 9.1, pg. 71). However, in the case of the bi-layered alloys we found that calcium carbonate compounds (CaCO_3) are deposited onto the substrates showing that collagen and chitosan strongly influence the composition of the corrosion products. The latter should be of major importance for researchers. Since collagen is the most abundant protein in human bones it can be expected that the corrosion products of the Mg implant *in vivo* will have more complex composition than that of corrosion products of Mg assessed *in vitro* in inorganic solutions. Regarding the second statement declared by Retting et al. [197] we can say that our findings show that corrosion evolution of Mg alloys is a time-dependent process. As aforementioned, the corrosion behavior of Mg alloys depends on metallurgical factors —microstructure, processing—, on the nature of the ions and its concentration in the corrosive solution as well as on the solution pH. Furthermore, formation of the corrosion layer is the first stage of the corrosion process. The second stage is grow and densification of the corrosion layer leading to variations on its properties and hence on its protective character. In most of cases, *in vitro* corrosion test of Mg alloys are performed for short periods of time usually not exceeding more than one week. This is the case of the study made by Retting et al. [197] who evaluated *in vitro* corrosion response for 5 days.

Taken together, from the results here presented so far we can summarize the corrosion behavior of AZ31 and ZE41 alloys with the different surface conditions in inorganic SBF as follows:

- 1) Al and Zn have a stabilizing effect on the corrosion layer of AZ31 alloy. The ZE41 has lower corrosion resistance at early stages of immersion comparatively with AZ31.
- 2) For the silane/ TiO_2 coated alloys, RE elements promoted formation of a thick layer (20–40 μm) of corrosion products that provides protection to the Mg substrate in the long term —beyond 2 weeks—, however, with wide variations on the corrosion activity.

- 3) The silane/TiO₂ coating promotes the deposition of non-stoichiometric poorly crystalline hydroxyapatite in larger amount than that of the uncoated conditions.
- 4) The presence of collagen and chitosan as top-most layers strongly influences the composition of the corrosion products of both AZ31 and ZE41 alloys. Carbonated compounds such as MgCO₃ and CaCO₃ were built into the corrosion products. In the case of AZ31_SC its corrosion layer showed providing effective protection to the alloy reaching impedance values of $\sim 4 \times 10^8 \Omega \text{ cm}^2$ after week 7th, more than three orders of magnitude higher than the remaining conditions.

Then we can say that more realistic approaches aiming to elucidate corrosion degradation processes of a Mg implant are still needed. It is possible to infer that organic components of the *in vivo* body environment would redefine the corrosion behavior and hence the corrosion products of Mg alloys.

10.2.2. Localized impedance in SBF

Localized electrochemical impedance spectroscopy (LEIS) is a spatially resolved technique that allows measuring localized electrochemical activity. Samples presenting two regions with different surface coatings were prepared to determine the influence of the top-biopolymer layers on the barrier properties of the silane-based coating: (i) half of the scanned area was silane-TiO₂ coated and (ii) the other half was coated with the bi-layered system: collagen or chitosan (Fig. 8.3, pg. 60). LEIS mapping of the local admittance —inverse of impedance— were taken to monitor simultaneously the two different regions during immersion in 25% SBF at room temperature for 24h. Henceforth, samples will be referred as alloy_S/SC and alloy_S/SK alluding to the coverage of half surface with collagen or chitosan, respectively.

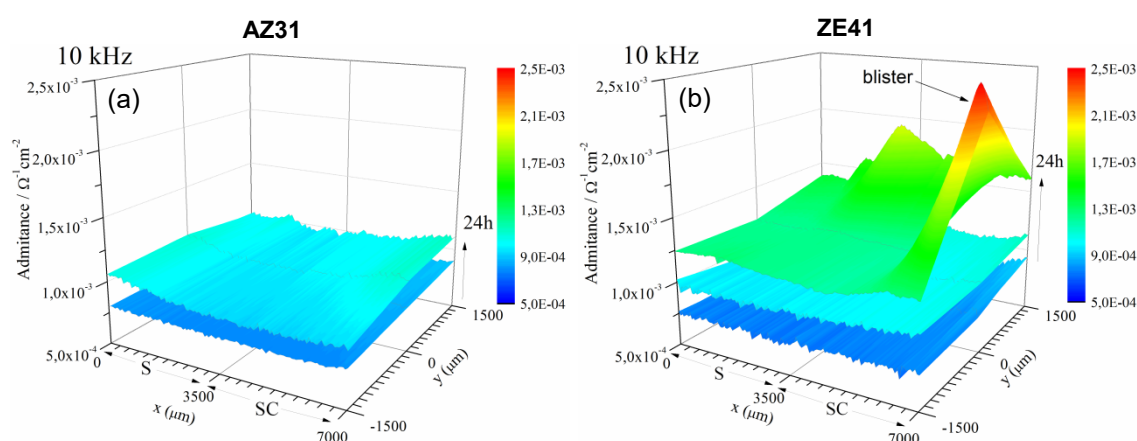


Fig. 10.8. LEIS maps for (a) AZ31_S/SC and (b) ZE41_S/SC for different immersion times in 25% SBF. Maps recorded at different time points are shifted upwards with the time progress (S: sol-gel, SC: sol-gel+collagen).

The LEIS maps in admittance mode of AZ31_S/SC and ZE41_S/SC are depicted in Fig. 10.8. The midpoint in “x” axis defines the boundary line between the two surface preparations, the silane-based coating corresponds to $0 < x < 3500$ and the silane-based + collagen to $3500 < x < 7000$.

The AZ31_S/SC sample did not show significant variations over the 24h of immersion (Fig. 10.8a). Admittance values remained nearly constant around $1 \times 10^{-3} \Omega^{-1} \text{cm}^{-2}$. Moreover, the collagen layer seemed to not induce detrimental effects on the silane-TiO₂ barrier properties since there were no apparent differences in corrosion activity between S (sol-gel) and SC (sol-gel+collagen) sides. On the other hand, ZE41_S/SC presented some changes with immersion time (Fig. 10.8). At early immersion, admittance values were $\sim 7.5 \times 10^{-4} \Omega^{-1} \text{cm}^{-2}$ over the entire scanned surface. Next, corrosion activity started to increase slowly. Admittance values slightly increased to $\sim 10^{-3} \Omega^{-1} \text{cm}^{-2}$ indicating that the coating barrier properties started to deteriorate due to coating swelling. Still, there were no evident differences in corrosion activity between S and SC side. However, after 24h corrosion activity started to increase mainly on the SC side with some new localized active areas of higher admittance. During the experiments, formation of blisters on the SC side of ZE41_S/SC was observed (Fig. 10.9a). It seemed that the collagen layer trapped the evolved H₂ gas avoiding it from being release into the solution. This phenomenon did not occur on the S side. In the neighboring of blisters (SC side) admittance values increased by a factor of 1.5 compared to the values on the S side. Fig. 10.9 shows pictures of LEIS samples with blister formation around 24h of immersion. In Fig. 10.9b it is possible to see that accumulation of H₂ gas led to local delamination of the coating increasing corrosion activity that was detected through the pores of the coating.

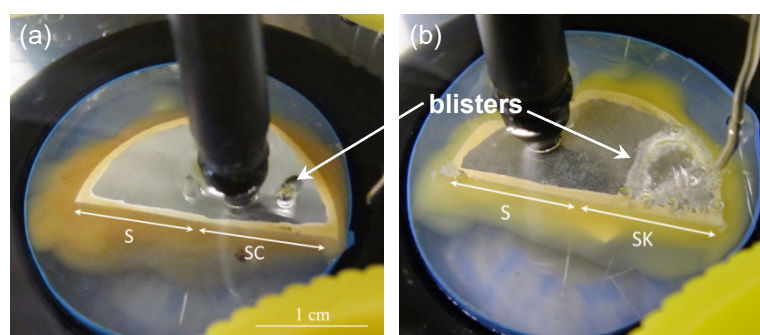


Fig. 10.9. Pictures of samples used for LEIS experiments after 24h with formation of some blisters due to accumulation of H₂ gas on the bi-layered side. (a) ZE41_S/SC and (b) AZ31_S/SK.

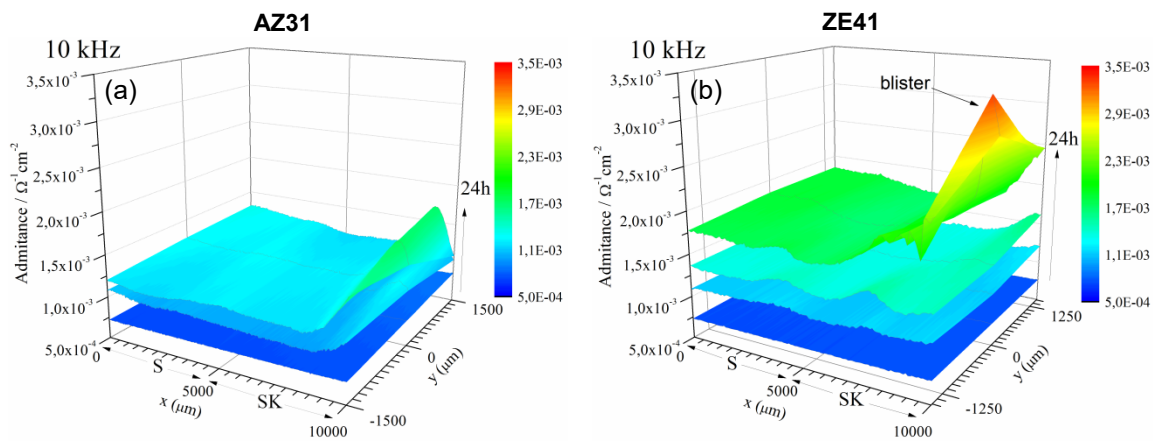


Fig. 10.10. LEIS maps for (a) AZ31_S/SK and (b) ZE41_S/SK for different immersion times in 25% SBF. Maps recorded at different time points are shifted upwards with the time progress (S: sol-gel, SK: sol-gel+chitosan).

Fig. 10.10 depicts the LEIS maps for AZ31_S/SK and ZE41_S/SK. The admittance changes of these conditions showed a trend similar to that observed with the samples with collagen. However, in the vicinity of the blister on AZ31_S/SK admittance showed increased values (Fig. 10.9b) produced by the same mechanism above discussed. In the case of ZE41_S/SK, admittance values showed the same trend as ZE41_S/SC. However, while admittance around the blister on ZE41_S/SC reached values of $\sim 2.5 \times 10^{-3} \Omega^{-1} \text{cm}^{-2}$, in ZE41_S/SK it reached values of $\sim 3.5 \times 10^{-3} \Omega^{-1} \text{cm}^{-2}$. The initial values at early immersion were $\sim 8 \times 10^{-4} \Omega^{-1} \text{cm}^{-2}$ and $\sim 7.5 \times 10^{-4} \Omega^{-1} \text{cm}^{-2}$, respectively.

From these results, it can be then considered that collagen and chitosan layers do not have a detrimental effect on the barrier properties of the silane-TiO₂ coating. In fact, collagen showed to enhance hydrophobicity of the sol-gel coating particularly on the ZE41 alloy, as evidenced from contact angle results with SBF in Fig. 10.4 (pg. 89). On the other hand, contact angle of samples with chitosan showed similar values to those of the silane-based coating. Moreover, collagen and chitosan top-layers trapped the evolved H₂ gas that with time forms gas pockets. These pockets appeared around 24h of immersion. In practical terms, this suggests that a Mg implant coated with our bi-layered system would delay hydrogen gas to be released into the body environment. Moreover, accumulation of evolved hydrogen gas would lead to a stronger alkalinization of the fluid at the substrate/coating interface which has been found to have a stabilizing effect of the corrosion products of Mg alloys. Thirumalaikumarasamy et al. [200] made an exhaustive and comparative evaluation of the corrosion behavior of AZ31B Mg alloy in NaCl solution at different chloride ion concentrations, pH values and exposure time. They reported a list of corrosion rates obtained from immersion and potentiodynamic polarization tests as a function of the above-mentioned parameters. They found that the solution pH is inversely proportional to corrosion rate of the alloy. Compared to neutral pH, lower corrosion rates of AZ31B alloy were observed in alkaline solutions [200]. Furthermore, Thirumalaikumarasamy et al. [200] reported that the

rate of corrosion slightly decreased with increasing exposure time which in turn resulted from increased H_{evo} with the exposure time. Other authors have also discussed that alkalization of the corrosive solution stabilize the formed Mg hydroxides within the corrosion layer [13].

Since hydrogen pockets were not found on the silane-TiO₂ coated side (S) in any of the samples, it is possible to presume that collagen and chitosan are responsible for the condition that promoted formation of these pockets. Some authors still argue that hydrogen evolution remains a problem during degradation of Mg alloys. However, it is necessary reasoning in terms of the targeted application. For example, hydrogen evolution in cardiovascular stents seems to be of minor importance. Some clinical studies have shown good biocompatibility with minimal inflammatory reactions and complete absorption within two months postimplantation [201]. Stents are separated from the blood stream by only thin neointimal diffusion barriers which would allow diffusion of H₂ gas out the implanted site [202]. Witte et al. [13] investigated in vivo degradation of four different Mg alloys at the bone-implant interface of guinea pigs for 18 weeks. They reported that subcutaneous gas bubbles appeared within one week after surgery and disappeared after 2–3 weeks with no adverse effect observed in the guinea pigs [13]. Hypothesizing, our bi-layered systems could delay releasing of high quantities of evolved H₂ gas from the implant into the body environment during the first hours post-implantation. Although gas pockets would provoke local delamination of the coating, the alkaline conditions would stabilize the corrosion products protecting the implant from early accelerated corrosion. Certainly, this feature would need further assessment and more detailed characterization to better explain the role of these outer coating layers.

10.2.3. Corrosion behavior in organic DMEM

Corrosion resistance of Mg and its alloys have been widely studied in several simulated body fluid solutions that contain inorganic components similar to those of human body plasma (see [Table 3.2](#)). However, body physiological media has much more complex composition than inorganic body fluid solutions making reasonable to presume that organic components such as proteins, amino acids, lipids and even cells may modify the corrosion response of Mg alloys.

In order to determine the corrosion performance of AZ31 and ZE41 alloys and the corrosion barrier properties of our coating systems in organic solutions, we performed EIS experiments in Dulbecco's modified Eagle's medium (DMEM). We reproduced the electrochemical experiments for all surface conditions of both Mg alloys under the same experimental conditions (37±1°C, 7 weeks). The final impedance Bode plots are summarized in [Fig. 10.11](#).

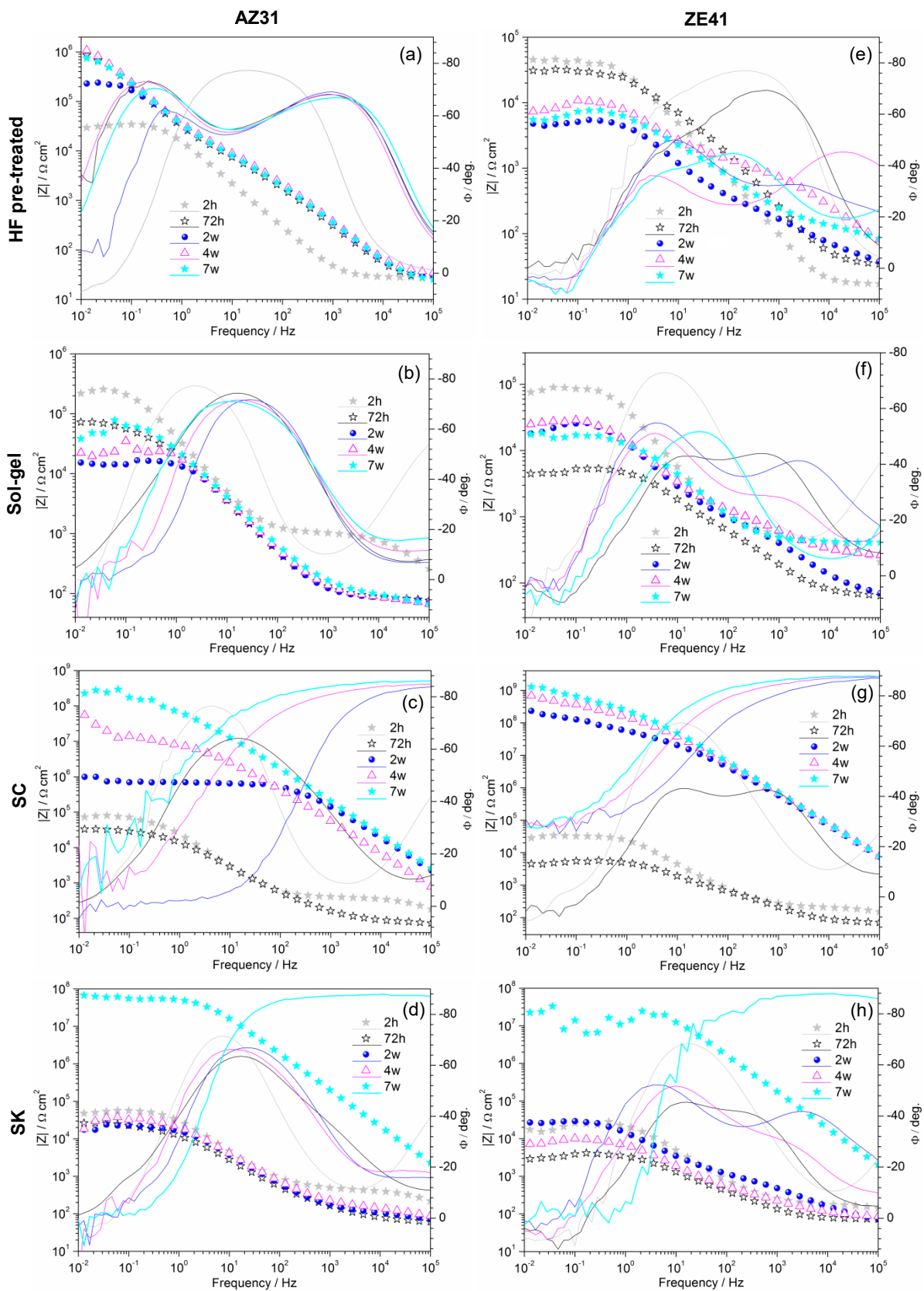


Fig. 10.11. Bode plots of the different surface conditions for both alloys immersed in DMEM at 37°C for 7 weeks. Left hand column corresponds to all surface conditions of AZ31 and right hand column to all surface conditions of ZE41. (a) AZ31, (b) AZ31_S, (c) AZ31_SC, (d) AZ31_SK, (e) ZE41, (f) ZE41_S, (g) ZE41_SC and (h) ZE41_SK.

Important differences between the pre-treated alloys were observed (Fig. 10.11a,e). The low frequency (10^{-2} - 10^{-1} Hz) impedance modulus at 2 hours of immersion was similar for both alloys ($\sim 3 \times 10^4 \Omega \cdot \text{cm}^2$). Afterwards, the impedance of AZ31 increased up to $10^6 \Omega \cdot \text{cm}^2$ from 2h to 72h and remained quite stable around this value over 7 weeks indicating the formation of a stable corrosion products layer (Fig. 10.11a). In the case of ZE41, the impedance dropped in one order of magnitude after 72h. The sharpening of the time constant around 10 Hz between 2 and 7 weeks (Fig. 10.11e) indicated the formation of a layer of corrosion products, but less protective compared to the one formed on AZ31.

The increase in the low frequency impedance values of AZ31_S and ZE41_S compared to the pre-treated samples confirmed that the sol-gel coating provided a barrier effect (Fig. 10.11b,f). Unlike to AZ31, AZ31_S low frequency impedance decreased gradually over 2 weeks. The time constant shifting toward higher frequencies indicated the deterioration of the coating barrier properties (Fig. 10.11b). The coating underwent faster deterioration on ZE41_S during the first 72h (Fig. 10.11f). Later, an increase of the impedance together with the formation of an additional time constant at middle-low frequencies (1-10 Hz) evidenced the onset and growth of a layer of corrosion products at the coating/substrate interface. Once again, the differences between AZ31_S and ZE41_S observed in Fig. 10.11b and Fig. 10.11f showed that the coating protection ability depended upon the alloy.

The Bode plots in Fig. 10.11c and Fig. 10.11g showed that the collagen layer did not have a detrimental impact on the coating barrier properties. Instead, the collagen seemed to slow down the coating deterioration. The low frequency impedance of AZ31_SC gradually increased over immersion showing very active corrosion behavior after 4 weeks. After 7 weeks, impedance reached values of more than three orders of magnitude higher ($\sim 2 \times 10^8 \Omega \cdot \text{cm}^2$) compared to values at early immersion (Fig. 10.11c). This suggested the formation of a highly protective corrosion layer on AZ31_SC, much more protective than those formed on AZ31 and AZ31_S. Similar behavior was observed on ZE41_SC, however, it seemed that growing and densification of the corrosion layer occurred faster on this condition reaching impedance values of $\sim 10^9 \Omega \cdot \text{cm}^2$ after 2 weeks (Fig. 10.11g). The ZE41_SC showed the highest impedance among all tested conditions after 7 weeks.

High impedance values were also observed on the samples bi-layered with chitosan (Fig. 10.11d,h). Low frequency impedance of AZ31_SK and ZE41_SK reached values of $\sim 7 \times 10^8 \Omega \cdot \text{cm}^2$ and $\sim 2 \times 10^8 \Omega \cdot \text{cm}^2$ after week 7th, respectively. From 2h to 4 weeks impedance modulus of both SK coated alloys remained nearly stable with minor fluctuations. The ZE41_SK still showed high corrosion activity after 7 weeks.

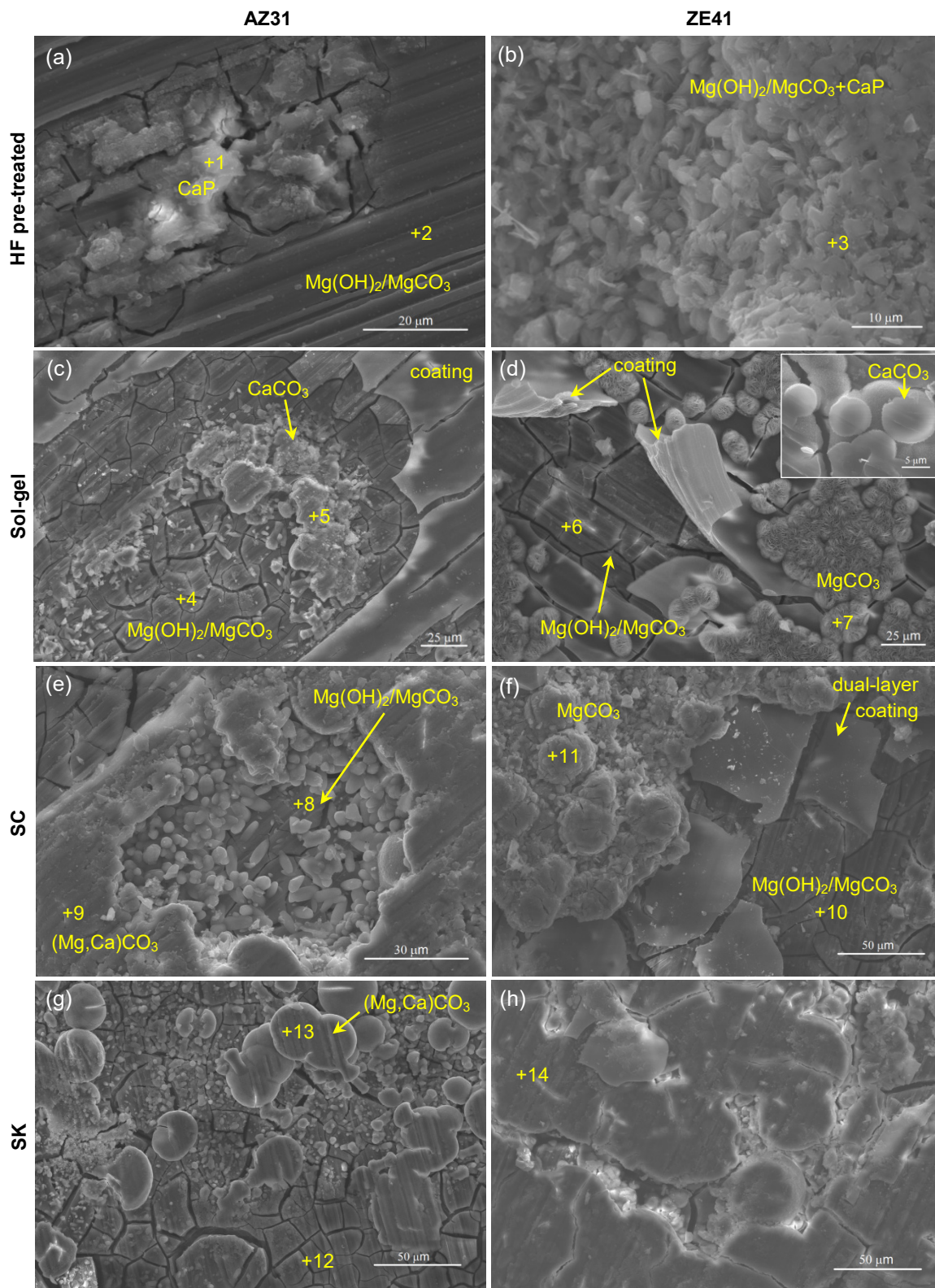


Fig. 10.12. Morphology of corroded substrates after EIS experiments in DMEM for 7 weeks at 37 ± 1°C. Left column shows all surface conditions for AZ31 (a,c,e,g) and right column all surface conditions for ZE41 (b,d,f,h). The inset in (d) shows the aggregates found on the corrosion layer of ZE41_S.

Table 10.1. Surface chemical composition of all condition after EIS experiments in DMEM at $37 \pm 1^\circ\text{C}$ measured by EDX. The points measured are indicated in Fig. 10.12.

Point	Atomic %							
	Mg	C	O	Ca	P	Cl	Al	Zn
+1	5.51	32.17	45.24	9.37	5.49	–	0.87	0.23
+2	47.73	39.43	8.40	0.61	0.73	–	0.84	0.42
+3	12.58	43.17	42.24	1.17	0.59	0.15	–	0.10
+4	17.15	20.86	56.88	2.17	–	0.50	2.15	0.27
+5	20.00	18.29	44.36	16.43	0.53	–	–	0.39
+6	19.52	16.43	58.65	0.48	0.36	–	–	1.62
+7	18.89	28.65	50.19	0.69	0.53	–	–	1.05
+8	17.46	30.67	48.46	0.62	0.23	0.21	2.03	0.26
+9	5.07	30.72	53.87	10.05	0.05	–	–	0.17
+10	16.63	24.80	56.44	0.96	0.09	–	–	1.00
+11	13.55	30.67	54.56	0.59	0.11	–	–	0.51
+12	22.78	32.06	38.00	0.44	1.08	0.25	1.84	0.43
+13	9.14	24.30	50.52	15.61	0.36	0.07	–	–
+14	14.07	34.00	50.95	0.71	0.15	–	–	0.12

Fig. 10.12 depicts the morphology of the corroded substrates for all conditions after EIS experiments in DMEM at $37 \pm 1^\circ\text{C}$ for 7 weeks. EDX results aided to interpret the composition of the corrosion products and the results are summarized in Table 10.1. From the micrographs in Fig. 10.12 and the chemical composition results in Table 10.1, it is possible to see that there are wide variety of corrosion products in terms of morphology and composition even when comparing between two different surface conditions for the same alloy. Once again, we did not succeed extracting relevant information from XRD and Raman techniques. A complete description of the corrosion products would require further characterization using additional techniques that allow determining the precise composition of the deposits. Furthermore, to the best of our knowledge there is scarce information available in literature on corrosion products and degradation of Mg alloys in such organic solutions in the long term. There is one investigation published in 2010 by Zheng et al. [203] that reported the composition of the corrosion products of Mg-Ca composites after EIS experiments in DMEM for 72h. They found that a protective surface film composed of CaCO_3 , $\text{MgCO}_3 \cdot 3\text{H}_2\text{O}$, HAP and $\text{Mg}(\text{OH})_2$ formed quickly at initial immersion stages. Additionally, they demonstrated that with increasing immersion time the surface film became compact decreasing the corrosion rate of the Mg-Ca composites around 72h [203]. In 2009, Gu et al. [204] investigated the corrosion behavior of three different Mg alloys in Hank's solution, DMEM and DMEM with additions of fetal bovine serum (FBS) for a period of 7 days. Mg-Ca, AZ31 and AZ91 alloys exhibited higher corrosion resistance in DMEM than in Hank's solution [204]. In 2013, Tang et al. [205] monitored the pH evolution of a Mg-Zr alloy coated by microarc oxidation (MAO) and electrophoresis deposition (EDP) in DMEM for 11 days. Their goal was to determine the coating with the best corrosion barrier properties through determination of OH^- concentration; however, monitoring of the corrosion evolution by electrochemical techniques or characterization of the corrosion products was not carried out.

Also in 2013, Degner et al. [206] coated 99.9% pure Mg with polycaprolactone (PCL) and characterized the corrosion behavior of coated and uncoated specimens stored up to 30 days in DMEM at 37°C by polarization curves. The aim was to investigate the protective effect of the PCL coating and to determine its long term stability as a function of the thickness [206]. In this case, the authors did not characterize the composition of the corrosion products either. In 2015, Zeng et al. [85] investigated the corrosion evolution of 99.9% pure Mg at room temperature in Hank's and 0.9 wt.% NaCl solutions with different amounts of glucose by EIS technique for a maximum period of 72h. They showed that glucose accelerates corrosion of pure Mg in saline solution, whereas lowers it in Hank's solution. According to their results, glucose promotes formation of Ca-P precipitates on pure Mg immersed in Hank's solution which can be accounted for the decreased corrosion rate [85]. Finally, Marco et al. [207] compared corrosion of Mg-Ag, Mg-Gd and Mg4Y3RE alloys with pure Mg in two different media: phosphate buffered saline (PBS) and DMEM with 5% CO₂ at 37°C for 7 days. Their work showed how much the degradation behavior of Mg and its alloys was influenced by the physiological testing environments. Under more physiological conditions —DMEM and 5% CO₂ at 37°C— all the tested alloys presented similar behavior [207]. The authors pointed out the fact that *in vitro* corrosion tests should be carried out under more realistic conditions and stressed in the importance of considering experiments in the long term.

From the chemical compositions reported in [Table 10.1](#) we can suggest that our results are in agreement with the results reported by Zheng et al. [203]. In most of cases the corrosion products seemed to be a combination of Mg(OH)₂, MgCO₃ and CaCO₃. From the micrographs in [Fig. 10.12](#) it is evidenced that corrosion products of some tested conditions are formed by several layers of variable composition. Certainly, this variability in the results demands further assessment. We consider to present detailed characterization of these complex corrosion products in future works. Henceforth, we will focus on the bi-layered alloys and will refer to the uncoated and sol-gel coated ones mainly for comparative purposes.

For a better understanding of the corrosion processes evolution, we made additional characterization of the corrosion products after week 1st of EIS experiments in DMEM. [Fig. 10.13](#) shows the morphology of the corrosion products of SC and SK bi-layered alloys. Spherical calcium phosphate (CaP) aggregates hierarchically arranged were found on the corrosion layer of bi-layered samples. These aggregates grew over a dense-homogeneous magnesium hydroxide layer rich in Ca and P, as confirmed by the EDX results (not shown). It is important to remark that CaP aggregates were found on all the coated conditions and not on the pre-treated alloys. This suggested that the silane-TiO₂ coating promoted the formation and growth of CaP aggregates in DMEM.

Kokubo [191] described the mechanisms of bone-like apatite formation on metallic surfaces. The author discussed that metals with suitable surface treatments may form a dense-uniform apatite layer on their surfaces in acellular simulated body fluids with ion

concentrations similar to those of human bone plasma [191]. On the other hand, some bioceramics have shown bonding to living bone through an apatite layer formed on their surfaces induced by the presence of Si-OH group [191].

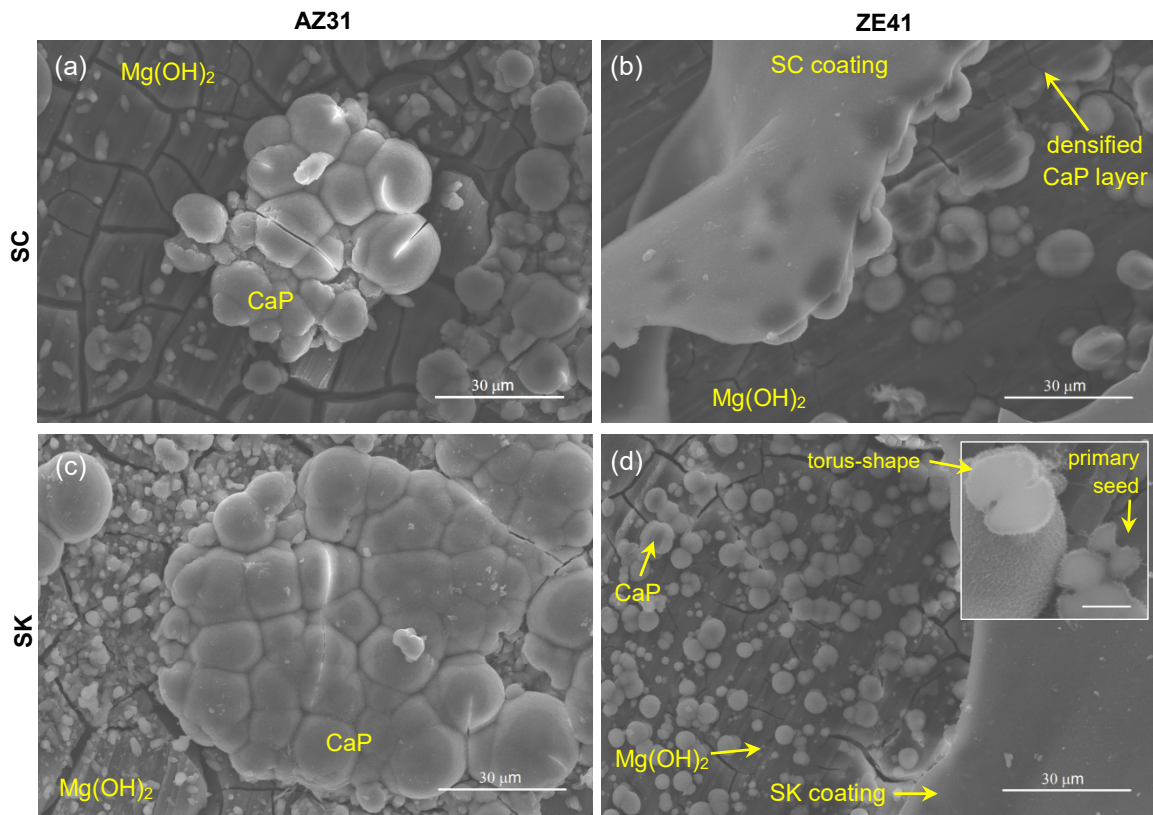


Fig. 10.13. SEM images of the corrosion products layer of (a) AZ31_SC, (b) ZE41_SC, (c) AZ31_SK and (d) ZE41_SK after 1 week of EIS experiments in DMEM at $31 \pm 1^\circ\text{C}$. The inset in (d) shows the cross-section of a sphero-aggregate and a primary seed (scale bar: $2.5 \mu\text{m}$).

In the present case, Si-O-metal bonds are responsible for the adhesion of the silane-TiO₂ coating to the substrates. As immersion time elapses, the electrolyte solution gradually permeates the coating reaching the underlying metal. When it reaches the metallic surface, Mg cations form at the anodic sites, while OH⁻ ions are released from the cathodic sites according to anodic and cathodic reactions (pg. 75), respectively. Hydrated silica has shown to have a catalytic effect for apatite nucleation on its surface in SBF as demonstrated by observations on pure silica gel prepared by a sol-gel method [191]. In addition to silica gels, sol-gel derived titania coatings were also found to induce apatite nucleation [208]. Then, in terms of surface chemistry the hybrid silane-TiO₂ coating seems to provide suitable conditions for apatite nucleation, as observed in Fig. 10.13. In addition, Zeng et al. [85] demonstrated that glucose promotes formation of spherical-shaped CaP precipitates on the surface of pure Mg immersed in Hank's solution due to the fact that glucose coordinates Ca²⁺ ions in this solution.

The inset in Fig. 10.13d shows the cross section of an individual sphero-aggregate. The torus-shaped morphology is characteristic of fractal growth that initially takes place at the ends of a primary seed. Gobél et al. [209] investigated the morphological development of CaP-gelatine composite aggregates by double diffusion of calcium- and phosphate/fluoride-solutions into a tube filled with gelatin gel. They performed 2D-simulations of the aggregates upgrowth and achieved a fractal growth model. The equatorial notch of the spheres becomes less dominant as the spheroaggregates growth which was clearly supported by experimental observations [209].

Raman results of the corrosion layer of ZE41_SC after week 1st of immersion confirmed that the CaP formed corresponds to hydroxyapatite (HAP, $\text{Ca}_5(\text{PO}_2)_3(\text{OH})$). The peak around 440 cm^{-1} in Fig. 10.14 represents the double degenerate bending mode of O-P-O bond of the free PO_4^{3-} group (ν_2). The characteristic PO_4^{3-} band (ν_1) of hydroxyapatite (HAP) appeared about 950 cm^{-1} . This peak represents the symmetric stretching mode of the P-O bond. Variations of the band around 950 cm^{-1} such as broadening, are normally associated to poorly crystalline samples since this peak represents the grade of crystallinity of the material [210,211]. In the present case, EDX results (not shown) revealed that the spheroaggregates in Fig. 10.13 have Mg and Zn content. Non stoichiometric CaPs can be obtained in the presence of foreign ions [210] e.g. carbonates, chlorides and oxides, among others. Then CaPs that exhibit many different ions substitutions and vacancies can alter the regularity of the lattice and cause variations in the Raman spectra, as observed in Fig. 10.14. The other two vibrational frequencies of the PO_4^{3-} of HAP were detected at $\nu_3 \approx 1080\text{ cm}^{-1}$ and $\nu_4 \approx 560\text{ cm}^{-1}$.

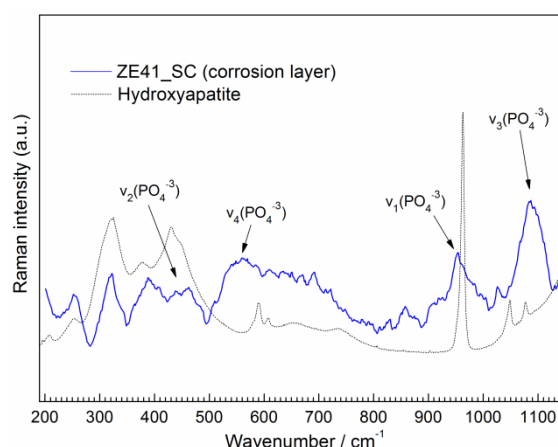


Fig. 10.14. Raman spectra of the corrosion layer of ZE41_SC after 1 week of EIS experiments in DMEM compared to RUFFTM pattern [179] of hydroxyapatite (Ref. 060180).

Other authors have also discussed the crystallinity and morphological variations of HAPs depending upon precipitation conditions such as reaction temperature and reaction pH [211]. Local alkalinization at the coating/substrate interface is expected to increase the ion

strength of the solution inducing nucleation and growth of the CaP aggregates. Yang et al. [212] investigated the formation process of apatite on the Mg-7Zn-2Ca alloy focusing on the effect of H₂ gas bubbles. Nucleation and growth of CaP coatings was explored by immersing the Mg alloy in supersaturated calcification solutions (SCSs) with different concentrations of Cl⁻ which could adjust the hydrogen evolution (H_{evo}). Nucleation of flower- and grass-like CaP compounds occurred next to H₂ bubbles and it was controlled by the number of pores formed during H_{evo}. The structure and morphology of the CaP coatings on the Mg-7Zn-2Ca alloy was adjusted by controlling the Ca-to-P ratios in the SCSs [212]. Furthermore, the authors detected the incorporation of Mg into the components of the deposited CaP coatings.

Our results evidenced that the composition of the corrosion layers of AZ31 and ZE41 Mg alloys with the different surface conditions varied with the immersion time. Initially, Mg(OH)₂ and non-stoichiometric HAP were the main corrosion products; nevertheless, as immersion time elapsed they transformed into magnesium carbonates and calcium carbonates compounds. Moreover, crystallinity of the corrosion layers decreased with increasing immersion time. After 7 weeks of immersion in DMEM, XRD measurements (not shown) of all tested conditions indicated that the corrosion layers have predominantly amorphous structure since only peaks from the Mg substrate were detected. Furthermore, densification and thickening of these layers were observed after 7 weeks [Fig. 10.12](#). These structural variations of the corrosion layers were reflected in the EIS results with high impedance values at advanced stages of immersion, particularly in case of the bi-layered alloys with both collagen and chitosan biopolymers ([Fig. 10.11](#)).

To further elucidate the corrosion mechanisms of the coated alloys we performed numerical modeling of the EIS data. We are going to focus on the conditions that exhibited the best corrosion behavior, that is to say the bi-layered samples with silane-TiO₂+collagen. The detailed analysis of the corrosion processes is presented in the next section.

10.2.3.1. Corrosion modelling of silane/TiO₂+collagen coated alloys

To detail the corrosion mechanisms numerical fitting of the EIS data was carried out using the equivalent circuits depicted in [Fig. 10.15a](#). We are going to focus on fitting AZ31_SC and ZE41_SC results since these conditions were the ones with the best corrosion results showing the highest impedance values. Constant phase elements (CPE) accounting for the behavior of the electrode were used instead of pure capacitors. Three time constants were assigned to the equivalent circuits in [Fig. 10.15a](#): (i) one at high frequencies describing the barrier properties of the bi-layered coating; (ii) a second one in the middle frequency range describing the properties of an interfacial layer that may include the insoluble corrosion products and, a third one assigned to the corrosion activity. The χ^2 of the regression was around 10⁻³.

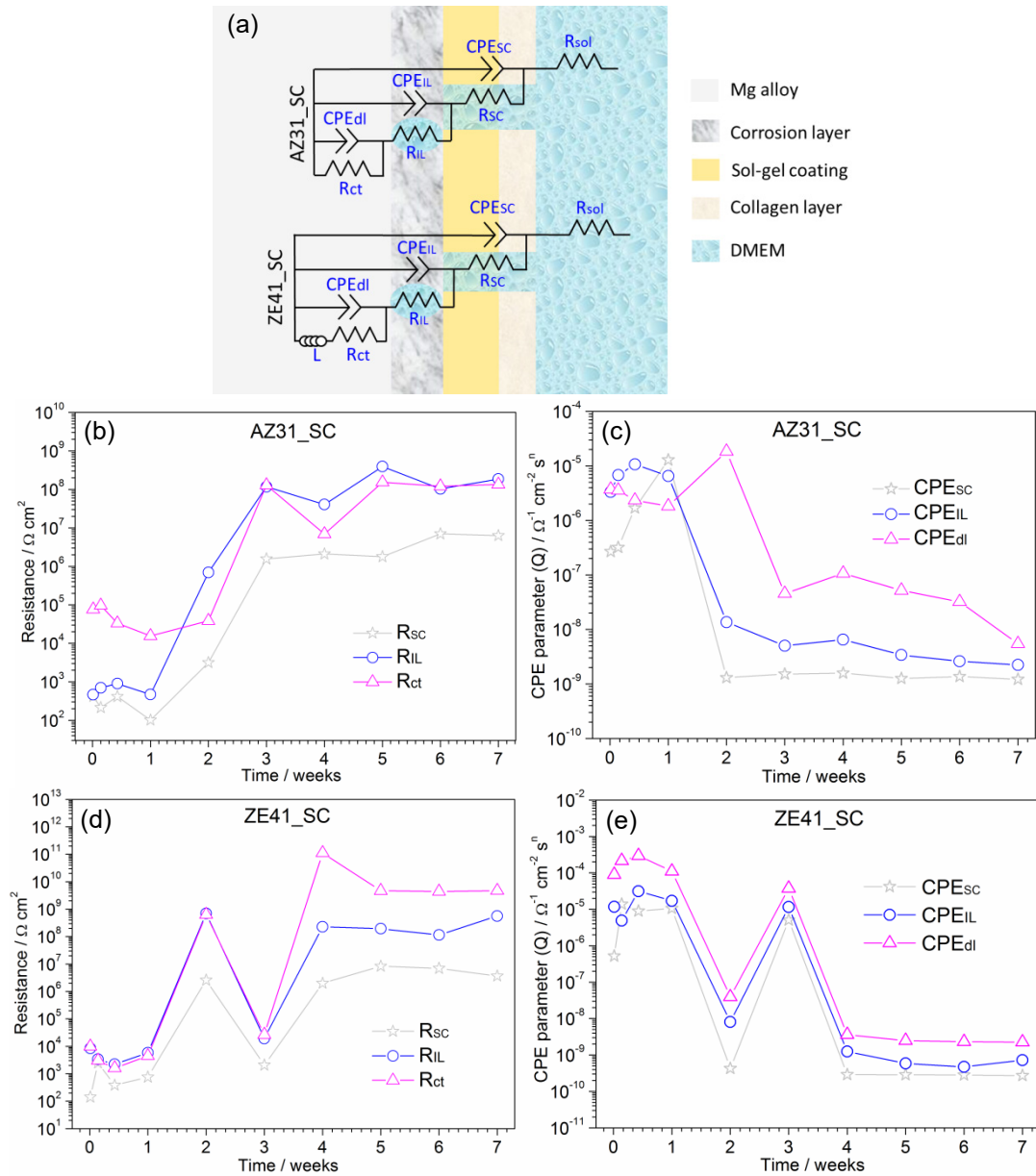


Fig. 10.15. (a) Equivalent circuits used to fit EIS data of AZ31_SC and ZE41_SC and values extracted from the fitting. (b),(d) show evolution of resistance and (c),(e) CPE parameter Q for AZ31_SC and ZE41_SC, respectively.

In Fig. 10.15b and Fig. 10.15d R_{SC} and R_{IL} account for the resistance of the electrolyte inside the coating pores and for the resistance of the corrosion layer, respectively. Likewise, CPE_{SC} accounts for the capacitive response of the sol-gel+collagen coating and CPE_{IL} for the capacitive response of the corrosion layer. The barrier properties of the bi-layered coatings can be then characterized by R_{SC} and CPE_{SC} .

During first 24h of immersion R_{SC} of both AZ31_SC and ZE41_SC increased but after 1 week R_{SC} gradually decreased, probably due to formation of pores and coating damage. In parallel, CPE_{SC} of both bi-layered alloys increased. A decrease in R_{SC} along with an increase in CPE_{SC} indicates that the coating barrier properties deteriorate and its protective character

decreases. The values of the Q parameter for CPE_{SC} were $0.65 < n < 0.97$ for ZE41_SC (Fig. 10.15e). The evolution of the CPE_{SC} suggested that at early immersion the coating barrier properties deteriorates faster on ZE41_SC compared to AZ31_SC in which the coating seemed started to deteriorate only after 24h. Between week 1st and week 3rd, R_{SC} of AZ31_SC increased from $\sim 10^2 \Omega \text{ cm}^2$ to $\sim 10^6 \Omega \text{ cm}^2$. This suggests that during this period precipitation/accumulation of corrosion products sealed the pores of the coating blocking the pathways through which aggressive ions were able to reach the substrate, resulting in an increase in R_{SC} of AZ31_SC. As immersion elapsed, these pathways reactivated due to nucleation and grow of new defects in the coating and corrosion processes can proceed. The stable response of R_{SC} of AZ31_SC observed after week 3rd suggested that during this period the coating barrier properties either do not deteriorate or deteriorated much slower. The latter could be confirmed by the steady CPE_{SC} response of AZ31_SC (Fig. 10.15c) after 2 weeks. This behavior was also observed in the CPE_{SC} of ZE41_SC (Fig. 10.15e) after 4 weeks. However, between 2 and 4 weeks there were wide fluctuations of the resistance and capacitive response of the bi-layered coating on ZE41_SC. The decrease in R_{SC} and the increase in CPE_{SC} suggested deterioration of the coating barrier properties; however, after 2 weeks it was expected that a large area of the coating was already delaminated due to the formation of the layer of corrosion products. This means that, at that point, the overall impedance response should be governed by the process with the highest CPE value, CPE_{dl} according to plots in Fig. 10.15e.

SEM imaging revealed precipitation of corrosion products onto the dual-layer coating on both alloys which composition was determined by EDX analysis. Some CaP compounds were found on AZ31_SC (Fig. 10.16a); however, the smooth surface of the coating prevailed. On the other hand, a dense-rough and apparently thick layer of $MgCO_3$ was found on the coating surface of ZE41_SC (Fig. 10.16b). This layer was not continuous; however, it covered a large area of the overall coating surface. Formation of $MgCO_3$ with flower-like morphology was also found on the coating surface of ZE41_S (see Fig. 10.12d, point 7). Precipitation of corrosion products onto the coating surface can result in an increase in the coating resistance as evidenced from R_{SC} values in Fig. 10.15b and Fig. 10.15d due to blockade of defects and pores.

R_{IL} and CPE_{IL} ($0.53 < n < 0.99$) in Fig. 10.15b-c showed that the corrosion layer of AZ31_SC provided more effective corrosion protection to the substrate with R_{IL} increasing over immersion. This layer seemed to be quite stable at the beginning of the immersion — from 2h to week 1st — and after week 3rd. From 2h to 3 weeks it seemed that the AZ31_SC corrosion layer underwent thickening and probably densification, as suggested by the decrease in CPE_{IL} and the increase in R_{IL} , respectively. It was the same case of the corrosion layer of ZE41_SC until 2 weeks, thereafter wide fluctuations in R_{IL} and CPE_{IL} were observed between 2st and 4th week (Fig. 10.15d-e).

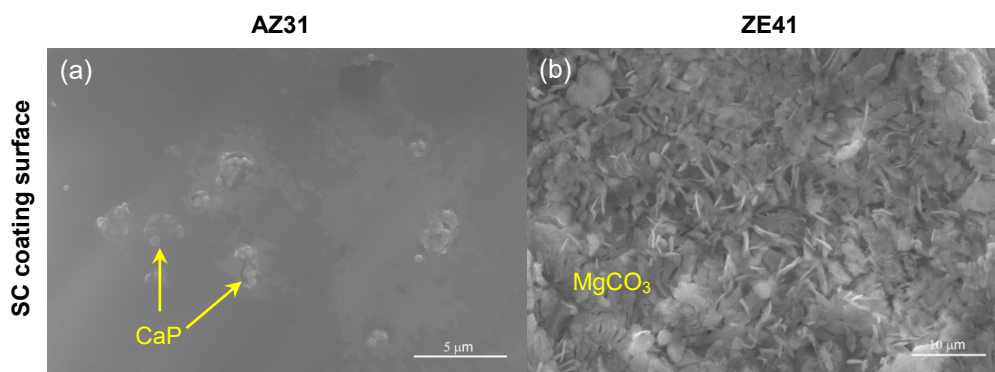


Fig. 10.16. SEM micrographs showing the surface morphology of the bi-layered coatings on (a) AZ31_SC and (b) ZE41_SC after EIS experiments in DMEM for 7 weeks at $31 \pm 1^\circ\text{C}$.

As demonstrated by SEM images in Fig. 10.13 and Raman results in Fig. 10.14 after 1st week of immersion the corrosion products consisted of $\text{Mg}(\text{OH})_2$ and HAP sphero-aggregates. Then, over immersion they transformed into $\text{Mg}(\text{OH})_2/\text{MgCO}_3+\text{CaCO}_3$. The fitted results suggested that the corrosion layers formed on both SC coated alloys after week 7th are much more protective than those of the layer formed during week 1st of immersion. Furthermore, formation of MgCO_3 onto the coating surface of ZE41_SC indicated that at advanced immersion times there is still sufficient amount of Mg ions in solution to react and form this compound. The wide fluctuations in R_{IL} and CPE_{IL} of ZE41_SC from 2 to 4 weeks (see Fig. 10.15d-e) may be due to the local rupture of the IL that resulted in the sharp decrease in resistance and the corresponding CPE increase after 2 weeks. It was the same behavior observed in the IL of ZE41_S from EIS results in SBF, as described in chapter 9.5. On the other hand, since formation of MgCO_3 on the coating surface of AZ31_SC was not found (Fig. 10.16a) it is possible to infer that the corrosion layer of this condition can effectively isolate the substrate from the corrosive solution, hindering dissolution of the substrate and hence production of Mg ions. The latter can be supported by the evolution of R_{IL} and CPE_{IL} of AZ31_SC in Fig. 10.15a-b. This is in close agreement with the findings of Xin et al. [195] who reported that carbonate ions in sodium chloride solution initially promote dissolution of a AZ31 Mg alloy and then induce rapid surface passivation due to precipitation of magnesium carbonate, which effectively inhibits pitting corrosion.

Differences in the stability of the corrosion layers of AZ31_SC and ZE41_SC may be due to differences in both substrates bulk composition. Since the ILs of both bi-layered alloys were made predominantly of the same compounds, incorporation of alloying elements into the corrosion products are expected to impact on the properties of these layers. As already discussed, Al has a stabilizing effect on the hydroxides formed on Mg alloys in chloride environments [13].

The evolution of R_{ct} and CPE_{dl} ($0.68 < n < 0.99$) in Fig. 10.15b-c showed that at early immersion the corrosion response of AZ31_SC was governed by the corrosion resistance of

the alloy, whereas at advanced immersion stages the corrosion response was determined by the stability of the corrosion layer. The higher corrosion resistance of AZ31 compared to the ZE41 can delay delamination of the coating owing to the slower rate of formation of the corrosion layer. On the other hand, R_{ct} and CPE_{dl} ($-0.99 < n < 0.95$) evolution in Fig. 10.15d-e showed that the corrosion response of ZE41_SC was mainly controlled by the barrier properties of the layer of corrosion products. The faster deterioration of the coating barrier properties on this condition along with its higher reactivity promotes the formation of the corrosion layer at early stages. For ZE41_SC there was occurrence of inductive loops. Inductive loops are related to dynamics of adsorption-desorption reactions involved in the dissolution mechanisms of the corrosion layer [213]. The fact that this feature was not observed on the AZ31_SC reinforces the outcome of the stable corrosion layer that forms on the AZ31 alloy.

Then, from the results here presented concerning the corrosion behavior of the AZ31 and ZE41 alloys with the different surface conditions in organic DMEM we can say that:

- 1) The pre-treated AZ31 rapidly (2h-72h) is prone to the formation of a homogeneous layer of corrosion products that remains quite stable over the 7 weeks of immersion with almost no variation of the impedance modulus. This layer has much higher corrosion resistance than that of the one formed on the same condition in SBF solution (chapter 9.3). It was the same case of the pre-treated ZE41 alloy, the corrosion layer formed in DMEM is much more protective than the one formed in SBF. Differences in morphology and chemical composition of these layers are responsible for the different responses.
- 2) At early immersion the silane-TiO₂ coating promotes formation and grow of HAP sphero-aggregates hierarchically arranged over a Mg(OH)₂ layer on both alloys. This is due to the fact that glucose coordinates Ca²⁺ ions in solution [85]. As immersion elapses, these compounds transform into a mixture of Mg(OH)₂, MgCO₃ and CaCO₃ that constitutes a corrosion layer of much higher corrosion resistance than that of the initial layer formed by Mg(OH)₂/HAP sphero-aggregates.
- 3) The SC and SK coated alloys presented the highest impedance values among all tested conditions. This was particularly evidenced for the alloys bi-layered with collagen. It seems that at initial immersion stages the top-most biopolymer layers contribute to create a microenvironment at the coating/substrate interface that provides the suitable conditions for stabilization of the corrosion products. The formation of H₂ gas pockets —as evidenced from the results reported in chapter 10.2.2— would promote the local alkalization of the solution on the metal side, reaching higher pH values than the ones expected for the samples coated with the silane-TiO₂ only. Formation of gas pockets was not observed on these conditions. The above mentioned is consistent with contact angle values of DMEM with the SC bi-layered alloys (Fig. 10.4, pg. 89).

Our findings contribute to elucidating the corrosion degradation mechanisms of Mg alloys in organic solutions in the long term under more realistic conditions mimicking the physiological environment. The use of organic solutions, such as DMEM, in combination with the nature of the alloying elements, the surface functionalization method and the evaluation techniques employed clearly allowed at clarifying several aspects related to the corrosion response of Mg alloys. Nevertheless, the high number of parameters and the dynamic time evolution would require further efforts, particularly in terms of physico-chemical characterization to better understand the corrosion processes. There is no doubt that Mg alloys are quite interesting materials that offer a wide variety of properties for several applications. Nevertheless, our results suggest that it is probably the time to step forward the currently adopted approaches for researching Mg alloys and bridge the gap between short-term laboratory evaluation and the real application of these materials as biodegradable orthopaedic implants.

11. IN VITRO BIOLOGICAL PERFORMANCE OF BI-LAYERED AZ31 & ZE41 ALLOYS

This chapter addresses the results obtained with cells, *in vitro*, with primary human osteoblasts (HOB) and normal human dermal fibroblasts (NHDF) seeded on the various samples with the different surface conditions: (i) HF pre-treated alloys, (ii) sol-gel coated alloys, (iii) and sol-gel/biopolymer coated alloys. By performing the Alamarblue® assay osteoblasts and fibroblasts viability/proliferation was determined at different time-points. Indirect contact assays, allowed determining the role of the alloys composition on the cell viability. Furthermore, the coatings layered architecture aided to ascertain the role of each component in the biological responses of the sets in terms of cell viability/morphology.

11.1. CELL RESPONSE TO THE SURFACE CONDITION

11.1.1 Cell viability on uncoated alloys

Firstly, the fate of fibroblasts and osteoblasts cells seeded on the HF pre-treated alloys (AZ31 and ZE41) was evaluated. Fig. 11.1 summarizes the cell viability results of both cell types on all the surface conditions. After one day, fibroblasts exhibited the same ability to adhere to the surface of the uncoated alloys than to the culture plastic plate (control), as indicated by the comparison of cell viability in Fig. 11.1a. After 3 days, the fibroblasts population on AZ31 decreased by ca. 30% whereas on ZE41 and on the control surface increased. This indicates a detrimental effect of AZ31 on fibroblast viability and a positive effect of ZE41 on cell proliferation. Viability of osteoblasts on the uncoated alloys after one day showed similar adhesion on both materials (Fig. 11.1b). However, the decreased cell viability after 3 days evidenced an adverse effect of AZ31 on osteoblasts whereas ZE41 allowed increasing the osteoblasts population over 7 days in culture.

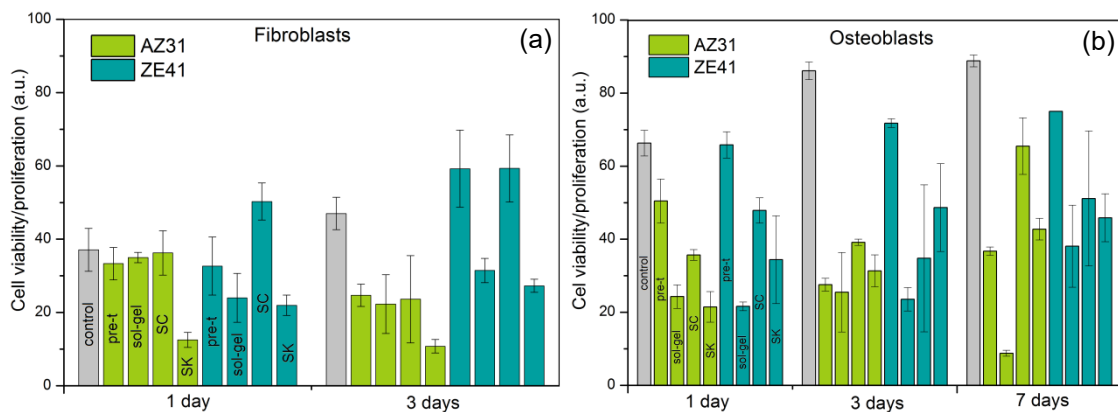


Fig. 11.1. Cell viability of (a) fibroblasts and (b) osteoblasts seeded on the different surfaces, as obtained by the Alamarblue® test. pre-t: 12% HF pre-treated, sol-gel: silane-TiO₂, SC: sol-gel+collagen, SK: sol-gel+chitosan.

The differences in cell response after 1 day of culture observed on each alloy may arise from several factors such as topology of the surfaces that may impact on the initial cell adhesion, composition of the corrosion products as well as the kinetics of the corrosion processes. In terms of topography the initial surface conditions on both AZ31 and ZE41 were similar. On the other hand, at early immersion stages in cell culture medium the corrosion activity of both alloys was high and the progressive formation of a layer of corrosion products at the alloys surface may hinder initial cell attachment. To further elucidate the parameters influencing cell viability, we carried out indirect contact assays. Pre-treated discs of both alloys were incubated at $37 \pm 1^\circ\text{C}$ in cell culture medium for 7 days and supernatants incubated with the discs collected at day 1, 3 and 7 were tested on cells adhered onto multi-well culture plates. As observed in Fig. 11.2, supernatants from AZ31 seemed toxic for fibroblasts after 1 day and for osteoblasts after 3 days, hindering cells proliferation, whereas supernatants from ZE41 only had minor effects on cell viability. These findings are in good correlation with the previous observations of cells in direct contact with the pre-treated alloys.

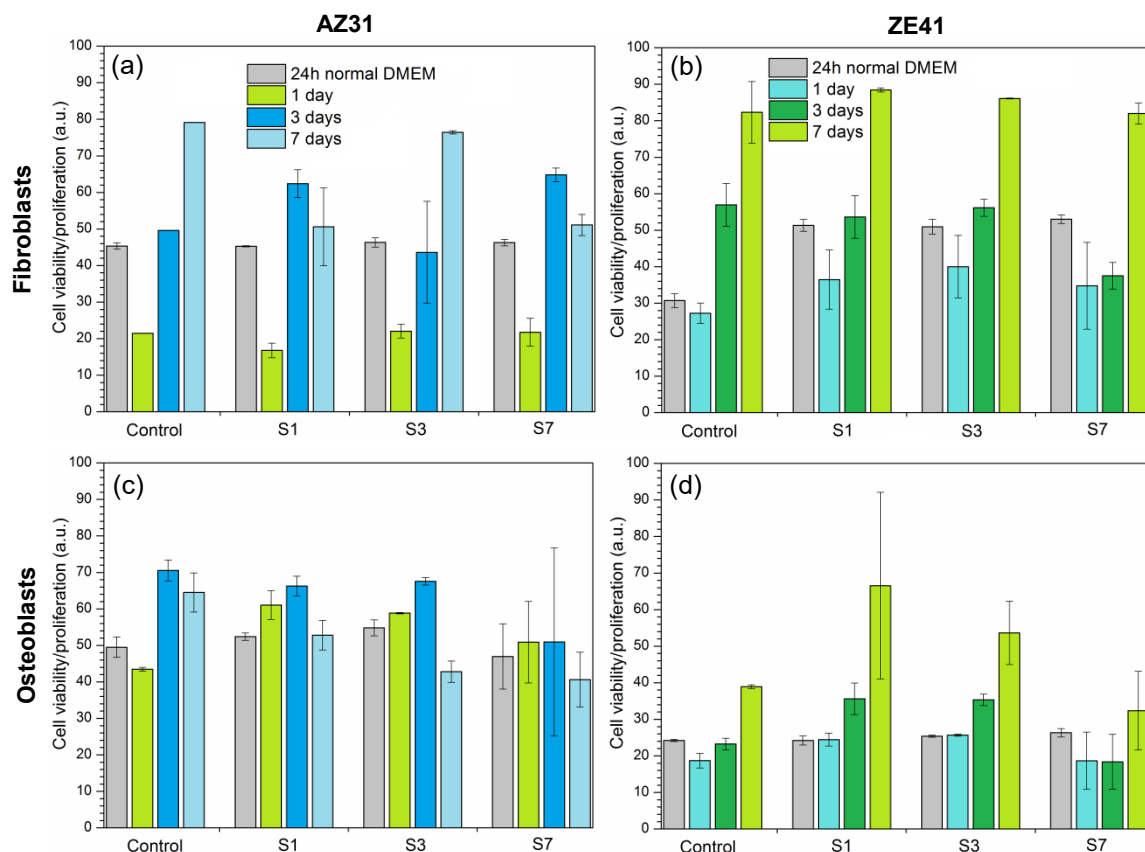


Fig. 11.2. Indirect contact assay results showing viability of both cell types for 7 days of culture in supernatants prepared by immersion of pre-treated alloys in cell culture medium at $37 \pm 1^\circ\text{C}$. Aliquots of supernatants were collected at day 1 (S1), day 3 (S3) and day 7 (S7). Fibroblasts and osteoblasts were seeded in multi-well plates and incubated for 24h to allow normal adhesion (gray bars); next, aliquots of supernatants (S1, S3, S7) were added to adhered cells and incubated for 7 days. Cell viability was measured at day 1, day 3 and day 7 for each set of cells in supernatants. Fibroblasts viability in supernatants with (a) AZ31 and (b) ZE41. Osteoblasts viability in supernatants with (c) AZ31 and (d) ZE41.

11.1.2. Cell viability on silane-based coated and bi-layered alloys

The effects of the different coatings on cell adhesion and proliferation were also studied. In the case of fibroblasts, the sol-gel coating did not impact the cellular adhesion (day 1) on AZ31_S and had a slightly negative effect on ZE41_S (Fig. 11.1a). Furthermore, the addition of the top-collagen layer dramatically promoted fibroblast adhesion on ZE41_SC (by ca. 50% compared to ZE41_S) but did not have a significant improvement on AZ31_SC. On the contrary, chitosan inhibited fibroblast adhesion on both alloys. This detrimental effect was more significant on AZ31_SK (ca. 70% compared to AZ31_S) than on ZE41_SK. The same trend was observed from cell viability tests performed on glass slides coated with the silane-TiO₂ and the bi-layered systems. This configuration allowed determining the contribution of the coatings to the cell response without the influence of the alloys. Cell viability results in Fig. 11.3a indicated that in the present case the chemical nature of the biopolymers is a prevalent factor for fibroblast adhesion.

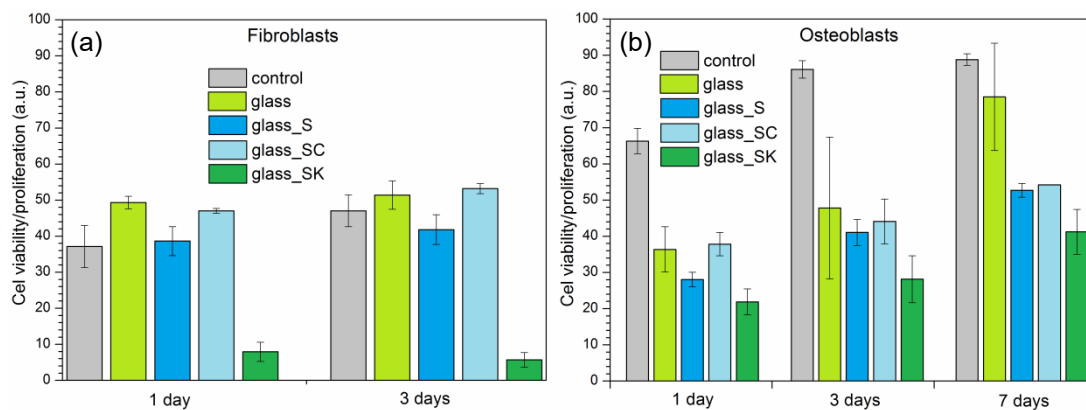


Fig. 11.3. Cell viability of (a) fibroblasts and (b) osteoblasts seeded on glass coated with the silane-TiO₂ and the bi-layered coatings. S: silane-TiO₂, SC: sol-gel+collagen, SK: sol-gel+chitosan.

With respect to fibroblasts proliferation (day 3) it was not evidenced on the AZ31 alloy, regardless the surface condition (Fig. 11.1a). Instead, cell viability decreased by ca. 40% between day 1 and day 3 for all conditions. In contrast, fibroblast proliferation was observed on ZE41_SC where the number of cells increased by 20% whereas no significant variation of cell population was evidenced on ZE41_S and ZE41_SK.

Osteoblasts also exhibited a high sensitivity to the surface composition (Fig. 11.1b). The sol-gel coating on ZE41_S led to a decrease by about 60 % of cell adhesion compared to the pre-treated alloy. The addition of collagen and chitosan allowed the partial recovery of cell adhesion onto ZE41_SC and ZE41_SK. Moreover, the biopolymer top-layers favoured cell proliferation over 7 days. Unlike fibroblasts, osteoblasts clearly benefited from the presence of the chitosan layer (Fig. 11.1b). In parallel, the sol-gel coating on AZ31_S had also a detrimental impact on osteoblast adhesion compared to the pre-treated alloy and had a

dramatic negative effect on cell viability over 7 days. The latter effect was significantly attenuated by the presence of both collagen and chitosan biopolymers. Cell viability tests on coated glass slides confirmed that collagen and chitosan have similar influence on osteoblasts fate (Fig. 11.3b).

11.1.3. Cell morphology on the different surfaces

Cell morphology may reflect the extent of cell adhesion to surfaces and can therefore be used as an indicator to estimate the biointegration of materials. The morphology of viable cells was evaluated after 1 day by fluorescence microscopy using a live/dead kit and after 3 and 7 days by SEM for fibroblasts and osteoblasts, respectively.

When cultured on AZ31 for 1 day, fibroblasts exhibited a spindle-like shape (inset Fig. 11.4a). This morphology is characteristic of a good adherence on the surface. In contrast, cells seemed to weakly adhere to ZE41 surface after 1 day as the cells had a contracted-rounded shape (inset Fig. 11.4b). This is consistent with the presence of red-fluorescing cells corresponding to non-adherent dead fibroblasts. After 3 days, fibroblasts were slightly spread on pre-treated AZ31 and showed finger-like protrusions known as lamellipodia (Fig. 11.4a). Fibroblasts on ZE41 were fully spread after 3 days and exhibited a large cell area (Fig. 11.4b). This morphology is similar to that usually observed on plastic dishes, indicating good adhesion to the material surface. The sol-gel coating drastically impacted the fibroblast morphology on AZ31_S and ZE41_S. After 3 days, cells had a rounded shape, typical of a weak attachment on the material surface (Fig. 11.4c-d). It is important to remark that this morphology was specific of the sol-gel layer deposited on both alloys since the same coating on glass slides allowed significant fibroblast spreading (Annex 1, pg. 133).

When a collagen layer was added onto the sol-gel coated alloys, fibroblasts morphology indicated that they recovered adhesion and exhibited membrane protrusions forming clusters, which indicated good cell-to-cell contacts from day 1 (insets Fig. 11.4e and f) to day 3 (Fig. 11.4e-f). Worth of notice is the fact that when AZ31_SC and ZE41_SC conditions were soaked in DMEM a fibrillar collagen network (Fig. 11.4e) was formed through a sol/gel transition of the type I collagen phase by neutralization (pH 7). This morphogenesis process is called fibrillogenesis and it was already described in chapter 5.1. Fibrils are not readily observable in Fig. 11.4f due to the low magnification. A SEM micrograph where fibrils can be better distinguished is showed in Fig. 11.5. In contrast, the addition of a chitosan layer negatively impacted fibroblasts morphology. Few cells were found at the coating surface and all were round-shaped (Fig. 11.4g-h). This morphology was similar to that observed on glass slides coated with chitosan, thereby evidencing the direct effect of this biopolymer on fibroblast morphology (Annex 1, pg. 133).

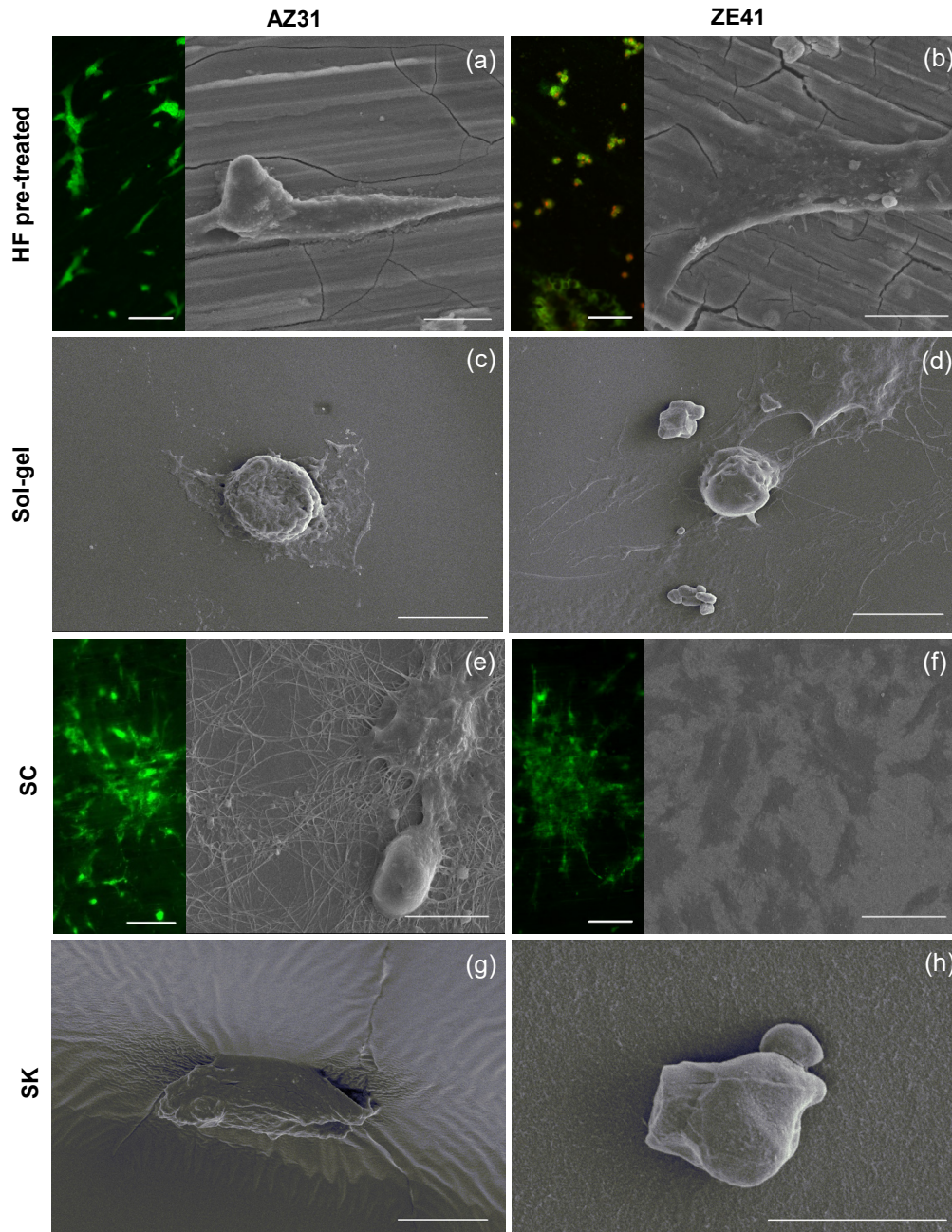


Fig. 11.4. SEM images of fibroblasts morphologies on AZ31 (left hand column) and ZE41 (right hand column) with the different surface conditions after 3 days of incubation (scale bar 10 μm , (f) 100 μm , (h) 5 μm). The insets are fluorescence microscopy images of the cells using live/dead staining after 1 day of incubation (scale bar 100 μm). (a) AZ31, (b) ZE41, (c) AZ31_S, (d) ZE41_S, (e) AZ31_SC, (f) ZE41_SC, (g) AZ31_SK and (h) ZE41_SK.

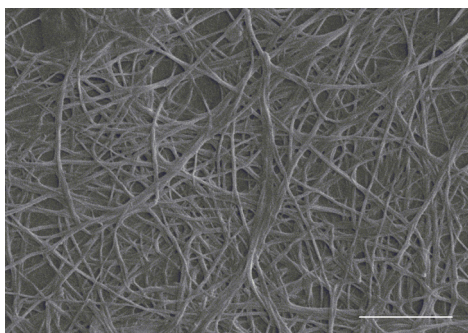


Fig. 11.5. Scanning electron micrograph of fibrillar collagen on ZE41_SC after immersion in DMEM for 7 days at 37°C (95% air with 5% CO₂). Scale bar: 2.5 μm.

The morphology of osteoblasts after 1 day was similar to that of fibroblasts on ZE41 and AZ31 alloys (insets Fig. 11.6a and b). The morphologies changed after 7 days with the presence of rounded cells on AZ31 (Fig. 11.6a) and spread cells on ZE41 (Fig. 11.6b). Similarly to fibroblasts, osteoblasts adopted rounded shape on AZ31_S and ZE41_S which is characteristic of weak cell adhesion (Fig. 11.6c-d). This outcome confirms the detrimental effect of the sol-gel coating on the adhesion of osteoblasts (Fig. 11.1b). Unlike AZ31_S and ZE41_S, sol-gel coated glass slides allowed stronger adhesion and spreading of osteoblast cells (see Fig. 11.3b and Annex 1), as already observed in the case of fibroblasts on glass_S.

Osteoblasts seeded on ZE41_SC exhibited spread morphology and were found gathered in bundles, probably due to local proliferation (Fig. 11.6e). They showed a cuboid shape characteristic of osteoblastic cells. Osteoblasts on AZ31_SC had the same morphology; however, they were scattered on the surface (Fig. 11.6f). In the case of bi-layered samples with chitosan, osteoblasts showed the same cuboid morphology, regardless of the nature of the substrate (Fig. 11.6g-h). This characteristic shape of osteoblasts evidenced that chitosan provided appropriate conditions for cell attachment and proliferation.

The results showed that fibroblasts and osteoblast are high sensitive to the surface composition, particularly fibroblast cells. At first, it appeared that the elemental composition of the alloys influenced cells behavior. The ZE41 seemed to have a positive effect on adhesion and proliferation of both cell types. On the other hand, the AZ31 provided good conditions for cell adhesion only. Lozano et al. [214] investigated the response of different cells seeded onto a fluoride surface-modified AZ31 alloy. They observed no significant changes in apoptosis or viability rates of osteoblasts (MC3T3-E1) and fibroblasts (L929) when cultured on HF-treated AZ31. However, there was an oxidative stress effect in cell cultures caused by a deleterious effect on the cell plasma membrane produced by fluoride-treated AZ31 alloy [214]. The latter could explain fibroblasts and osteoblasts morphologies observed in Fig. 11.4a and Fig. 11.6a, respectively. The spindle and round shapes of fibroblasts and osteoblasts, respectively, on pre-treated AZ31 suggested that cells preferred to minimize the membrane contact area with the alloy surface.

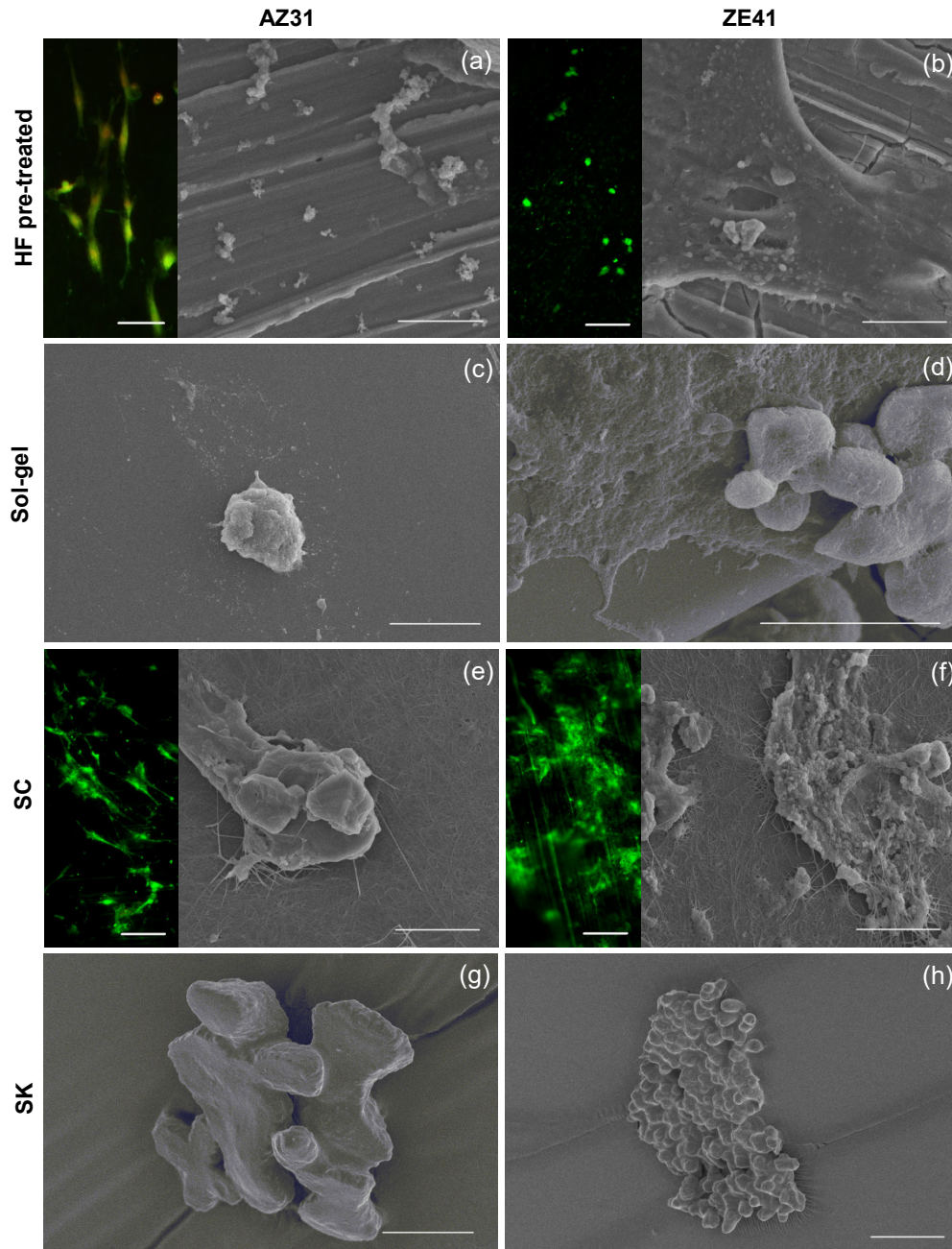


Fig. 11.6. SEM images of osteoblasts morphologies on AZ31 (left hand column) and ZE41 (right hand column) with the different surface conditions after 7 days of incubation (scale bar 10 μm , (d) 5 μm , (h) 20 μm). The insets are fluorescence microscopy images of the cells using live/dead staining after 1 day of incubation (scale bar 100 μm). (a) AZ31, (b) ZE41, (c) AZ31_S, (d) ZE41_S, (e) AZ31_SC, (f) ZE41_SC, (g) AZ31_SK and (h) ZE41_SK.

Although some researchers argue that biocompatibility of Al is limited, it seems to be a valid alloying element for Mg alloys in body contact [13]. Witte et al. [13] demonstrated that an AZ91 alloy showed enhanced osteoblastic activity in the surrounding guinea pig femora. New bone mass surrounding the Mg alloy rod implant was found after 18 weeks post-implantation, which implies an osteoblastic response to the degrading material [13]. Similarly,

Lozano et al. [214] observed new bone formation around a fluoride-treated AZ31 alloy implanted in the femur of a New Zealand white rabbit after 60 days post-implantation. Additional EDS analysis on the surface of the extracted implant indicated the presence of Ca and P, suggesting that *in vivo* mineralization occurred [214]. Kinetics of the corrosion processes is also expected to influence cell behavior. The AZ31 alloy exhibited a high corrosion activity within first 24h of immersion in DMEM. The impedance modulus increased in more than one order of magnitude from 2h to 24h (not shown), indicating the fast formation of a layer of corrosion products within this period. SEM observations showed that this layer seemed to have a strong adherence to the substrate, what means that corrosion products stay on the material surface. Then, the decreased viability of fibroblasts observed from indirect contact assays in Fig. 11.2a, suggested that there were probably some ions from the alloying elements of AZ31 released into the supernatants that promoted a decrease in cell viability. In the case of ZE41 alloy, the results showed that the nature of this alloy has no a detrimental effect on viability of both cell types, in accordance to the larger spreading and close membrane contact with the surface (Fig. 11.4b and Fig. 11.6b).

The silane-TiO₂ coating showed a detrimental effect on fibroblasts and osteoblasts viability. This trend was also observed on the glass slides with the silane-based coating; however, less marked. The latter suggested that there is a combined effect of the silane-based coating and the nature of the alloys on the cells fate. On the other hand, silicon has shown to have interesting biological properties. Some studies have demonstrated that silicon plays a physiological role in bone calcification processes improving the rate of bone mineralization [215]. An acceleration of normal wound healing of an injured bone would allow faster recuperation of a patient. Furthermore, bone formation ability onto the surface of the implant would provide fixation between the bone and the implant that would allow immediate loading of the device [216]. In the present case, the silane-TiO₂ coating promoted HAP sphero-aggregates formation onto the surfaces of the alloys immersed in DMEM as demonstrated in chapter 10.2.3. This HAP layer would provide good integration of the bone and the implant, providing also a proper surface for bone cell adhesion. Additional SEM observations of the sol-gel coated alloys after *in vitro* cell experiments, with osteoblasts, revealed that cells adhered onto the sphero-aggregates (Fig. 11.7). The gradual degradation of the coating barrier properties over immersion along with the set-up and posterior grow of the corrosion products at the metal/coating interface induced mechanical stresses to the coating leading to its failure. Cell can then migrate and reach the underlying metal through the coating cracks.

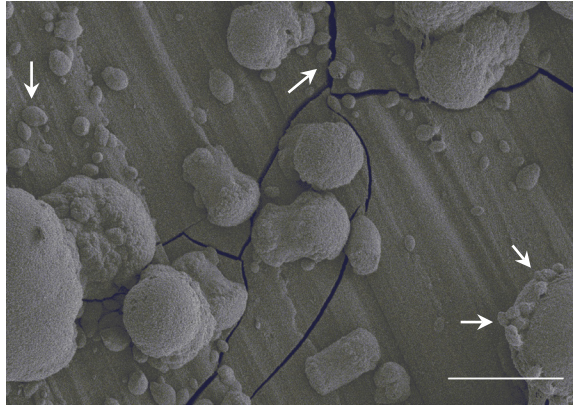


Fig. 11.7. HAP sphero-aggregates formed on AZ31_S under the sol-gel coating after 7 days in cell culture with osteoblasts. Cells are indicated by arrows. Scale bar: 25 μm .

The addition of the biopolymers to the sol-gel coating significantly improved fibroblasts and osteoblast viability, particularly on the ZE41 alloy. Kim et al. [217] investigated the effect of fibrillar and non-fibrillar collagens coatings applied on Ti and the corresponding osteoblast cells responses. The authors demonstrated that fibrillar assembly of collagen significantly improved the level of osteoblasts (MG63) attachment and proliferation. In addition, after testing in DMEM for 3 days the fibrillar-assembled collagen coating showed significantly higher chemical stability than the unassembled one [217]. This higher chemical stability of fibrillar collagen may explain the increased impedance modulus of AZ31_SC and ZE41_SC as observed in Fig. 10.11c and Fig. 10.11g. The increase in the impedance modulus at middle-high frequencies after 72h of immersion on these conditions suggested that at that point fibrillar collagen had already formed resulting in enhanced barrier properties of the silane-TiO₂+collagen. Nevertheless, it was expected that collagen degradation occurred too. It has been reported that high pH values could lead to fast degradation of collagen fibers, which in turn could interact with magnesium degradation [218]. Then, the increased electrolyte pH due to OH⁻ production from Mg cathodic reaction can lead to degradation of the collagen fibers; the by-products may interact with the corroding Mg alloy resulting in formation of corrosion products with high carbon content, as in the case of AZ31_SC and ZE41_SC in SBF. Carbonated compounds were not found in the corrosion products of AZ31_S and ZE41_S immersed in SBF. Jiang et al. [219] investigated the mechanisms of collagen assembly varying the pH and electrolyte of the buffer solution. They found that assembly of type I collagen into a network of microfibrils critically depends on the pH and the electrolyte composition of the buffer solution. Certainly, collagen provides an excellent basis for surface functionalization of biomaterials. Its multiple characteristics in terms of microstructure and mechanical properties as well as its intrinsic biocompatibility, make it suitable for a wide variety of applications. We consider that, in the present case, it is still necessary to gain more insights into the collagen structure and assembly processes under the conditions selected.

Chitosan has shown good in vitro and in vivo cytocompatibility with fibroblasts [131]. However, it has been evidenced that as the degree of deacetylation (DD) increases, the interactions between chitosan and the cells increase due to the presence of free amino groups which improves cell adhesion and proliferation [131]. Moreover, cell response is also dependent on both the cell type and the DD [131]. The above mentioned may explain the lower fibroblast viability observed on the bi-layered samples with chitosan (Fig. 11.1a and Fig. 11.3a, pg. 115 and 117). The DD of the chitosan we used ($\geq 75\%$ deacetylated) probably hindered fibroblast adhesion and proliferation. Then, fibroblasts response to our bi-layered systems with chitosan could be improved by using a chitosan of higher DD. On the other hand, chitosan in bone tissue engineering has shown to promote osteoblasts growth and mineral rich matrix deposition [131]. The two previous statements are in close agreement with the findings in this work. Several studies have focused on chitosan-CaP composites to produce porous structures to allow osteoconduction [147,149,150,220] since chitosan has shown to minimize local inflammatory reactions [131].

Then, the present results showed that the proposed bi-layered systems are viable strategies to functionalize the surface of Mg alloys intended for bone repair applications. The silane-TiO₂ coating provided effective corrosion protection to the alloys at early immersion in both SBF and DMEM, while the stabilized layer of corrosion products provided additional barrier effect at advanced immersion periods. The outcomes showed that there is a synergistic response of the bi-layered systems depending on the alloy/dual-layer-coating/cell-type combinations. This evidences the fact that our bi-layered coatings in combination with the Mg alloys are highly complex systems. Nevertheless, it is clearly noticeable that:

- 1) Pre-treated ZE41 alloy has better cell compatibility than pre-treated AZ31 with improved adhesion and higher proliferation degree of both fibroblast and osteoblast cells. This is supported by the results from indirect contact assays.
- 2) The silane-TiO₂ coating has a slight detrimental effect on cell viability; however, this effect is efficiently compensated by the addition of the biopolymer layers. Particularly, fibroblasts have enhanced adhesion/proliferation when seeded on ZE41_SC as well as osteoblasts seeded on AZ31_SC, ZE41_SC and ZE41_SK. Osteoblasts showed affinity for the HAP promoted by the presence of the silane-TiO₂ coating, colonizing some large sphero-aggregates.
- 3) The collagen top-layer transforms into a fibrillar network through a sol/gel transition of the type I collagen phase by neutralization (pH 7). The fibers trap the cells in a sort of loss 3D mesh. The latter may signify that our bi-layered coating with collagen is biomimetic.

Among all tested combinations the most successful ones in terms of corrosion barrier properties and biological performances are the AZ31_SC and ZE41_SC. High corrosion resistance in inorganic and organic solutions, improved fibroblast and osteoblast responses along with good bone formation ability make these materials suitable for considering the fabrication of biodegradable implants for bone repair applications. Certainly, collagen structure and assembly mechanisms allow a wide range of alternatives that offers novel ways to functionalize the surface of biomaterials. The increasing number of publications on collagen-based materials during the last years evidences this fact.

No claim is made here to extrapolate these data to the *in vivo* condition. Further characterization and *in vivo* evaluation would be required to determine the effects of the dynamic-load-bearing conditions and the complexity of the biological fluids on the performance of the here proposed bi-layered systems.

12. INTEGRATED OVERVIEW AND CONCLUSIONS

From the beginning, the motivation of this project arose from the prospective of a metallic implant providing support to an injured bone of a patient for the period of time needed until its healing and degrading harmlessly afterward. This certainly is a prospective ambitioned by patients, clinicians and hence by researchers. This concept of a biodegradable implant has been revolutionizing the field of biomaterials since some decades. Among biodegradable metals there is no doubt Mg is outstanding by all factors already discussed. Being the topical issue, Mg is widely studied as biomaterial with the number of research papers per year increasing exponentially since 2000.

At first, there was the big question: What is still to be done? Three and a half years before when this project was initiating a new generation of Mg alloys contemplated as biodegradable implants for bone repair applications was being introduced to researchers: Mg-Ca alloys. Mg alloys have shown improved mechanical and anticorrosive properties by modification of the bulk composition; however, it has been evidenced that even with the improvement of these properties these materials need further treatment to control their intrinsic high degradation rate and enhance biological performances. Integration of an implant into the bone takes place largely at the implant-tissue interface, then, the proper design of the surface of the implant is crucial in the performance of the device [216]. Designing this interface include several factors such as the nature of the material, topography and surface chemistry, among others. Functionalizing the surface seemed to be a wise option since the final strategy implemented could be extrapolated specifically for Mg alloys and, why not, for other type of biomaterials requiring improved surface properties. Furthermore, in order to focus on the biological performances at the implant surface—in practical terms that is saying the phenomena at the implant-tissue interface—the here adopted strategy was selecting traditional Mg alloys of well-known properties—AZ31 and ZE41 alloys—as well as selecting a simple method to functionalize the surface of the alloys. Surface coating by the sol-gel route was then the choice. It is a simple method that does not require specialized technology and allows modifying the properties of the coating by either reformulating its chemical composition or adjusting the parameters of deposition. Sol-gel films including TiO₂ and silanes have shown providing good corrosion protection to Mg alloys. Moreover, biocompatible coatings prepared by the sol-gel method have shown to be more bioactive than those of the same composition applied using other methods.

With the objective of not avoiding, but controlling the corrosion rate of the Mg alloys to biocompatible levels, we reformulated the silane-TiO₂ coating composition proposed by Lamaka et al. [172] and adjusted it to obtain the desired corrosion response. At this point was possible to draw the first conclusion:

- 1) The coating barrier properties degrade faster on the ZE41 than on the AZ31 alloy in SBF solution due to the decreased corrosion resistance of ZE41 at early stages of immersion. The presence of the coating determines the composition of the calcium and phosphate compounds formed resulting in the formation of a corrosion layer of $\text{Mg}(\text{OH})_2$ /hydroxyapatite poorly crystalline on both alloys.

Cell viability experiments with fibroblast and osteoblast cells showed that the silane- TiO_2 coating was not efficient enough in promoting cell growth and proliferation. Then, collagen and chitosan biopolymers were added as top-most layers in order to improve biological responses. The second conclusion was then:

- 2) Collagen and chitosan layers improve adhesion/proliferation of osteoblast cells on the sol-gel coating. In the case of fibroblast the improvement in viability was observed when seeded on the sol-gel coating with the collagen layer only. The deacetylation degree of the chitosan used in this work did probably decrease fibroblast viability. Furthermore, the collagen layer formed a fibrillar network trapping the cells in a loose 3D mesh by neutralization, displaying biomimetic ability.

At this point determining if the addition of collagen and chitosan layers modifies in any way the barrier properties of the silane- TiO_2 coating was important. The approach was to step forward current methodologies for testing corrosion behavior of Mg alloys. Some few authors had already advised in considering characterizing the corrosion response of these materials in organic solutions, since corrosion rates from *in vitro* tests in saline inorganic solutions had shown to differ from the corrosion rates found *in vivo*. We made then a comparative study on the corrosion mechanisms of bi-layered ZE41 and AZ31 Mg alloys with collagen and chitosan in both SBF and DMEM with additions of serum, penicillin, streptomycin and fungizone. Important conclusions can be made:

- 3) Collagen and chitosan layers strongly influence the composition of the corrosion products of both Mg alloys in SBF. Differently from the silane-based coated alloys the corrosion products of the bi-layered ones with collagen and chitosan consisted of carbonated compounds such as MgCO_3 and CaCO_3 in combination with $\text{Mg}(\text{OH})_2$. This corrosion layer showed providing effective corrosion protection to the substrate at advanced immersion stages. These carbonated compounds above mentioned were also found in sol-gel coated and bi-layered alloys tested in DMEM displaying good barrier properties too.
- 4) At early immersion (< 1 week) in DMEM the silane- TiO_2 coating promotes formation and growth of hierarchically arranged sphero-aggregates of HAP deposited over a layer of $\text{Mg}(\text{OH})_2$. After 7 weeks, this layer transforms into the corrosion layer with the carbonated compounds described before. A schematic representation of the evolution of the corrosion processes of the samples bi-layered with collagen is made in [Fig. 12.1](#).

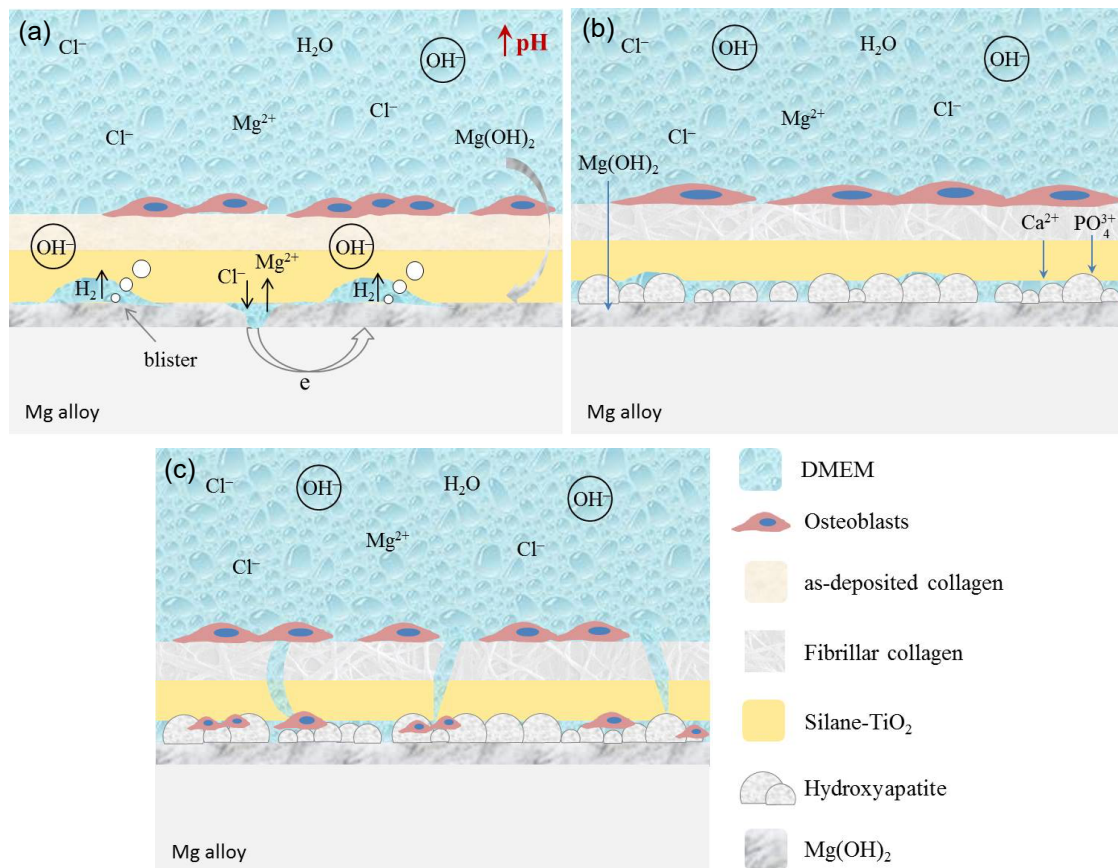


Fig. 12.1. Schematic representation of the corrosion evolution of the Mg alloys over ~1 week of immersion in the presence of cells. (a) Blisters formation due to evolution of H₂ gas along with the formation of a Mg(OH)₂ corrosion layer at the substrate/coating interface; (b) precipitation of hydroxyapatite sphero-aggregates over the Mg(OH)₂ layer and collagen fibrillogenesis; (c) as immersion time elapses the coating barrier properties deteriorates and the growing corrosion products induce cracking to the coating. Cells are able to reach the underlying substrate through the cracks and colonize some sphero-aggregates.

Coating with calcium phosphates is among the most popular strategies to functionalize the surface of Mg alloys for biomedical applications. These coatings have proven to possess bioactivity and bone inductivity. Electrodeposition, sol-gel/dip coating, hydrothermal treatment, wet-chemical precipitation and spray coating are some of the most commonly used deposition techniques. Nevertheless, the high chemical reactivity and the low melting point of Mg alloys demand specific parameters for successful deposition of calcium phosphates [221]. Because of this, these coatings face insufficient adhesion to the Mg substrates. In the present case, we managed to build a coating that provides the suitable conditions for *in situ* deposition of HAP sphero-aggregates.

It is possible to say that the testing hypothesis is then validated: *The hybrid sol-gel coating increases the corrosion resistance of the Mg alloys while the biopolymer layers enhance cell response and viability.*

In the same way, the findings provide enough evidences to answer the addressed questions:

- *Do the biopolymer top layers modify the barrier properties of the sol-gel coating?*

From EIS and LEIS results it can be then considered that collagen and chitosan layers do not have a detrimental effect on the barrier properties of the silane-TiO₂ coating. In fact, collagen showed to enhance hydrophobicity of the sol-gel coating particularly on the ZE41 alloy.

- *Does the nature of the substrate influence the bi-layered coatings performance?*

EIS results in both SBF and DMEM and cell viability results on bi-layered glass slides suggest that there is a combined effect of the bi-layered coatings and the nature of the alloys on their final corrosion response and on the fate of the cells.

- *Does the in vitro testing electrolyte affect the corrosion response and the bioactivity of the Mg alloys?*

The composition of the electrolyte solution does influence significantly the nature of the corrosion products. Considering the simplest case, the corrosion layers on the pre-treated alloys resulted on different morphologies and compositions in both SBF and DMEM. In the case of the silane-TiO₂ coated alloys, the SBF promotes the build-up of a single layer of Mg(OH)₂/hydroxyapatite while the DMEM promotes precipitation and the posterior grow of HAP aggregates hierarchically arranged over a layer of Mg(OH)₂ at early stages of immersion.

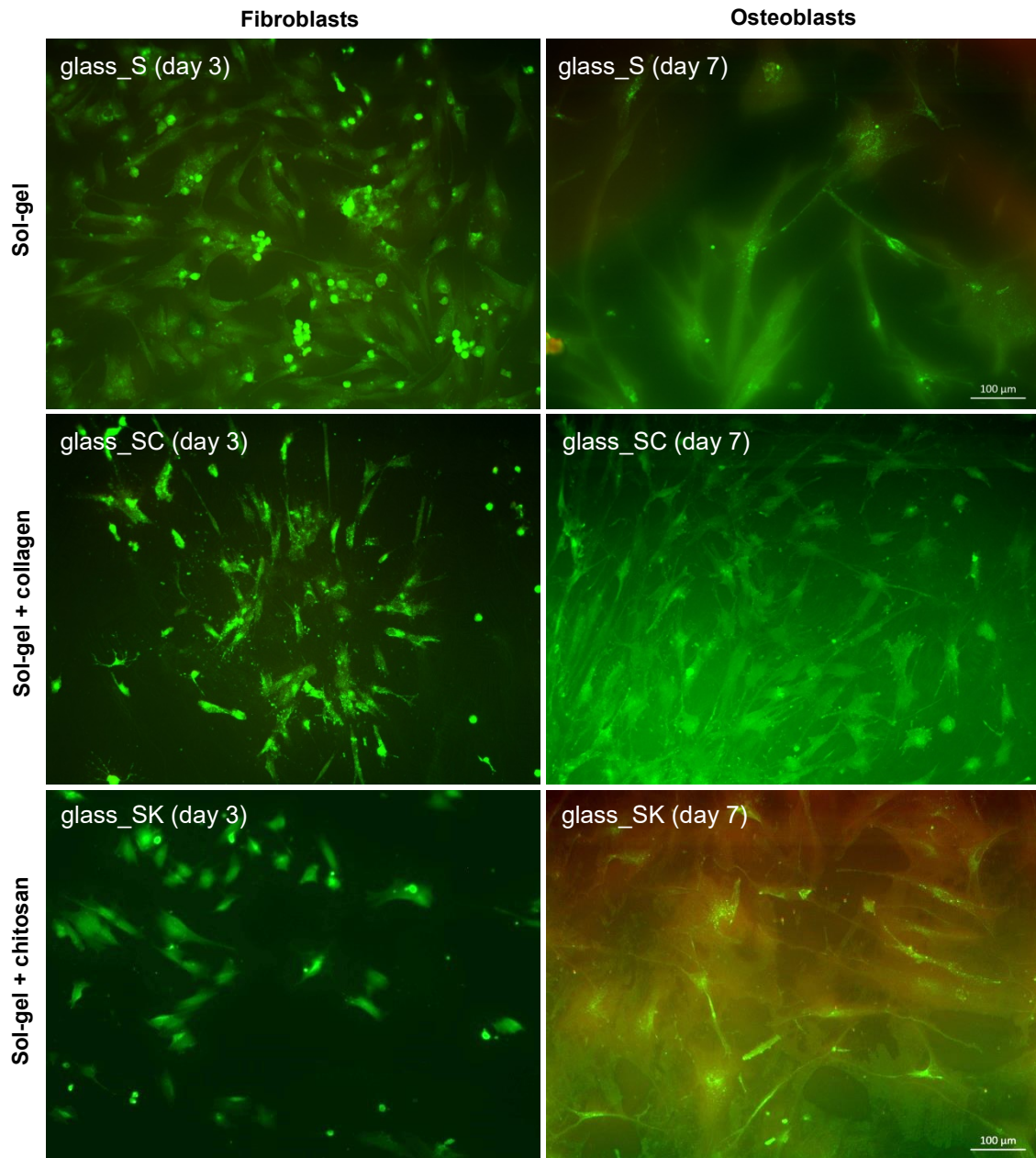
Hypothesizing, the deposition of a corrosion layer containing hydroxyapatite on the metal surface should favours bone deposition on the implant at early stages post-implantation; next, conversion of this layer into stabilized calcium carbonated corrosion products should limit metallic ions accessibility into the body fluids, as evidenced from the electrochemical impedance results. In this sense, this study contributes with the development of a novel-simple route to efficiently control the corrosion degradation of Mg alloys, improving biological performances and providing a biomimetic method for in situ deposition of modified HAP. In the same way, the here reported findings contribute to elucidating corrosion processes of Mg alloys in organic solutions in the long-term.

13. OUTLOOK

During last 10 years there have been a considerable high number of papers published on Mg and its alloys. These materials offer several structural functionalities due to its particular combination of properties. Temporary bone support is probably the application most contemplated for Mg alloys. Then, why it still seems there is a long way to go before producing a Mg-based biodegradable implant as a final product? The complexity and variability in the corrosion response as well as in the physical and mechanical properties as a function of the elemental composition of these materials certainly demand copious characterization. However, limiting researching of Mg alloys to produce knowledge of the materials properties under several experimental conditions instead of adopting meticulous approaches seems is not stimulating researchers towards the materialization of the final application. To what extent gaining knowledge is valuable when not applied to the real life situation? Knowledge is useful when applied and we should not forget that the final goal is contributing to improve people's life. From there and aiming to move forward on these direction, we consider that from the results in the present research work there are some topics that are worth of further assessment and refinement. Some of those topics are:

- 1) Detailed characterization of the corrosion products of the alloys tested in DMEM to determine their precise stoichiometry and composition.
- 2) Further characterization of the barrier properties of the corrosion layers at advanced immersion stages (~7 weeks) in order to characterize the elemental dissolution rates too and correlate with the ion release rate from the metal into the body fluids. Atomic emission spectroelectrochemistry is recommended.
- 3) To determine the collagen stability as a function of the pH. This would also contribute to detail the corrosion mechanisms of the samples bi-layered with collagen. Furthermore, to elucidate the collagen fibrils assembly processes under the here selected conditions.
- 4) To evaluate fibroblasts and osteoblasts response to the bi-layered samples with a chitosan layer of higher DD (> 75%).
- 5) To contemplate *in vivo* evaluation in order to determine the effects of the dynamic-load-bearing conditions and the complexity of the biological fluids on the performance of the here proposed bi-layered systems.

ANNEX 1



Fluorescence microscopy images of fibroblasts (left hand column) and osteoblasts (right hand column) seeded on coated glass slides using live/dead staining after 3 and 7 days of incubation, respectively.

14. BIBLIOGRAPHY

- [1] C.P. Bergmann, S. Aisha, *Dental Ceramics*, Rio Grande do Sul, 2013. doi:10.1007/978-3-642-38224-6.
- [2] H. Hendra, R. Dadan, D.J. R.P, *Metals for Biomedical Applications*, in: *Biomed. Eng. - From Theory to Appl.*, 2011: pp. 411–431. doi:10.5772/2629.
- [3] H. Hermawan, D. Mantovani, *Degradable metallic biomaterials: the concept, current developments and future directions*, *MINERVA BIOTEC*. 21 (2009) 207–16.
- [4] R. Mittal, J. Morley, H. Dinopoulos, E.G. Drakoulakis, E. Vernani, P.V. Giannoudis, *Use of bio-resorbable implants for stabilisation of distal radius fractures: the United Kingdom patients' perspective Injury*, *Int. J. Care Inj.* 36 (2005) 333–38.
- [5] Dean Carolyn, *The miracle of Magnesium*, 1st ed., The Random House Publishing Group, New York, 2003.
- [6] E. Zhang, H. Chen, F. Shen, *Biocorrosion properties and blood and cell compatibility of pure iron as a biodegradable biomaterial*, *J. Mater. Sci. Mater. Med.* 21 (2010) 2151–2163. doi:10.1007/s10856-010-4070-0.
- [7] Q. Chen, G.A. Thouas, *Metallic implant biomaterials*, *Mater. Sci. Eng. R Reports*. 87 (2015) 1–57. doi:10.1016/j.mser.2014.10.001.
- [8] R. Zeng, W. Dietzel, F. Witte, N. Hort, C. Blawert, *Progress and Challenge for Magnesium Alloys as Biomaterials*, *Adv. Eng. Mater.* 10 (2008) B3–B14. doi:10.1002/adem.200800035.
- [9] Z. Zhen, T.F. Xi, Y.F. Zheng, *A review on in vitro corrosion performance test of biodegradable metallic materials*, *Trans. Nonferrous Met. Soc. China (English Ed)*. 23 (2013) 2283–2293. doi:10.1016/S1003-6326(13)62730-2.
- [10] F. Witte, J. Fischer, J. Nellesen, H.-A. Crostack, V. Kaese, A. Pisch, et al., *In vitro and in vivo corrosion measurements of magnesium alloys*, *Biomaterials*. 27 (2006) 1013–1018. doi:10.1016/j.biomaterials.2005.07.037.
- [11] J. Hofstetter, E. Martinelli, A.M. Weinberg, M. Becker, B. Mingler, P.J. Uggowitzer, et al., *Assessing the degradation performance of ultrahigh-purity magnesium in vitro and in vivo*, *Corros. Sci.* 91 (2015) 29–36. doi:10.1016/j.corsci.2014.09.008.
- [12] J. Hofstetter, E. Martinelli, S. Pogatscher, P. Schmutz, E. Povoden-Karadeniz, a. M. Weinberg, et al., *Influence of trace impurities on the in vitro and in vivo degradation of biodegradable Mg–5Zn–0.3Ca alloys*, *Acta Biomater.* 23 (2015) 0–6. doi:10.1016/j.actbio.2015.05.004.
- [13] F. Witte, V. Kaese, H. Haferkamp, E. Switzer, a. Meyer-Lindenberg, C.J. Wirth, et al., *In vivo corrosion of four magnesium alloys and the associated bone response*, *Biomaterials*. 26 (2005) 3557–3563. doi:10.1016/j.biomaterials.2004.09.049.
- [14] N.T. Kirkland, J. Lespagnol, N. Birbilis, M.P. Staiger, *A survey of bio-corrosion rates of magnesium alloys*, *Corros. Sci.* 52 (2010) 287–291. doi:10.1016/j.corsci.2009.09.033.

- [15] a. Zomorodian, F. Brusciotti, a. Fernandes, M.J. Carmezim, T. Moura e Silva, J.C.S. Fernandes, et al., Anti-corrosion performance of a new silane coating for corrosion protection of AZ31 magnesium alloy in Hank's solution, *Surf. Coatings Technol.* 206 (2012) 4368–4375. doi:10.1016/j.surfcoat.2012.04.061.
- [16] A. Zomorodian, M.P. Garcia, T. Moura e Silva, J.C.S. Fernandes, M.H. Fernandes, M.F. Montemor, Biofunctional composite coating architectures based on polycaprolactone and nanohydroxyapatite for controlled corrosion activity and enhanced biocompatibility of magnesium AZ31 alloy, *Mater. Sci. Eng. C.* 48 (2015) 434–443. doi:10.1016/j.msec.2014.12.027.
- [17] B.R. Sunil, T.S.S. Kumar, U. Chakkingal, V. Nandakumar, M. Doble, V.D. Prasad, et al., In vitro and in vivo studies of biodegradable fine grained AZ31 magnesium alloy produced by equal channel angular pressing, *Mater. Sci. Eng. C.* 59 (2016) 356–367. doi:10.1016/j.msec.2015.10.028.
- [18] R. Waksman, R. Pakala, P.K. Kuchulakanti, R. Baffour, D. Hellings, R. Seabron, et al., Safety and efficacy of bioabsorbable magnesium alloy stents in porcine coronary arteries., *Catheter. Cardiovasc. Interv.* 68 (2006) 607–17; discussion 618–9. doi:10.1002/ccd.20727.
- [19] N. Angrisani, J. Reifenrath, J. Seitz, A. Meyer-lindenberg, Rare Earth Metals as Alloying Components in Magnesium Implants for Orthopaedic Applications, *InTech.* (2012) 1–22.
- [20] W. Jin, G. Wu, H. Feng, W. Wang, X. Zhang, P.K. Chu, Improvement of corrosion resistance and biocompatibility of rare-earth WE43 magnesium alloy by neodymium self-ion implantation, *Corros. Sci.* 94 (2015) 142–155. doi:10.1016/j.corsci.2015.01.049.
- [21] M. Salahshoor, Y. Guo, Biodegradable Orthopedic Magnesium-Calcium (MgCa) Alloys, Processing, and Corrosion Performance, *Materials (Basel)*. 5 (2012) 135–155. doi:10.3390/ma5010135.
- [22] A.V. Koltygin, V.E. Bazhenov, E.A. Belova, A.A. Nikitina, Development of a magnesium alloy with good casting characteristics on the basis of Mg–Al–Ca–Mn system, having Mg–Al₂Ca structure, *J. Magnes. Alloy.* 1 (2013) 224–229. doi:10.1016/j.jma.2013.10.002.
- [23] L.C. Trincă, M. Fântânariu, C. Solcan, A.E. Trofin, L. Burtan, D.M. Acatrinei, et al., In vivo degradation behavior and biological activity of some new Mg–Ca alloys with concentration's gradient of Si for bone grafts, *Appl. Surf. Sci.* 352 (2015) 140–150. doi:10.1016/j.apsusc.2015.03.136.
- [24] J. Walker, S. Shadanbaz, T.B.F. Woodfield, M.P. Staiger, G.J. Dias, Magnesium biomaterials for orthopedic application: A review from a biological perspective, *J. Biomed. Mater. Res. - Part B Appl. Biomater.* 102 (2014) 1316–1331. doi:10.1002/jbm.b.33113.
- [25] J. Wang, J. Tang, P. Zhang, Y. Li, J. Wang, Y. Lai, et al., Surface modification of magnesium alloys developed for bioabsorbable orthopedic implants: A general review, *J. Biomed. Mater. Res. Part B Appl. Biomater.* 100B (2012) 1691–1701. doi:10.1002/jbm.b.32707.

- [26] C.Y. Wu, J. Zhang, State-of-art on corrosion and protection of magnesium alloys based on patent literatures, *Trans. Nonferrous Met. Soc. China (English Ed.* 21 (2011) 892–902. doi:10.1016/S1003-6326(11)60799-1.
- [27] W.L. Stoppel, C.E. Ghezzi, S.L. McNamara, L.D.B. III, D.L. Kaplan, Clinical Applications of Naturally Derived Biopolymer-Based Scaffolds for Regenerative Medicine, *Ann. Biomed. Eng.* 43 (2015) 657–680. doi:10.1007/s10439-014-1206-2.
- [28] F. Witte, The history of biodegradable magnesium implants: A review, *Acta Biomater.* 6 (2010) 1680–1692. doi:10.1016/j.actbio.2010.02.028.
- [29] A. Lambotte, Technique et indications d'elea prothèse perdue dans la traitement des fractures, *Press. Med Belge.* 17 (1909) 321–323.
- [30] A. Lambotte, L'utilisation du magnésium comme matériel perdu dans l'ostéosynthèse, *Bull Mém Soc Nat Cir.* 28 (1932) 1325–1334.
- [31] J. Verbrugge, Le matériel métallique résorbable en chirurgie osseuse, *La Press Medicale.* 23 (1934) 460–465.
- [32] E.D. McBride, Absorbable metal in bone surgery, *J AmMed Assoc.* 27 (1938) 2464–2467.
- [33] S. Housh, B. Mikucki, A. Stevenson, Properties and Selection: Nonferrous Alloys and Special-Purpose Materials, *ASM Handb.* (1992) 1424–1432.
- [34] L. Xu, E. Zhang, D. Yin, S. Zeng, K. Yang, In vitro corrosion behavior of Mg alloys in a phosphate buffered solution for bone implant application, *J. Mater. Sci. Mater. Med.* 19 (2008) 1017–1025. doi:http://dx.doi.org/10.1007/s10856-007-3219-y.
- [35] L. Xu, F. Pan, G. Yu, L. Yang, E. Zhang, K. Yang, In vitro and in vivo evaluation of the surface bioactivity of a calcium phosphate coated magnesium alloy, *Biomaterials.* 30 (2009) 1512–1523. doi:10.1016/j.biomaterials.2008.12.001.
- [36] M.P. Staiger, A.M. Pietak, J. Huadmai, G. Dias, Magnesium and its alloys as orthopedic biomaterials: A review, *Biomaterials.* 27 (2006) 1728–1734. doi:10.1016/j.biomaterials.2005.10.003.
- [37] J. Vormann, Magnesium: nutrition and metabolism., *Mol. Aspects Med.* 24 (2003) 27–37. doi:10.1016/S0098-2997(02)00089-4.
- [38] Y. Yamasaki, Y. Yoshida, M. Okazaki, a. Shimazu, T. Uchida, T. Kubo, et al., Synthesis of functionally graded MgCO₃ apatite accelerating osteoblast adhesion, *J. Biomed. Mater. Res.* 62 (2002) 99–105. doi:10.1002/jbm.10220.
- [39] H. Zreiqat, C.R. Howlett, a. Zannettino, P. Evans, G. Schulze-Tanzil, C. Knabe, et al., Mechanisms of magnesium-stimulated adhesion of osteoblastic cells to commonly used orthopaedic implants, *J. Biomed. Mater. Res.* 62 (2002) 175–184. doi:10.1002/jbm.10270.
- [40] Y. Chen, Z. Xu, C. Smith, J. Sankar, Recent advances on the development of magnesium alloys for biodegradable implants, *Acta Biomater.* 10 (2014) 4561–4573. doi:10.1016/j.actbio.2014.07.005.

- [41] E.D. McBride, Absorbable metal in bone surgery a further report on the use of Mg alloys, *J. Am. Med. Assoc.* 111 (1938) 2464–2467. doi:10.1001/jama.1938.02790530018007.
- [42] P.K. Bowen, J. Drelich, J. Goldman, Zinc Exhibits Ideal Physiological Corrosion Behavior for Bioabsorbable Stents., *Adv. Mater.* (2013) 1–6. doi:10.1002/adma.201300226.
- [43] R.J. Werkhoven, W.H. Sillekens, J.B.J.M. van Lieshout, Magnesium 2011, in: *Magnes. Technol.*, Warrendale, PA, USA, 2011: p. 419.
- [44] M. Moravej, D. Mantovani, Biodegradable Metals for Cardiovascular Stent Application: Interests and New Opportunities, *Int. J. Mol. Sci.* 12 (2011) 4250–4270. doi:10.3390/ijms12074250.
- [45] Y. Onuma, J. Ormiston, P.W. Serruys, Bioresorbable Scaffold Technologies, *Circ. J.* 75 (2011) 509–520. doi:10.1253/circj.CJ-10-1135.
- [46] G. Song, Control of biodegradation of biocompatible magnesium alloys, *Corros. Sci.* 49 (2007) 1696–1701. doi:10.1016/j.corsci.2007.01.001.
- [47] F. Witte, N. Hort, F. Feyerabend, C. Vogt, *Corrosion of Magnesium Alloys*, Woodhead, Philadelphia, PA, USA, 2011.
- [48] X. Gu, Y. Zheng, Y. Cheng, S. Zhong, T. Xi, In vitro corrosion and biocompatibility of binary magnesium alloys, *Biomaterials.* 30 (2009) 484–498. doi:10.1016/j.biomaterials.2008.10.021.
- [49] E. Britannica, Bone remodeling, *Encycl. Br. Online.* (2015). <http://www.britannica.com/science/bone-remodeling> (accessed November 25, 2015).
- [50] V.I. Sikavitsas, J.S. Temenoff, A.G. Mikos, Biomaterials and bone mechanotransduction, *Biomaterials.* 22 (2001) 2581–2593. doi:10.1016/S0142-9612(01)00002-3.
- [51] E. Britannica, Bone remodeling, *Encycl. Br. Online.* (2015).
- [52] R. Hambli, E. Lespessailles, C.-L. Benhamou, Integrated remodeling-to-fracture finite element model of human proximal femur behavior, *J. Mech. Behav. Biomed. Mater.* 17 (2012) 89–106. doi:10.1016/j.jmbbm.2012.08.011.
- [53] R.. Martin, Toward a unifying theory of bone remodeling, *Bone.* 26 (2000) 1–6. doi:10.1016/S8756-3282(99)00241-0.
- [54] H.B.V. SURIN, Stress shielding effect of the shaft component, (2005).
- [55] J.-P. Boutrand, Methods and interpretation of performance studies for bone implants, in: *Biocompat. Perform. Med. Devices*, Woodhead Publishing Series, 2012: pp. 271–307. doi:10.1533/9780857096456.3.269.
- [56] E. Zhang, L. Xu, G. Yu, F. Pan, K. Yang, In vivo evaluation of biodegradable magnesium alloy bone implant in the first 6 months implantation., *J. Biomed. Mater. Res. A.* 90 (2009) 882–893. doi:10.1002/jbm.a.32132.

- [57] R. Erbel, C. Di Mario, J. Bartunek, J. Bonnier, B. de Bruyne, F.R. Eberli, et al., Temporary scaffolding of coronary arteries with bioabsorbable magnesium stents: a prospective, non-randomised multicentre trial, *Lancet*. 369 (2007) 1869–1875. doi:10.1016/S0140-6736(07)60853-8.
- [58] M. Bosiers, AMS INSIGHT—Absorbable Metal Stent Implantation for Treatment of Below-the-Knee Critical Limb Ischemia: 6-Month Analysis, *Cardiovasc. Intervent. Radiol.* 32 (2009) 424–435. doi:10.1007/s00270-008-9472-8.
- [59] B.L. Mordike, T. Ebert, Magnesium Properties - applications - potential, *Mater. Sci. Eng. A*. 302 (2001) 37–45. doi:10.1016/S0921-5093(00)01351-4.
- [60] Y. Xin, T. Hu, P.K. Chu, In vitro studies of biomedical magnesium alloys in a simulated physiological environment: A review, *Acta Biomater.* 7 (2011) 1452–1459. doi:10.1016/j.actbio.2010.12.004.
- [61] a. Pardo, M.C. Merino, a. E. Coy, R. Arrabal, F. Viejo, E. Matykina, Corrosion behavior of magnesium/aluminium alloys in 3.5wt.% NaCl, *Corros. Sci.* 50 (2008) 823–834. doi:10.1016/j.corsci.2007.11.005.
- [62] R. Pinto, M.G.S. Ferreira, M.J. Carmezim, M.F. Montemor, The corrosion behavior of rare-earth containing magnesium alloys in borate buffer solution, *Electrochim. Acta*. 56 (2011) 1535–1545. doi:10.1016/j.electacta.2010.09.081.
- [63] T.J. Haley, Pharmacology and toxicology of the rare earth elements, *J. Pharm. Sci.* 54 (1965) 663–670.
- [64] F. Feyerabend, J. Fischer, J. Holtz, F. Witte, R. Willumeit, H. Drücker, et al., Evaluation of short-term effects of rare earth and other elements used in magnesium alloys on primary cells and cell lines, *Acta Biomater.* 6 (2010) 1834–1842. doi:10.1016/j.actbio.2009.09.024.
- [65] G. Pagano, M. Guida, F. Tommasi, R. Oral, Health effects and toxicity mechanisms of rare earth elements—Knowledge gaps and research prospects, *Ecotoxicol. Environ. Saf.* 115 (2015) 40–48. doi:10.1016/j.ecoenv.2015.01.030.
- [66] X.N. Gu, Y.F. Zheng, A review on magnesium alloys as biodegradable materials, *Front. Mater. Sci. China*. 4 (2010) 111–115. doi:10.1007/s11706-010-0024-1.
- [67] Y. Zhu, G. Wu, Y.H. Zhang, Q. Zhao, Growth and characterization of Mg(OH)₂ film on magnesium alloy AZ31, *Appl. Surf. Sci.* 257 (2011) 6129–6137. doi:10.1016/j.apsusc.2011.02.017.
- [68] K. Braszczyńska, Precipitates of γ -Mg₁₇Al₁₂ Phase in AZ91 Alloy, *Magnesium Alloy. - Des. Process. Prop.* (2011) 95–112. doi:10.5772/560.
- [69] H. Zhang, S. Hu, Z. Wang, Y. Liang, The effect of welding speed on microstructures of cold metal transfer deposited AZ31 magnesium alloy clad, *Mater. Des.* 86 (2015) 894–901. doi:10.1016/j.matdes.2015.07.143.
- [70] A.E. Coy, F. Viejo, P. Skeldon, G.E. Thompson, Susceptibility of rare-earth-magnesium alloys to micro-galvanic corrosion, *Corros. Sci.* 52 (2010) 3896–3906. doi:10.1016/j.corsci.2010.08.006.

- [71] H. SUN, C. LI, Y. XIE, W. FANG, Microstructures and mechanical properties of pure magnesium bars by high ratio extrusion and its subsequent annealing treatment, *Trans. Nonferrous Met. Soc. China.* 22 (2012) s445–s449. doi:10.1016/S1003-6326(12)61744-0.
- [72] T.V. Padfield, *Metallography and Microstructures of Magnesium and Its Alloys*, in: A. International (Ed.), Vol. 9, ASM Handb., 2004: pp. 801–815.
- [73] M. Alvarez-Lopez, M.D. Pereda, J. a del Valle, M. Fernandez-Lorenzo, M.C. Garcia-Alonso, O. a Ruano, et al., Corrosion behavior of AZ31 magnesium alloy with different grain sizes in simulated biological fluids., *Acta Biomater.* 6 (2010) 1763–71. doi:10.1016/j.actbio.2009.04.041.
- [74] W.C. Neil, M. Forsyth, P.C. Howlett, C.R. Hutchinson, B.R.W. Hinton, Corrosion of magnesium alloy ZE41 - The role of microstructural features, *Corros. Sci.* 51 (2009) 387–394. doi:10.1016/j.corsci.2008.11.005.
- [75] S. Thomas, N.V. Medhekar, G.S. Frankel, N. Birbilis, Corrosion mechanism and hydrogen evolution on Mg, *Curr. Opin. Solid State Mater. Sci.* 19 (2015) 85–94. doi:10.1016/j.cossms.2014.09.005.
- [76] M. Taheri, J.R. Kish, N. Birbilis, M. Danaie, E.A. McNally, J.R. McDermid, Towards a Physical Description for the Origin of Enhanced Catalytic Activity of Corroding Magnesium Surfaces, *Electrochim. Acta.* 116 (2014) 396–403. doi:10.1016/j.electacta.2013.11.086.
- [77] J.L. Robinson, P.F. King, Electrochemical Behavior of the Magnesium Anode, *J. Electrochem. Soc.* 108 (1961) 36–41. doi:10.1149/1.2428007.
- [78] P.F. King, Magnesium as a Passive Metal, *J. Electrochem. Soc.* 110 (1963) 1113–1116. doi:10.1149/1.2425600.
- [79] G. Williams, N. Birbilis, H.N. McMurray, The source of hydrogen evolved from a magnesium anode, *Electrochem. Commun.* 36 (2013) 1–5. doi:10.1016/j.elecom.2013.08.023.
- [80] M.P. Brady, M. Fayek, H.H. Elsentriecy, K. a. Unocic, L.M. Anovitz, J.R. Keiser, et al., Tracer Film Growth Study of Hydrogen and Oxygen from the Corrosion of Magnesium in Water, *J. Electrochem. Soc.* 161 (2014) C395–C404. doi:10.1149/2.0821409jes.
- [81] M. Danaie, R.M. Asmussen, P. Jakupi, D.W. Shoesmith, G. a. Botton, The role of aluminum distribution on the local corrosion resistance of the microstructure in a sand-cast AM50 alloy, *Corros. Sci.* 77 (2013) 151–163. doi:10.1016/j.corsci.2013.07.038.
- [82] N.T. Kirkland, N. Birbilis, M.P. Staiger, Assessing the corrosion of biodegradable magnesium implants: A critical review of current methodologies and their limitations, *Acta Biomater.* 8 (2012) 925–936. doi:10.1016/j.actbio.2011.11.014.
- [83] J. Zhang, N. Kong, Y. Shi, J. Niu, L. Mao, H. Li, et al., Influence of proteins and cells on in vitro corrosion of Mg-Nd-Zn-Zr alloy, *Corros. Sci.* 85 (2014) 477–481. doi:10.1016/j.corsci.2014.04.020.
- [84] A.H. Martinez Sanchez, B.J.C. Luthringer, F. Feyerabend, R. Willumeit, Mg and Mg

- alloys: how comparable are in vitro and in vivo corrosion rates? A review., *Acta Biomater.* 13 (2015) 16–31. doi:10.1016/j.actbio.2014.11.048.
- [85] R.-C. Zeng, X.-T. Li, S.-Q. Li, F. Zhang, E.-H. Han, In vitro degradation of pure Mg in response to glucose, *Sci. Rep.* 5 (2015) 13026. doi:10.1038/srep13026.
- [86] C. Liu, Y. Xin, X. Tian, P.K. Chu, Degradation susceptibility of surgical magnesium alloy in artificial biological fluid containing albumin, *J. Mater. Res.* 22 (2007) 1806–1814. doi:10.1557/jmr.2007.0241.
- [87] S.A. Salman, Anodization of magnesium (Mg) alloys to improve corrosion resistance, in: G.-L. Song (Ed.), *Corros. Prev. Magnes. Alloy.*, Woodhead Publishing Limited, 2013: pp. 197–231. doi:10.1533/9780857098962.2.197.
- [88] X.-B. Chen, M.A. Easton, N. Birbilis, Corrosion-resistance electrochemical plating of magnesium (Mg) alloys, in: G.-L. Song (Ed.), *Corros. Prev. Magnes. Alloy.*, Woodhead Publishing Limited, 2013: pp. 315–346. doi:10.1533/9780857098962.3.315.
- [89] B.L. Jiang, Y.F. Ge, Micro-arc oxidation (MAO) to improve the corrosion resistance of magnesium (Mg) alloys, in: G.-L. Song (Ed.), *Corros. Prev. Magnes. Alloy.*, Woodhead Publishing Limited, 2013: pp. 163–196. doi:10.1533/9780857098962.2.163.
- [90] Y. Li, F. Lu, H. Li, W. Zhu, H. Pan, G. Tan, et al., Corrosion mechanism of micro-arc oxidation treated biocompatible AZ31 magnesium alloy in simulated body fluid, *Prog. Nat. Sci. Mater. Int.* 24 (2014) 516–522. doi:10.1016/j.pnsc.2014.08.007.
- [91] V.K. Champagne, B. Gabriel, J. Villafuerte, Cold spray coatings to improve the corrosion resistance of magnesium (Mg) alloys, in: G.-L. Song (Ed.), *Corros. Prev. Magnes. Alloy.*, Woodhead Publishing Limited, 2013: pp. 414–445. doi:10.1533/9780857098962.3.414.
- [92] S.M. Hassani-Gangaraj, A. Moridi, M. Guagliano, Critical review of corrosion protection by cold spray coatings, *Surf. Eng.* 31 (2015) 803–815. doi:10.1179/1743294415Y.0000000018.
- [93] A.C.W. Noorakma, H. Zuhailawati, V. Aishvarya, B.K. Dhindaw, Hydroxyapatite-coated magnesium-based biodegradable alloy: Cold spray deposition and simulated body fluid studies, *J. Mater. Eng. Perform.* 22 (2013) 2997–3004. doi:10.1007/s11665-013-0589-9.
- [94] Q. Li, Sol-gel coatings to improve the corrosion resistance of magnesium (Mg) alloys, in: G.-L. Song (Ed.), *Corros. Prev. Magnes. Alloy.*, Woodhead Publishing Limited, 2013: pp. 469–485. doi:10.1533/9780857098962.3.469.
- [95] C.J. Brinker, G.W. Scherer, Sol-gel processing, in: *Sol-Gel Sci.*, Academic Press, 2010: pp. 2–11.
- [96] M. Zheludkevich, I. Salvado, M. Ferreira, Sol-gel coatings for corrosion protection of metals, *J. Mater. Chem.* 15 (2005) 5099–5111. doi:10.1039/b419153f.
- [97] T. Chou, Organic inorganic hybrid coatings for corrosion protection, *J. Non. Cryst. Solids.* 290 (2001) 153–162. doi:10.1016/S0022-3093(01)00818-3.

- [98] J. Ma, M. Thompson, N. Zhao, D. Zhu, Similarities and differences in coatings for magnesium-based stents and orthopaedic implants, *J. Orthop. Transl.* 2 (2014) 1–13. doi:10.1016/j.jot.2014.03.004.
- [99] G.X. Shen, Y.C. Chen, C.J. Lin, Corrosion protection of 316 L stainless steel by a TiO₂ nanoparticle coating prepared by sol-gel method, *Thin Solid Films.* 489 (2005) 130–136. doi:10.1016/j.tsf.2005.05.016.
- [100] J. Harle, H.W. Kim, N. Mordan, J.C. Knowles, V. Salih, Initial responses of human osteoblasts to sol-gel modified titanium with hydroxyapatite and titania composition, *Acta Biomater.* 2 (2006) 547–556. doi:10.1016/j.actbio.2006.05.005.
- [101] H. Tang, T.Z. Xin, Y. Luo, F.P. Wang, In vitro degradation of AZ31 magnesium alloy coated with hydroxyapatite by sol-gel method, *Mater. Sci. Technol.* 29 (2013) 547–552. doi:10.1179/1743284712Y.0000000180.
- [102] E.D. Mekeridis, I.A. Kartsonakis, G.C. Kordas, Multilayer organic-inorganic coating incorporating TiO₂ nanocontainers loaded with inhibitors for corrosion protection of AA2024-T3, *Prog. Org. Coatings.* 73 (2012) 142–148. doi:10.1016/j.porgcoat.2011.10.005.
- [103] L.M. Rueda, C. Nieves, C.A. Hernández Barrios, A.E. Coy, F. Viejo, Design of TEOS-GPTMS sol-gel coatings on rare-earth magnesium alloys employed in the manufacture of orthopaedic implants, *J. Phys. Conf. Ser.* 687 (2016) 012013. doi:10.1088/1742-6596/687/1/012013.
- [104] C.A. Hernández-Barrios, N.Z. Duarte, L.M. Hernández, D.Y. Peña, A.E. Coy, F. Viejo, Synthesis of hybrid sol-gel coatings for corrosion protection of we54-ae magnesium alloy, *J. Phys. Conf. Ser.* 466 (2013) 012011. doi:10.1088/1742-6596/466/1/012011.
- [105] M.F. Montemor, Functional and smart coatings for corrosion protection: A review of recent advances, *Surf. Coatings Technol.* 258 (2014) 17–37. doi:10.1016/j.surfcoat.2014.06.031.
- [106] C. Liu, Y. Xin, X. Tian, J. Zhao, P.K. Chu, Corrosion resistance of titanium ion implanted AZ91 magnesium alloy, *J. Vac. Sci. Technol. A Vacuum, Surfaces, Film.* 25 (2007) 334. doi:10.1116/1.2699371.
- [107] Y. Xin, C. Liu, W. Zhang, K. Huo, G. Tang, X. Tian, et al., Corrosion resistance of ZrO₂-Zr-coated biodegradable surgical magnesium alloy, *J. Mater. Res.* 23 (2011) 312–319. doi:10.1557/JMR.2008.0040.
- [108] Z. Chun-Yan, Z. Rong-Chang, L. Cheng-Long, G. Jia-Cheng, Comparison of calcium phosphate coatings on Mg-Al and Mg-Ca alloys and their corrosion behavior in Hank's solution, *Surf. Coatings Technol.* 204 (2010) 3636–3640. doi:10.1016/j.surfcoat.2010.04.038.
- [109] J.M. Seitz, K. Collier, E. Wulf, D. Bormann, F.W. Bach, Comparison of the corrosion behavior of coated and uncoated magnesium alloys in an in vitro corrosion environment, *Adv. Eng. Mater.* 13 (2001) 313–23. doi:10.1002/adem.201080144.
- [110] H.M. Wong, K.W.K. Yeung, K.O. Lam, V. Tam, P.K. Chu, K.D.K. Luk, et al., A biodegradable polymer-based coating to control the performance of magnesium alloy

- orthopaedic implants, *Biomaterials*. 31 (2010) 2084–2096.
doi:10.1016/j.biomaterials.2009.11.111.
- [111] S. V. Dorozhkin, Calcium orthophosphate coatings on magnesium and its biodegradable alloys, *Acta Biomater.* 10 (2014) 2919–2934.
doi:10.1016/j.actbio.2014.02.026.
- [112] H. Hornberger, S. Virtanen, A.R. Boccaccini, Biomedical coatings on magnesium alloys - A review, *Acta Biomater.* 8 (2012) 2442–2455.
doi:10.1016/j.actbio.2012.04.012.
- [113] J.X. Yang, F.Z. Cui, I.S. Lee, Y. Zhang, Q.S. Yin, H. Xia, et al., In vivo biocompatibility and degradation behavior of Mg alloy coated by calcium phosphate in a rabbit model, *J. Biomater. Appl.* 27 (2012) 153–64. doi:10.1177/0885328211398161.
- [114] A. Roy, S.S. Singh, M.K. Datta, B. Lee, J. Ohodnicki, P.N. Kumta, Novel sol–gel derived calcium phosphate coatings on Mg4Y alloy, *Mater. Sci. Eng. B.* 176 (2011) 1679–1689. doi:10.1016/j.mseb.2011.08.007.
- [115] J. JH, H. JY, S. KS, K. HE, K. YH., Enhancing biocompatibility and corrosion resistance of Mg implants via surface treatments, *J. Biomater. Appl.* 27 (2012) 469–76. doi:10.1177/0885328211412633.
- [116] A. Abdal-Hay, N.A.M. Barakat, J.K. Lim, Hydroxyapatite-doped poly(lactic acid) porous film coating for enhanced bioactivity and corrosion behavior of AZ31 Mg alloy for orthopedic applications, *Ceram. Int.* 39 (2013) 183–195.
doi:10.1016/j.ceramint.2012.06.008.
- [117] H.R. Bakhsheshi-Rad, M.H. Idris, M.R. Abdul-Kadir, Synthesis and in vitro degradation evaluation of the nano-HA/MgF₂ and DCPD/MgF₂ composite coating on biodegradable Mg-Ca-Zn alloy, *Surf. Coatings Technol.* 222 (2013) 79–89.
doi:10.1016/j.surfcoat.2013.02.007.
- [118] J. Niu, G. Yuan, Y. Liao, L. Mao, J. Zhang, Y. Wang, et al., Enhanced biocorrosion resistance and biocompatibility of degradable Mg-Nd-Zn-Zr alloy by brushite coating, *Mater. Sci. Eng. C.* 33 (2013) 4833–4841. doi:10.1016/j.msec.2013.08.008.
- [119] C.F. Dunne, G.K. Levy, O. Hakimi, E. Aghion, B. Twomey, K.T. Stanton, Corrosion behavior of biodegradable magnesium alloys with hydroxyapatite coatings, *Surf. Coatings Technol.* 289 (2016) 37–44. doi:10.1016/j.surfcoat.2016.01.045.
- [120] S. Singh, R. Manoj Kumar, K.K. Kuntal, P. Gupta, S. Das, R. Jayaganthan, et al., Sol-Gel Derived Hydroxyapatite Coating on Mg-3Zn Alloy for Orthopedic Application, *Jom.* 67 (2015). doi:10.1007/s11837-015-1364-1.
- [121] Z. Yao, Q. Xia, L. Chang, C. Li, Z. Jiang, Structure and properties of compound coatings on Mg alloys by micro-arc oxidation/hydrothermal treatment, *J. Alloys Compd.* 633 (2015) 435–442. doi:10.1016/j.jallcom.2015.02.008.
- [122] C. Santos, C. Piedade, P.J. Uggowitzer, M.F. Montemor, M.J. Carmezim, Parallel nano-assembling of a multifunctional GO/HapNP coating on ultrahigh-purity magnesium for biodegradable implants, *Appl. Surf. Sci.* 345 (2015) 387–393.
doi:10.1016/j.apsusc.2015.03.182.

- [123] R. ZENG, Y. HU, F. ZHANG, Y. HUANG, Z. WANG, S. LI, et al., Corrosion resistance of cerium-doped zinc calcium phosphate chemical conversion coatings on AZ31 magnesium alloy, *Trans. Nonferrous Met. Soc. China*. 26 (2016) 472–483. doi:10.1016/S1003-6326(16)64102-X.
- [124] H.R. Bakhsheshi-Rad, E. Hamzah, R. Ebrahimi-Kahrizangi, M. Daroonparvar, M. Medraj, Fabrication and characterization of hydrophobic microarc oxidation/poly-lactic acid duplex coating on biodegradable Mg–Ca alloy for corrosion protection, *Vacuum*. 125 (2016) 185–188. doi:10.1016/j.vacuum.2015.12.022.
- [125] H.R. Bakhsheshi-Rad, E. Hamzah, A.F. Ismail, M. Daroonparvar, M.A.M. Yajid, M. Medraj, Preparation and characterization of NiCrAlY/nano-YSZ/PCL composite coatings obtained by combination of atmospheric plasma spraying and dip coating on Mg-Ca alloy, *J. Alloys Compd.* 658 (2016) 440–452. doi:10.1016/j.jallcom.2015.10.196.
- [126] A. Zomorodian, C. Santos, M.J. Carmezim, T.M.E. Silva, J.C.S. Fernandes, M.F. Montemor, “In-vitro” corrosion behavior of the magnesium alloy with Al and Zn (AZ31) protected with a biodegradable polycaprolactone coating loaded with hydroxyapatite and cephalixin, *Electrochim. Acta*. 179 (2015) 431–440. doi:10.1016/j.electacta.2015.04.013.
- [127] S. Shen, S. Cai, G. Xu, H. Zhao, S. Niu, R. Zhang, Influence of heat treatment on bond strength and corrosion resistance of sol-gel derived bioglass-ceramic coatings on magnesium alloy, *J. Mech. Behav. Biomed. Mater.* 45 (2015) 166–174. doi:10.1016/j.jmbbm.2015.02.005.
- [128] B.M. Wilke, L. Zhang, W. Li, C. Ning, C. Chen, Y. Gu, Corrosion performance of MAO coatings on AZ31 Mg alloy in simulated body fluid vs. Earle’s Balance Salt Solution, *Appl. Surf. Sci.* 363 (2016) 328–337. doi:10.1016/j.apsusc.2015.12.026.
- [129] P. Tian, X. Liu, Surface modification of biodegradable magnesium and its alloys for biomedical applications, *Regen. Biomater.* (2015) 135–151. doi:10.1093/rb/rbu013.
- [130] F.-M. Chen, X. Liu, Advancing biomaterials of human origin for tissue engineering, *Prog. Polym. Sci.* (2015). doi:10.1016/j.progpolymsci.2015.02.004.
- [131] M. Dash, F. Chiellini, R.M. Ottenbrite, E. Chiellini, Chitosan - A versatile semi-synthetic polymer in biomedical applications, *Prog. Polym. Sci.* 36 (2011) 981–1014. doi:10.1016/j.progpolymsci.2011.02.001.
- [132] I.-Y. Kim, S.-J. Seo, H.-S. Moon, M.-K. Yoo, I.-Y. Park, B.-C. Kim, et al., Chitosan and its derivatives for tissue engineering applications, *Biotechnol. Adv.* 26 (2008) 1–21. doi:10.1016/j.biotechadv.2007.07.009.
- [133] F. Gobeaux, G. Mosser, a. Anglo, P. Panine, P. Davidson, M.-M. Giraud-Guille, et al., Fibrillogenesis in Dense Collagen Solutions: A Physicochemical Study, *J. Mol. Biol.* 376 (2008) 1509–1522. doi:10.1016/j.jmb.2007.12.047.
- [134] J.K. Mouw, G. Ou, V.M. Weaver, Extracellular matrix assembly: a multiscale deconstruction, *Nat. Rev. Mol. Cell Biol.* 15 (2014) 771–785. doi:10.1038/nrm3902.
- [135] C. NA, *Biologie*, in: É. Du, R.P. Inc. (Eds.), *Biologie*, Première é, Saint-Laurent, 1995.

- [136] G. Matton, a. Anseeuw, F. De Keyser, The history of injectable biomaterials and the biology of collagen, *Aesthetic Plast. Surg.* 9 (1985) 133–140. doi:10.1007/BF01570345.
- [137] R.L. Trelstad, K. Hayashi, J. Gross, Collagen fibrillogenesis: intermediate aggregates and suprafibrillar order., *Proc. Natl. Acad. Sci. U. S. A.* 73 (1976) 4027–31. doi:10.1073/pnas.73.11.4027.
- [138] D.E. Birk, J.M. Fitch, J.P. Babiartz, K.J. Doane, T.F. Linsenmayer, Collagen fibrillogenesis in vitro: interaction of types I and V collagen regulates fibril diameter., *J. Cell Sci.* 95 (Pt 4) (1990) 649–657. doi:2384532.
- [139] K.E. Kadler, A. Hill, E.G. Canty-Laird, Collagen fibrillogenesis: fibronectin, integrins, and minor collagens as organizers and nucleators, *Curr. Opin. Cell Biol.* 20 (2008) 495–501. doi:10.1016/j.ceb.2008.06.008.
- [140] F.M. Chen, H.H. Sun, H. Lu, Q. Yu, Stem cell-delivery therapeutics for periodontal tissue regeneration, *Biomaterials.* 33 (2012) 6320–6344. doi:10.1016/j.biomaterials.2012.05.048.
- [141] M.M. Giraud Guille, C. Helary, S. Vigier, N. Nassif, Dense fibrillar collagen matrices for tissue repair, *Soft Matter.* 6 (2010) 4963. doi:10.1039/c0sm00260g.
- [142] D. Mushahary, C. Wen, J.M. Kumar, J. Lin, N. Harishankar, P. Hodgson, et al., Collagen type-I leads to in vivo matrix mineralization and secondary stabilization of Mg–Zr–Ca alloy implants, *Colloids Surfaces B Biointerfaces.* 122 (2014) 719–728. doi:10.1016/j.colsurfb.2014.08.005.
- [143] Z.L. Wang, Y.H. Yan, T. Wan, H. Yang, Poly(L-lactic acid)/hydroxyapatite/collagen composite coatings on AZ31 magnesium alloy for biomedical application, *Proc. Inst. Mech. Eng. H.* 227 (2013) 1094–103. doi:10.1177/0954411913493845.
- [144] H.C. Park, H.R. Pant, C.S. Kim, Effect on Corrosion Behavior of Collagen Film/Fiber coated AZ31 Magnesium Alloy, *Dig. J. Nanomater. Biostructures.* 8 (2013) 1227–1234.
- [145] M.C. Gómez-Guillén, B. Giménez, M.E. López-Caballero, M.P. Montero, Functional and bioactive properties of collagen and gelatin from alternative sources: A review, *Food Hydrocoll.* 25 (2011) 1813–1827. doi:10.1016/j.foodhyd.2011.02.007.
- [146] M.N.. Ravi Kumar, A review of chitin and chitosan applications, *React. Funct. Polym.* 46 (2000) 1–27. doi:10.1016/S1381-5148(00)00038-9.
- [147] T. Kawakami, M. Antoh, H. Hasegawa, T. Yamagishi, M. Ito, S. Eda, Experimental study on osteoconductive properties of a chitosan-bonded hydroxyapatite self-hardening paste, *Biomaterials.* 13 (1992) 759–63. doi:10.1016/0142-9612(92)90014-F.
- [148] F. Zhao, Y. Yin, W.W. Lu, J.C. Leong, W. Zhang, J. Zhang, et al., Preparation and histological evaluation of biomimetic three-dimensional hydroxyapatite/chitosan-gelatin network composite scaffolds, *Biomaterials.* 23 (2002) 3227–34. doi:10.1016/S0142-9612(02)00077-7.
- [149] Q. Hu, B. Li, M. Wang, J. Shen, Preparation and characterization of biodegradable chitosan/hydroxyapatite nanocomposite rods via in situ hybridization: a potential

- material as internal fixation of bone fracture, *Biomaterials*. 25 (2004).
doi:10.1016/S0142-9612(03)00582-9.
- [150] Y. Yin, F. Ye, J. Cui, F. Zhang, X. Li, K. Yao, Preparation and characterization of macroporous chitosan-gelatin/beta-tricalcium phosphate composite scaffolds for bone tissue engineering., *J. Biomed. Mater. Res. A*. 67 (2003) 844–855.
doi:10.1002/jbm.a.10153.
- [151] a. M. Fekry, a. a. Ghoneim, M. a. Ameer, Electrochemical impedance spectroscopy of chitosan coated magnesium alloys in a synthetic sweat medium, *Surf. Coatings Technol.* 238 (2014) 126–132. doi:10.1016/j.surfcoat.2013.10.058.
- [152] J.D. Bumgardner, R. Wisner, P.D. Gerard, P. Bergin, B. Chestnutt, M. Marin, Chitosan: potential use as a bioactive coating for orthopaedic and craniofacial/dental implants, *J. Biomater. Sci. Polym. Ed.* 14 (2003) 423–38. doi:10.1163/156856203766652048.
- [153] J. Zhang, C. Dai, J. Wei, Z. Wen, S. Zhang, C. Chen, Degradable behavior and bioactivity of micro-arc oxidized AZ91D Mg alloy with calcium phosphate/chitosan composite coating in m-SBF, *Colloids Surfaces B Biointerfaces*. 111 (2013) 179–187. doi:10.1016/j.colsurfb.2013.05.040.
- [154] A. Hunter, C.W. Archer, P.S. Walker, G.W. Blunn, Attachment and proliferation of osteoblasts and fibroblasts on biomaterials for orthopaedic use, *Biomaterials*. 16 (1995) 287–295. doi:10.1016/0142-9612(95)93256-D.
- [155] I.E. Wang, J. Shan, S. Oh, C.K. Kepler, F.H. Chen, H.H. Lu, Role of osteoblasts-fibroblasts in the formation of the ligament to bone interface, *J. Orthopaedic Res.* 25 (2007) 1609–1620. doi:10.1002/jor.20475.
- [156] K. Anselme, Osteoblast adhesion on biomaterials, *Biomaterials*. 21 (2000) 667–681. doi:10.1016/S0142-9612(99)00242-2.
- [157] S. Rhee, F. Grinnell, Fibroblast mechanics in 3D collagen matrices, *Adv. Drug Deliv. Rev.* 59 (2007) 1299–1305. doi:10.1016/j.addr.2007.08.006.
- [158] Encyclopædia Britannica, Fibroblast, *Encycl. Br. Online*. (2016).
<http://www.britannica.com/science/fibroblast> (accessed January 5, 2016).
- [159] L.C. Baxter, V. Frauchiger, M. Textor, R.G. Richards, I. Biology, FIBROBLAST AND OSTEOBLAST ADHESION AND MORPHOLOGY ON CALCIUM PHOSPHATE SURFACES, 4 (2002) 1–17.
- [160] S. Porter, The role of the fibroblast in wound contraction and healing, *Wounds UK*. 3 (2007) 33–40.
- [161] Mmblxbx, Human osteoblast, *Scienceay*. (2009).
<http://sciencerey.com/biology/microbiology/osteoblast/>.
- [162] A.K. Nair, A. Gautieri, S.-W. Chang, M.J. Buehler, Molecular mechanics of mineralized collagen fibrils in bone, *Nat. Commun.* 4 (2013) 1724. doi:10.1038/ncomms2720.
- [163] S. Viguet-Carrin, P. Garnero, P.D. Delmas, The role of collagen in bone strength, *Osteoporos. Int.* 17 (2006) 319–336. doi:10.1007/s00198-005-2035-9.

- [164] Encyclopædia Britannica, Osteoblast, *Encycl. Br. Online*. (2016).
<http://www.britannica.com/science/osteoblast> (accessed January 4, 2016).
- [165] T.P. Kunzler, T. Drobek, M. Schuler, N.D. Spencer, Systematic study of osteoblast and fibroblast response to roughness by means of surface-morphology gradients, *Biomaterials*. 28 (2007) 2175–2182. doi:10.1016/j.biomaterials.2007.01.019.
- [166] K.D. Chessel, C.C. Clark, C.T. Brighton, J. Black, Cellular responses to chemical and morphologic aspect of biomaterial surfaces. II. The biosynthetic and migratory response of bone cell population, *J. Biomed. Mater. Res. A*. 29 (1995) 1101–10. doi:10.1002/jbm.820290910.
- [167] R.M. Shelton, A.C. Rasmussen, J.E. Davies, Protein adsorption at the interface between charged polymer substrata and migrating osteoblast, *Biomaterials*. 9 (1998) 24–9. doi:10.1016/0142-9612(88)90065-8.
- [168] B.D. Boyan, T.W. Hummert, D.D. Dean, Z. Schwartz, Role of material surfaces in regulating bone and cartilage cell response, *Biomaterials*. 17 (1996) 137–146. doi:10.1016/0142-9612(96)85758-9.
- [169] H.R. Bakhsheshi-Rad, M.H. Idris, M.R.A. Kadir, M. Daroonparvar, Effect of fluoride treatment on corrosion behavior of Mg-Ca binary alloy for implant application, *Trans. Nonferrous Met. Soc. China (English Ed.)* 23 (2013) 699–710. doi:10.1016/S1003-6326(13)62519-4.
- [170] S. Kunjukunju, A. Roy, M. Ramanathan, B. Lee, J.E. Candiello, P.N. Kumta, A layer-by-layer approach to natural polymer-derived bioactive coatings on magnesium alloys, *Acta Biomater.* 9 (2013) 8690–8703. doi:10.1016/j.actbio.2013.05.013.
- [171] M. Carboneras, M.C. García-Alonso, M.L. Escudero, Biodegradation kinetics of modified magnesium-based materials in cell culture medium, *Corros. Sci.* 53 (2011) 1433–1439. doi:10.1016/j.corsci.2011.01.014.
- [172] S. V. Lamaka, G. Knörnschild, D. V. Snihirova, M.G. Taryba, M.L. Zheludkevich, M.G.S. Ferreira, Complex anticorrosion coating for ZK30 magnesium alloy, *Electrochim. Acta*. 55 (2009) 131–141. doi:10.1016/j.electacta.2009.08.018.
- [173] M.G. Taryba, S. V. Lamaka, D. V. Snihirova, M.G.S. Ferreira, M.F. Montemor, W.K. Wijting, et al., The combined use of scanning vibrating electrode technique and micro-potentiometry to assess the self-repair processes in defects on smart coatings applied to galvanized steel, *Electrochim. Acta*. 56 (2011) 4475–4488. doi:10.1016/j.electacta.2011.02.048.
- [174] K. Aoki, Nernst equation complicated by electric random percolation at conducting polymer-coated electrodes, *J. Electroanal. Chem. Interfacial Electrochem.* 310 (1991) 1–12. doi:10.1016/0022-0728(91)85247-M.
- [175] S. V. Lamaka, G. Knörnschild, D. V. Snihirova, M.G. Taryba, M.L. Zheludkevich, M.G.S. Ferreira, Complex anticorrosion coating for ZK30 magnesium alloy, *Electrochim. Acta*. 55 (2009) 131–141. doi:10.1016/j.electacta.2009.08.018.
- [176] H. Ding, L. Liu, S. Kamado, W. Ding, Y. Kojima, Study of the microstructure, texture and tensile properties of as-extruded AZ91 magnesium alloy, *J. Alloys Compd.* 456

- (2008) 400–406. doi:10.1016/j.jallcom.2007.02.045.
- [177] M. Jamesh, S. Kumar, T.S.N.S. Narayanan, Corrosion behavior of commercially pure Mg and ZM21 Mg alloy in Ringer ' s solution – Long term evaluation by EIS, *Corros. Sci.* 53 (2011) 645–654. doi:10.1016/j.corsci.2010.10.011.
- [178] R.C. Zeng, Y. Hu, S.K. Guan, H.Z. Cui, E.H. Han, Corrosion of magnesium alloy AZ31: The influence of bicarbonate, sulphate, hydrogen phosphate and dihydrogen phosphate ions in saline solution, *Corros. Sci.* 86 (2014) 171–182. doi:10.1016/j.corsci.2014.05.006.
- [179] S.N. (2015) Lafuente B, Downs R T, Yang H, The power of databases: the RRUFF project., 2015. ruff.info.
- [180] S. Koutsopoulos, Synthesis and characterization of hydroxyapatite crystals : A review study on the analytical methods, *J. Biomed. Mater. Res.* 62 (2002) 600–612.
- [181] X. Li, Z. Weng, W. Yuan, X. Luo, H.M. Wong, X. Liu, et al., Corrosion resistance of dicalcium phosphate dihydrate/poly(lactic-co-glycolic acid) hybrid coating on AZ31 magnesium alloy, *Corros. Sci.* 102 (2016) 209–221. doi:doi:10.1016/j.corsci.2015.10.010.
- [182] H.E. Friedrich, B.L. Mordike, *Magnesium Technology*, Springer-Verlag Berlin Heidelberg, 2006. doi:10.1007/3-540-30812-1.
- [183] S.K. Poznyak, M.L. Zheludkevich, D. Raps, F. Gammel, K.A. Yasakau, M.G.S. Ferreira, Preparation and corrosion protective properties of nanostructured titania-containing hybrid sol–gel coatings on AA2024, *Prog. Org. Coatings.* 62 (2008) 226–235. doi:doi:10.1016/j.porgcoat.2007.12.004.
- [184] J. Meng, Z.T. W. Sun, X. Qiu, D. Zhang, 2 – Corrosion performance of magnesium (Mg) alloys containing rare-earth (RE) elements, *Corros. Prev. Magnes. Alloy.* (2013) 38–60. doi:10.1533/9780857098962.1.38.
- [185] A. Ulrich, N. Ott, A. Tournier-Fillon, N. Homazava, P. Schmutz, Investigation of corrosion behavior of biodegradable magnesium alloys using an online-micro-flow capillary flow injection inductively coupled plasma mass spectrometry setup with electrochemical control, *Spectrochim. Acta Part B At. Spectrosc.* 66 (2011) 536–545. doi:10.1016/j.sab.2011.04.009.
- [186] M. Ascencio, M. Pekguleryuz, S. Omanovic, An investigation of the corrosion mechanisms of WE43Mg alloy in a modified simulated body fluid solution: The effect of electrolyte renewal, *Corros. Sci.* 91 (2015) 297–310. doi:10.1016/j.corsci.2014.11.034.
- [187] R. Yibin, H. Jingjing, Z. Bingchun, Y. Ke, Preliminary study of biodegradation of AZ31B magnesium alloy, *Front. Mater. Sci. China.* 1 (2007) 401–404. doi:10.1007/s11706-007-0073-2.
- [188] M. Ascencio, M. Pekguleryuz, S. Omanovic, An investigation of the corrosion mechanisms of WE43 Mg alloy in a modified simulated body fluid solution: The influence of immersion time, *Corros. Sci.* 87 (2014) 489–503. doi:10.1016/j.corsci.2014.07.015.

- [189] G. Baril, N. Pébère, Corrosion of pure magnesium in aerated and deaerated sodium sulphate solutions, *Corros. Sci.* 43 (2001) 471–484. doi:10.1016/S0010-938X(00)00095-0.
- [190] Z. Li, X. Gu, S. Lou, Y. Zheng, The development of binary Mg-Ca alloys for use as biodegradable materials within bone, *Biomaterials*. 29 (2008) 1329–1344. doi:10.1016/j.biomaterials.2007.12.021.
- [191] T. Kokubo, Formation of biologically active bone-like apatite on metals and polymers by a biomimetic process, *Thermochim. Acta.* 280–281 (1996) 479–490. doi:http://dx.doi.org/10.1016/0040-6031(95)02784-X.
- [192] P. Zhu, Y. Masuda, K. Koumoto, The effect of surface charge on hydroxyapatite nucleation, *Biomaterials*. 25 (2004) 3915–3921. doi:10.1016/j.biomaterials.2003.10.022.
- [193] A.S. Gnedenkov, S.L. Sinebryukhov, D. V. Mashtalyar, S. V. Gnedenkov, Localized corrosion of the Mg alloys with inhibitor-containing coatings: SVET and SIET studies, *Corros. Sci.* 102 (2015) 269–278. doi:10.1016/j.corsci.2015.10.015.
- [194] Y. Xin, K. Huo, T. Hu, G. Tang, P.K. Chu, Corrosion products on biomedical magnesium alloy soaked in simulated body fluids, *J. Mater. Res.* 24 (2009) 2711–2719. doi:10.1557/jmr.2009.0323.
- [195] Y. Xin, K. Huo, H. Tao, G. Tang, P.K. Chu, Influence of aggressive ions on the degradation behavior of biomedical magnesium alloy in physiological environment, *Acta Biomater.* 4 (2008) 2008–2015. doi:10.1016/j.actbio.2008.05.014.
- [196] R. Of, T. Draft, a R.E. Invited, W.T. Comments, O.F. Any, R. Patent, et al., Draft International Standard Iso / Fdis, English. 2005 (2005) 42.
- [197] R. Rettig, S. Virtanen, Composition of corrosion layers on a magnesium rare-earth alloy in simulated body fluids, *J. Biomed. Mater. Res. - Part A.* 88 (2007) 359–369. doi:10.1002/jbm.a.31887.
- [198] F.C. Tai, Clifford Y., Polymorphism of CaCO₃, precipitated in a constant-composition environment, *AIChE J.* 44 (1998) 1790–1798.
- [199] X.-L.P. Jun-Yen Uan, Bing-Lung Yu, Morphological and Microstructural Characterization of the Aragonitic CaCO₃/Mg,Al-Hydroxycalcite Coating on Mg-9 Wt Pct Al-1 Wt Pct Zn Alloy to Protect against Corrosion, *Metall. Mater. Trans. A.* 39 (2008) 3233–3245. doi:10.1007/s11661-008-9669-0.
- [200] D. Thirumalaikumarasamy, K. Shanmugam, V. Balasubramanian, Comparison of the corrosion behavior of AZ31B magnesium alloy under immersion test and potentiodynamic polarization test in NaCl solution, *J. Magnes. Alloy.* 2 (2014) 36–49. doi:10.1016/j.jma.2014.01.004.
- [201] B. Zberg, P.J. Uggowitzer, J.F. Löffler, MgZnCa glasses without clinically observable hydrogen evolution for biodegradable implants., *Nat. Mater.* 8 (2009) 887–91. doi:10.1038/nmat2542.
- [202] A.H. B. Heublein, R. Rohde, V. Kaese, M. Niemeyer, W. Hartung, Biocorrosion of

- magnesium alloys: a new principle in cardiovascular implant technology?, *Heart*. 89 (2003) 651–656. doi:10.1136/heart.89.6.651.
- [203] Y.F. Zheng, X.N. Gu, Y.L. Xi, D.L. Chai, In vitro degradation and cytotoxicity of Mg/Ca composites produced by powder metallurgy, *Acta Biomater.* 6 (2010) 1783–1791. doi:10.1016/j.actbio.2009.10.009.
- [204] X.N. Gu, Y.F. Zheng, L.J. Chen, Influence of artificial biological fluid composition on the biocorrosion of potential orthopedic Mg-Ca, AZ31, AZ91 alloys., *Biomed. Mater.* 4 (2009) 065011. doi:10.1088/1748-6041/4/6/065011.
- [205] J. Tang, J. Wang, X. Xie, P. Zhang, Y. Lai, Y. Li, et al., Surface coating reduces degradation rate of magnesium alloy developed for orthopaedic applications, *J. Orthop. Transl.* 1 (2013) 41–48. doi:10.1016/j.jot.2013.06.003.
- [206] J. Degner, F. Singer, L. Cordero, A.R. Boccaccini, S. Virtanen, Electrochemical investigations of magnesium in DMEM with biodegradable polycaprolactone coating as corrosion barrier, *Appl. Surf. Sci.* 282 (2013) 264–270. doi:10.1016/j.apsusc.2013.05.115.
- [207] M. Iñigo, F. Feyerabend, R. Willumeit-Römer, O. Van der Biest, Influence on testing environment in the degradation of behavior of magnesium alloys for bioabsorbable implants, in: *TMS2015 Annu. Meet. Suppl. Proc.*, John Wiley & Sons, New Jersey, 2015: pp. 499–506.
- [208] X. Wang, S. Hayakawa, K. Tsuru, O. A., Bioactive titania-gel layers formed by chemical treatment of Ti substrate with a H₂O₂/HCl solution, *Biomaterials.* 23 (2002) 1353–7. doi:10.1016/S0142-9612(01)00254-X.
- [209] C. Gobel, P. Simon, J. Buder, H. Tlatlik, R. Kniep, Phase formation and morphology of calcium phosphate-gelatine-composites grown by double diffusion technique: the influence of fluoride, *J. Mater. Chem.* 14 (2004) 2225. doi:10.1039/b403503h.
- [210] C. Combes, C. Rey, Amorphous calcium phosphates: Synthesis, properties and uses in biomaterials, *Acta Biomater.* 6 (2010) 3362–3378. doi:10.1016/j.actbio.2010.02.017.
- [211] M. Manoj, R. Subbiah, D. Mangalaraj, N. Ponpandian, C. Viswanathan, K. Park, Influence of Growth Parameters on the Formation of Hydroxyapatite (HAp) Nanostructures and Their Cell Viability Studies, *Nanobiomedicine.* (2015) 1. doi:10.5772/60116.
- [212] J.X. Yang, Y.P. Jiao, Q.S. Yin, Y. Zhang, T. Zhang, Calcium phosphate coating on magnesium alloy by biomimetic method: Investigation of morphology, composition and formation process, *Front. Mater. Sci. China.* 2 (2008) 149–155. doi:10.1007/s11706-008-0025-5.
- [213] P. Cordoba-Torres, M. Keddad, R.P. Nogueira, On the intrinsic electrochemical nature of the inductance in EIS. A Monte Carlo simulation of the two-consecutive-step mechanism: The flat surface 2 D case, *Electrochim. Acta.* 54 (2008) 518–523. doi:10.1016/j.electacta.2008.07.023.
- [214] R.M. Lozano, B.T. Pérez-Maceda, M. Carboneras, E. Onofre-Bustamante, M.C. García-Alonso, M.L. Escudero, Response of MC3T3-E1 osteoblasts, L929 fibroblasts,

- and J774 macrophages to fluoride surface-modified AZ31 magnesium alloy, *J. Biomed. Mater. Res. - Part A*. 101 (2013) 2753–2762. doi:10.1002/jbm.a.34579.
- [215] Edith Muriel Carlisle, Silicon, in: E. Frieden (Ed.), *Biochem. Essent. Ultratrace Elem.*, Plenum Press, New York, 1984: pp. 257–291. doi:10.1007/978-1-84996-417-3.
- [216] D. a Puleo, a Nanci, Understanding and controlling the bone implant-interface, *Biomaterials*. 20 (1999) 2311–21. doi:10.1016/S0142-9612(99)00160-X.
- [217] H.W. Kim, L.H. Li, E.J. Lee, S.H. Lee, H.E. Kim, Fibrillar assembly and stability of collagen coating on titanium for improved osteoblast responses, *J. Biomed. Mater. Res. - Part A*. 75 (2005) 629–638. doi:10.1002/jbm.a.30463.
- [218] N. Zhao, B. Workman, D. Zhu, Endothelialization of novel magnesium-rare earth alloys with fluoride and collagen coating, *Int. J. Mol. Sci.* 15 (2014) 5263–5276. doi:10.3390/ijms15045263.
- [219] F. Jiang, H. H??rber, J. Howard, D.J. M??ller, Assembly of collagen into microribbons: Effects of pH and electrolytes, *J. Struct. Biol.* 148 (2004) 268–278. doi:10.1016/j.jsb.2004.07.001.
- [220] S. Tang, B. Tian, Y.-J. Guo, Z.-A. Zhu, Y.-P. Guo, Chitosan/carbonated hydroxyapatite composite coatings: Fabrication, structure and biocompatibility, *Surf. Coatings Technol.* 251 (2014) 210–216. doi:10.1016/j.surfcoat.2014.04.028.
- [221] S. V. Dorozhkin, Calcium orthophosphate coatings on magnesium and its biodegradable alloys, *Acta Biomater.* 10 (2014) 2919–2934. doi:10.1016/j.actbio.2014.02.026.
- [222] G.-L. Song, *Corrosion prevention of magnesium alloys*, Woodhead, Philadelphia, PA, USA, Philadelphia, 2013.
- [223] K. Yang, L. Tan, Control of biodegradation of magnesium (Mg) alloys for medical applications, in: G.-L. Song (Ed.), *Corros. Prev. Magnes. Alloy.*, Woodhead Publishing Limited, 2013: pp. 509–538. doi:10.1533/9780857098962.4.509.
- [224] Miller-Keane Encyclopedia and Dictionary, Cortical bone, (2003). <http://medical-dictionary.thefreedictionary.com/cortical+bone> (accessed December 27, 2015).
- [225] Farlex Partner Medical Dictionary, Homeostasis, (2012). <http://medical-dictionary.thefreedictionary.com/homeostasis> (accessed December 22, 2015).
- [226] The American Heritage® Medical Dictionary, hypermagnesemia, (2007). <http://medical-dictionary.thefreedictionary.com/hypermagnesemia> (accessed December 22, 2015).
- [227] A. International Handbook Committee, Volume 14: Forming and Forging, 1993. doi:10.1007/s13398-014-0173-7.2.
- [228] A. International Handbook Committee, *Mechanical Testing and Evaluation Handbook*, ASM International, 2000. www.asminternational.org.
- [229] Miller-Keane Encyclopedia and Dictionary, Apposition, (2003). <http://medical-dictionary.thefreedictionary.com/bone+apposition> (accessed December 27, 2015).

- [230] Encyclopaedia Britannica, Trabecular bone, *Encycl. Br. Online*. (2015). <http://www.britannica.com/science/cancellous-bone> (accessed December 28, 2015).
- [231] W. Baldwin, *Metallography and Microstructures Handbook*, 2004. doi:10.1361/asmhba0003771.
- [232] B. Craig, S.L. Pohlman, Forms of Corrosion, in: *ASM Met. Handb. - Vol. 13*, 1992: p. 183.
- [233] A.S.M. International, H. Committee, *ASM Metals Handbook Volume 13, Corrosion*, United States of America, 1992.
- [234] American Heritage® Dictionary of the English Language Fifth Edition, Chelating, Free Dict. by Farlex Online. (2011). <http://www.thefreedictionary.com/chelating> (accessed January 8, 2016).
- [235] F.E. American Heritage® Dictionary of the English Language, Albumin, Free Dict. by Farlex Online. (2011). <http://www.thefreedictionary.com/albumin> (accessed March 25, 2016).
- [236] American Heritage® Dictionary of the English Language Fifth Edition, Polyelectrolyte, Free Dict. by Farlex Online. (2011). <http://www.thefreedictionary.com/polyelectrolyte> (accessed January 11, 2016).
- [237] A Dictionary of Biology, Deacetylation, *Encyclopedia.com*. (2004). <http://www.encyclopedia.com>.
- [238] American Heritage® Dictionary of the English Language Fifth Edition, Oligosaccharides, Free Dict. by Farlex Online. (2011). <http://www.thefreedictionary.com/Oligosaccharides> (accessed January 12, 2016).
- [239] Gale Encyclopedia of Medicine, osteoconduction, Free Dict. by Farlex Online. (2008). <http://medical-dictionary.thefreedictionary.com/osteoconduction> (accessed January 12, 2016).
- [240] Farlex Partner Medical Dictionary, Fibrocartilage, (2012). <http://medical-dictionary.thefreedictionary.com/fibrocartilage> (accessed January 2, 2016).
- [241] T.E. The American Heritage® New Dictionary of Cultural Literacy, Cellular differentiation, *Dictionary.com*. (2005). <http://dictionary.reference.com/browse/cellular-differentiation> (accessed January 23, 2016).
- [242] American Heritage® Dictionary of the English Language Fifth Edition, Vascularity, Free Dict. by Farlex Online. (2011).
- [243] C.E. Dictionary, Haemostasis, Free Dict. by Farlex Online. (2003). <http://www.thefreedictionary.com/haemostasis> (accessed January 5, 2016).
- [244] American Heritage® Dictionary of the English Language Fifth Edition, Growth factor, Free Dict. by Farlex Online. (2011). <http://www.thefreedictionary.com/growth+factor>.
- [245] S.E. Miller-Keane Encyclopedia and Dictionary of Medicine, Nursing, and Allied Health, Osteoid, Free Dict. by Farlex Online. (2003). [152](http://medical-</p>
</div>
<div data-bbox=)

dictionary.thefreedictionary.com/osteoid (accessed January 4, 2016).

- [246] Illustrated Dictionary of Podiatry and Foot Science by Jean Mooney, Bone mineralization, Free Dict. by Farlex Online. (2009). <http://medical-dictionary.thefreedictionary.com/bone+mineralization>.
- [247] The American Heritage® Medical Dictionary, Osteoclast, Free Dict. by Farlex Online. (2007). <http://medical-dictionary.thefreedictionary.com/osteoclast> (accessed January 4, 2016).
- [248] The American Heritage® Medical Dictionary, Cytoskeleton, Free Dict. by Farlex Online. (2007). <http://medical-dictionary.thefreedictionary.com/cytoskeleton> (accessed January 4, 2016).
- [249] N. and A.H.S.E. Miller-Keane Encyclopedia and Dictionary of Medicine, Actin, Free Dict. by Farlex Online. (2003). <http://medical-dictionary.thefreedictionary.com/actin> (accessed January 6, 2016).